GRADUATE COURSE IN PHYSICS
UNIVERSITY OF PISA

A real time glance at the Lepton Flavor Violating decay $\mu \to \mathrm{e}\gamma$ in the MEG experiment

PhD Thesis

Candidate

Dr. Luca Galli

Supervisor

Dr. Marco Grassi

October 2010

This thesis has been partially financed by the Italian Istituto Nazionale di Fisica Nucleare (INFN) and the Swiss federal laboratory Paul Scherrer Institut (PSI).

Non posso non pensare, pensò.

E. Hemingway, Il vecchio e il mare

Contents

Introduction

The MEG experiment investigates the lepton flavor violating decay $\mu \rightarrow e\gamma$ with a sensitivity on the branching ratio B($\mu \rightarrow e\gamma$) of 10^{-13}, 100 times lower than the current limit.

The Standard Model (SM) assumes complete conservation of the leptonic number and then predicts B($\mu \rightarrow e\gamma$)=0 at all the order of the theory. A modified Standard Model to contain the neutrino oscillation phenomena predicts B($\mu \rightarrow e\gamma$)$\approx 10^{-55}$, an unmeasurable number.

Supersymmetric and grand unification extensions of the SM predict the $\mu \rightarrow e\gamma$ process to lie around the MEG sensitivity. The experimental search to the LFV in this channel will lead to the first observation on physics beyond the standard model, or set strong constraints on those theories.

The MEG experiment was proposed and accepted by the host laboratory, the Paul Scherrer Institute in Villigen Switzerland, in 1999. The MEG collaboration developed an innovative technology based on the liquid Xenon scintillation indispensable for this ambitious project. The experiment is completely operative since the 2007, the physics data taking started officially in 2008 and will last until 2012 when the sufficient statistic is supposed be collected.

The MEG collaboration gathers ≈ 60 physicists from 5 different countries, namely: Italy, Japan, Switzerland, United States of America and Russia.

The first chapter of this Phd thesis discusses the theoretical motivations supporting this experiment. The principles of the Standard Model are shown, and its modification to contain the neutrino oscillation phenomena. The principal aspects of the SUSY-GUT theories are discussed together with their predictions regarding the $\mu \rightarrow e\gamma$ decay.

The second chapter describes the state of art of the LFV decay search, in particular in the μ sector, providing also a comparison with the τ one. The second part of the chapter is focused in the $\mu \rightarrow e\gamma$ search giving an historical introduction and a description of the last experimental result obtained by the MEGA experiment. The chapter ends presenting the experimental requirements for an experiment that aims at 10^{-13} level of sensitivity.

The third chapter exposes the MEG detector providing a description of the beam line setup, the magnetic spectrometer, the photon detector and the electronic acquisition system. The algorithm reconstruction used in the physics analysis are described in the fourth chapter.

The chapters from the fifth to the ninth talk about the MEG trigger system. Starting from the experimental needs, we show the algorithms developed for the real-time selection. A detailed description of the reconstruction of each observable is given. The custom electronic boards designed for the experiment are presented, particular emphasis is given to the system synchronization technique adopted and the LVDS data transfer between different boards. The firmware implementation of the selection algorithms is described in chapter 7. It illustrates the basic concepts of the code and dedicates particular attention to the use of the Look Up Tables and the live time measurement. Chapter 8 and 9 illustrate the procedure developed for the algorithms calibration and the system monitoring. In particular the chapter 9 explain in details the pulse shape discrimination trigger used to select α events in the photon detector starting from the Firmware development, the algorithm calibration and the obtained results.

The last part of this thesis, from chapter 10 to chapter 13, is dedicated to the description of the first physics run taken in the 2008. The tenth chapter describes the physics run, in particular for the detector performance from an hardware point of view.

Chapter 11 presents the online selection efficiencies for the $\mu \to e\gamma$ signal. A detailed description of the resolutions obtained for the reconstruction of the online observables is given. Finally a discussion about the global DAQ efficiency as a function of the online selection efficiency and the DAQ live time is given.

Th normalization scheme is described in chapter 12 with a description of the idea behind the normalization scheme. It explains in the details the measurement of all the normalization factors and gives the final result.

The physics analysis procedure, based on a mixture of blind and likelihood analysis is presented in chapter 13. The chapter discusses the principles of the analysis: the definition of the blinding region and the likelihood fit. The probability density functions of the physics observables for the $\mu \to e\gamma$ signal, the physics and accidental background extraction are described. The experiment sensitivity for the run has been estimated by using the data just outside the blinded region and simulations methods. Finally the result from the 2008 run is quoted.

Part I

Theory and phenomenology

Chapter 1

Theoretical introduction

Modern physics aims at understanding the laws of Nature studying its fundamental components: the elementary particles. Theoretical in parallel with experimental particle physics are revolutionizing human knowledge of natural phenomena. Modern research can be divided in two branches: research of new interactions and particles and precision measurement of known processes in order to find deviations from theoretical predictions.

The MEG experiment aims at measuring with unprecedented sensitivity the $\mu^+ \to e^+\gamma$ decay.

This process is strongly depressed by the present theory of particle physics, the Standard Model, to an unmeasurable level. Therefore observing $\mu^+ \to e^+\gamma$ will lead to a incontrovertible evidence of new physics beyond the Standard Model.

This chapter discusses the theory of the Standard Model and its extension to include neutrino oscillation, and the SUSY-GUT theories.

1.1 The standard model

The state-of-art theory of particle physics is the Standard Model (SM) [1]. The SM predictions have been confirmed by all experimental precision measurements, no clear evidence of disagreement has been found to date. Its description embeds three of the four fundamental interactions: electromagnetic, weak and strong interactions, leaving out only the gravitational one.

Elementary particles are classified in two classes: leptons and quarks; both are fermions, spin = 1/2, but they completely differ in the phenomenology of them interactions. One angular stone of the theory is the experimental evidence that quarks are subject to all the three interactions, while leptons are not subject to the strong one. Particles with integer spin, called gauge bosons, carry the interaction between fermions.

The SM is a gauge theory based on the group $\mathrm{SU(3)_C} \otimes \mathrm{SU(2)_L} \otimes \mathrm{U(1)_Y}$ spontaneously broken at low energy to $\mathrm{SU(3)_C} \otimes \mathrm{U(1)_{EM}}$. Free fermionic fields, bosons and the Higgs boson are introduced as elementary fields. The coupling of fermions and gauge bosons with the Higgs field gives the mass of the particles in a renormalizable theory framework.

The notation for quarks fields will be q_{ij} and l_{ij} for leptons fields (while ψ_{ij} will be used for a generic fermionic field) where $\mathrm{i} = 1,\ 2,\ 3$ runs on the 3 flavor families and $\mathrm{j} = \mathrm{L,R}$ distinguishes left or right chirality. Boson fields associated to the symmetry groups are indicated with G_μ for SU(3) with generators λ_{a} ($\mathrm{a} = 1,\ 8$, Gell-Mann's matrices), W^μ for SU(2) with generators τ_{a} ($\mathrm{a} = 1,\ 3$ Pauli's matrices) and B^μ for U(1). The SM Lagrangian, $\mathcal{L}_{\mathrm{SM}}$, consists of three parts, which are for the gauge interaction between fermions and gauge bosons, the Higgs potential and the Yukawa interaction between elementary particles and the Higgs field ($\mathcal{H}$) [2]:

$$\mathcal{L}_{\mathrm{SM}} = \mathcal{L}_{\mathrm{Gauge}} + \mathcal{L}_{\mathrm{Higgs}} + \mathcal{L}_{\mathrm{Yukawa}} \tag{1.1}$$

The Lagrangian for the gauge interaction, $\mathcal{L}_{\mathrm{Gauge}}$, is given by

$$\mathcal{L} = \sum_{\mathrm{SU(3),SU(2),U(1)}} \mathcal{F}^{\mathrm{a}}_{\mu\nu}\mathcal{F}^{\mathrm{a}\mu\nu} + \sum_{q,l} i\overline{\psi_{ij}}\gamma^\mu\mathcal{D}_\mu\psi_{ij} + |\mathcal{D}_\mu\mathcal{H}|^2 \tag{1.2}$$

where $\mathcal{F}^{\mathrm{a}}_{\mu\nu}$ is the gauge field tensor defined as:

$$\mathcal{F}^{\mathrm{a}}_{\mu\nu} = \partial_\mu \mathrm{T}^{\mathrm{a}}_\nu - \partial_\nu \mathrm{T}^{\mathrm{a}}_\mu - \mathrm{c}\mathrm{f}_{\mathrm{abc}}\mathrm{T}^{\mathrm{b}}_\mu\mathrm{T}^{\mathrm{c}}_\nu \tag{1.3}$$

T_μ is a generic gauge boson field, $\mathrm{f}_{\mathrm{abc}}$ are the structure constants of the correspondent group and c is the coupling constant (g_{s} for SU(3), g for SU(2) and $g\prime$ for U(1)); $\mathcal{D}_\mu$ is the covariant derivative defined as:

$$\mathcal{D}_\mu = \partial_\mu + ig_{\mathrm{s}}\frac{\lambda^{\mathrm{a}}}{2}G^{\mathrm{a}}_\mu + ig\frac{\tau^{\mathrm{a}}}{2}W^{\mathrm{a}}_\mu + ig\prime Q_{\mathrm{Y}}B_\mu \tag{1.4}$$

The Lagrangian for the Higgs potential, $\mathcal{L}_{\mathrm{Higgs}}$, is given in terms of two parameters μ and λ:

$$\mathcal{L}_{\mathrm{Higgs}} = \left(\mu^2|\mathcal{H}|^2 - \lambda|\mathcal{H}|^4\right) \tag{1.5}$$

After electroweak spontaneous symmetry breaking three of the four bosons of the theory acquire a mass different from 0, the photon remaining massless. The masses of the particles are found in terms of the parameters of the theory as shown in Table 1.1. A new parameter of theory can

$\mathrm{m}_W = gv/2$
$\mathrm{m}_Z = \sqrt{g^2 + g\prime^2}v/2$
$\mathrm{m}_W/\mathrm{m}_{\mathrm{Z}} = \mathrm{g}/\sqrt{\mathrm{g}^2 + \mathrm{g}'^2} = \sqrt{1-\sin^2(\theta_{\mathrm{W}})}$
$\mathrm{m}_H = \sqrt{2\lambda}v$
$\sin(\theta_{\mathrm{W}}) = g\prime/\sqrt{g^2 + g\prime^2}$
$\mathrm{e} = g\sin(\theta_{\mathrm{W}})$

Table 1.1: Electroweak bosons masses, Higgs boson mass, $\sin(\theta_{\mathrm{W}})$ and electric charge e in function of theory parameters.

be defined in terms of the couplings constants as shown in the table, it is called the Weinberg angle (θ_W). θ_W, m_W and m_Z were measured separately and their values are coherent with theory expectations [3].

$$\sin^2(\theta_W) = 0.223 \pm 0.004 \tag{1.6}$$

$$m_W = (80.41 \ \pm \ 0.10) \ \mathrm{GeV/c^2} \tag{1.7}$$

$$m_Z = (91.187 \ \pm \ 0.008) \ \mathrm{GeV/c^2 s} \tag{1.8}$$

Standard Model predictions are confirmed combining results of experimental measurements as shown above.

The Yukawa interaction part of the Lagrangian is given by

$$\mathcal{L}_{\mathrm{Yukawa}} = -\left[\overline{e}_{iR}(m_e)_{\mathrm{ij}} e_{\mathrm{jL}} + \overline{d}_{\mathrm{iR}}(m_d)_{\mathrm{ij}} d_{\mathrm{jL}} + \overline{u}_{\mathrm{iR}}(m_u)_{\mathrm{ij}} u_{\mathrm{jL}}\right] + \mathrm{HC} \tag{1.9}$$

obtained substituting the vacuum expectation value for the Higgs field. It generates the mass terms for quark and leptons in terms of Yukawa is coupling constants:

$$(m_X)_{\mathrm{ij}} = -(y_X)_{\mathrm{ij}}(v/\sqrt{2}) \tag{1.10}$$

with $X = e, \ d, \ u$. Neutrinos were excluded because there was no evidence of their mass being different from 0. Each mass matrix is diagonalized by unitary transformations for left-handed fermions and right-handed fermions with the same charge. Since the unitary matrices for the left-handed up-type quark and the left-handed down-type quark are generally different, flavor mixing is induced in the charged weak interaction for quarks. It is given by

$$\mathcal{L} = -\frac{g}{\sqrt{2}}\left[\overline{u}_{\mathrm{iL}}\gamma^{\mu}(V_{\mathrm{CKM}})_{\mathrm{ij}} d_{\mathrm{jL}} W^{+}_{\mu} + \overline{d}_{\mathrm{iL}}\gamma^{\mu}(V_{\mathrm{CKM}})^{*}_{\mathrm{ij}} u_{\mathrm{jL}} W^{-}_{\mu}\right] \tag{1.11}$$

where the $(V_{\mathrm{CKM}})_{\mathrm{ij}}$ represents the flavor mixing matrix for the quark sector, *i.e.* Cabibbo-Kobayashi-Maskawa (CKM).

On the other hand the charged leptons mass matrix is fully diagonalized by unitary transformations on the lepton doublet fields (l_{iL}) and the lepton singlet fields (e_{jR}). In the mass diagonalized basis, the charged weak current interaction for leptons remain diagonal, as follows:

$$\mathcal{L} = -\frac{g}{\sqrt{2}}\left[\overline{\nu}_{\mathrm{iL}}\gamma^{\mu} e_{\mathrm{jL}} W^{+}_{\mu} + \overline{e}_{\mathrm{iL}}\gamma^{\mu}\nu_{\mathrm{jL}} W^{-}_{\mu}\right] \tag{1.12}$$

In the above basis, the lepton flavors can be defined for each generation, and are thus conserved. They are the electron number (L_e), the muon number (L_μ) and the tau number (L_τ). Therefore in this scheme the Lepton Flavor Violating decay $\mu \to e\gamma$ is forbidden.

Muon Interactions in the Standard Model At the tree level of the SM Lagrangian, the muon has three gauge interactions, namely those with the photon, the $W^{\pm}$ and Z^0 bosons, and also the Higgs interaction. They are given by:

$$\mathcal{L} = e\overline{\mu}\gamma^{\mu}\mu A_{\mu} - \frac{g}{\sqrt{2}}\left[\overline{\nu}_{\mathrm{L}}\gamma^{\mu}\mu_{\mathrm{L}} W^{+}_{\mu} + \overline{\mu}_{\mathrm{L}}\gamma^{\mu}\nu_{\mathrm{L}} W^{-}_{\mu}\right] - \sqrt{g^2 + g\prime^2} \times$$
$$\times\left[\overline{\mu}_{\mathrm{L}}\gamma^{\mu}\left(-1/2 + \sin^2(\theta_W)\right)\mu_{\mathrm{L}} + \overline{\mu}_{\mathrm{R}}\gamma^{\mu}\sin^2(\theta_W)\mu_{\mathrm{R}}\right] Z^{0}_{\mu} - \frac{m_\mu}{v}\overline{\mu}\mu\mathcal{H} \tag{1.13}$$

In addition to the electromagnetic interaction, the second and the third terms describe, respectively, the charged weak-current interaction mediated by the $W^{\pm}$ boson and the neutral weak-current interaction mediated by the Z^0 boson. The other charged leptons, electron and tau, have the same gauge interaction as the above, but the coupling constant to the Higgs boson is proportional to their mass.

The muon is an unstable particle, its decay is described in the SM by a charged weak-current interaction mediated by the W boson. It can be approximated at low energy ($E \ll m_W^2$), by a point-like four-fermion interaction given by

$$\mathcal{L}_{Fermi} \;=\; -\frac{G_F}{\sqrt{2}}\left[\overline{\mu}\gamma^{\mu}(1-\gamma^5)\nu_{\mu}\overline{e}\gamma^{\mu}(1-\gamma^5)\nu_e \;+\; \overline{\nu}_e\gamma^{\mu}(1-\gamma^5)e\overline{\mu}\gamma^{\mu}(1-\gamma^5)\nu_{\mu}\right] \tag{1.14}$$

where G_F is called the Fermi coupling constant. At tree level of the SM, this is given by

$$G_F \;=\; \frac{g^2}{4\sqrt{2}m_W^2} \tag{1.15}$$

where m_W is the W boson mass.

Muon properties The mass and the lifetime are fundamental inputs to the SM. The muon mass measured value is

$$m_{\mu} \;=\; 106.658389(34)\ \text{MeV [3]} \tag{1.16}$$

In the framework of the SM, the muon life time τ_{μ} is related to the Fermi coupling constant and the best estimate of G_F is obtained measuring muon life time which is

$$\tau \;=\; 2.197013(24)\ \mu\text{s [4]} \tag{1.17}$$

whence the Fermi coupling constant is determined to be $G_F \;=\; 1.16639 \;\times\; 10^{-5}\ \text{GeV}^{-2}$.

Muon decay modes The observed muon decay modes are three:

1. $\mu^+ \to e^+\nu_e\overline{\nu}_{\mu}$, called Michel decay;
2. $\mu^+ \to e^+\nu_e\overline{\nu}_{\mu}\gamma$, called radiative muon decay (RMD);
3. $\mu^+ \to e^+\nu_e\overline{\nu}_{\mu}e^+e^-$

The relative probability, called branching ratio (B), of those processes is reported in Table 1.2.

1.1.1 Neutrino oscillations

Within the minimal version of SM the lepton mass matrix can be diagonalized once neutrinos masses are set equal to zero, see section 1.1. In this framework each generation lepton flavor is conserved so $\mu^+ \to e^+\gamma$ decay is forbidden. In the last 10 years several experiments disclosed the

Decay Mode	**Branching ratio**
$\mu^+ \to e^+ \nu_e \overline{\nu}_\mu$	$\approx 100\%$
$\mu^+ \to e^+ \nu_e \overline{\nu}_\mu \gamma$	1.4±0.4% (for $E_\gamma \geq$10 MeV) [5]
$\mu^+ \to e^+ \nu_e \overline{\nu}_\mu e^+ e^-$	$(3.4 \pm 0.4) \times 10^{-5}$ [6]

Table 1.2: Measured muon decay modes

evidence of lepton flavor oscillation on neutrino side, this oscillation is possible only in case of massive neutrinos.

Given a known (in composition, intensity and energy) neutrino source those experiments measure the surviving flux at a well defined distance from that source. In case of no flavor oscillation we expect to measure the original neutrino flux (apart from geometrical effects) but, depending on experimental conditions (see Equation (1.20)), a decrease on that neutrino flux has observed. Several sources had been utilized: nuclear reactors (Chooz [7], KamLAND [8]), particles accelerators (K2K [9]), the sun (SupeKamiokande [10], SNO [11]) and cosmic rays (SuperKamiokande, MACRO [12]). This oscillation, in analogy with quark side, leads to a non diagonal mixing matrix into the electroweak Lagrangian. The mixing matrix is called Pontecorvo-Maki-Nakagawa-Sakata and defined as

$$\nu_\ell \;=\; \sum_k (V_{\mathrm{PMNS}})_{\ell k} \nu_k \tag{1.18}$$

where $\ell \;=\; \mathrm{e},\ \mu,\ \tau$ (flavor eigenstate), $\mathrm{k} = 1, 2, 3$ (mass eigenstate).

Thus the Lagrangian is given by

$$\mathcal{L} \;=\; -\frac{g}{\sqrt{2}}\big[\overline{\nu}_{\mathrm{iL}}\gamma^\mu (V_{\mathrm{PMNS}})_{\mathrm{ij}} e_{\mathrm{iL}} W^+_\mu \;+\; \overline{e}_{\mathrm{iL}}\gamma^\mu (V_{\mathrm{PMNS}})^*_{\mathrm{ij}} \nu_{\mathrm{jL}} W^-_\mu\big] \tag{1.19}$$

In the two states approximation the probability of flavor transition for a given neutrino ν_ℓ emitted from the source with energy E at distance L is

$$\mathrm{P}(\nu_\ell \to \nu_{\ell\prime}) \;=\; \sin^2(2\theta)\sin^2\big(1.27\frac{\Delta \mathrm{m}^2(\mathrm{eV}^2)\mathrm{L(m)}}{\mathrm{E(MeV)}}\big) \tag{1.20}$$

This SM minimal extension taking into account neutrinos oscillation allows $\mu^+ \to e^+\gamma$ with a B different from 0. The Feynman diagrams of such process are reported in Figure 1.1.

In this framework the $\mu \to e\gamma$ decay width can be evaluated to be [13].

$$\Gamma(\mu^+ \to e^+\gamma) \;=\; \frac{1}{16}\frac{\mathrm{G}_\mathrm{F}^2 \mathrm{m}_\mu^5}{128\pi^3}\frac{\alpha}{\pi}\big(\frac{\mathrm{m}_1^2 - \mathrm{m}_2^2}{\mathrm{M}_\mathrm{W}^2}\big)\sin^2(\theta)\cos^2(\theta) \tag{1.21}$$

where the equivalence $\sin^2(\theta)\cos^2(\theta) \;=\; \sum_\mathrm{i} |\mathrm{V}_{\mathrm{ei}}^2 \mathrm{V}_{\mu\mathrm{i}}^2|^2$ had been used. The $\mathrm{B}(\mu \to e\gamma\ )$ is easily obtained by normalizing for the total decay width $(\mathrm{G}_\mathrm{F}^2\mathrm{m}_\mu^5/192\pi^3)$

$$\mathrm{B}(\mu^+ \to e^+\gamma) \;=\; 5 \times 10^{-48}[\Delta \mathrm{m}^2(\mathrm{eV})^2]^2 \sin^2(\theta)\cos^2(\theta) \tag{1.22}$$

If we insert into Equation (1.22) the results of the KamLAND experiment, $\Delta \mathrm{m}_{12}^2 \;=\; 6.9 \times 10^{-5}\ \mathrm{eV}^2$ and $\sin(2\theta) \;=\; 0.91$ we obtain a $\mathrm{B} \approx\ 10^{-55}$: an unmeasurable number.

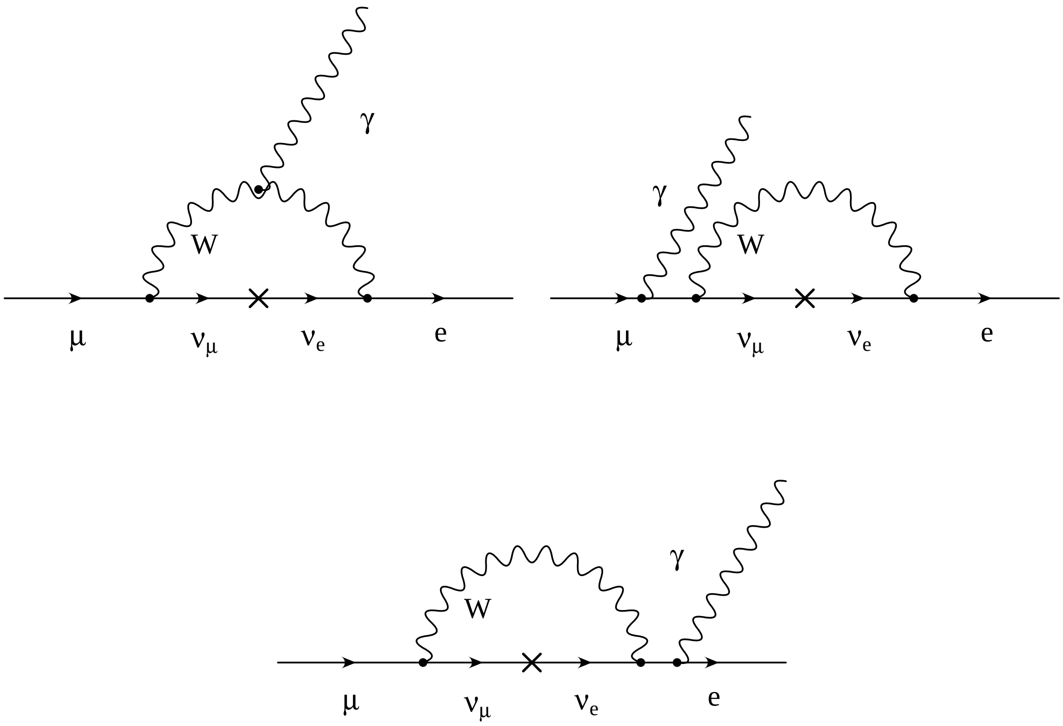

Figure 1.1: Feynman diagrams for the $\mu \to e\gamma$ decay in the Standard Model, extended to massive neutrinos.

Other theories tries to extend the SM to higher energies, e.g. SUSY-GUT theories, they predicts a B for $\mu \to e\gamma$ process close to the current limit obtained by the MEGA collaboration [14]. The next sections will shown some ideas of those theories and their prediction.

1.2 Beyond the Standard Model

The success of the SM is remarkable. However theoretical physics is moving to new theories beyond it to formulate an universal theory containing the SM as an effective low-energy theory. There are severals problems that the SM is not able to solve. Those can be divided in two categories: theoretical and observational [15], [16].

Theoretical problems

- All the masses and mixings terms are free parameters of the theory.
- There is no unification of the three interactions present in the theory.
- The hierarchy problem of the Higgs scalar mass and its loop-divergence.
- Gravitation is not taken into account.

- Quantization of the electric charge.

Observational problems

- Evidence on neutrino mixing and neutrino masses.
- Evidence that most of the matter in the Universe does not emit light, the Dark Matter, of non-baryonic nature.
- Evidence in the Universe of matter-antimatter asymmetry.
- Cosmological problems related with inflation.

1.2.1 Grand unification theories SU(5) and SO(10)

Corresponding to its symmetry group SU(3) $\times$ SU(2) $\times$ U(1) the SM has four diagonal generators, one for each gauge coupling. A possible way to unify the interaction is to use one with at least rank equal to four. The simplest viable candidate rank four group for grand unification is SU(5) [17].

In this scheme the fermions of the SM can be arranged in terms of the fundamental **5** and the antisymmetric **10** representation of SU(5). The theory also contains 24 gauge bosons where lie gluons, SM SU(2) mediators (W), and the U(1) mediator. New bosons, mediating new interaction in matter, are also predicted. In this model the problem of quantization of electric charge is solved because U(1) generator is a combination of SU(5) diagonal generators.

Another possible unification is provided by SO(10) group [18] [19]. Here there is also space for a singlet field corresponding to a right handed neutrino.

This GUT theories predict that all the interactions are unifIed at the $\mathrm{M_{GUT}}$ scale ($\approx 10^{15}$ GeV), at lower energies observed discrepancies in interactions are also predicted. Unification of coupling constants is related to θ_{W} value, this framework is also capable to predict its value.

A problem that is still remaining is the hierarchy problem and the loop-divergencies in Higgs mass correction calculation. This can be cured by SUSY theories, the idea is described in the next section.

1.2.2 Supersymmetric models

Phenomenological applications of SUSY theories have been considered since the late 70's on connection with the hierarchy problem in SM. To calculate correction to Higgs boson mass fermionic loop contributions lead to a divergence, it is given by

$$\delta m_H^2(f) \;=\; -2N_f\frac{|\lambda_f|^2}{16\pi^2}[\Lambda^2 \;+\; 2m_f^2\ln(\frac{\Lambda}{m_f})...] \quad \Lambda \approx M_{\mathrm{NewPhysics}} \tag{1.23}$$

The predicted value for the Higgs mass is dramatically higher than the expected value. apart from incredible fine tunings among all the parameters, arising a problem of naturalness. A way to solve this is to introduce a new symmetry that is able to keep the scalar mass under control, it is the supersymmetry SUSY.

Supersymmetry predicts for every particle a supersymmetric counterpart, which has the same internal quantum numbers and an intrinsic momentum angular which differs by half a unity from the first one. This particles are called squarks and sleptons, Table 1.3 lists some of them.

SM particles	**spin**	**SUSY partners**	**spin**
quark (q)	1/2	squark ($\tilde{q}$)	0
lepton (l)	1/2	slepton ($\tilde{l}$)	0
gluon(G)	1	gluino	1/2
$W^{\pm}, Z^0, \gamma$	1	chargino $\tilde{\chi}_i^{\pm}$ (i = 1-2)	1/2
Higgs boson H	0	neutralino $\tilde{\chi}_i^0$ (i = 1-4)	1/2

Table 1.3: Ordinary SM particles and SUSY partners.

Sparticles add new terms into $\delta \mathrm{m_H}$ evaluation, they have the same form but with opposite sign (given by the Fermi-Bose different statistic). Therefore in case of perfect SUSY symmetry the divergence would be cancelled having the supersymmetric counter part the same mass of the ordinary particle. There is no evidence of supersymmetric particles to date, so the loop correction to the Higgs mass is

$$\delta m_H^2 \approx g_i^2 (m_{f_i}^2 \;-\; m_{\tilde{f}_i}^2) \tag{1.24}$$

where i runs on the fermion families and super partner masses are indicated with $m_{\tilde{f}}$. Thus this divergency is under control if that difference is of the order of 1 TeV providing the scale of SUSY theories.

Another result of SUSY theories is to predict a particle, the neutralino (stable, spin 1/2, neutral, weakly interacting and non baryonic), as one of the components of the Dark Matter.

1.2.3 $\mu \to \mathrm{e}\gamma$ decay in SUSY-GUT

Grand unified theories provide an elegant unification of the strong and electroweak forces and together with the addiction of supersymmetry represent a viable candidate to describe physics beyond the Standard Model [20], [21], [22].

In SM, baryonic number (B), individual lepton numbers (L_{e}, L_μ and L_τ) and the total lepton number (L) are accidentally conserved symmetries. SUSY-GUT theories remove any fundamental distinction between leptons and quarks so at the scale of those theories SM symmetries are broken. Three possible signatures of SUSY-GUT effects at SM energy scale are:

- B: Proton decay;
- L: neutrino masses;

- L_i: $\mu \to e\gamma$.

The main contribution predicted by supersymmetric models in lepton flavor violating branching ratios are the non diagonal terms in the slepton flavor matrix.

A mismatch in flavor space between the lepton and slepton mass matrices generates tree-level transitions between different leptonic generations. If we indicate the mixing angles between the first two generations of sleptons schematically by $\theta_{\tilde{e}\tilde{\mu}}$ we obtain [23]

$$B(\mu \to e\gamma) \propto \frac{\alpha^3 \pi \theta^2_{\tilde{e}\tilde{\mu}}}{{G_F}^2 \tilde{m}^4} \tan^2(\beta) \tag{1.25}$$

where $\tilde{m}$ is a typical supersymmetric mass. For a generic value of 1 TeV the experimental limits on rare muon decays transforms in stringent upper limits on $\theta_{\tilde{e}\tilde{\mu}}$, being of the order of current sensitivities.

In this scheme the prediction on the Lepton flavor violation (LFV) is governed by the slepton mixing matrix coefficients. Theoretical physicists, in analogy with SM physics, attempt to model the slepton mixing matrix to be similar to the quark mixing matrix (CKM model) or to the neutrino mixing matrix (PMNS model). The U_{e3} parameter of the PNMS matrix has not been measured yet. However the CHOOZ collaboration set to be < 0.07 90% CL [7]. The slepton PMNS-like mixing matrix are modeled in two possible configurations: the first has U_{e3} at 0.07 the coupling between the selectron and the third slepton mass eigenstate, and the second has with $U_{e3} = 0$. Figure 1.6 shows the SO(10) SUSY-GUT predicted value of the $\mu \to e\gamma$ decay in the region of parameters that will be scanned by the LHC experiments in terms of $\tan(\beta)$ and the $\tilde{\chi}_0$ mass ($M_{1/2}$). The MEG experiment, having a sensibility down to 10^{-13} will explore a relevant part of the theory predictions. It is also important to cite the complementarity of the LHC and the MEG experiment in the validation of new physics models. No measurement at the LHC collider is expected to measure the slepton mixing matrix coefficients.

In all the predictions the $\mu \to e\gamma$ decay rate increases with increasing $\tan(\beta)$[1], the ratio of the two SUSY Higgs boson VEVs, see Figure 1.3 and 1.5. The coupling of the particles to the supersymmetric partners is peculiar of the SUSY-GUT theory.

The SUSY-SU(5) theory predicts a B in the range $10^{-15} \div 10^{-13}$ depending on the unknown value of the theory parameters[2], see Figure 1.2 and Figure 1.3.The SUSY-SO(10) theory predicts even larger rates, from 10^{-13} to 10^{-11}, see Figure 1.4 and Figure 1.5.

LFV in τ and in μ Equation (1.25) can be generalized easily generalized [24]:

$$B(l_i \to l_j\gamma) \propto \frac{\alpha^3 \pi \theta^2_{\tilde{j}\tilde{i}}}{G_F^2 \tilde{m}^4} \tan^2(\beta) \tag{1.26}$$

The ratio of the $\tau \to \mu\gamma$ to $\mu \to e\gamma$ is:

[1] $\tan(\beta) = \langle H_2^0 \rangle / \langle H_1^0 \rangle$

[2] $\tan(\beta)$, the mass scale of supersymmetry and the slepton mixing factors.

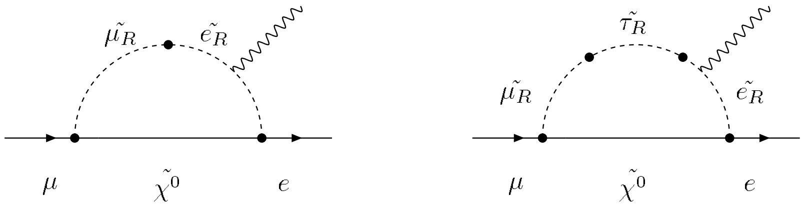

Figure 1.2: Feynman diagrams for $\mu \to e\gamma$ decay in SU(5) SUSY-GUT theories.

$$\frac{\mathrm{B}(\tau \to \mu\gamma)}{\mathrm{B}(\mu \to \mathrm{e}\gamma)} = \frac{\theta^2_{\tilde{\mu}\tilde{\tau}}}{\theta^2_{\tilde{\mathrm{e}}\tilde{\mu}}} \tag{1.27}$$

The ratio in Equation (1.27) can be evaluated by modeling the slepton mixing matrix to be CKM-like or PMNS-like. The mixing angles are proportional to:

$$\begin{aligned} \theta_{\tilde{\mu}\tilde{\mathrm{e}}} &\propto \mathrm{V_{td}V_{ts}} \qquad \mathrm{CKM-like} \\ \theta_{\tilde{\tau}\tilde{\mu}} &\propto \mathrm{V_{tb}V_{ts}} \\ \\ \theta_{\tilde{\mu}\tilde{\mathrm{e}}} &\propto \mathrm{U_{e3}U_{\mu 3}} \qquad \mathrm{PMNS-like} \\ \theta_{\tilde{\tau}\tilde{\mu}} &\propto \mathrm{U_{\mu 3}U_{\tau 3}} \end{aligned}$$

The coupling of the third generation in the slepton mixing matrix in the τ case leads to a enhancement of the LFV τ channel by a factor from 500 to 10^4 depending on the model.

Figure 1.7 shows the correlation between the $\mathrm{B}(\tau \to \mu\gamma)$ and $\mathrm{B}(\mu \to \mathrm{e}\gamma)$ in the SO(10) SUSY-GUT theory for three slepton mixing models, namely CKM (slepton mixing as in the quark sector) and 2 PMNS (neutrino mass mixing with $\theta_{13} = 0$ and $\theta_{13} = 0.07$). Note that the $\mathrm{B}(\tau)$ is multiplied per 10^7 and the $\mathrm{B}(\mu)$ for 10^{11}.

However, from an experimental point of view, the μ-sector is preferable with respect to the τ one, this will be explained in the next chapter. This thesis will report on the construction, set up and analysis of a new generation experiment searching for the LFV violation in the $\mu \to \mathrm{e}\gamma$ decay.

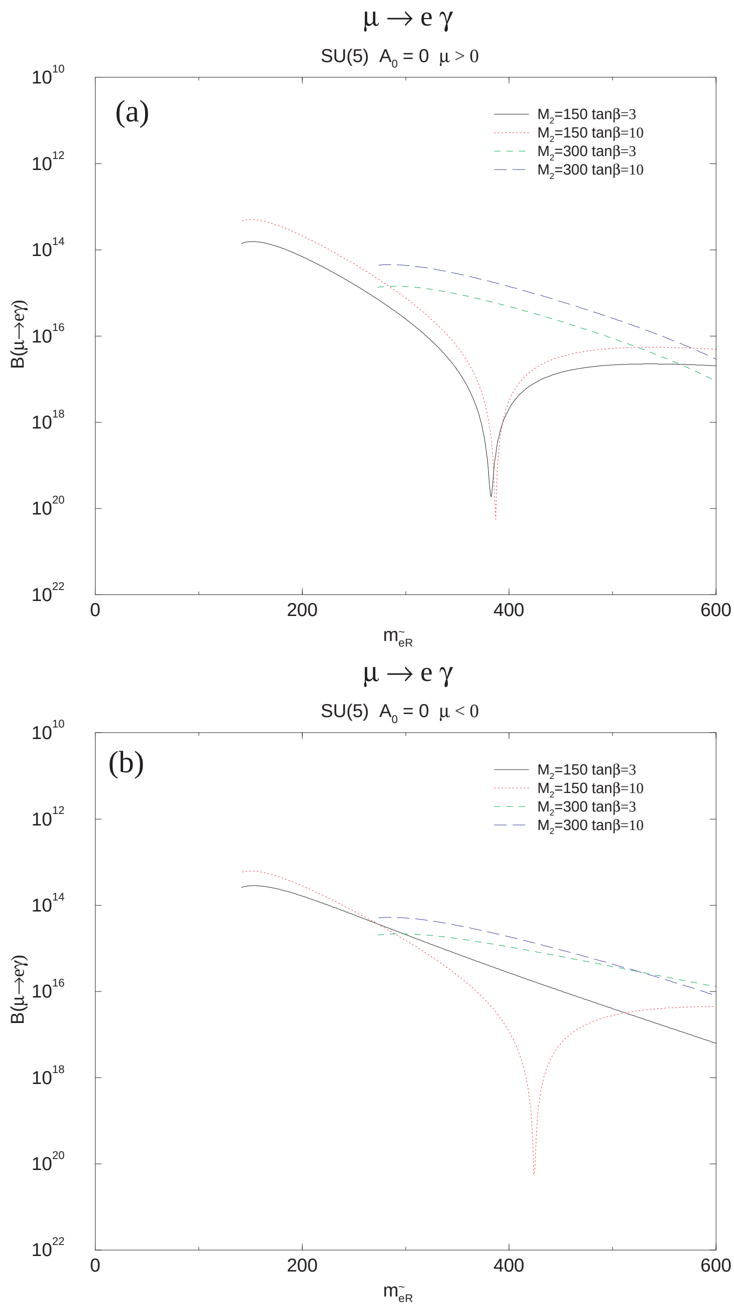

Figure 1.3: Branching ratio predictions for $\mu \to e\gamma$ decay in SU(5) SUSY-GUT theories.

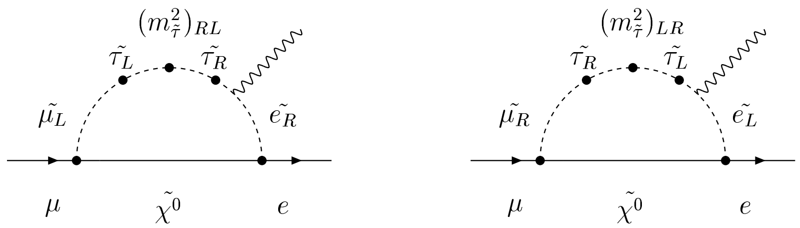

Figure 1.4: Feynman diagrams for $\mu \to e\gamma$ decay in SO(10) SUSY-GUT theories.

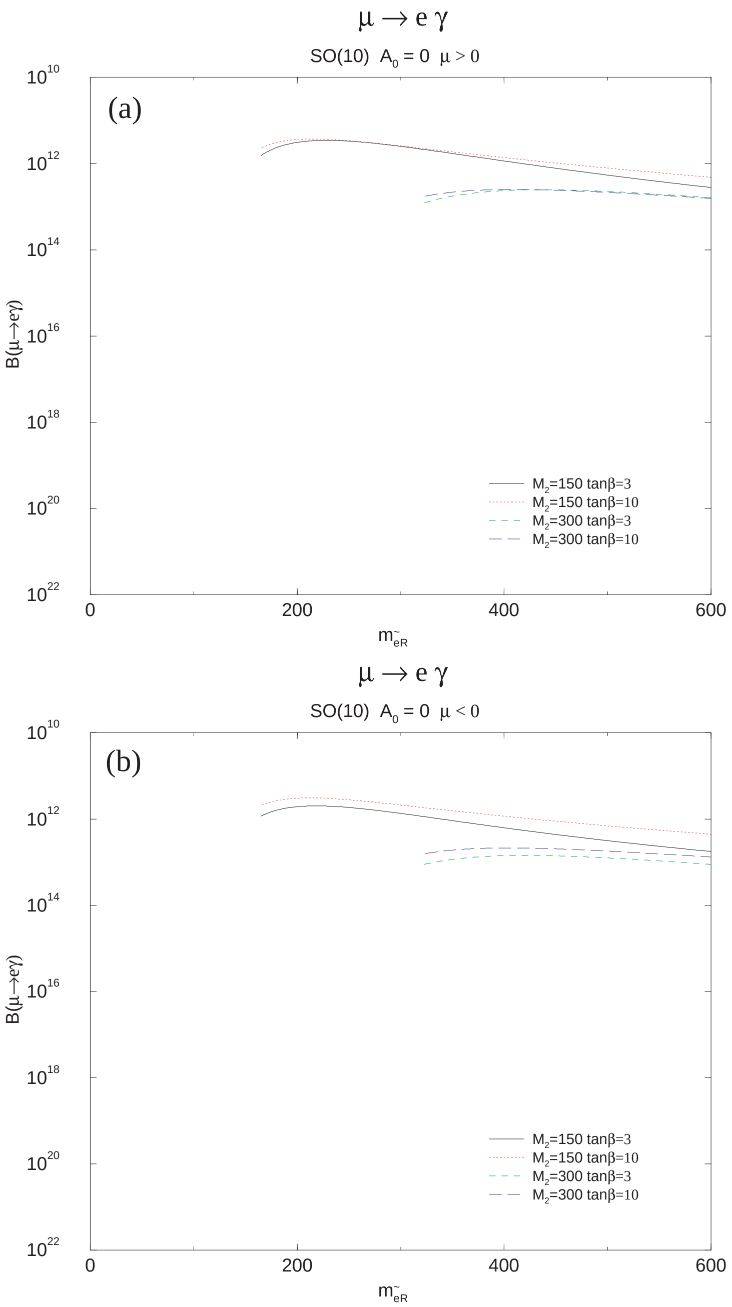

Figure 1.5: Branching ratio predictions for $\mu \to e\gamma$ decay in SO(10) SUSY-GUT theories.

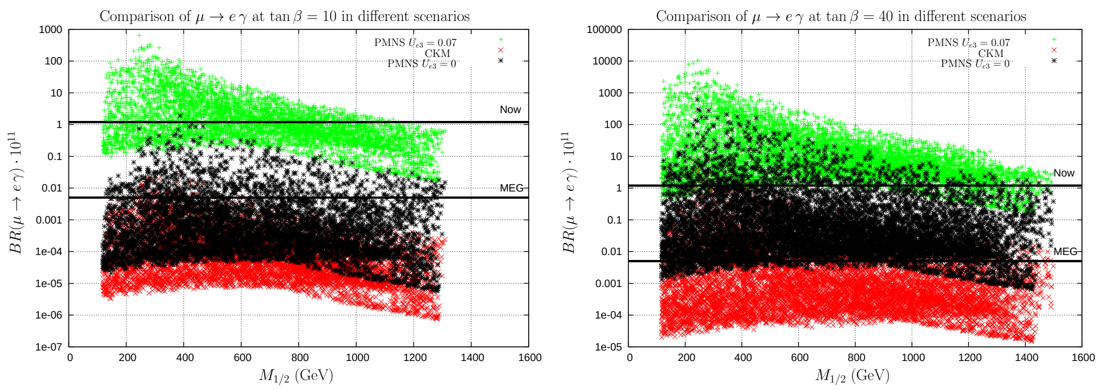

Figure 1.6: BR($\mu \to e\,\gamma$) as a probe of different SUSY–GUT scenarios. The plots are obtained by scanning the LHC accessible parameter space at fixed $\tan\beta$. The lines are the present (MEGA) and future (MEG) experimental sensitivities. We see that MEG will completely test the PMNS scenario for $\mathrm{U_{e3}}$ close to the CHOOZ bound and severely constrain it for $\mathrm{U_{e3}} = 0$.

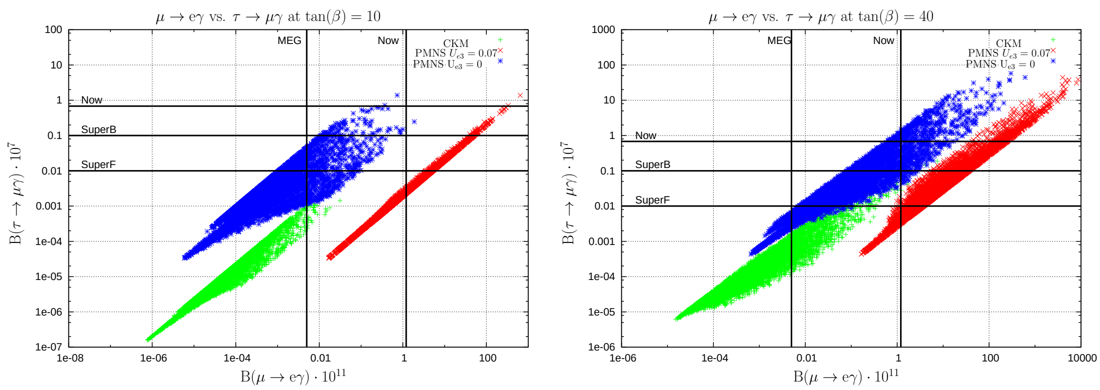

Figure 1.7: Comparison of $\mu \to e\gamma$ and $\tau \to \mu\gamma$ as a probes of SUSY-GUT scenarios. The plots are done by scanning the LHC accessible parameter space at fixed $\tan(\beta)$. The lines are the present bounds and future sensitivities. Let us note that the interplay between MEG and a Super Flavor factory will leave unscathed only the low $\tan(\beta)$ CKM case.

Chapter 2

Search for LFV in muon decay

This chapter presents the status of the search for new physics beyond the Standard Model looking for LFV processes, in particular in the muon sector.

The search for rare muon decays is an important tool to investigate crucial theoretical issues. The repeated experiments, performed over the years, were characterized by the use of muon beams of increasing intensity together with the use of detectors continuously improving resolutions. This allowed an increasing sensitivity in the search for the rare decays.

The case of the $\mu \to \mathrm{e}\gamma$ decay is presented in details. An historical introduction is performed and the principles for a new $\mu \to \mathrm{e}\gamma$ experiment, in terms of resolutions and background rejections, are presented.

2.1 Main LFV processes and limits

Over the last few decades, particle physics has witnessed the extraordinary success of the Standard Model, which explains most observed phenomena in terms of gauge theories.

However, the Standard Model, is not able to answer fundamental physics questions, like [25]:

- what is the origin of widely different masses of elementary particles, including neutrinos;
- what are the origins of the different fundamental forces;
- why is the proton stable;
- what is the origin of matterantimatter asymmetry in the universe;
- what is the composition of dark matter and the nature of dark energy in the universe.

However, reliable experimental observations (as for example neutrino oscillations, WMAP results) suggest that extensions to the Standard Model are required.

This begs the question, how should we look for new physics beyond the Standard Model?

Laboratory exploration in particle physics has traditionally progressed along different but complementary lines. One has been striving for higher energies to access new degrees of freedom directly, the other aiming for higher precision in the study of rare processes.

The large hadron collider (LHC) at CERN has opened a new domain of energies, thus providing answers to a number of previous questions, in particular exploring the domain of the electroweak symmetry breaking, and investigating the existence and nature of the Higgs boson and supersymmetric particles.

Nevertheless, many of the unanswered questions require different means of investigation with very detailed studies of the properties of already known particles. Well-controlled experimental conditions as well as high statistics will be the characteristic features of this alternative and complementary way of exploration.

Muon physics played a fundamental role in establishing the V-A structure of weak interactions and the validity of quantum electrodynamics. For the future, muons may provide crucial information regarding one of the most fundamental quests in modern physics: the structure of the theory which lies beyond the Standard Model of particle physics. Indeed one of the main interests in muon physics lies in the search for processes violating the muon number. The discovery of decays such as $\mu \to e\gamma$ and $\mu \to eee$ or of μ-e conversion in nuclei would be an indisputable proof of new dynamics beyond the Standard Model.

Furthermore, the information that can be extracted from the study of rare muon processes is, in many cases, not accessible to high-energy colliders. For example, even if LHC will find the supersymmetric sleptons and measure their masses, it would not be able to compete with muon decay experiments in constraining the sleptons mixing angles.

Table 2.1 lists the upper limits of various lepton-flavor violating precesses. They involve decay of muons and tau leptons in neutrino less final states, as well as those of heavy bosons, π, K and Z^0, in pairs of leptons of different generations. The sensitivity of LFV, with respect to the theoretical predictions, is superb in the muon system, even if in the τ sector the LFV would be at higher values, see section 1.2.3.

The SUSY-GUT theories predict a ratio between the $B(\tau \to \mu\gamma)$ and $B(\mu \to e\gamma)$ to be at the order of 500 in case SU(5) SUSY-GUT theory and 10^4 in case of SO(10) SUSY-GUT one. This assumption may lead to the conclusion that the τ is the best candidate for a LFV search.

Muon and the tau differs in the mass and lifetime, having the muon lower mass and longer lifetime of several order of magnitude. Low energy muons can be produced by charged π decays, collected in a monochromatic beam and stopped into a target. This is not true in tau case, the primary beam energy has to be higher more than an order of magnitude, and they cannot be collected in a beam because of their tiny lifetime (10^{-15} s). The most intense τ factories are indeed the B-factories, being the τ produced by the e^+e^- annihilation at the $\Upsilon(4S)$ ($m_{\Upsilon(4S)} = 10.58$ GeV, $\Gamma_{\Upsilon(4S)} = 20$ MeV [3]) resonance, and 10.54 GeV, $\sigma(e^+e^-) \to \tau^+\tau^- = 0.89 \pm 0.02$ nb, [29], and decay in flight in the laboratory system. The typical number of produced τ in one year of data taking is order of 10^8 τ/year, it is up to 10^{13} μ/year in case of muons. This difference leads the

Process	**Upper limit**	**Reference**
$\mu \to e\gamma$	$< 1.2\ 10^{-11}$	[14]
$\mu \to eee$	$< 1.0\ 10^{-12}$	[26]
$\mu^- Ti \to e^- Ti$	$< 6.1\ 10^{-13}$	[27]
$\mu^+ e^- \to \mu^- e^+$	$< 3\ 10^{-13}$	[28]
$\tau \to e\gamma$	$< 3.3\ 10^{-8}$	[29]
$\tau \to \mu\gamma$	$< 4.4\ 10^{-8}$	[29]
$\tau \to \mu\mu\mu$	$< 3.2\ 10^{-8}$	[30]
$\tau \to eee$	$< 3.6\ 10^{-8}$	[30]
$\pi^0 \to \mu e$	$< 8.6\ 10^{-9}$	[31]
$K_L^0 \to \mu e$	$< 4.7\ 10^{-12}$	[32]
$K^+ \to \pi^+ \mu^+ e^-$	$< 2.1\ 10^{-10}$	[33]
$K_L^0 \to \pi^0 \mu^+ e^-$	$< 4.4\ 10^{-10}$	[34]
$Z^0 \to \mu e$	$< 1.7\ 10^{-6}$	[35]
$Z^0 \to \tau e$	$< 9.8\ 10^{-6}$	[35]
$Z^0 \to \tau\mu$	$< 1.2\ 10^{-5}$	[36]

Table 2.1: Limits for the branching ratio of the lepton-flavor violating processes involving muons, taus, pions, kaons, and Z bosons. For the muon capture process the limit of the relative probability with respect to the SM predicted processes is given.

experimental sensitivity in the muon sector to be several order of magnitudes higher with respect to the τ one, of the order of 10^5, more than compensating the difference in the predicted LFV branching ratios.

Figure 1.7 shows the correlation between the $B(\tau \to \mu\gamma)$ and $B(\mu \to e\gamma)$ in the SO(10) SUSY-GUT model for three slepton mixing models, namely CKM (slepton mixing as in the quark sector) and PMNS (neutrino mass mixing with two hypothesis on U_{e3}). Note that the $B(\tau)$ is multiplied per 10^7 and the $B(\mu)$ for 10^{11}.

A new generation $\mu \to e\gamma$ experiment, the MEG experiment, is presently taking data at PSI in Switzerland. This experiment will search for signal of new physics with unprecedented sensitivity: 2 order of magnitude better than the experiments. On the other channel the new planned B factories will extend the sensitivity on the τ channels by more than one order of magnitude. The two LFV processes rely on different slepton mixing constants and then provide complementary measurements.

The processes involving muon decays can be grouped in three categories:

1. Direct muon decays ($\mu \to e\gamma$ or $\mu \to eee$);
2. Muon conversion on heavy elements, as Titanium or Gold;
3. Muonium anti-muonium conversion.

As apparent from Table 2.1 the best limits are obtained for $\mu \to$ eee and muon conversion on heavy elements. This is due to the clear signature of the processes which allows for a search in a background-free environment. However the sensitivity to new physics of these two processes is comparable to that of $\mu \to e\gamma$ decay because of the presence of the electromagnetic vertex in the related Feynman diagrams leads to:

$$\frac{\mathrm{B}(\mu \to \mathrm{e}\gamma)}{\mathrm{B}(\mu \to \mathrm{eee})} \approx 10^2$$
$$\frac{\mathrm{B}(\mu \to \mathrm{e}\gamma)}{\mathrm{B}(\mu \to \mathrm{e})} \approx 10^2$$

The existence of $\Delta \mathrm{L_i} = \pm 2$ processes, on the other way, is constrained by limits in the muonium anti-muonium conversion.

2.1.1 The $\mu^+ \to e^+e^-e^+$ process

The present experimental limit on the $\mu^+ \to e^+e^-e^+$ decay branching ratio [6] is $\mathrm{B} < 1 \times 10^{-12}$ at 90% C.L., obtained by the SINDRUM experiment [26] in 1988. From the experimental point of view, this decay produces only charged particles in the final state, simplifying the detector layout. However, the energy spectrum of the decay products reaches low energy. This requires a tracking system capable of sustaining the entire flux of Michel positron from the normal muon decay [2].

The SINDRUM detector was a solenoidal spectrometer equipped with MWPCs system coaxial with the beam. Three-dimensional hit positions were determined by means of cathode strips oriented at $\pm$ 45° relative to the sense wires. The angular acceptance was 24% of 4π with a momentum resolution of 10%. A continuous muon beam of 25 MeV/c was stopped on a low-density target, 11 mg/cm^2, at a rate of 6×10^6 μ^+/s. The candidate event selection was based on kinematical criteria. The three final particles had to have the muon invariant mass, zero total momentum, a common vertex and had to be emitted at the same time. The event background was subdivided into two classes, the correlated background and the uncorrelated one. The first class was generated by the internal conversion of radiative muon decays, $\mu^+ \to e^+e^-e^+\overline{\nu_\mu}\nu_e$. The uncorrelated background was produced by the accidental coincidence of a normal Michel positron with an e^+e^- pair produced by the Bhabha scattering in the target of another Michel positron. We noted that the correlated background scaled linearly with the muon stop rate in the target, while the uncorrelated one scaled quadratically. The data sample collected by SINDRUM was background free, meaning that the background equivalent Branching Ratio was $\mathrm{B_{acc}}$ 10^{-13} for a beam intensity of $6 \times 10^6 \mu^+$/s. The SINDRUM detector characteristics are listed in Table 2.2.

Future prospects Since 1988 there have been no new experimental proposals for $\mu^+ \to e^+e^-e^+$. Any future proposal should aim at a single-event sensitivity of the order of 10^{-16} and would therefore require a beam of 10^{10} μ/s. At this stop rate, the background would scale up to $\mathrm{B_{unc}} \approx 10^{-10}$ given the SINDRUM detector resolutions. The quadratic dependence of the uncorrelated

Parameter	**SINDRUM**
Stop rate	$6 \times 10^6\ \mu/s$
Muon beam momentum	25 MeV/c
Magnetic Field	0.33 T
Ang acceptance	24%
Momentum resolution	10% FWHM
Vertex resolution	$\approx$ 2 mm^2
Timing resolution	1 ns
Target length	220 mm
Target density	11 mg/mm^2

Table 2.2: Summary of the SINDRUM detector performances relevant for $\mu^+ \to e^+e^-e^+$ decay search.

background rate on the muon stop rate would require, even on best assumptions, substantial detector improvements.

Table 2.2 lists the SINDRUM detector parameters. To reach the stated sensitivity, a background suppression factor of ≈ 6 orders of magnitude has to be obtained. Such a huge factor is probably not achievable, even with improved present-day experimental techniques. The $\mu^+ \to e^+e^-e^+$ search demands innovative detectors.

2.1.2 The $\mu^- \to e^-$ conversion process

When μ^- are brought at rest in matter, muonic atoms in the ground state are quickly formed.

These atoms decay by either muon decay in orbit (MDIO) $\mu^-\mathrm{N_Z} \to e^-\overline{\nu_e}\nu_\mu\mathrm{N_Z}$ or nuclear muon capture (MC) $\mu^-\mathrm{N_Z} \to \nu_\mu\mathrm{N}^*_{Z-1}$. The amplitude of the latter decay mode increases with the atomic number, thus reducing the muonic atom lifetime to less than 100 ns for atoms heavier than lead.

The $\mu^- \to e^-$ conversion occurs in the nucleus field with a branching ratio which can vary by one order of magnitude depending on the atomic number Z. The coherent conversion, which occurs when the recoiling nucleus remains in the ground state is expected to be enhanced. In this case, the emitted electrons have the MDIO-decay end-point energy. The signature is a single electron emerging from the target with an energy of $\approx$ 100 MeV . The present experimental limits on the conversion on different materials were obtained by the SINDRUM- II experiment operated in different configurations: B($\mu^- \to e^-$ on Ti) $\leq 1.7 \times 10^{-12}$ at 90% C.L. [38], B($\mu^- \to e^-$ on Au) $\leq 3 \times 10^{-13}$ at 90% C.L [28]. From the experimental point of view, this decay has only one detectable particle in the final state. This has the consequence that only physical processes contribute to the background. The accidental coincidence of events in the target, which was the source of the uncorrelated background in the previous two LFV processes, has no influence in this case. The background rate is expected to increase only linearly with the muon stopping rate.

High energy electrons may originate from the MDIO or from the radiative muon capture (RMC, $\mu^-\mathrm{N} \to \nu_\mu\gamma\mathrm{N}^*$), often called muon-decay related background. The radiative pion capture (RPC,

$\pi^- N \to \nu_\mu \gamma X$), and the beam contamination by electrons are examples of beam related background. The first background class can be reduced mainly by improving the detector resolution, while the second has to be prevented by searching for the signal in a high purity environment. The electron momentum spectra, measured by the SINDRUM-II detector during the $\mu^- \to e^-$ conversion search on gold, is shown in Figure 2.1 for three different beam configurations.

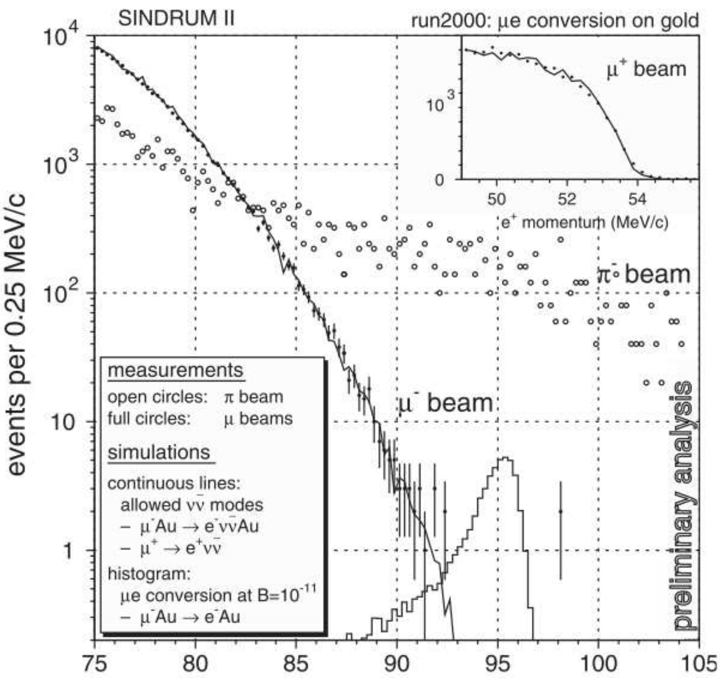

Figure 2.1: The electron momentum spectra measured with: μ^+ to measure the detector resolution, π^- to evaluate the RPC background and μ^- for the $\mu^- \to e^-$ search. Data were collected with different lifetimes. The expected momentum distribution for signal events is also shown.

Future prospects Two experiments are currently in the research and development phase in the $\mu^- \to e^-$ research field. The main feature for a new experiment is an intense muon beam coupled with a very low proton contamination. In fact there is no problem of accidental background contamination while the π decay in orbit would gives a significant contribution in the electron energy spectrum around the signal region.

The first experiment is the PRIME detector [39] is coupled to the PRISM beam line [40] at J-PARKin Japan. This experiment is expected to aim at a sensitivity of 5×10^{-19} on the branching ratio.

PRISM is designed to deliver a high intensity muon beam of 10^{11}-10^{12} μ/s, with a narrow momentum spread of $\pm$ 2%, a kinetic energy of $\approx$ 20 MeV and a negligible π contamination. The layout of the PRISM beam line is presented in Figure 2.2. It is planned to achieve the aforementioned features by using a fixed field alternating gradient (FFAG) accelerator ring. The

FFAG will operate a rotation of the muon energy-time phase space, thus reducing the momentum-spread down to the quoted value. With such a performing beam, the PRIME muon target could be made very thin. The resulting electron multiple scattering in the target is estimated to contribute to the momentum resolution only for ≈ 100 keV/c, thus helping to reduce the MDIO background.

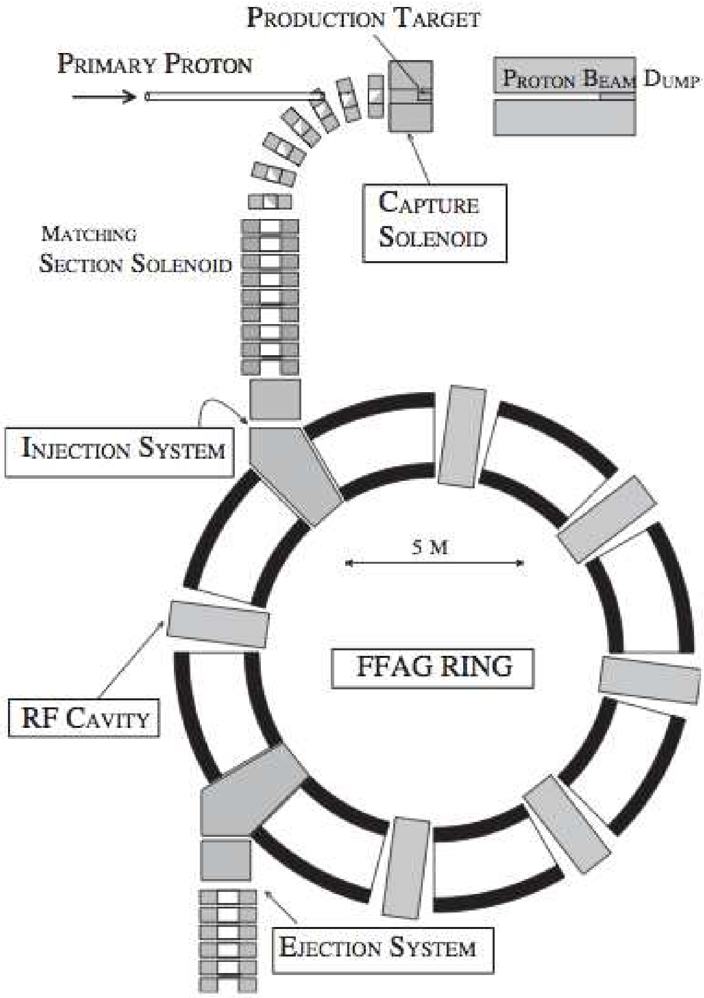

Figure 2.2: Layout of the PRISM muon source.

The second one is the Muon to Electron Conversion Experiment (Mu2e) [41, 42]. It requests a total delivery of 4×10^{20} protons on target per year for two years of running. Muons are to be produced and brought onto an aluminum stopping target in narrow (<200 ns) time bursts, separated by intervals of about 1.5μs, somewhat larger than the lifetime of muonic aluminum. Muon to electron conversion data would be taken between bursts, after waiting a sufficient time (≈700 ns) for the prompt π background to subside. A suppression (extinction) of the primary proton beam between bursts by a factor of 10^{-9} relative to the burst itself is necessary to control the π related prompt background. The sketch of the beam line and detector set up of the Mu2e experiment is reported in Figure 2.3.

The expected sensitivity is similar to the one f the PRIME experiment.

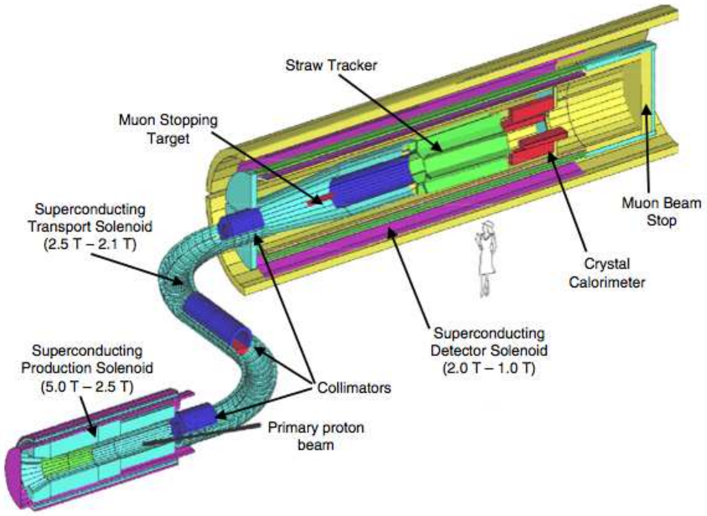

Figure 2.3: Layout of the Mu2e project.

2.2 History of $\mu \to e\gamma$ search

The lepton μ has been discovered in 1937 by Neddermeier and Anderson by looking at cloud chamber pictures exposed to cosmic rays [43]. They had noticed particles that curved in a manner distinct from that of electrons and other known particles, when moving through a magnetic field. In particular, these new particles were negatively charged but curved to a smaller degree than electrons, but more sharply than protons, for particles of the same velocity. It was assumed that the magnitude of their negative electric charge was equal to that of the electron, and so to account for the difference in curvature, it was supposed that these particles were of intermediate mass (lying somewhere between that of an electron and that of a proton). It was thought to coincide with the one predicted by Yukawa as the short-range strong force mediator.

A decade later Conversi, Paccini and Piccioni [44] observed the muon to behave like a heavy electron, it interacts with matter through the electromagnetic interaction but not through the strong force. The muon has been discovered to be a particle with a limited lifetime of the order of $2{\cdot}10^{-6}$ s decaying into an electron. Then if the muon was simply an heavy electron it would also decay into an electron and a gamma ray. Later on the first upper limit was set to be $B(\mu \to e\gamma) \leq 10\%$ by Pontecorvo and Hincks [45]. This was the beginning of the search for the lepton flavor violation.

As it will presented later on, the sensitivity to the search for the $\mu \to e\gamma$ signal depends on the background rejection capability of the measurement apparatus and on the statistics collected.

In a background-free experiment the suitable sensitivity B is proportional to $1/N_\mu$; the event data taking time is typically from few months to few years and cannot be easily incremented since human lifetime is limited. A considerable experiment sensitivity improvement comes from the usage of intense muon sources. With the use of particles accelerators instead of cosmic rays the $\mu \to e\gamma$ upper limit has been lowered by several order of magnitude. From the theoretical point of view the studies on the μ decay leaded to the assumption that in the SM the leptonic number is conserved. In Table 2.3 and 2.4 the most important accelerator-based experiments are reported, enhancing the beam intensity and the detector resolutions. The beam is characterized by its intensity and its duty cycle[1]; as shown in section 2.3.2 the accidental background scale quadratically with the instantaneous beam intensity.

	Year	**Beam Intensity (μ/s)**	**$\delta t/\Delta t$**	**Upper Limit**	**Reference**
TRIUMF	1977	2×10^5	-	$< 3.6 \times 10^{-9}$	[46]
SIN	1980	5×10^5	30%	$< 1.0 \times 10^{-9}$	[47]
LANL	1982	2.4×10^6	6.4%	$< 1.7 \times 10^{-10}$	[48]
CrystalBox	1986	3×10^5	5÷10%	$< 4.9 \times 10^{-11}$	[49]
MEGA	1999	1.5×10^7	6%÷9%	$< 1.2 \times 10^{-11}$	[14, 50]

Table 2.3: Experiments dedicated to the $\mu \to e\gamma$ search in the last 30 years: characteristics of the beam and published results.

	Year	$\Delta E_e/E_e$	$\Delta E_\gamma/E_\gamma$	$\Delta t_{e\gamma}$	$\Delta\theta_{e\gamma}$
TRIUMF	1977	10%	8.7%	6.7 ns	-
SIN	1980	8.7%	9.3 %	1.4 ns	-
LANL	1982	8.8%	8%	1.8 ns	37 mrad
CrystalBox	1986	8%	8%	1.8 ns	87 mrad
MEGA	1999	1.2%	4.5%	1.6 ns	15 mrad

Table 2.4: Experiments dedicated to the $\mu \to e\gamma$ search in the last 30 years: achieved experimental resolutions.

In Figure 2.4 the experimental upper limit for the $\mu \to e\gamma$ decay as a function of time is presented, the use of dedicated beams brought to an improvement of experimental sensitivities.

As an example of a $\mu \to e\gamma$ search detector in the following paragraph the MEGA experiment is presented.

MEGA experiment The MEGA experiment searched for the decay $\mu \to e\gamma$ decay with a project sensitivity better than 10^{-13}. Consequently, the collaboration began to develop a system of high precision magnetic spectrometer with two separate and distinct parts: one part was a system of multi-wire proportional chamber (MWPCs) to track the positron trajectory and a set

[1]defined as $\delta t/\Delta t$; Δt is the period of one beam cycle, δt is the amount of time when particles are delivered to the target in a beam cycle

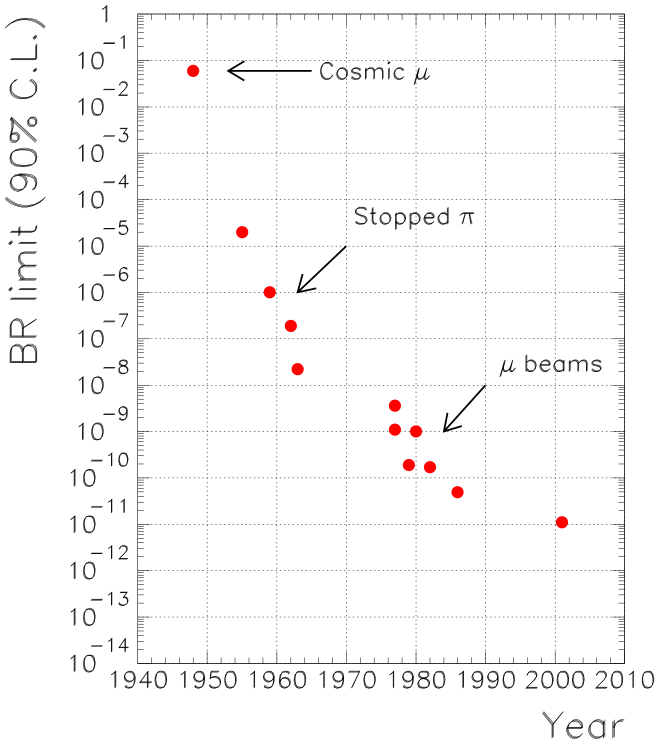

Figure 2.4: $\mu \to e\gamma$ experimental upper limit as a function of time; different muon source used by the experiments are indicated.

of plastic scintillators to determine the positron time; a second section was composed of a set of pair spectrometers to detect the photons and measure their energy, direction of propagation and conversion time and location see Figure 2.5. The photon detection system was almost entirely enclosed on the positron detection in order to maximize the detector acceptance. Both the positron and the photon spectrometer systems were contained within the 1.5 T magnetic field produced by a superconducting solenoid magnet. As reported in Table 2.3 the MEGA collaboration utilized a muon beam intensity of 1.5×10^7 μ/s and a duty cycle of 6%÷9%. The muon beam was stopped in a thin elliptical target in the center of the detector with a slant angle of 83° with respect to the beam direction. The positron spectrometer had a 30 cm outer radius, large enough to contain all the positrons that were produced by muons decay at the target. The timing information was given by two ring-shape sub detectors, made of plastic scintillators positioned near the ends of the drift chambers system. Each pair spectrometer used two sheets of lead to convert high energy photons in e^+e^- pairs. A MWPC located between the two sheets converters determined the photon conversion point, another system of plastic scintillators measured the time. This detector guaranteed a resolution of 1.2% FWHM for the positron energy, 4.5% FWHM for the γ energy and 1.6 ns for $T_{e\gamma}$. The results of MEGA were, however, different from those expected. In fact, the collaboration of MEGA aim at a sensitivity on B($\mu \to e\gamma$) $\approx 9\times10^{-14}$, as the resolutions and the detector acceptance design. Furthermore engineering considerations reduced the expected sensitivity to 9×10^{-13} due to three main reasons: the first reason was that the solenoid could hold only three spectrometers photons instead of five, the second reason was that each photon spectrometer had only two sheets of conversion to lead instead of three because the conversion of photons that were occurring in the innermost layer had a low efficiency of reconstruction, the third reason was that the total solid angle achievable was 30% in order to keep under control the background. Finally the positron and photon reconstruction efficiency was much lower than expected. This low efficiency of reconstruction was attributed to signal induction between the anode and the cathode of the positron spectrometer and to electrons and positrons of low longitudinal momentum spiraling along the magnetic field lines producing large fractions of the spectrometer dead time. The fraction of data analyzed and reconstructed was modest. The final result obtained by MEGA was B($\mu \to e\gamma$) $\leq 1.2 \times 10^{-11}$ at 90% confidence level.

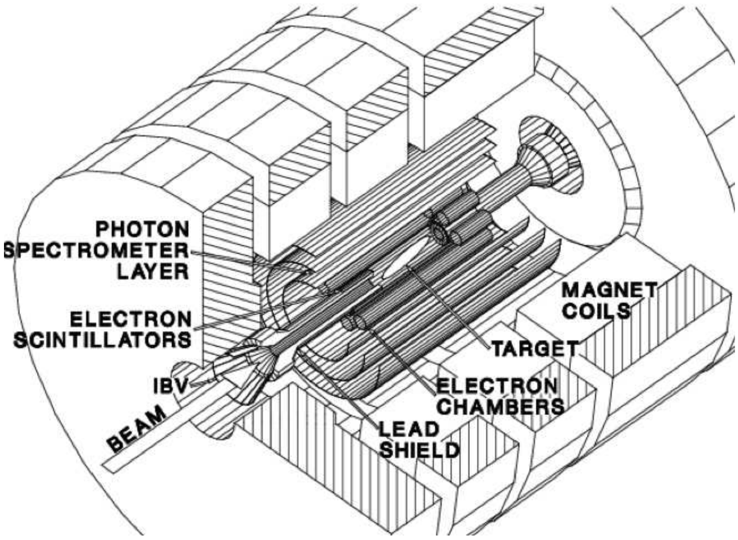

Figure 2.5: Sketch of the detector of the MEGA experiment (2002). The most recent $\mu \to e\gamma$ experiment

2.3 $\mu \to e\gamma$ phenomenology

In the center of mass reference system, the $\mu \to e\gamma$ decay shows defined and simple kinematic characteristics :

1. the outgoing particles have energy equal to $m_\mu/2$;
2. the particles are emitted in opposite directions;

3. are issued simultaneously.

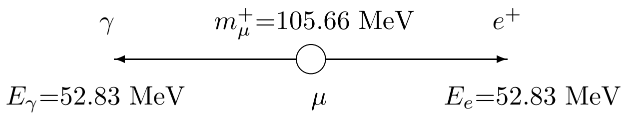

To exploit conveniently this simple kinematic, all experiments that have studied this decay so far have stopped the positive muon beam[2] on a target and observed the decay products in the system of the laboratory. A signal event therefore appears as a positron and a photon of equal momentum issued in collinear and temporal coincidence.

Two basic categories of background events can mimic the event signature, these are:

1. correlated background

2. accidental background

In the following discussion with Δx is denoted the experimental FWHM resolution for the measurement of that variable, with ∂x the selection window for signal events, corresponding to 90% probability of containing the signal ($\partial \mathrm{x} = 1.4\ \Delta \mathrm{x}$ in case of Gaussian), and $\delta \mathrm{x} = \partial \mathrm{x}/2$ is half selection window.

2.3.1 Correlated background

The correlated background is given by the radiative muon decay $\mu^+ \rightarrow \mathrm{e}^+ \nu_\mathrm{e} \overline{\nu}_\mu \gamma$ where the neutrinos have little energy, while the positron and the photon are emitted nearly in the same direction and opposite orientations [2]. The spectrum of photons from the radiative decay is presented in Figure 2.6.

The differential radiative decay width is usually expressed in terms of $\mathrm{x} = 2\mathrm{E_e}/\mathrm{m}_\mu$, $\mathrm{y} = 2\mathrm{E}_\gamma/\mathrm{m}_\mu$, $\mathrm{z} = \pi - \theta_{\mathrm{e}\gamma}$. For values of $\mathrm{x} = 1$, $\mathrm{y} = 1$and $\mathrm{z} = 0$, corresponding to the region of signal, the width of decay vanishes; on the other hand the finite experimental resolutions introduce background events that ultimately limit the achievable sensitivity.

Given the experimental resolutions, and integrating the differential decay width in the intervals $[1 - \delta\mathrm{x}, 1]$ and $[1 - \delta\mathrm{y}, 1]$ the probability of a background event to fall in the signal region is easily computed. Figure 2.7 shows the evolution of this probability as a function of δx and δy, under the hypothesis that $\delta\mathrm{z} \leq 2\sqrt{\delta\mathrm{x}\delta\mathrm{y}}$. To achieve an experimental sensibility of 10^{-15} resolutions of the order of 0.01 on both γ and positron energy are required.

[2]It is not possible to use a beam of negative muons because of the large cross section for capture in matter.

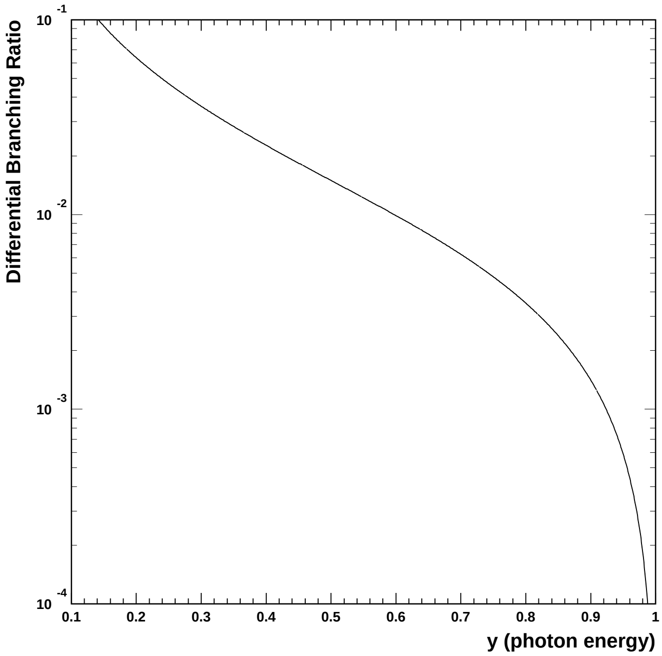

Figure 2.6: Photon spectrum from the muon radiative decay in terms of reduced photon energy $y=\frac{2E_\gamma}{m_\mu}$.

2.3.2 Accidental background

An accidental background event is produced when a positron and a photon, emitted by two distinct processes, are in temporal and spatial coincidence. The use of a pure muon beam ensures that the unique source of positrons is the muon decay . The same argument however cannot be applied to photons. In fact there are several sources of high energy photons in the experimental environment:

- radiative muon decay;
- positrons interaction in the detector, with annihilation in flight or Brehmstrahlung;
- cosmic muons;
- neutrons interaction with the surrounding materials.

Apart from cosmic rays interactions, each contribution is proportional to the muon flux on the target.

The integrated photon yield for photons with energy between a given threshold and $m_\mu/2$ and emitted in the LXe acceptance is shown in Figure 2.8.

The effective rate of accidental background events falling into the signal region, R_{acc}, is given by [2]

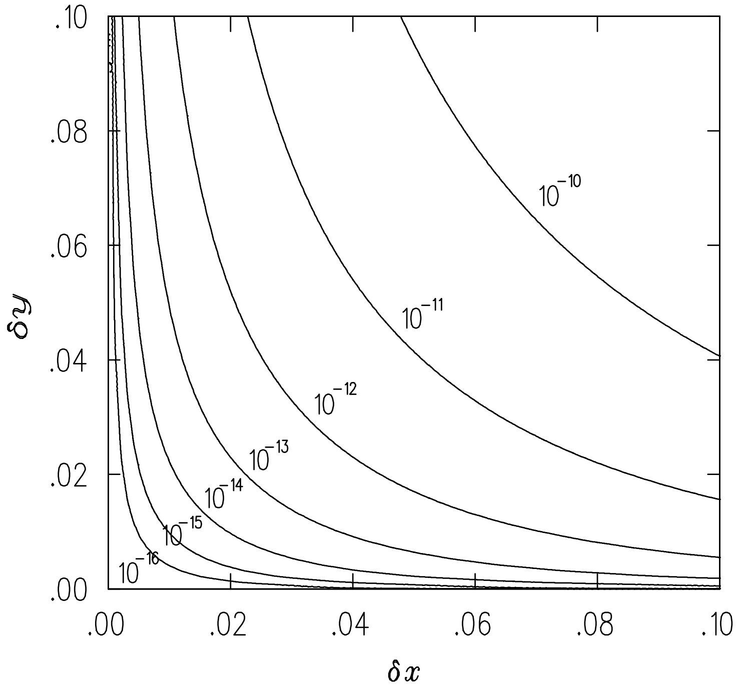

Figure 2.7: Fraction of decays $\mu^+ \rightarrow e^+\nu_e\overline{\nu}_\mu\gamma$ mistaken for $\mu^+ \rightarrow e^+\gamma$ as a function of the positron and the photon energy resolutions.

$$R_{acc} \;=\; \frac{\alpha}{2(2\pi)^3} R_\mu^2 \delta x(\delta y)^2 \delta t_{e\gamma}(\delta\theta_{e\gamma})^2(\ln(\delta y) \;+\; 7.33) \tag{2.1}$$

It has been evaluated by using the normalized variables $x = 2E_e/m_\mu$ and $y = 2E_\gamma/m_\mu$ and integrating them in the intervals $[1-\delta x, 1]$ and $[1-\delta y, 1]$ over x and y energy spectra. R_{acc} increases quadratically with the muon beam intensity, becoming predominant for intense beams.

On the other hand R_{acc} can be written as:

$$R_{acc} \;=\; R_\mu \times B_{acc} \tag{2.2}$$

B_{acc} is the probability of a background event to be recognized as signal, this is the ratio between the number of accidental events interpreted as $\mu \rightarrow e\gamma$ events compared to the total number of decays observed. The experiment sensitivity scales inversely with the experiment statistics collected only in case of background free experiment, it is not true if the number of expected background events is greater than 1. In order to keep it under control, the detector needs to have as good as possible performances in the photon energy and relative gamma-positron direction measurement.

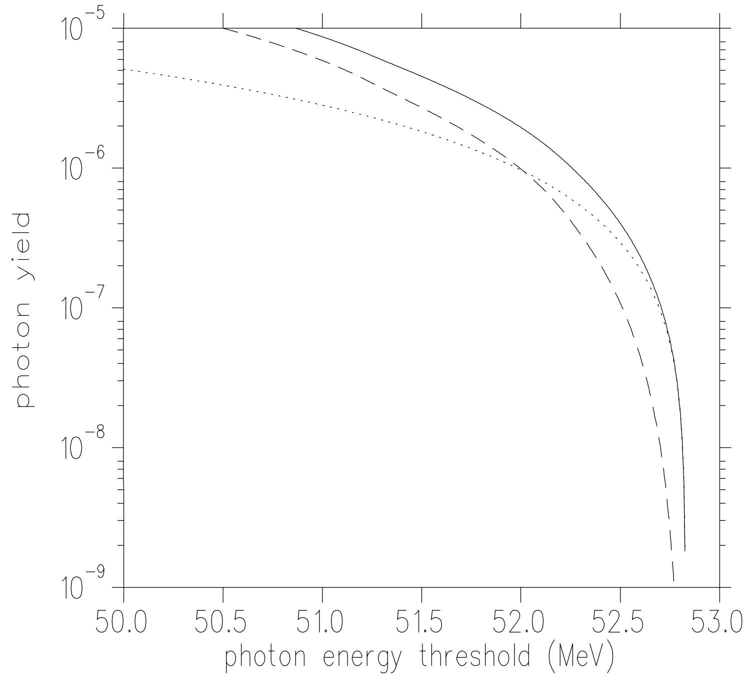

Figure 2.8: Integrated spectra of photons from a defined threshold to the end-point: the dashed line indicates the radiative decay, the dotted line the positron annihilation flight, the solid line the sum of the two.

2.4 Single event sensitivity

The average number of $\mu \to e\gamma$ events expected in experiment is:

$$\mathrm{N_{events}} = \mathrm{R}_\mu \mathrm{T} \frac{\Omega}{4\pi} \varepsilon_e \varepsilon_\gamma \varepsilon_{sel} \mathrm{B}(\mu \to e\gamma) \tag{2.3}$$

where R_μ indicates the beam intensity, T the live time of data taking, Ω the solid angle covered by the apparatus, with ε_e and ε_γ the probability that positron and a photon reaches the respective detectors and the efficiency ε_{sel} the efficiency of the signal selection. ε_e and ε_γ are linked to the detector geometry and used materials, while the selection efficiency is due to experimental resolutions. The single event sensitivity (SES) is defined as the Branching Ratio of $\mu \to e\gamma$ decay for which the average number of expected events is equal to one. Imposing $\mathrm{N_e} = 1$ in Equation (2.3), we obtain:

$$\mathrm{B}(\mu \to e\gamma) = \frac{4\pi}{\mathrm{R}_\mu \mathrm{T}\Omega} \times \frac{1}{\varepsilon_e \varepsilon_\gamma \varepsilon_{sel}} \tag{2.4}$$

2.4.1 New $\mu \to e\gamma$ experiment sensitivity expectations

A new $\mu \to e\gamma$ experiment has been designed exploiting the present-day detector technologies. The expected resolutions, evaluated by Monte Carlo simulations, are listed in Table 2.5. The detector is currently operative at the Paul Scherrer Institute [51] in Switzerland.

Parameter	**FWHM**
$\Delta E_\gamma/E_\gamma$	5%
$\Delta E_e/E_e$	0.7÷0.9%
$\Delta\theta_{e\gamma}$	17÷20.5 mrad
$\Delta T_{e\gamma}$	150 ps

Table 2.5: Expected experimental resolutions values expressed in FWHM for the MEG experiment.

Referring to the considerations of section 2.3.1, using the design resolutions and applying selection windows of the events that preserve 90% of the signal, the correlated background is expected to be limited to a branching ratio of $B_{cor} \approx 4 \times 10^{-15}$.

The accidental background can be estimated based on the section 2.3.2. Given the expected resolutions, and requiring a signal selection efficiency $\varepsilon_{sel} = 90\%$ the selection windows are therefore defined as follow: $\delta x \approx 0.7\%$, $\delta y \approx 5\%$, $\delta\theta_{e\gamma} \approx 2 \times 10^{-4}$ sr and $\delta t_{e\gamma} \approx 0.15$ ns. Using a muon stop rate on the target equal to $R_\mu \approx 3 \times 10^7$ μ/s from Equation (2.1) the equivalent branching ration due to accidental background is estimated to be $B_{acc} \approx 6 \times 10^{-14}$.

According to Equation (2.4) the MEG single event sensitivity is equal to $B(\mu \to e\gamma) \approx 3.8 \times 10^{-14}$ using $\Omega/4\pi = 0.1$, $\varepsilon_e = 0.9$, $\varepsilon_\gamma = 0.6$, $\varepsilon_{sel} = 0.7$, $R_\mu = 3{\times}10^7$ μ/s, $T = 2.6{\times}10^7$ s.

The value of the single event sensitivity (SES) does not define the value of the sensitivity of the experiment. This value is calculated using the theory of probability [52].

Given the true value of the $B(\mu \to e\gamma)$ the number μ of expected events is:

$$\mu = R_\mu T \frac{\Omega}{4\pi} \varepsilon_e \varepsilon_\gamma \varepsilon_{sel} B(\mu \to e\gamma) \tag{2.5}$$

and follows a Poisson distribution. Let define k as the number of detected signal events,, this is a measurement of the true value μ extracted from the aforementioned Poisson distribution.

Based on the reported evaluations of the backgrounds we expect about 0.5 events at the end of two years of data taking. The strategy adopted to extract a limit on the branching ratio from the number of detected signal events is based on the Feldman and Cousins prescriptions [53]. In this frequentistic approach and in the case that any event is recognized as signal, the final limit reachable by the MEG experiment is:

$$B < 1.5 \times 10^{-13} \text{ @90\%C.L.} \tag{2.6}$$

Finally Figure 2.9 shows the 90% confidence intervals for the variable μ as a function of the number k of events detected in the experiment in the presence of 0.5 background events.

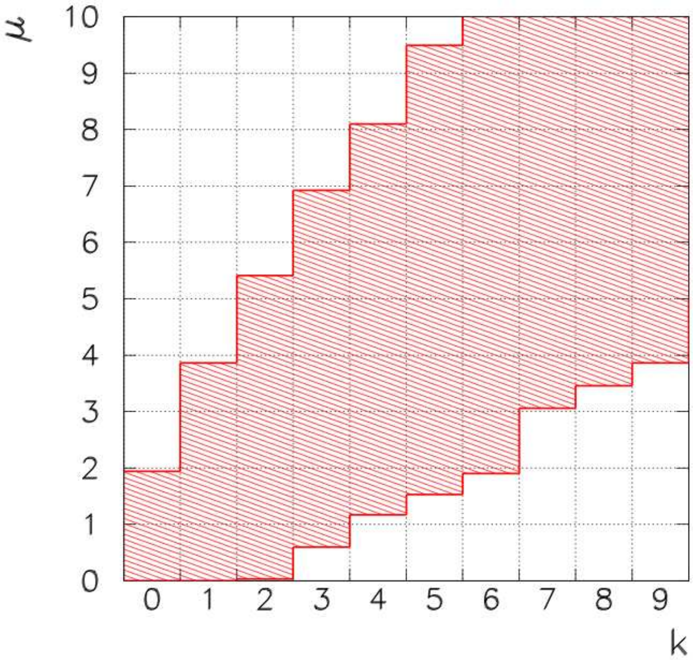

Figure 2.9: 90% confidence belt for the average number of signal events μ, depending on the observed number of events k in presence of 0.5 background event.

2.5 Final remarks

Muon physics has played in the past a fundamental role in the construction of the standard model of particle physics. Nowadays muon physics has not yet exhausted its potential. Precise measurement of the muon lifetime and of the Michel parameters provide indication of the Lorentz structure of the weak interaction, test of CPT and QED, and measurements of fundamental constants. The determination of the muon anomalous magnetic moment and the search for muon electric dipole moment may provide hints for new physics beyond the Standard Model. Low energy muons are widely used probes in condensed matter sciences. The discovery of Lepton Flavor Violation (LFV) in muon decays, such as $\mu^+ \to e^+\gamma$, $\mu^+ \to e^+e^-e^+$ and $\mu^- \to e^-$ conversion in nuclei, would be an indisputable proof of the existence of new dynamics beyond the Standard Model.

New measurements of all LFV channels in the charged sector, including $\tau \to \mu\gamma$, but also new measurements of g_μ-2 and muon electric dipole model, have solid theoretical motivations. Furthermore, the predicted branching ratios are not far from present experimental upper limits.

In the search for LFV in $\mu \to e\gamma$ decay it is possible to improve the sensitivity to the 10^{-13} level, the MEG experiment is designed to accomplish this task and is currently in data acquisition at the Paul Scherrer Institut at PSI. In the next chapters the MEG experiment is presented, together with its set up and the results from the first run of physics data taking.

Part II

The MEG experiment

Chapter 3

The MEG experiment

The search for a rare process, such as $\mu \to e\gamma$, requires an extremely precise measurement of the decay products kinematic variables. As noted in the previous chapter, this demand is becoming more stringent with increasing beam intensities to keep the accidental background under control. For each of the two decay products a dedicated detection system is reserved: the photon is revealed by means of a Liquid Xenon detector (LXe) while the positron is analyzed by a drift chamber tracker (DC) immersed in the non homogeneous magnetic field of the COBRA magnet and finally detected by a scintillating bar hodoscope (TC). The tracking system defines the direction of emission and the momentum of the e^+ and the TC measures its time. As seen from the diagrams shown in Figure 3.1 and 3.2, the detector does not completely cover the solid angle around the target, but only a fraction of about 10%, for cost and detector optimization reasons. The detector signals are connected to the acquisition system driven by the trigger system.

The sensitivity to rare decay, as defined in Equation (2.4), is in inverse proportion to the number of decays as the background is maintained below the signal. In section 2.3.2 the muon beam parameters have been introduced; they are the intensity and the duty cycle $\delta t/\Delta t$ (δt is the period of beam on and Δt is the full period of a beam pulse). The goal of having an average stopping rate equal to 10^7 μ/s, in order to collect 10^{13} μ-stop on target in less than three years of data taking, can be accomplished by both a continuous or a pulsed beam. At this muon stop rate the background is dominated by the accidental component whose rate depends quadratically to the instantaneous stop rate, as reported in section 2.3. To explore branching ratio value well below the current predicted upper limit, it is required the ever-more intense muon source available in the world: this beam is located at the Paul Scherrer Institute (PSI) in Villigen, Switzerland.

As a reference for next sections, the reference system of the experiment has the origin ($x = y = z = 0$) at the center of the muon target, the z axis is directed along the beam direction, y is directed towards high and the calorimeter his located in the half-space at $x < 0$; see Figure 3.2.

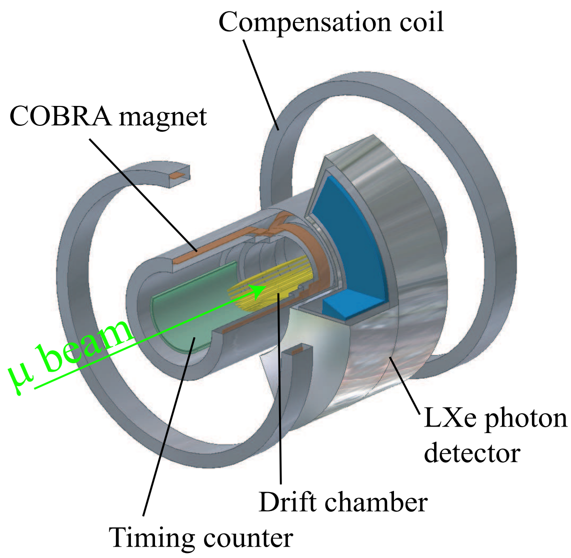

Figure 3.1: Three-dimensional view of the detectors used in the MEG experiment.

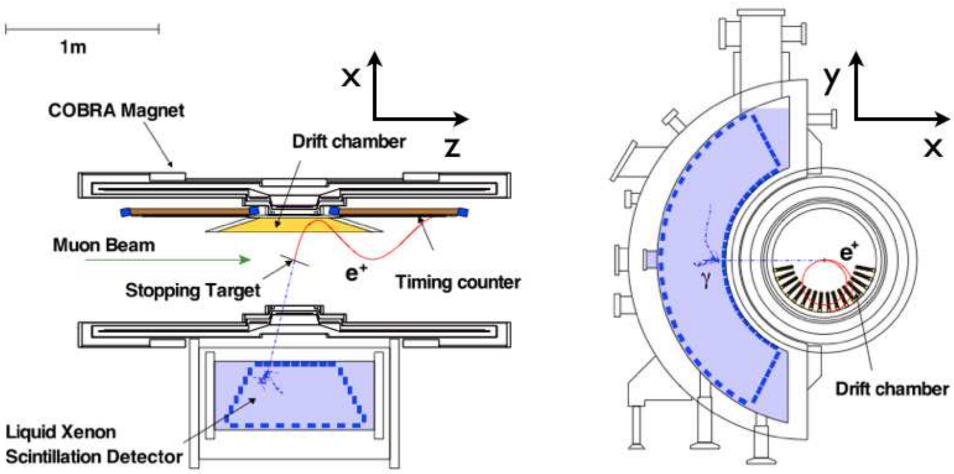

Figure 3.2: Schematic view of the detectors used in the MEG experiment.

3.1 Beam and target

A proton beam of 590 MeV and intensity 1.8 mA, accelerated with a cyclotron, is carried on two targets in sequence. They are shaped like a truncated cone of half-open α compounds of graphite and tilted of the same angle α with respect to the beam axis of, see Figure 3.3. They have different thicknesses, respectively 7 mm for the thin target, called the M-target, and 40 or 60 mm for the thicker one, called E-target. The targets are cooled down by the emission of radiation and are kept in rotation against thermal stresses.

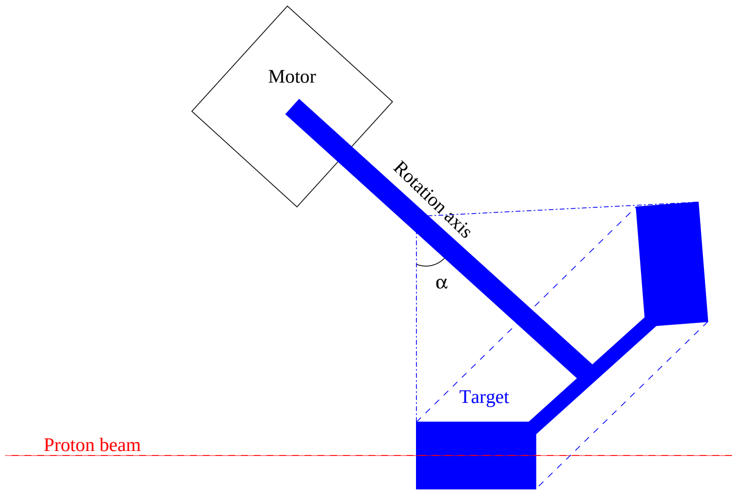

Figure 3.3: Schematic section of the target and the beam of protons.

The proton interaction mostly products neutrons and pions, since the available energy is under the K production threshold. The pions decay both in flight and inside the graphite target producing muons and electrons. The two targets branch seven beam lines available simultaneously.

Muons from π decays at rest on the surface of the target are called "surface muons"; they are totally polarized and boosted with a momentum of 29 MeV/c. The MEG collaboration is exploiting πE5 beam line, the one with highest acceptance for "surface muons" at PSI [54, 55].

The expected μ and π flows depend on the particles momentum accepted by the magnetic channel of πE5, the measured fluxes are presented in Figure 3.4 for various particles and different momenta; for a momentum of 29 MeV/c there is a conspicuous increase of μ^+ flux coming from "surface muons". The characteristics of the beam line are shown in Table 3.1.

The πE5 beam is focused on the experiment target after a stage in which the beam positrons, that are more abundant that muons, are swept away by an electrostatic separator. Moreover, the muons momentum, 29 MeV/c, is reduced so that they can be stopped in the thin experiment target.

Transportation and purification of the beam has been studied by using a beam optics simulator (TRANSPORT [56]) and a program of beam tracking (TURTLE[57]). The particle flow, the

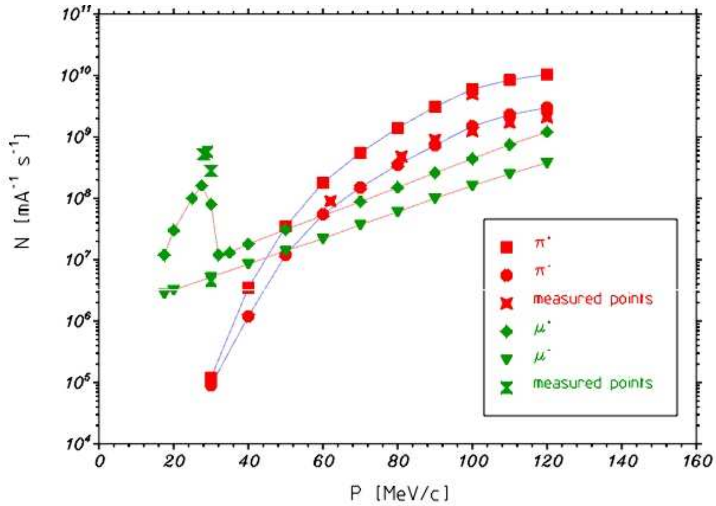

Figure 3.4: Muon flux and pions in the beam line πE5 as a function of the momentum.

Parameter	**Value**
Length of the beam line	10.4 m
Momentum range	20÷120 MeV/c
Momentum resolution	2%
Solid angle	150 msr
Beam spot(FWHM)	15×20 mm^2
Horizontal divergence(FWHM)	450 mrad
Vertical divergence(FWHM)	120 mrad

Table 3.1: πE5 beam line properties.

positron contamination and the beam transverse size were also measured experimentally at the exit of the πE5 beam line [58]. These studies, confirmed by our measurements, have led to the choice of the additional magnetic and electrostatic elements used to connect the existing beam line to the magnet COBRA. They are shown in Figure 3.5 and are listed here:

- A triplet of quadrupoles;
- An electrostatic separator that operates as a speed selection to create a spatial separation between muons and electrons equal to 11 cm at a distance of about 2 m from the target, equivalent to 7 σ, where σ is the combined RMS of the two spatial distributions shown in Figure 3.6.
- A second triplet quadrupole is inserted after this filter to refocus the beam;
- a beam transport solenoid (BTS) is used as a junction between the last quadrupole magnet and the COBRA magnet. Inside the BTS a foil of polyethylene is inserted to reduce the muon momentum.

The target is positioned at an angle of 20.5° with respect to beam in order to increase the target thickness crossed by the muons and to minimize the thickness traversed by the decay positron. The positron multiple scattering is kept low by using He atmosphere.

Three possible target materials are simulated by using the GEANT code [59] . In Table 3.2 the material thickness crossed by the muons before coming to stop and relative dispersion in RMS are reported. The polyethylene is chosen as target material. Figure 3.7 shows a picture of the MEG target.

Simulated material	**R(μm)**	σ_R**(μm)**
Polyethylen $(CH_2)_n$	1100	86
Mylar $(C_5H_4O_2)_n$	870	71
Kapton $(C_{22}H_{10}N_2O_5)_n$	870	71

Table 3.2: Value of average thickness of material traversed by muons before stopping (R) and their dispersion in RMS (σ_R) of the three materials considered for the target.

The target thickness was chosen equal to 205 μm and this is fixed at an angle of 20.5° with respect to the μ beam direction. In this way the target material seen by the muons is 5 times the range dispersion of 29 MeV/c muons in polyethylene. The remaining material needed to stop the muons is placed inside the absorber placed at the center of the BTS.

The target is provided by 6 holes, aligned in horizontal and vertical directions, used to measure the tracking resolution on decay vertex reconstruction.

Under these conditions the beam has a maximum intensity of 2.0×10^8 μ/sec and, taking into account the magnetic properties of the beam line, it can be focused on an ellipse of calculated dimensions $\sigma_y = \sigma_x \approx 5.$ mm. The multiple scattering in the material present on the muon line

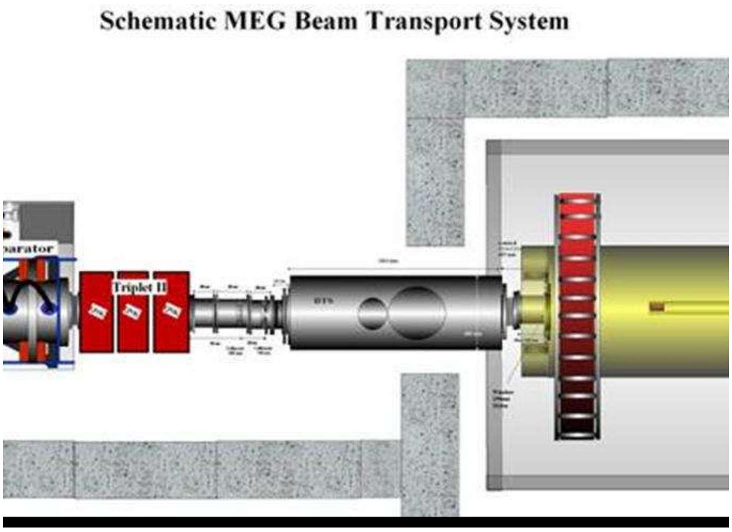

Figure 3.5: Diagram of the muon beam line in πE5.

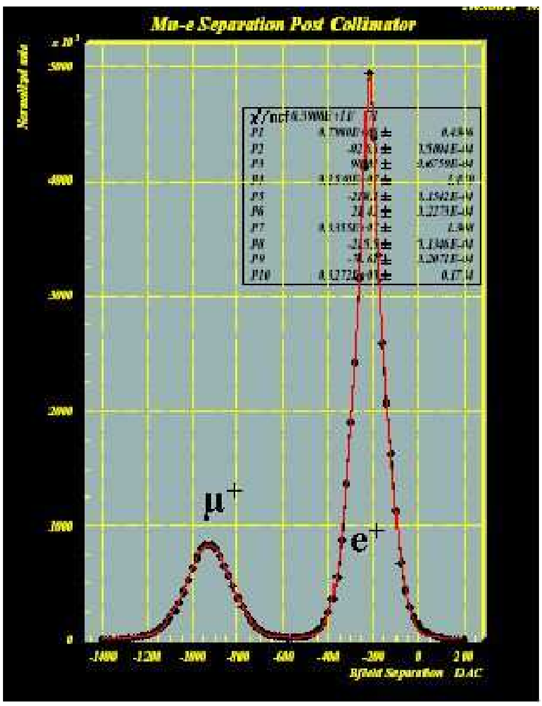

Figure 3.6: Spatial separation between muons and positrons in arbitrary units measured in the experimental area πE5 two meters far from electrostatic separator.

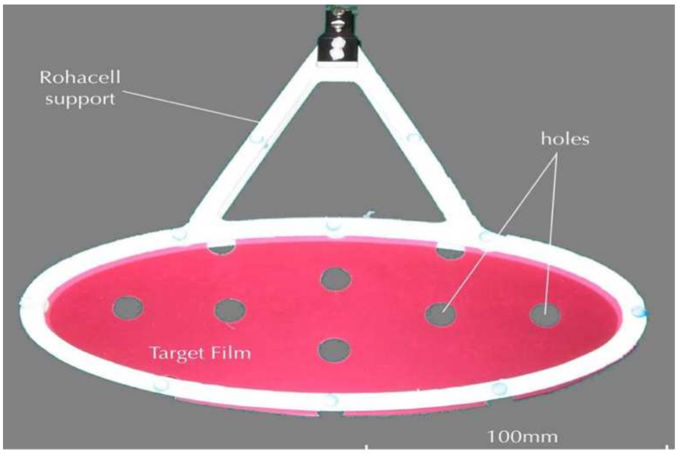

Figure 3.7: Picture of the polyethylene elliptic target of the MEG experiment.

of flight from the BTS to the target (separator, vacuum window and helium atmosphere) spreads the transverse dimensions of 10 mm for both axes.

3.2 Positron detector

The positron detection system is essentially composed of two parts: a magnetic spectrometer and a set of counters for time of flight measurement. Two schematic cross sections of the positron detector are shown in Figure 3.8.

In the following sections, the whole tracking system will be presented.

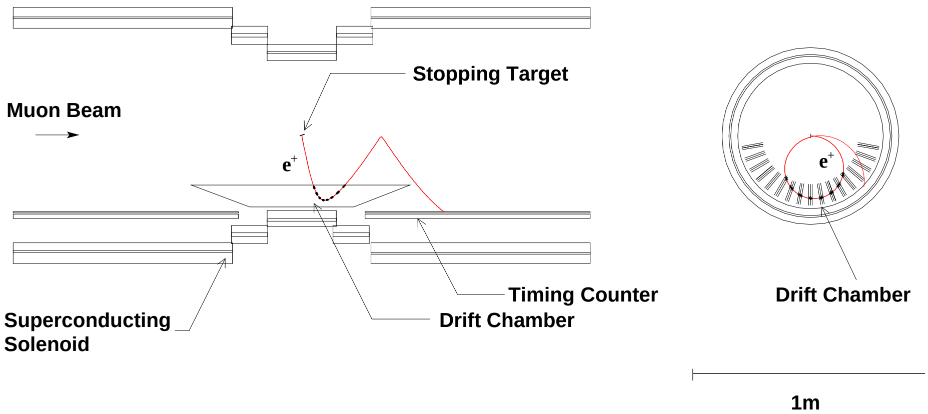

Figure 3.8: Schematic view of the positron spectrometer, left r - z projection and right r - φ.

3.2.1 Magnetic spectrometer

General issues The positron tracking device is immersed in an inhomogeneous solenoidal magnetic field with cylindrical symmetry along the z axis, and intensity decreasing for increasing |z|. This field configuration, compared to an uniform field, leads to twofold advantages:

a) A positron emitted close to 90° to the magnetic field axis would be quickly expelled from the drift chambers region (Figure 3.9 (a)). While in case of an uniform field it could cross many times the tracker, thus increasing the chamber occupancy (Figure 3.9 (b));

b) The gradient field can be chosen so that, in the range of the experiment acceptance, the distance of the inverting point of a positron trajectory from the beam axis depends on the total momentum and not on its transverse component (Figure 3.10). Here it comes the acronym COBRA: Constant Bending Radius. This simplifies the search for high momentum tracks.

COBRA magnet

COBRA [60] is a thin wall superconducting magnet capable of generating an axial field that is maximum at the center, 1.27 Tesla, and decreases along the axis of the beam as shown in Figure 3.11. The superconducting magnet consists of five coils with three different radii; one central coil, two gradient coils, and two end coils. The end coil is separated into inner and outer parts with different current densities. The gradient field is obtained by arranging the five coils in a step-structure and adjusting the winding density in each coil. A pair of compensation coils surround the ends COBRA magnet to cancel the stray magnetic field at the location of the photon detector. The stray field could degrade the performance of the photon detector because the gain of the photomultiplier tubes drops down as the strength of the external magnetic field increases. The stray field need to be reduced down to 50 Gauss level around the photon detector, see Figure 3.12 (b).

Within the acceptance of the photon detector ($|\cos(\theta)| \leq 0.35$), the thickness of the magnet is reduced down to 0.197 X_0 so that the photons from the target placed at center of the magnet can traverse it.

The magnetic field of COBRA was measured “in situ” on a map of over 25000 points with a one-dimensional Hall probe, intercalibrated with a NMR probe. The agreement of the measured values with respect to theoretical prediction was measured at $\sigma = 0.2\%$ over the volume. The stability of the field was also verified with a NMR probe on a one-week period and it was found stable within 20 ppm.

Drift chambers

The measurement of the positron momentum is carried out by means of 16 trapezoidal drift chambers, each one formed by two independent planes, two pictures of the DC modules are reported in Figure 3.13). The wires of two different planes are shifted by half anode wire spacing to resolve the left to right ambiguity [61, 62].

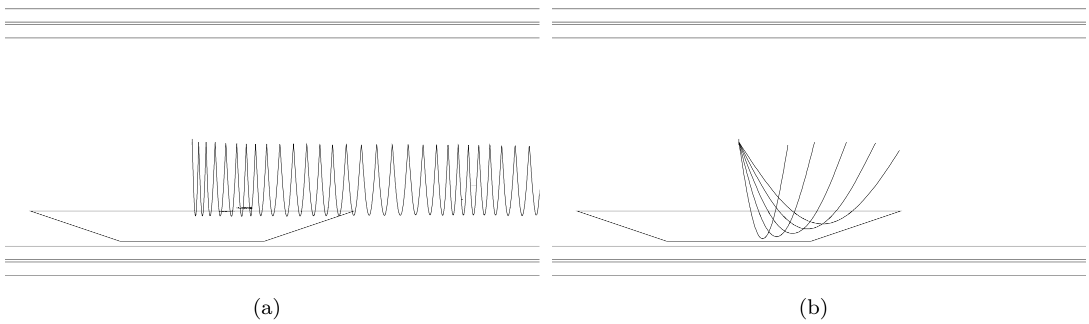

Figure 3.9: Positron trajectory in a uniform magnetic field: (a) (r - z projection) positron emitted at an angle of 88° relative to the direction of the field, in (b) positron pulse of 52.8 MeV/c issued different angles show that the point of reversal of the trajectory depends on the angle of emission.

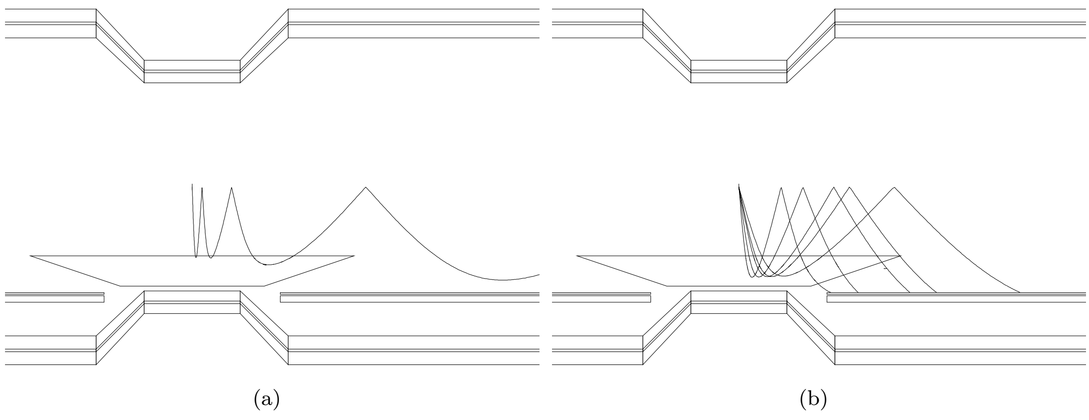

Figure 3.10: Advantages equipped with a gradient magnetic field: in (a) (r - z projection) a particle emitted at 88° is rapidly extracted from the area occupied by drift chambers; in (b) monochromatic particles emitted at different angles show how to, inside the acceptance of the experiment, the radial position of the first point of reversal does not depend on the angle.

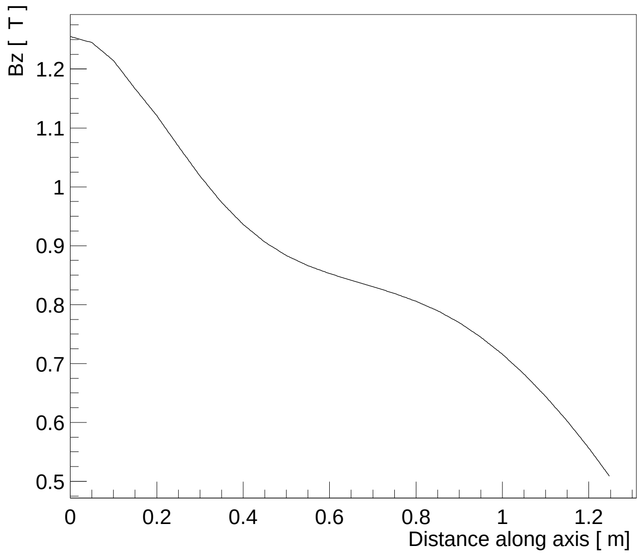

Figure 3.11: Magnetic field intensity along the z axis.

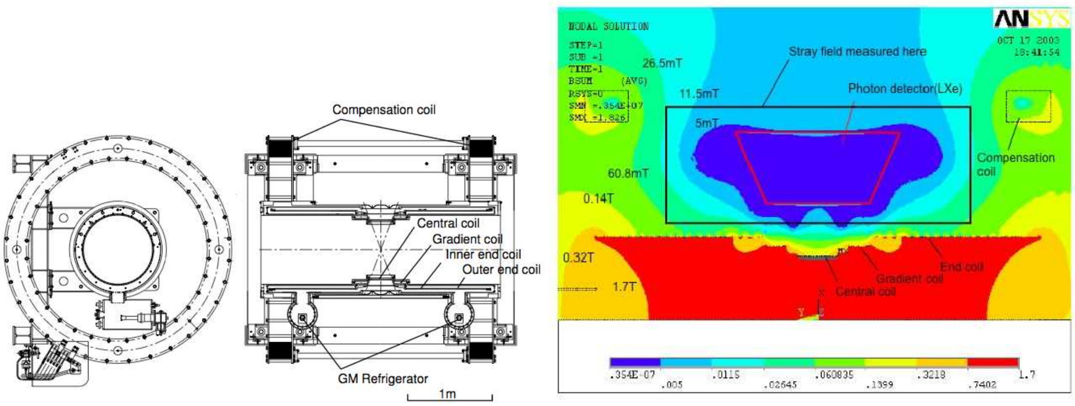

(a) (b)

Figure 3.12: (a) Schematic drawing of the COBRA magnet and (b) generated magnetic field in the area of the MEG experiment.

The chambers are placed radially at 10.5° intervals. The sensitive area of of the chambers covers radially the space from r = 19.3 cm and r = 27 cm, and longitudinally the region with $|z| \leq 50$ cm. The distance between the chambers and the muon target reduces the overcrowding

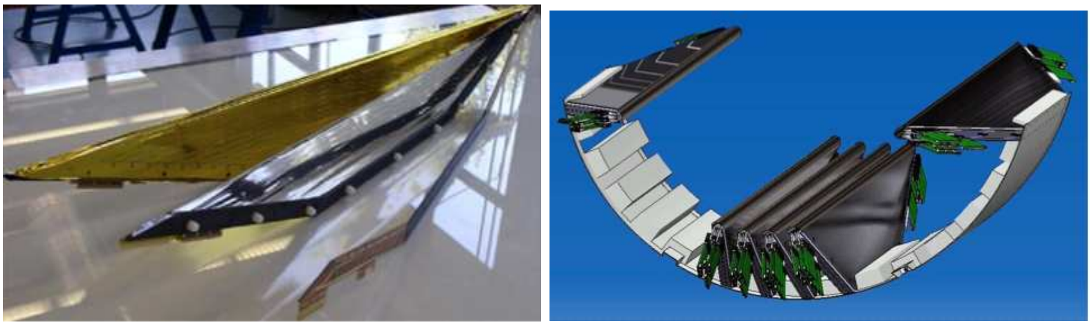

(a) (b)

Figure 3.13: Picture of one drift chamber module (a) and scheme of the whole system.

of the low momentum Michel positrons. In the case of positrons from 52.8 MeV the angular coverage of this geometry is $|\cos(\theta)| \leq 0.35$ and $-60^\circ \leq \varphi \leq 60^\circ$. The chamber volume is filled with a mixture of He and C_2H_6 at the same concentration. This mixture was chosen to accommodate the energy loss for ionization (≈ 65 e^-/cm at the ionization minimum) reducing the multiple scattering ($X_0 \approx 650$ m).

The r-coordinate of a track is measured by means of the time difference between the wire signals with respect to the absolute track time given by the TC. Since the resolution on the drift time ≈ 5 ns, considering the e^- drift speed in the gas mixture of about 4 cm/μsec for an electric field of ≈ 1.5 kV/cm, the estimated resolution on the radial coordinate is $\delta r \approx 150 \div 200$ μm.

An excellent position resolution is necessary not only for the transverse direction but also for the longitudinal direction. Furthermore, realizing this without increasing the number of readout channels and related front-end electronics is preferred because of the amount of material that could provoke γ-ray background. To accomplish this, a "vernier pad" method [63] has been adopted. Initially, the z-coordinate is derived from the ratio of the charges measured at both ends of the hit wire with an accuracy of 1 cm, then a more accurate z position is calculated by using the vernier pad information. A 5cm zig-zag strip is etched on the cathode planes on both sides of the sense wire plane, so that there are four cathode pads for one sense wire, see Figure 3.14. The induced charge on each vernier pad is related to the z-coordinate due to this zig-zag shape. Thus the ratios of the charges induced on the four pads can be used to accurately determine the z-coordinate. This resolution for the z-coordinate was measured to be 300 $\div$500 μm in a chamber prototype.

The momentum resolution is estimated by a Monte Carlo simulation incorporating the basic performance of the drift chamber described above. For momenta around 52 Mev/c, the track reconstruction should be performed by an adaptive fitting method taking into account both multiple scattering and energy loss. The resolution is estimated to be 0.25$\div$0.48% in standard deviations when employing the Kalman filter technique [64].

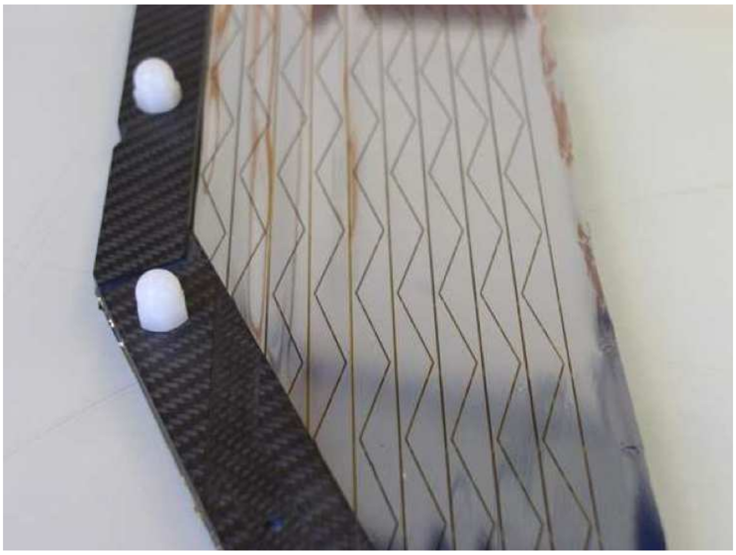

Figure 3.14: Picture showing a zoom on the vernier pad design.

3.2.2 Timing counter

The role of the "Timing Counter" (TC) is to provide a measurement of positron time of flight. The detector consists of two equal cylindrical-shaped sections whose axis of symmetry coincides with the z axis. The two sections are placed symmetrically with respect to the position of the target and they are 31 cm far from the axis z, covering an angular interval of 145° in φ and 31$\leq |z| \leq$ 111 cm. Each section consists of 15 plastic scintillator (BC404) bars, of square section (l = 4 cm), 80 cm long and aligned to the axis of symmetry; in Figure 3.15 a tridimensional drawing of one part of the TC is shown, while in Figure 3.8 the location of the TC in the experiment is reported. Given the geometry of the magnetic field, positrons emitted with $|\cos(\theta)| \leq 0.35$ hit the TC after completing $\approx$ 1.5 turns of the r-φ plane. The scintillator bars are coupled at the ends to two "fine mesh" type PMTs which are less sensitive to high magnetic fields. Even in this case a suitable orientation of the PMTs was adopted to minimize the gain drop and the dispersion on transit time between dynodes due to COBRA field. Figure 3.16 shows the orientation of the PMTs and the scintillating bar with respect to the magnetic field.

Each section is covered in the inner side with 256 scintillating fibers oriented along the azimuthal coordinate. The fibers have a square section with 0.5 cm side and are read out by avalanche photodiodes (APD). By combining the reading of the fiber and the bar signals it is possible to get a bidimensional reconstruction of the positron impact point on TC useful to determine the relative direction of the positron and the photon for trigger purposes.

The timing resolution of TC bars was measured by exposing the 15 bars to an electron beam available in Frascati (Rome, Italy). The measure was performed on 8 different points along the bar for a total of 105 points, yielding a resolution better than the project one, as shown in Figure 3.17. The contribution to the temporal measurement of the multiple scattering suffered by positrons

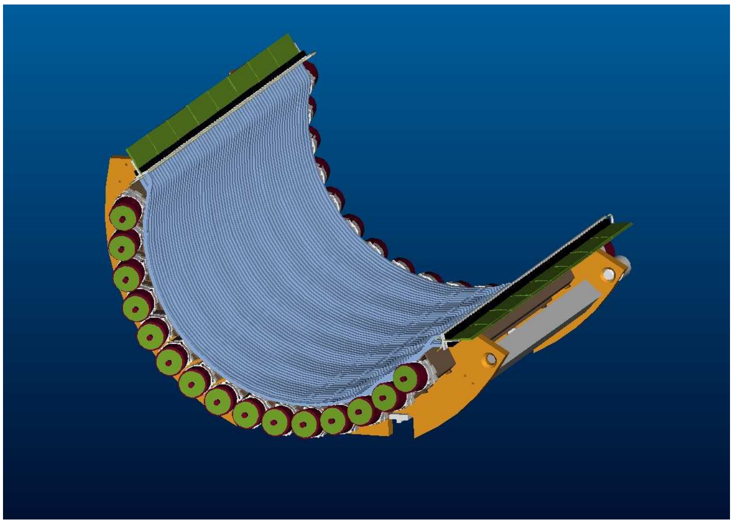

Figure 3.15: Three-dimensional view of a section of the Timing Counter.

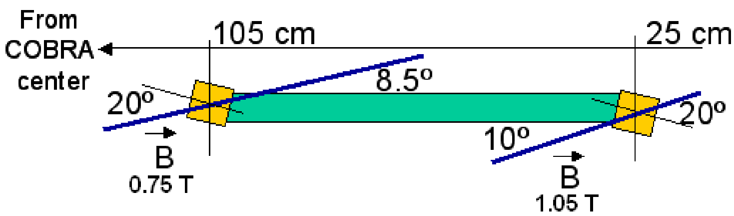

Figure 3.16: Schematic of a TC bar with PMTs location.

in the tracking system has been studied with Monte Carlo methods and found to be negligible ($\approx$ 20 ps).

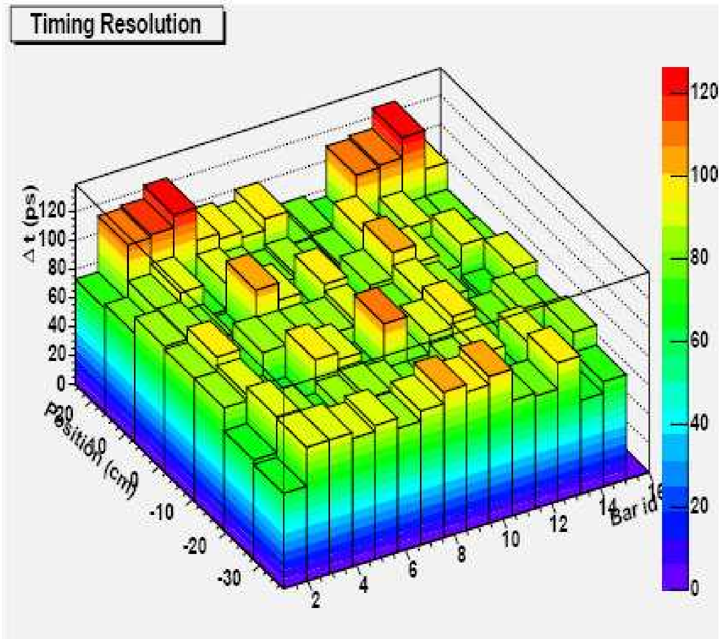

Figure 3.17: Experimental timing resolutions for the 15 bars of a the section of the TC, each one measured in 7 different locations.

A PMT has a limited lifetime when immersed in the atmosphere with high He concentration. For this reason, the TC is isolated from the tracker through a bag of plastic material, internally flushed with nitrogen.

3.3 Gamma detector

The MEG experiment has adopted, for the photon detection, an innovative technique based on liquid Xenon scintillation. This technique combines an efficient light yield, typical of inorganic crystals, with a fast response close to that of organic scintillators. The design and characterization of this calorimeter is one of the main task of the Pisa group [65, 66, 67, 68].

3.3.1 Xenon scintillation

Among the noble gases, the Xe has the advantage of a high boiling point (equal to 165 K at 1 atm, the highest among noble gases) and a high atomic number (Z = 54) which, combined with a great density in liquid phase ($\rho = 2.95$ g/cm^3), makes it an excellent scintillator ($X_0 = 2.77$ cm). For these reasons, a high resolution liquid Xe calorimeter can be designed with considerably compact size. The salient properties of the Xe are shown in Table 3.3.

Parameter	**Value**
Density	2.95 g/cm^3
Boiling and liquefaction temperature	165 K, 161 K
Energy deposit per scintillation photon (γ/α)	24 eV/19 eV
Radiation length	2.77 cm
Decay time	4.2 ns, 22 ns, 45 ns
Scintillation light emission wave length	178 nm
Scintillation light absorbtion length	$\geq$ 100 cm
Attenuation length	$\approx$ 40 cm
Refractive index	1.6 $\div$ 1.72

Table 3.3: LXe optical properties.

The LXe has important properties as a scintillation mean. The number of scintillation photons emitted per unit of energy deposited is comparable to the scintillator crystals (e.g. NaI), so that an excellent energy resolution can be obtained. Moreover, the short scintillation time makes it preferable to the latter, first because it provides a temporal resolution compatible with the experiment requirements, on the other hand significantly reduces the probability of having "pile-up" events, which constitutes an important element in an experiment with high crowding as MEG.

The emission occurs in the VUV with a wavelength equal to 178 $\pm$ 13 nm. The scintillation mechanism involves excited Xe atoms (Xe*) and Xe$^+$ ions produced by charged particles and can be described as follows:

$$\text{Xe}^*\text{+Xe}\rightarrow \text{Xe}_2^* \rightarrow \text{2Xe+ } h\nu$$

or

$$\text{Xe}^+\text{+Xe}\rightarrow \text{Xe}_2^+,$$

$$\text{Xe}_2^+\text{+e}\rightarrow \text{Xe + Xe}^{**},$$

$$\text{Xe}^{**} \rightarrow \text{Xe}^* \text{ + heat},$$

$$\text{Xe}^* \text{ + Xe}\rightarrow \text{Xe}_2^* \rightarrow \text{2Xe+}h\nu$$

where $h\nu$ is an ultraviolet photons emitted per de-excitement of Xe_2 excimer. The bending energy of the excited excimer is significantly less than the first excited state of a Xe atom. Moreover the excimer does not exist in the ground state but only in the excited level. Consequently the Xe is transparent to its scintillation light and the absorption length can be $\gg$ 1 m.

The presence of even small concentrations of impurities can induce absorption of light that would spoil the uniformity of the calorimeter response, with dramatic consequences on the energy resolution. In particular the molecules of oxygen (O_2) and water vapor (H_2O) have non-zero absorption spectra around the Xe emission wavelength, as is evident from Figure 3.18 and 3.19. It is estimated that the contamination by these molecules has to be kept below a few tens of parts per billion. A complex Xe purification system has been designed for this purpose operating on both liquid and gaseous phases. The Xe is circulated in liquid phase through a series of purification cartridges and in gas phase through a heater getter.

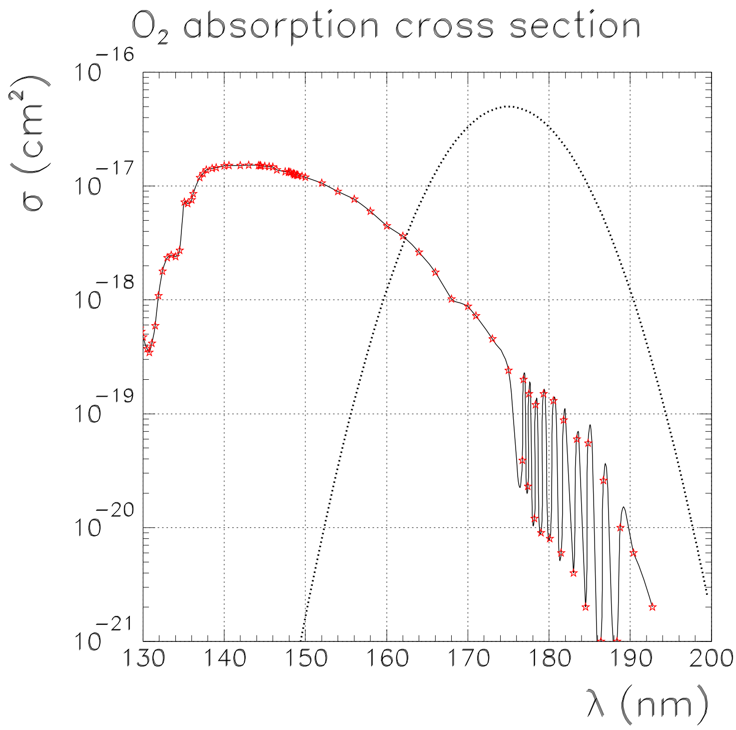

Figure 3.18: Absorption cross section for O_2 with superimposed spectrum of the Xe scintillation liquid (arbitrary scale).

3.3.2 Geometry and detector perfomance

Figure 3.20 shows the design of the calorimeter in which the cylindrical symmetry of the apparatus is preserved, so that photons produced in the target impact perpendicularly on the calorimeter inner surface. An active volume of 0.8 m^3 is read by about 850 Hamamatsu R9299 [69] PMTs sensitive to ultraviolet light. The photocathodic density is not uniform, it is higher in the inner face of the calorimeter where the highest amount of the energy is released and lowers with the distance from the target. The detector covers an angular range defined by $|\cos(\theta)| \leq 0.35$ and $120°$ in φ, corresponding to approximately 10% of the solid angle.

The resolutions expected for a photon of 52.8 MeV are of 150 ps FWHM for time measurement, and $\leq$ 5% for the energy, see Figure 3.21.

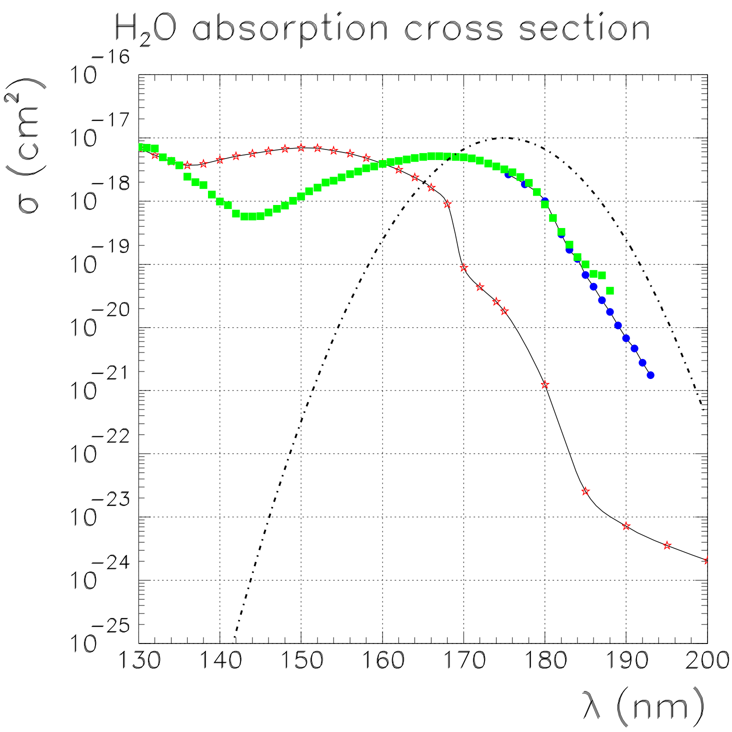

Figure 3.19: Absorption cross section for H_2O (red stars = liquid, blue squares = vapor) superimposed with the spectrum of the Xe scintillation liquid (arbitrary scale).

3.3.3 LXe detector calibration and monitoring

During the data taking, stability and performances of the calorimeter are continuously monitored. Several calibration procedures have been set up, they are divided in daily-based, weekly-based and year-based calibrations.

In this section all the implemented calibration methods are presented.

LED calibration

A system of LEDs is installed inside the detector so that it can fully illuminate the detector PMTs for a twofold purpose: to determine the PMT gains and to independently check the detector stability. The PMT gain evaluation is performed by firing the LEDs at various light intensities every day in dedicated acquisition runs. The check of the detector stability is achieved by firing the LEDs at fixed light intensity continuously during physics runs.

Suppose that N photoelectrons are emitted by the photocathode irradiated by a given amount of light. This signal is amplified by the PMT dynodic chain being the anodic charge q:

$$q = Ng + q_0 \tag{3.1}$$

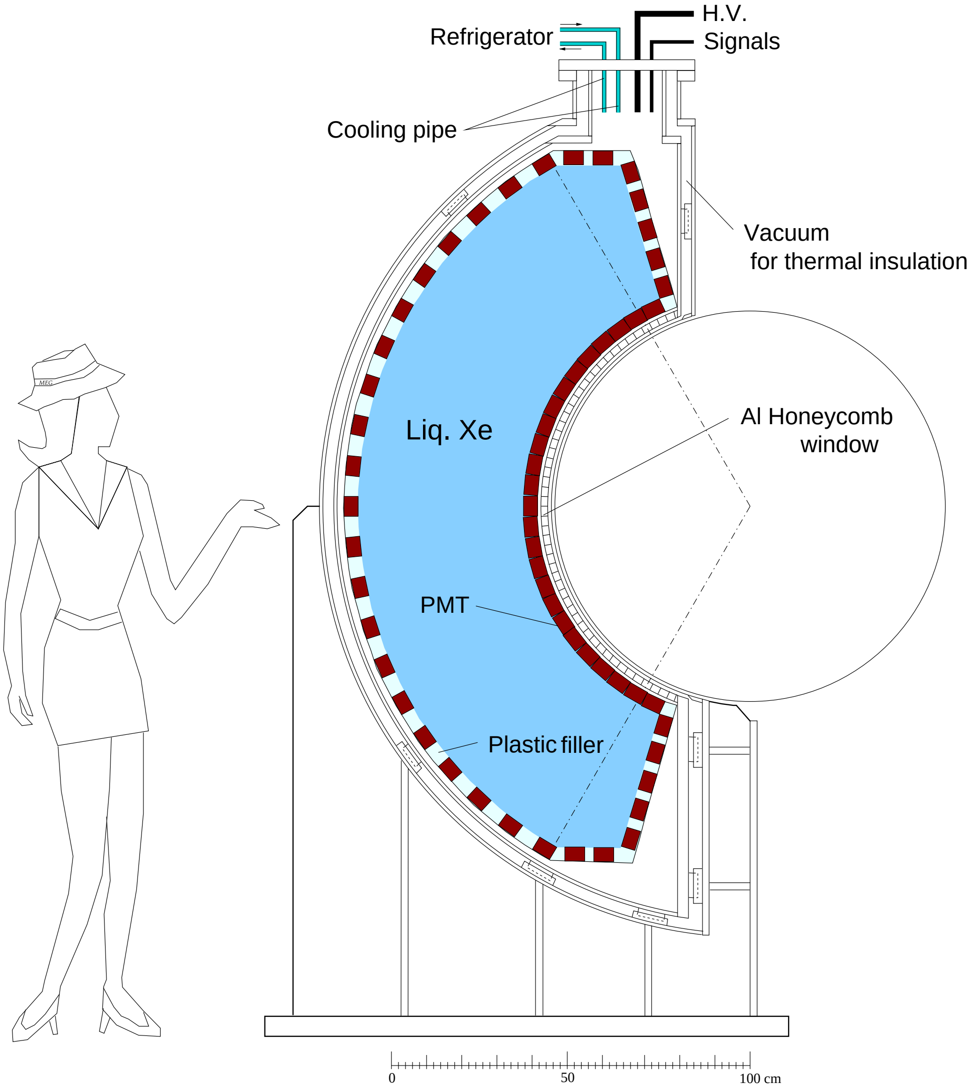

Figure 3.20: Schematic view of the LXe calorimeter.

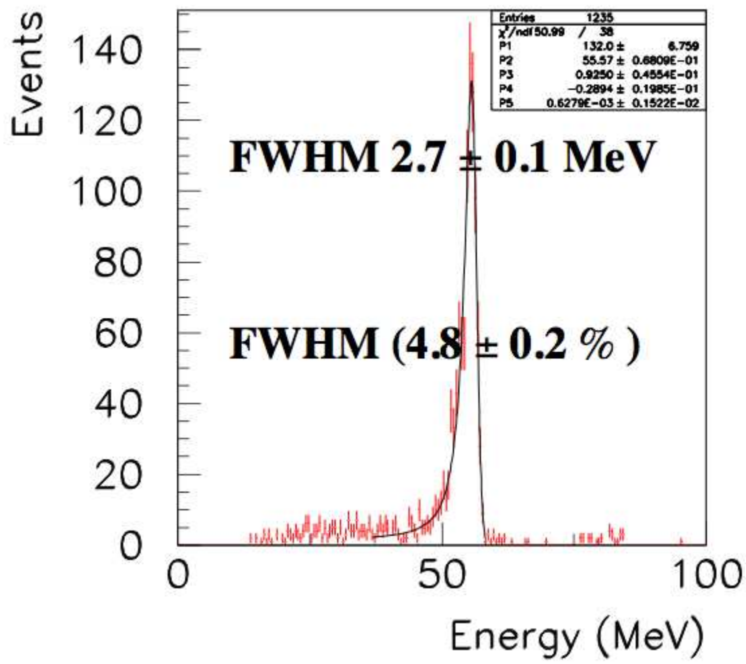

Figure 3.21: 55 MeV γ energy reconstruction using a prototype of the calorimeter called "Large Prototype".

where q_0 is the charge induced by the fluctuations of the baseline. The distribution of N is Poissonian so the variance of the q distribution is:

$$\sigma^2 = g^2 N + \sigma_0^2 \tag{3.2}$$

where σ_0 is the standard deviation of the baseline. Combining Equation (3.1) and (3.2) it is obtained that:

$$\sigma^2 = g(q - q_0) + \sigma_0^2 \tag{3.3}$$

The angular coefficient resulting form a linear interpolation of σ^2 as a function of $q - q_0$ is the gain g[1], as shown in Figure 3.22. The typical gain $g \approx 10^6$ for a PMT supply voltage of 800V.

This gain calibration method guarantees an uncertainty less than 4%, resulting in a contribution to the energy resolution of the calorimeter less than 1%.

α sources

Each PMT has its own quantum efficiency (QE) determined by the differences of the photocathodic thickness during the production. The knowledge of the PMT QE is necessary for the reconstruction of the γ observables [71].

[1] In the formulas the PMT intrinsic resolution corresponding to the impulse of a single photoelectron has been neglected.

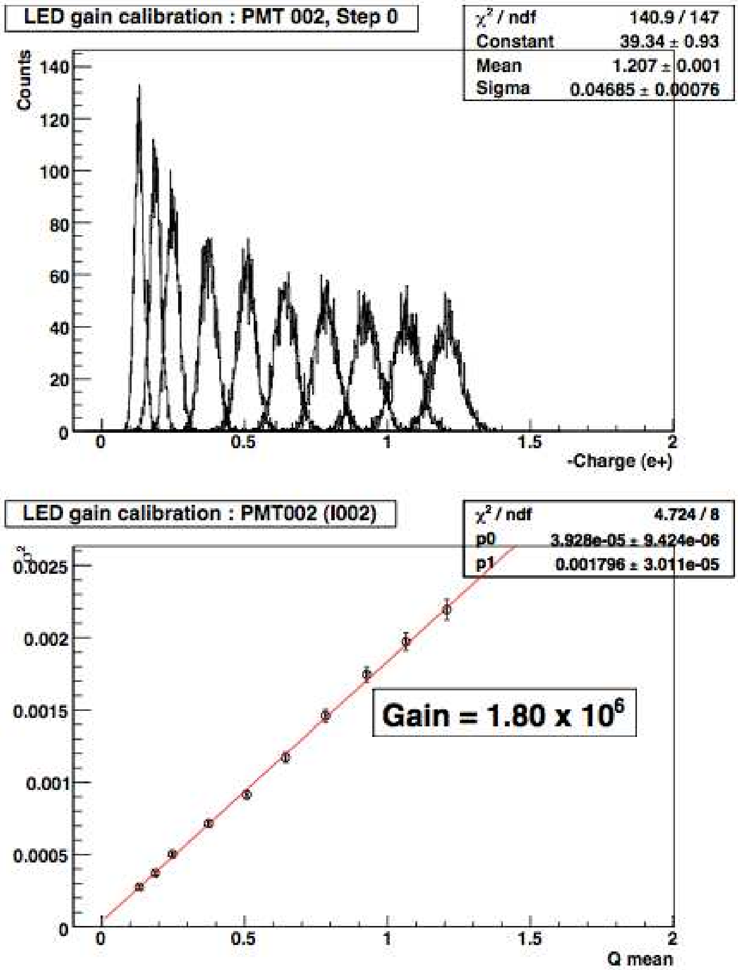

Figure 3.22: Gain measurement example.

The PMT QE are measured using α sources deposited on five 50 μm diameter wires immersed in the Liquid Xenon. The wires are placed parallel to the direction of the beam and anchored to the calorimeter walls. α particles are emitted in known position and their energy is deposited entirely within the Xenon in a region $\approx$ 40 μm around the source. Therefore the energy of the event and its location in space are easily simulated.

Each PMT collects the light emitted from more than a single source, the comparison of the number of photoelectrons for each PMT, obtained through Monte Carlo simulations and, the measured number recorded in an event of particle α provides an estimate of the quantum efficiency.

The variation in the number of photoelectrons as a function of distance between the PMTs and the α sources can also estimate the absorption of light inside the calorimeter, resulting in monitoring of impurities dissolved in the LXe.

A classic α emitter was chosen, ^{241}Am, which gives 5.44 MeV α well suited to experimental needs. The individual activities of each source is ≈ 200 Bq. The Americium is implanted on the surface of a gold leaf then wrapped and set for compression around the wires of 50 μm, see Figure 3.23.

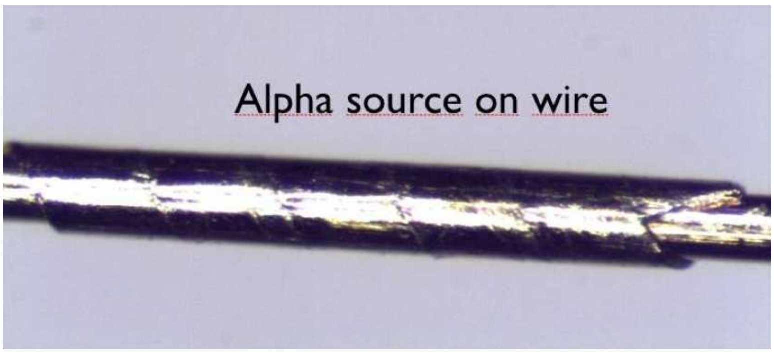

Figure 3.23: Americium source placed on a wire which diameter is 100 μm.

During detector filling, at the begin of the data taking period, and at the end, during the Xe recovery, calibration using α events in GXe are performed. During normal data taking the calibration with LXe is performed three times per week. In Figure 3.24 there is an example of a run taken when the detector was half filled. The presence of the LXe inside the detector is indicated by the rings associated with the α events from the lowermost two wires. The free mean path of the particles in the LXe is comparable with the wire thickness, thus it absorbs part of the emitted light. This shading effect create the ring shape.

Calibration using a dedicated CW accelerator

The use of a Cockroft-Walton (CW) proton accelerator is an optimal method to calibrate the calorimeter energy scale and the TC-LXe relative timing. This proton accelerator, through a dedicated beam line, induces nuclear reactions on a Lithium-tetraborate target, $Li_2B_4O_7$. The proton beam is tuned to excite Li reaction, used for E_γ energy scale, or the B one used for LXe-TC time cross-calibration.

The CW target during calibration is automatically inserted into COBRA in the position of the muon target, which is extracted. In Figure 3.25 the location of the CW in the MEG experiment and the beam line entering the COBRA magnet. A photography of the real proton beam line is also presented.

CW calibrations are performed three times per week.

Li resonance The lithium nuclear reaction, see Equation (3.4), is highly exothermic, and produces a single γ in the final state. The narrow resonance at $T_p = 440$ keV has $\sigma_R \approx 5$ mbarn and $\Gamma_R \approx 2.5$ keV .

$$p +^7_3 \mathrm{Li} \rightarrow {}^8_4\mathrm{Be}^* \rightarrow {}^8_4\mathrm{Be} + \gamma \tag{3.4}$$

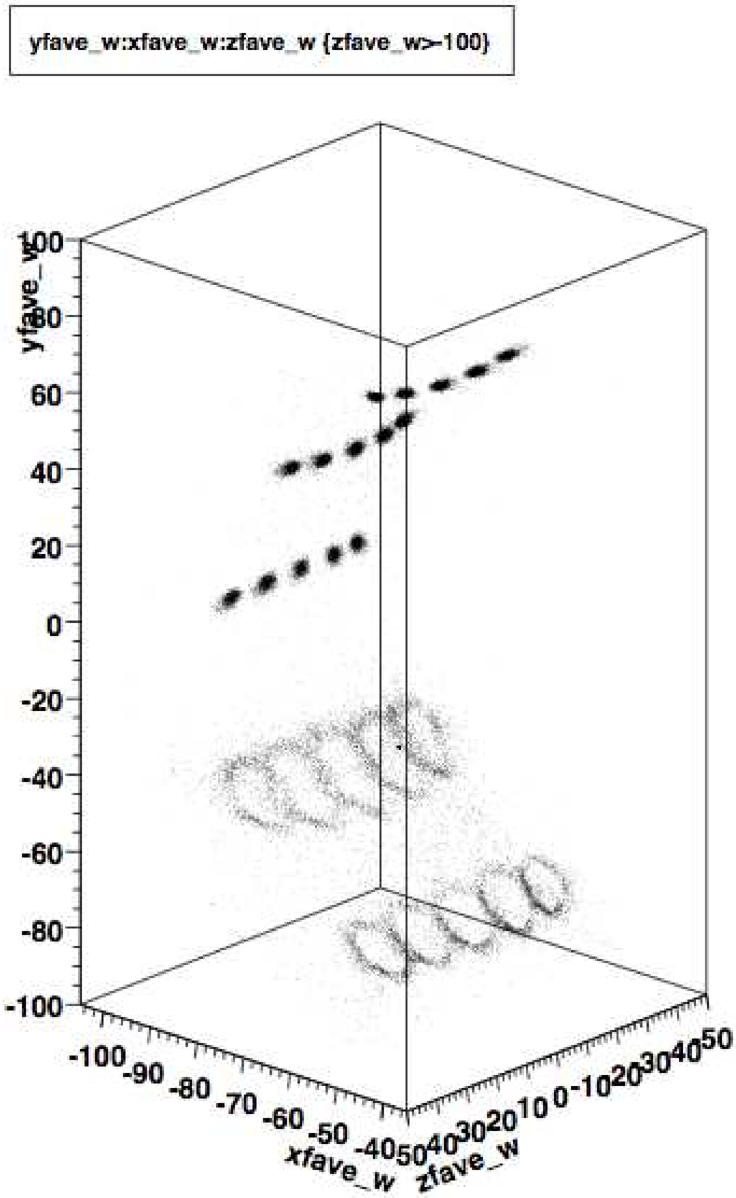

Figure 3.24: α events from the Am-sources on wire. The blobs and the rings are respectively associated with events in gas and in LXe.

The reaction reported in Equation (3.4) occurs through a resonance on ^{7}Li, which is the most abundant isotope, accounting for the 92.4% of the natural abundance. The γs have an energy of 17.6 MeV, roughly 1/3 of the signal energy, and thus they provide a reliable and fast calibration point.

An example of the result of one calibration is presented in Figure 3.26.

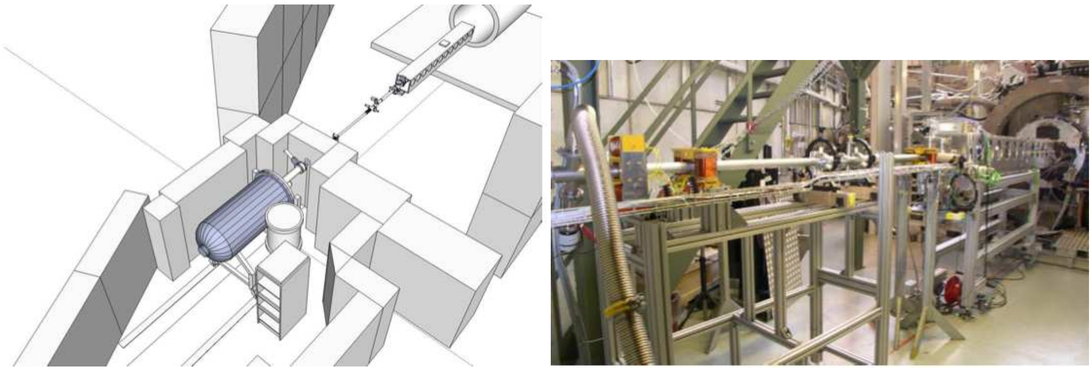

(a) (b)

Figure 3.25: (a) desing of the CW area and the beam line, the cylinder there is the COBRA magnet; (b) real picture of proton beam line.

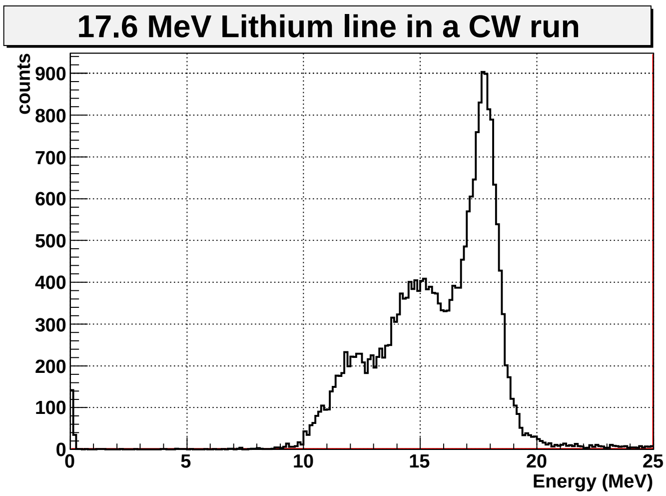

Figure 3.26: Results of a CW-Li calibration run; 1the 7.6 MeV γ line is clearly visible.

B resonance The CW proton accelerator energy can also be tuned at $T_p = 163$ keV resonant for the

$$p +^{11}_{5} B \rightarrow {}^{12}C^{*} \tag{3.5}$$

nuclear reaction ($\Gamma_R = 5.3$ keV). The $^{12}C^{*}$ goes back to the ground state through γ decay, a single γ_0 of 16.1 MeV is emitted when the transition occurs directly to the ^{12}C ground state. The transition to the ground state occurs more frequently by emitting 2 gammas γ_1 and γ_2 of energy 11.7 MeV and 4.4 MeV respectively. The γ_2 photon corresponds to a quadrupole transition of the first exited state of the ^{12}C ground level.

It is interesting to note that the 11.7 MeV and 4.44 MeV γs are emitted at the same time and this provides a unique opportunity for the relative timing of the LXe detector and the Timing Counter bars; in Figure 3.27 the scatter plot of energy deposit on LXe versus energy deposit on TC is shown. The ^{11}B(p, γ)^{12}C is the only proton-induced exothermic reaction, associated with the emission of two coincident γ-rays both at MeV energies.

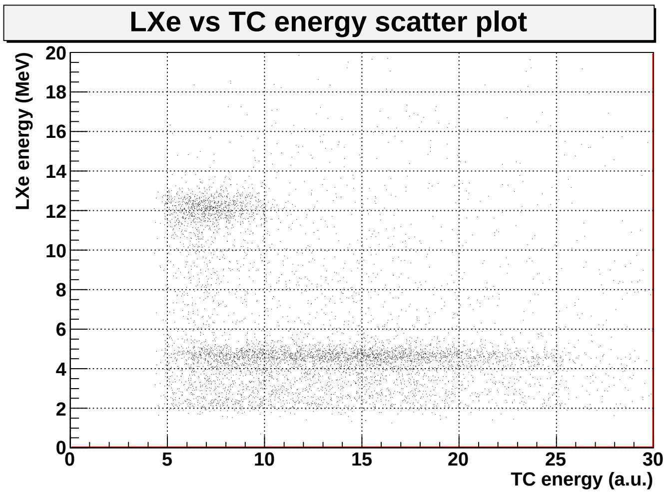

Figure 3.27: Correlation between the energy released inside the LXe detector and the Timing Counter; when the higher energy γ impacts the LXe detector the companion reaches the TC and vice versa.

Charge exchange calibration

The use of neutral pions is the only easy way to send photons with energies near 50 MeV in the calorimeter. The π^0 has spin 0 and decays in 98.8% of cases in two monochromatic photons both of energy 67.49 MeV, issued isotropically in the π^0 restframe.

Neutral pions can be produced by charge exchange reaction π^- on protons:

$$\pi^- + \mathrm{p} \;\rightarrow\; \pi^0 + \mathrm{n} \tag{3.6}$$

with the π^- at rest in the laboratory.

The beam line πE5 can be adjusted by varying the current and polarity of the magnets in order to send 70 MeV/c π^- on a liquid hydrogen target placed in the same position of the muon target. Such a type of calibration cannot be performed during the normal data taking but only in a dedicated time window inside the physics data taking.

The hydrogen target is a direct responsibility of the Pisa group. A new, *ad-hoc*, liquid hydrogen target (LHT) was therefore built to reach the COBRA center from the downstream region, while respecting the available space constraints. The LTH has a cylindric shape having radius = 2 cm and height = 7.5 cm, liquid helium is used as heat exchanger and flows in a 2 m long stainless steel pipe. The helium reaches a thick copper tube, wrapped around the LHT body, thus optimizing the cooling power. Figure 3.28 shows a sketch of the LHT target.

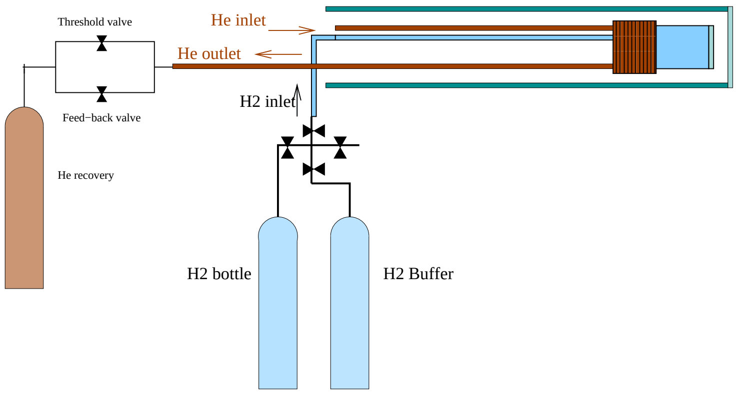

Figure 3.28: A scheme of the cryogenic gas/liquid handling system for liquid hydrogen target.

The outgoing pion acquires a kinetic energy of about 2.9 MeV for which the photons are no more monochromatic, their energy distribution is flat:

$$\frac{\mathrm{dN}}{\mathrm{dE}} = \frac{1}{2\beta\gamma(\mathrm{m}_{\pi^0}/2)} \tag{3.7}$$

where β is the speed of π^0 in the laboratory and γ the corresponding Lorentz parameter. The photons have flat energy distribution between:

$$\frac{\mathrm{m}_{\pi^0}}{2}\sqrt{\frac{1-\beta}{1+\beta}} \leq \mathrm{E}_\gamma \leq \frac{\mathrm{m}_{\pi^0}}{2}\sqrt{\frac{1+\beta}{1-\beta}} \tag{3.8}$$

Given the momentum of the π^0 in the laboratory system it is $54.9 \leq E_\gamma \leq 82.9$ MeV. The relationship between the photon energy and their angle θ is the following:

$$\mathrm{E}_\gamma = \frac{\mathrm{m}_{\pi^0}}{2}\gamma\left(1 \pm \sqrt{1 - \frac{2}{\gamma^2(1-\cos(\theta))}}\right) \tag{3.9}$$

with $\theta \geq 157°$, see Figure 3.29.

This relationship can be conveniently used to define the photon energy when the relative direction of the two photons is constrained. An auxiliary calorimeter, consisting in a 3×3 matrix of NaI crystals detects one photon while the other is measured by the LXe detector. It is placed on opposite side of the LXe detector to the target and it is mounted on a movable support to map the whole LXe detector inner face by means of a movable support, Figure 3.30. The NaI crystals are read out by avalanche effect photodiods (APD).

A fast pre-shower, made of a sandwich of scintillator and lead plates, is placed in front of the NaI detector, for a total thickness of $\approx$ 0.3 X_0, and it is read out by 4 PMTs. This detector is used to study the time resolution of the calorimeter at the signal energy scale.

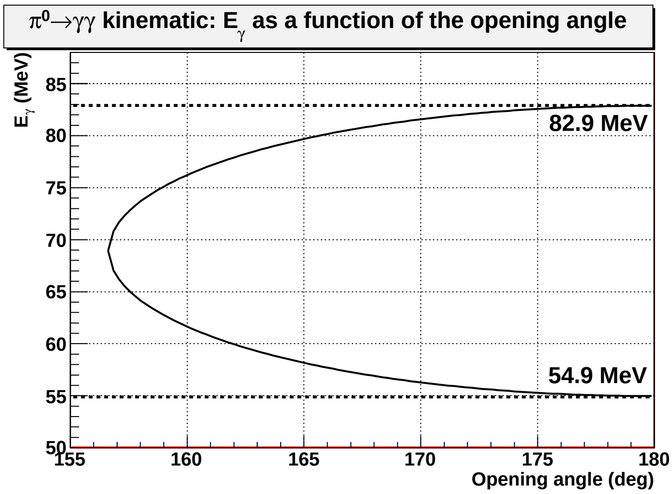

Figure 3.29: $\theta_{\gamma\gamma}$ vs E relationship.

An example of the LXe energy distribution obtained with the π^0 calibration is reported in Figure 5.13.

3.4 Electronics and DAQ

The MEG experiment looks for possible $\mu \to e\gamma$ signal in a very crowded environment, mainly in the unsegmented LXe detector. The pile-up rejection is one of the main feature to be accomplished by the DAQ system. The choice of the MEG collaboration is to equip all the channels with high frequency waveform digitizers, the DRS chip [75, 76].

The online event selection (trigger) operates in a single decision level exploiting the large computation power of field programmable gate arrays (FPGA). The kinematical variables used for trigger purposes are evaluated in a single pass with a latency of $\approx$ 500 ns which results shorter than the time depth of the DRS waveform digitizers ($\approx$ 600 ns).

The electronics is designed accordingly to VME standard, and it is arranged in 9 crates, each one is read out by dedicated online machine. The DAQ software is based on MIDAS [77] package (Maximum Integration Data Acquisition System), Figure 3.31 shows a sketch of the electronic and DAQ organization.

The trigger system has been projected, constructed and developed by the INFN Pisa group of the MEG experiment. The next part describes in detail the idea of the electronic trigger system, the custom electronic boards developed, the implementation in the MEG experiment [78, 79].

It is composed by 50 VME custom boards operating a synchronous height pulse ADC conversion at 100 MHz of the input signals and executing the selection algorithm into FPGA also running at 100 MHz. The boards are arranged in a multi layer system, the data transmission between different layers is operated by means of LVDS connections.

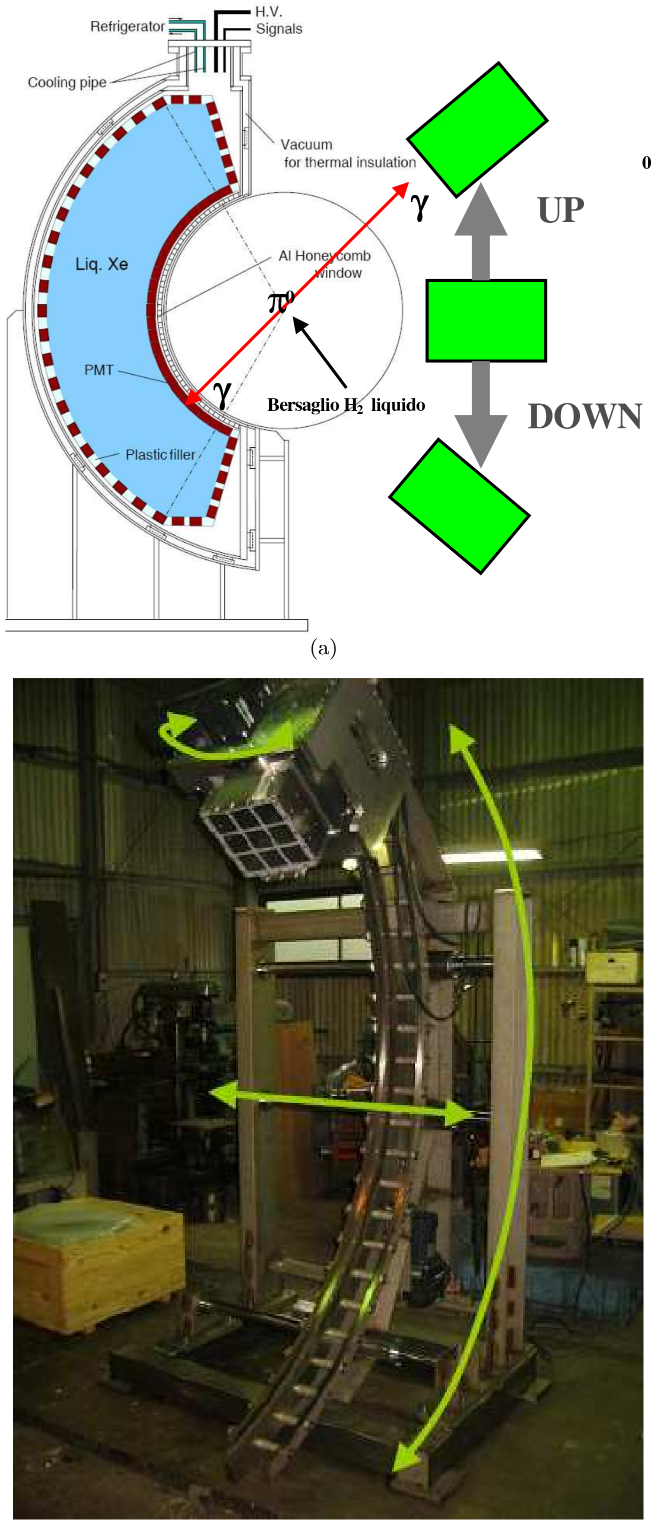

(a)

(b)

Figure 3.30: NaI mover, (a) possible configurations and (b) real picture.

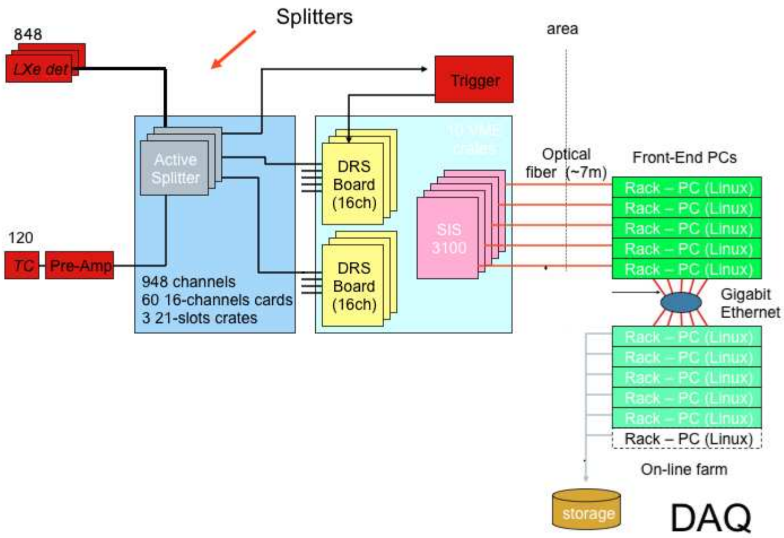

Figure 3.31: Scheme of the electronics and DAQ of the experiment.

3.4.1 The splitter system

LXe and TC signals are duplicated by the active splitter system. The scheme of the electronics is reported in Figure 3.31. A splitter board receives 16 single-ended signals form the detectors on coaxial cables and makes two differential copies of each input for the digitizer systems. The analogic differential output is linear on the 0÷3 V dynamic range (higher than the capability of MEG experiment digitizers) with a bandwidth up to 1 GHz in case of DRS outputs, and ≈ 100 MHz for trigger . The boards also provide an analog sum 4÷1 of the lateral faces LXe signals which are used by the trigger system. Figure 3.32 shows a picture of the splitter boards.

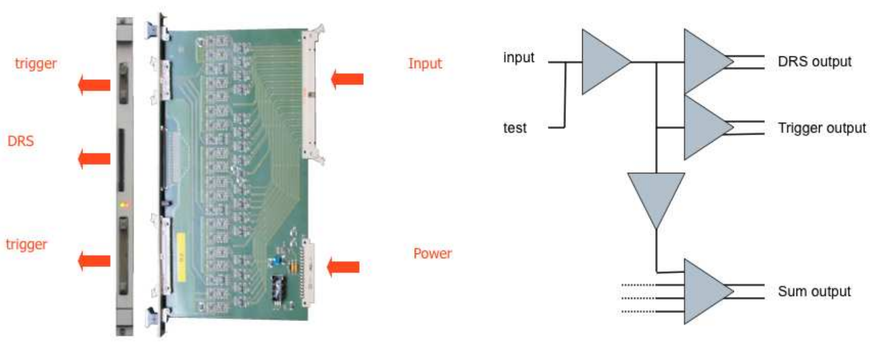

Figure 3.32: Picture of one splitter board and electric scheme of the signal splitting.

The input signal is received by a differential amplifier AD8009 [72] and then sent to two different amplifiers: THS4500 [73], bandwidth up to 1 GHz, for the DRS system, and AD8138 [74] for the trigger system. The 4÷1 output the inputs before reaching the AD8009 are analogically summed. Details in Figure 3.33.

3.4.2 The DRS chip

The use of commercial ADCs and TDCs would be inadequate and even too expensive for the MEG experiment, then a high frequency custom waveform digitizer had been developed in PSI.

The DRS chip is based on a ring of inverters on which a square domino signal propagates continuously. The domino signal enables the analog signal sampling on a parallel ring of capacitors, having deleted the sample stored in the previous turn of the domino signal, hence the name Domino Ring Sampler. A sketch of the operation principle of the DRS chip is shown in Figure 3.34. The propagation velocity of the domino signal is controllable in a wide range from 0.5 GHz to 4.5 GHz. A special tail-biting circuitry ensures that the width of the sampling signal is always four cells wide. Additional AND-gates allow to stop the domino signal in any cell by an external trigger signal. Since the storage depth is larger than a typical PMT signal width, the storage chain acts like an analog pipeline and makes delay cables unnecessary for trigger latencies up to $\approx$ 500 nsec. Since the speed of the domino wave depends on many factors like the temperature and the supply voltage, an external phase-locked loop (PLL) is used to lock the frequency and phase to a high precision quartz oscillator. By distributing this reference signal to all DRS2 chips, all domino waves in all chips run at the same phase and frequency with a relative timing jitter better than 200 ps.

The trigger signal stops the domino wave, freezing the contents of the sampling capacitors. The stored charges are shifted serially out of the chip and digitized externally by a 32 bit flash ADC at clock speed of 40 MHz. For high accuracy applications, a 20 MHz master clock signal and a voltage reference signal can be applied to channels 9 and 10, respectively, offering the possibility for an additional offline calibration. Using this technique, the required timing accuracy of 100 ps for the MEG experiment can be achieved.

The DAQ system of the MEG experiment will use exclusively the DRS chip on all 1000 PMT channels running at 1.6 GHz, $\approx$ 500 MHz bandwidth, and on all 3000 drift chamber channels (cathodes and anodes) at a speed of 500 MHz, delivering an excellent pile-up rejection. A timing calibration signal is distributed and sampled in all DRS chips, in order to meet the experiment requirement of 100 ps timing accuracy. The dynamic range is 0÷1 V with the chance of varying the input resistor to adjust it. The domino chain is digitized by 12-bit FADCs and stored into FPGAs and finally transferred to disk. In Figure 3.35 an example of the DRS waveform is shown.

The DRS2 version was used by the MEG collaboration in the physic RUN2008.

During the 2009 the new fourth Domino Sampling Chip was released, the DRS4. Several updates, sons of experience, were introduced to improve the ADC and time reconstruction.

The linear response of the digitizer was improved in the whole dynamic range, thus the offline calibration of the pulse height is no more needed. A clear-before-read cycle ensures that all sampling cells are free of residual charge from the previous revolution of the Domino Wave. The Bandwidth

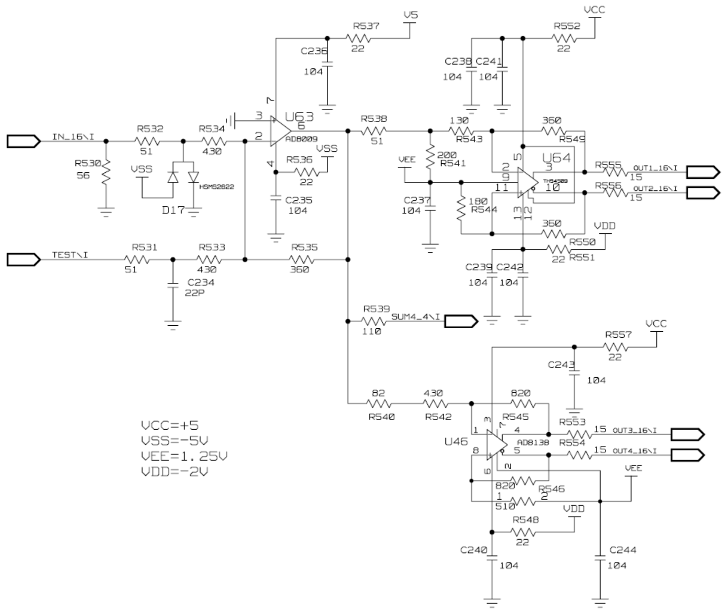

(a)

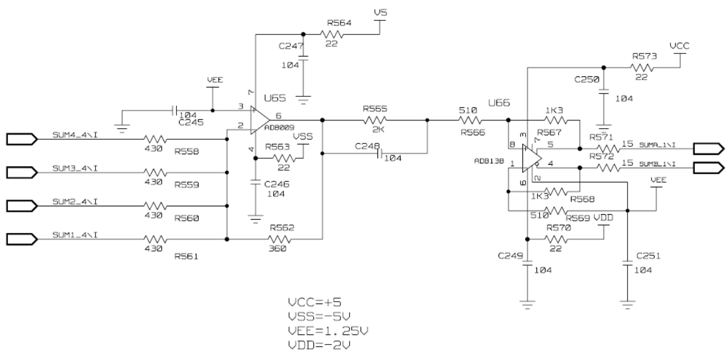

(b)

Figure 3.33: Electric design of the splitter 1÷1 amplification chain (a), and the 4÷1 (b).

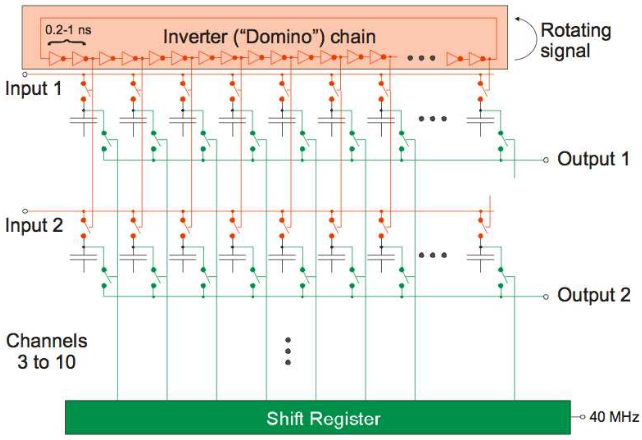

(a)

Figure 3.34: Simplified schematic of the DRS2 chip.

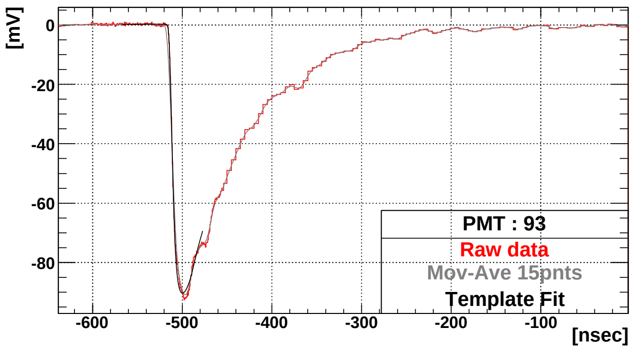

Figure 3.35: Example of a LXe waveform registered with the DRS chip.

is increased by a factor two with respect of the previous model, ≈ 1 GHz.

All the Domino Waves can be synchronized externally for all the chips of the DAQ system. The maximum residual jitter is measured to be less than 40 ps. Thus it is no more mandatory to register the 20 MHz reference clock of the experiment in one of the memories as in case of DRS2.

A flexible cascading scheme has been implemented, with which one can configure the DRS4 chip to have deeper sampling depths at the price of fewer channels. It can be configured as 8 channels with 1024 cells, 4 channels with 2048 cells, 2 channels with 4096 cells or one channel with 8192 cells. Furthermore, several DRS4 chips can be daisy-chained to form a channel with virtually unlimited sampling depth without compromising the bandwidth.

3.4.3 MIDAS DAQ

The DAQ system used by the MEG collaboration is based on the MIDAS package [77]. Besides all the necessary means of data readout, transport and storage, MIDAS contains a full slow control system, an integrated data analysis functionality and a Web interface for remote control.

The online cluster is composed by 10 machines, each one provided by 4 CPUs divided in master machine (MEGON) and 9 slave machines. The slave machines are connected to the corresponding VME crate, hosting the electronic digitizers and run the frontend code, namely *trg_fe* in case of trigger crates and *drs_fe* in case of DRS electronics.

At every event all data fragments, generated in the nine slave machines, are sent to MEGON, who merges them through the *eventbuilder* software. All the runs are finally copied to the offline data storage by the *lazylogger* task. All the operations are taken under control by the *logger* code, see Figure 3.36.

MIDAS also offers the chance of running the analysis code during the data acquisition, on a fraction of the acquired events, to check data quality. A set of helpful plots have been prepared by each experimental sub groups; in Figure see 3.36 an example of those monitor tools.

DAQ dead time

The bottle neck of the DAQ system speed, and the main source of the dead time, is the VME read out procedure. The VME transfer task runs in parallel on the nine slave machines and the event building task cannot be executed until all the fragments are collected by MEGON. The longest VME transfer time is the electronic crate with the biggest package to be read out.

The crates hosting the LXe and the DC DRS digitization boards are filled with 20 boards each. For these crates the amount of data to be transfered for each event is:

$$2\ \text{B} \times 1024 \times 32 \times 20 \approx 1.3\ \text{MB} \tag{3.10}$$

where 2B is the sample size in byte, 1024 is the number of bin per single channel, 32 is the number of channels per board and 20 is the number board per crate. The peak transfer speed of the VME double edge 32 protocol is quoted to be 80 MB/s. The effective read out speed is lower and depends on the protocol optimization in the Firmware of the custom boards. The contribution to the dead time is ≥ 16 ms, the limit for 80 MB transfer speed.

The read out dead time disable the trigger system by means of a BUSY signal. The width of the BUSY signal is 25 ms, corresponding to an effective transfer speed of 50 MB/s.

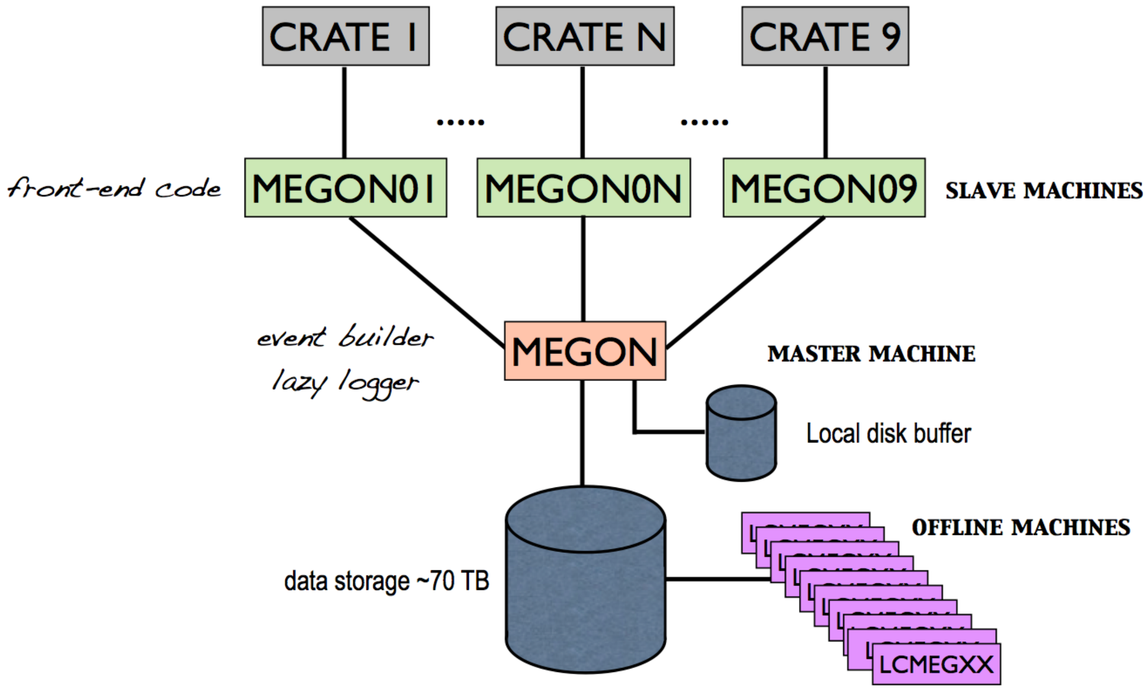

(a)

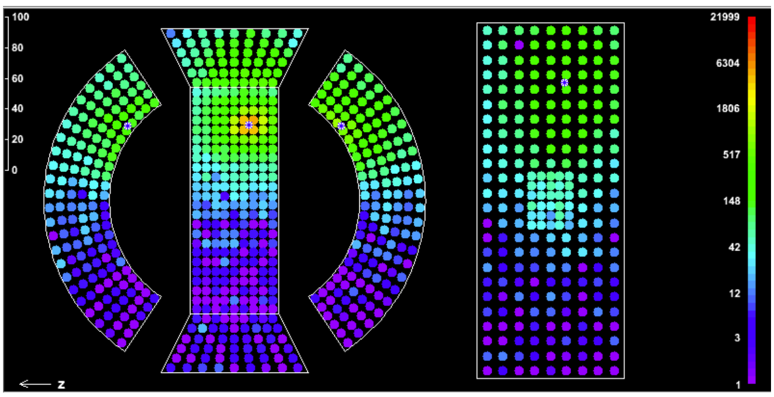

(b)

Figure 3.36: (a) Schematic view of the DAQ system of the MEG experiment, (b) example of LXe online monitor tool; each circle is one LXe PMT and the color is proportional to the measured charge.

Chapter 4

Reconstruction algorithms

This chapter describes the algorithms for the reconstruction of the physics observables.

The MEG experiment benefits of two independent digitizers, namely the DRS and the trigger systems, for the computation of the LXe and TC signals; the drift chamber system is digitized only by means of the DRS chip. The most performing digitizer of the experiment is the DRS, so all the official reconstruction is based on that information. The trigger waveforms are an important tool to cross check the goodness of the reconstruction algorithms, in particular for all the algorithms based only on charge information.

4.1 Gamma reconstruction

The LXe is a scintillator that combines a high light yield, of about 40000 ph/MeV comparable to the scintillators (like NaI), with a prompt scintillation light, few ns, as in case of organic scintillators. The choice of the MEG experiment is to take benefit only of the scintillation light for the reconstruction of the gamma characteristics; no attempt to use the ionization charge is performed. The ionization read out would lead to a longer integration time ($\approx$ μs) not feasible in such a crowded environment; the LXe detector gamma rate is of the order of $\approx$ 200 kHz.

The response of the LXe detector to a gamma of about 50 MeV is in the transient region from single process to electromagnetic shower development, being the critical energy of the Xenon 14 MeV. The typical shower is made of only few elementary interactions, from 2 to 3, and the fluctuations in the shower development are not negligible and have to be treated carefully in the reconstruction procedures.

4.1.1 Position

The gamma interaction point in the LXe sensitive region is reconstructed by using the PMT charge distribution. Given the center of the γ-induced electromagnetic shower, and supposing linear propagation of the scintillation photons, the amount of light collected by a PMT is given by the solid angle of the photocathode viewed by the interaction point. The solid angle of a photocathode with respect to an arbitrary point, $\Omega_i(x, y, z)$, is calculated numerically. The three dimensional position of the gamma interaction point is obtained by minimizing:

$$\chi^2_{pos} = \sum_i \frac{(n_{pho_i} - c \cdot \Omega_{i(x_\gamma, y_\gamma, z_\gamma)})^2}{\sigma^2_{pho_i}} \tag{4.1}$$

where n_{pho_i} are the scintillation photons detected by the PMT_i, c is a constant and one of the free parameters of the fitting and $\sigma_{pho_i} = \sqrt{n_{pho_i}}$. The minimization procedure returns a three-dimensional interaction point.

In order to take into account the shower fluctuations the minimization is iterated on different samples of PMTs chosen around the axis of the shower determined at the previous iteration.

4.1.2 Energy

50 MeV γs converting in the LXe detector deposit all of their energy in the active volume. The absence of any electric field guarantees that the electromagnetic shower induced electron cloud is re-absorbed by the LXe itself producing scintillation light, moreover the purity of the LXe guarantees that the emitted light can reach the detector PMTs. Therefore the energy initial gamma is converted into UV scintillation light and the number of collected scintillation photons by the PMTs is then proportional to the original gamma energy.

Based on this assumption, the E_γ estimator is given by the weighted sum of the charge as measured from each PMT waveforms:

$$E_\gamma = \sum_{i=0}^{NPMT} c_i Q_i \tag{4.2}$$

where c_i are the product of the PMT quantum efficiency (QE), the gain and a factor that takes into account the position of the PMT in the detector; the photocathodic coverage is not uniform inside the detector, it is higher in the inner face and lower in the outer. The coverage on the outer face is 2.6 times lower with respect to the inner one.

The existence of few dead channels leads to non-uniform response of the calorimeter all over the inner face area; this is correct by means of a set of parameters mapping the whole LXe sensitive area.

4.1.3 Time

The algorithm developed for the T_γ measurement exploits the 1.6 GHz sampling speed of the DRS chip. Trigger FADCs, running at 100 MHz, do not guarantee a time resolution adequate to the experimental needs.

Given the reconstructed interaction point, the gamma time measured by a the PMT is defined as:

$$\mathrm{T}_{\gamma_i} = \mathrm{T}_{\mathrm{PMT}_i} + \mathrm{T}_{\mathrm{propagate}_i} + \mathrm{T}_{\mathrm{offset}_i} \tag{4.3}$$

where $\mathrm{T}_{\mathrm{PMT}_i}$ is the time measured from each PMT by means of an offline constant fraction discriminator, $\mathrm{T}_{\mathrm{propagate}_i}$ is the propagation time of the γ from the target to the detector plus the propagation of the scintillation light from the conversion point to the PMT, and $\mathrm{T}_{\mathrm{offset}_i}$ is the peculiar offset of the electronic channel due essentially to differences in the cable lengths and the electron transit time of PMTs.

Given the set of T_{γ_i} the photon emission time $\mathrm{T}_{\mathrm{LXe}}$ is extracted with two different algorithms.

The first evaluates the time with a weighted mean of the single PMT time and the collected charge:

$$\mathrm{T}_{\mathrm{LXe}} = \frac{\sum_i \mathrm{Q}_i \cdot \mathrm{T}_{\gamma_i}}{\sum_i \mathrm{Q}_i} \tag{4.4}$$

Another possibility is to minimize the difference single PMT times to the gamma emission time. We define the χ^2 equal to:

$$\chi^2_{\mathrm{time}} = \sum_i \frac{(\mathrm{T}_{\gamma_i} - \mathrm{T}_{\mathrm{LXe}})^2}{\sigma^2_{\mathrm{T}_{\gamma_i}}(\mathrm{n_{pe}})} \tag{4.5}$$

where $\sigma^2_{\mathrm{T}_{\gamma_i}}(\mathrm{n_{pe}})$ is the time resolution of each PMT as a function of photoelectrons.

Both algorithms require an minimum energy PMT energy deposit of the order of 50 photoelectrons to take a part in the minimization.

The two algorithms give compatible results.

4.2 Positron reconstruction

The positron trajectory inside the COBRA volume is reconstructed by a system of 16 drift chambers. The positrons travel in helium atmosphere to minimize the multiple scattering. Only at the end of their trajectory they hit a scintillator hodoscope to measure the hit time. The positron momentum and the trajectory length is determined from the track parameters, while the positron emission time is evaluated from the hit time on the hodoscope.

This section describes the tracking algorithm adopted, starting from a description of the DC hit reconstruction, the time of flight measurement to the TC and the matching between a track and a hit on the TC are also discussed.

4.2.1 Positron track

The positron track reconstruction starts form the DC hits reconstruction them hits belonging to the same positron track are grouped in clusters and the track candidates are found. On all the track candidates the Kalman filter fit technique is applied and the track parameters are computed.

Hit reconstruction

Section 3.2.1 reports in details the geometry of a drift chamber module. The elementary cell of a drift chamber plane is made of an anode wire collecting the ionization generated by a crossing positron. The wire is read out by both sides, conventionally up-stream and down-stream. A thin aluminum layer is deposited on the kapton walls that define the cell geometry; the conductive aluminum layer is shaped so that it determines the hit position along the wire with a Vernier method.

Figure 4.1 shows an example of a DC cell and the signal connections is reported.

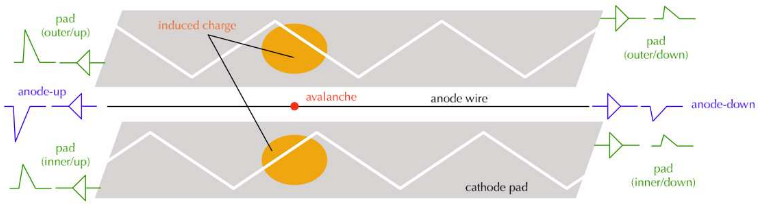

Figure 4.1: Read out scheme of an elementary cell of a DC module; the anode wire is read out from both sides, as in the case of the aluminum Vernier patterns.

r-coordinate The elementary DC cell of the DC has got a square cross section, 1 cm side. The composition of the electric field induced by the anode wire and the COBRA magnetic field defines the isochrones curves which are shown in Figure 4.2 (a).The minimum distance between the positron trajectory and the wire in the “isochrone geometry” establishes the occurrence of the wire signal.

The hit time is extracted by the rising edge of the anode wire signals; at this stage the isochrones are defined apart from a common offset, the trajectory time. It is define in the track finding stage.

z-coordinate A rough estimate of the hit z coordinate is given by the charge asymmetry measured at the ends of the anode wire. The resolution of this method is of $\approx$ 1.5 cm, too poor for the experimental needs, it is indeed used to define the pitch into the Vernier pattern, see Figure 3.14. The charge induced in the cathode pads depends on the avalanche point long the z direction reflected into the charge asymmetry between the two aluminum strip measurements.

The charge asymmetry, for example in the inner pad, is defined as:

$$\text{Charge asymmetry} = \frac{Q_{\text{innerdown}} - Q_{\text{innerup}}}{Q_{\text{innerdown}} + Q_{\text{innerup}}} \tag{4.6}$$

for the meaning of the variables refer to Figure 4.1

Given a value of the charge asymmetry there is still an ambiguity on defining the z coordinate. To solve this ambiguity the Vernier patterns on a cell walls are displaced by a quarter of period.

The scatter plot of the asymmetries of the two different aluminum foils charge asymmetries is a circle, see Figure 4.2 (a). The event phase in that circle is z coordinate.

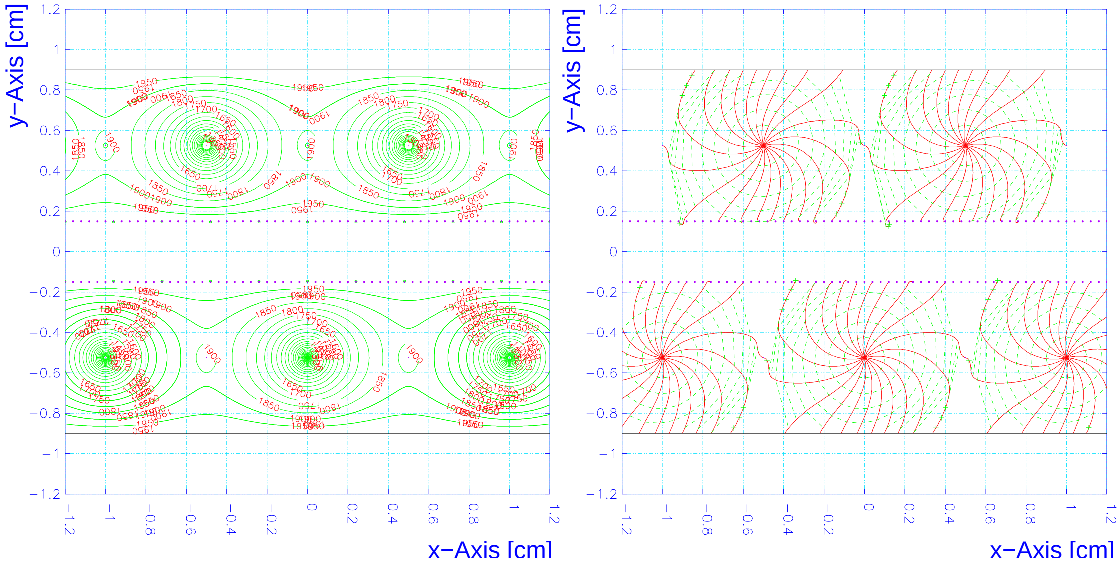

(a)

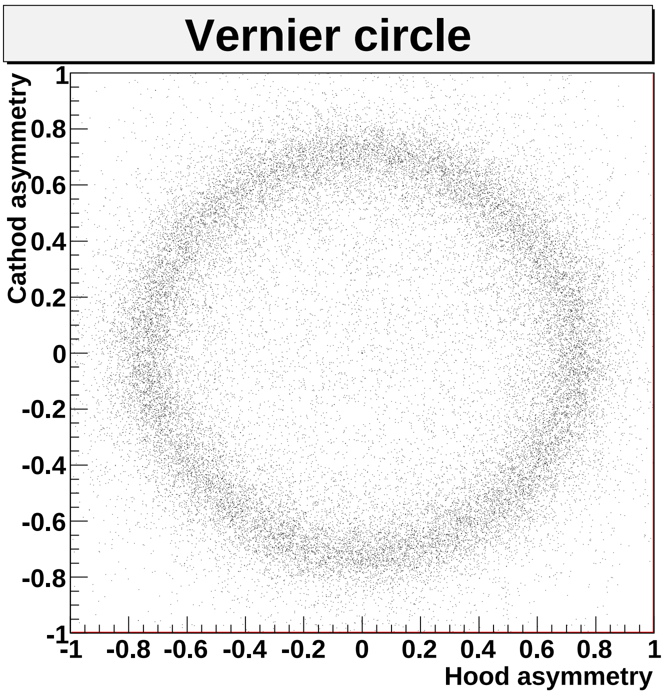

(b)

Figure 4.2: (a-left) Examples of DC isochrones, (b-right) ionization drift path; (b) example of Vernier circle obtained by charge asymmetry on the aluminum strips.

Track Finding

Using z coordinates and timing information the cluster associated with a single crossing positron are defined; in most of the case the left to right ambiguity is solved. Three clusters form a track seed. This can be fitted with a circle and used to connect near by clusters getting a track candidate. In this procedure the remaining left to right ambiguities are solved.

The track time T_0 is estimated for each track candidate. A first estimate is obtained by minimizing the distance of all the isochrones with respect to the track candidate direction and it is refined by adding the time of the TC hit related to the track. With the knowledge of the T_0 is possible to compute the drift time of the ionization in the crossed cells, and therefore the r coordinate $T_{cell} = T_{wire} - T_0$.

Finally with the drift times and the z coordinates is possible to compute precise (x,y) coordinates of the hits. This is obtained by means of the so-called TXY tables: these tables associate a drift time with (x,y) as a function of the magnetic field in the point and the track slant angle of the track, those curve are represented in Figure 4.2 (a).

Track fit

The track fitting benefits of the Kalman filter technique [64]. The Kalman filter was originally developed as a linear estimation for the state of a dynamic system from a series of incomplete and noisy measurements. It is also used extensively for track fitting in high-energy physics. It has the following features for an effective track fitting:

- multiple scattering and energy losses are included in natural way;
- a 3-dimensional trajectory that approximates closely the real one is computed;
- the computation load is less severe with respect to the standard least mean square fit that requires a $N \times N$ matrix inversion;
- control of error propagation is provided.

These features are suitable for the tracking of the MEG positron spectrometer.

The positron track in the magnetic field is defined by 5 parameters, 2 for the decay vertex coordinate, 2 for the direction of the emission and 1 for the momentum. The trajectory is reconstructed recursively by adding measurements, the adding procedure foresees a prediction of the new point based on the known measurements, the adding of this measurement with the appropriate weight and the smoothing of the track taking into account of the new point.

Figure 4.3 shows an example of a reconstructed track.

4.2.2 Positron time

Time of flight The TC PMT outputs are passively split to the DRS and trigger digitizers and to dedicated double-threshold discriminator cards. When a signal exceeds both thresholds a NIM

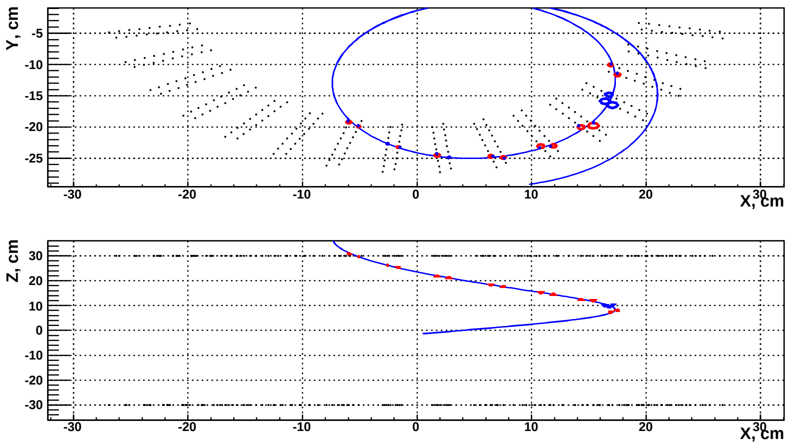

Figure 4.3: Example of a reconstructed DC track.

pulse is fired, whose timing is defined by the lower threshold, set as low as possible to minimize the time walk effect. The NIM pulse is digitized by the DRS electronic.

The positron hit time is the average of the time measured by the two PMTs belonging to the same bar, after correcting for the residual time-walk effect. The z coordinate is reconstructed by the PMT time difference.

In case of high momentum Michel positrons ≥ 50 MeV the number of crossed TC bars is usually more than one. The hit are clustered by means on their time and z coordinate; the hit time is given by the time of the first hit bar.

Muon decay time The positron emission time T_e is the positron hit time corrected for the track length. The positron traveling from the last DC to the timing counter might suffer from large angle scattering on the drift chamber support structure or electronics. To suppress this event class the Kalman track is extrapolated to the TC detector surface and a matching along z and rφ coordinates is required. Figure 4.4 shows an example of an extrapolation of the Kalman track through the COBRA volume to the TC.

The positron time is then:

$$T_e = T_{TC} - T_{track} \tag{4.7}$$

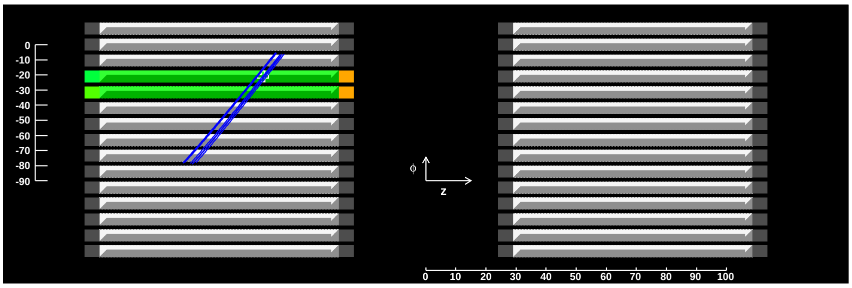

(a)

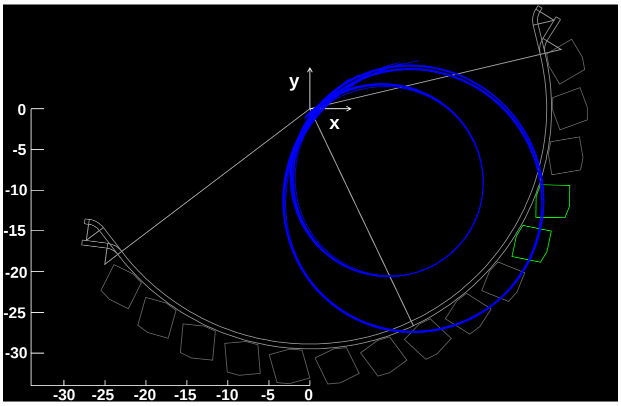

(b)

Figure 4.4: Example of track projection on the TC, (a) z-φ view and (b) x-y.

Part III

The trigger system

Chapter 5

Trigger selection algorithms

In this chapter the principles of the online selection are discussed. The physical observables available in real time processing are presented together with their application online selection algorithms. A special emphasis is given to the $\mu \to e\gamma$ trigger and to discriminate between α and γ events.

Finally the scheme of the data taking, based on masked and pre-scaled triggers, is described.

5.1 Observables

To accomplish a fast and efficient event selection, the trigger logic discriminates on variables being on one side a clear signature of the event and on the other fast to be reconstructed.

The $\mu \to e\gamma$ signature for muon decay at rest in the laboratory is fully determined by two-body kinematics already introduced in section 2.3. The DAQ system is based on GHz digitizers,the DRS chip presented in section 3.4.2. Data from signal sampling are directly sent to the data logger on disk, without further selections. So the trigger latency has to be shorter than the memory depth ($\approx$ 500 ns) of the digitizers. This requirement on the global trigger latency forces the system to use fast response detectors read out by PMTs, namely the LXe detector and the TC, and prevents us from using informations from the DC detector. However this choice does not compromise the background rejection capability of the trigger.

So the online algorithm discriminates on γ energy (E_γ), e^+ and γ time difference ($\Delta T_{e\gamma}$) and opening angle ($\theta_{e\gamma}$).

5.1.1 Gamma observables

All the gamma variables, namely the energy, time and direction of emission, are computed by means of the LXe PMTs signals, see section 3.3. The trigger system dedicates 400 channels to the digitization of LXe PMTs signals, for the details of channel assignment see section 6.1.

The algorithms used for reconstructing all the γ observables will be described in the following paragraphs.

Gamma energy The LXe detector is a good calorimeter therefore the weighted sum of the charges collected on all PMTs is a good estimator of the energy released in the active volume. The trigger system digitizes the PMT signal amplitudes at 100 MHz and operates a coherent sum of of all the 400 LXe signal amplitudes named A_{tot}. The quantity A_{tot} is assumed to be the estimator of E_γ. An online charge evaluation would imply a further delay of the algorithm, at least equal to the signal time width, and this is not compatible with the latency requirements. The sum is computed every 10 ns, and an example is shown in Figure 5.1. More precisely

$$A_{tot} = \sum_{i=0}^{NCHA} f_i A_i \tag{5.1}$$

where NCHA is the number of channels of the trigger system, f_i are the calibration factors of each channel and A_i are the signal samples.

A real time pedestal subtraction algorithm, described in section 7.2.1, is applied singularly on all the inputs.

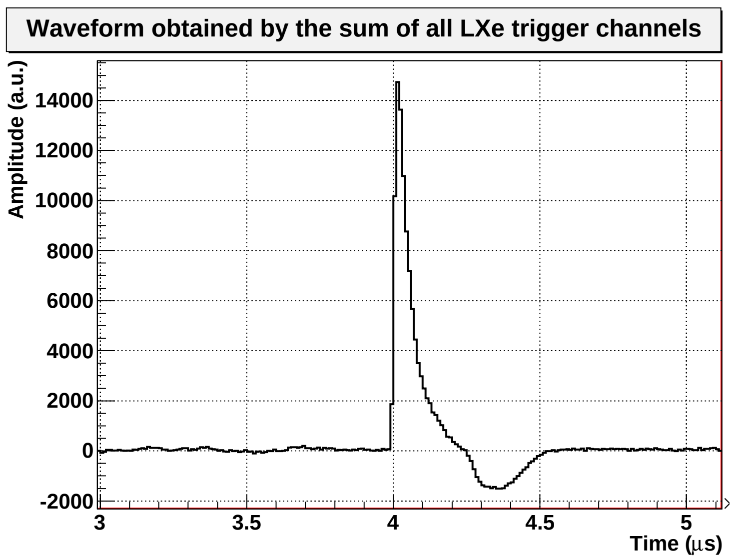

Figure 5.1: Online A_{tot} obtained by means of the coherent sum of 400 channels.

The baseline subtraction algorithm subtracts from the current signal sample the mean value of four consecutive samples acquired 20 clock (CLK) ticks (200 ns) before. That mean is computed by using the sample recognized as baseline accordingly to the condition:

$$| A_i - \langle A \rangle | \leq THR \tag{5.2}$$

where $\langle A \rangle$ is the current value of the baseline and THR is a dedicated threshold. This condition prevents physics signals to enter into the baseline chain and bias the subtraction; the typical value of this threshold is 5 ADC unit. Figure 5.1 demonstrates that this algorithm is able to set the baseline of the A_{tot} waveform at 0. The effect of the pedestal subtraction threshold is also visible just after the end of the waveform. In fact small pulses, pulse height of the order of the pedestal THR, can pass the condition reported in Equation 5.2 and produce a anomalous undershoot in the right tail of the waveform. The 200 ns length of the pipeline prevents this effect to spoil the quality of the E_γ estimator, being the maximum τ of the LXe de-excitation time of the order of 40 ns.

To compensate for different gains, QEs and positions of the LXe PMT, see for reference section 3.3, each channel is multiplied by a dedicated calibration factor f_i. The correct evaluation of these factors makes the online E_γ estimator more uniform with respect to the impinging point of the γ on the detector. The calibration factors are stored into the online database of the experiment and can be modified easily when needed; at the begin of each run of the data taking a set of programmable Look Up Tables (LUT) are automatically filled in with the database values. The FADC samples are automatically corrected for the data stored in the LUTs. This online calibration procedure costs 1 CLK tick, thus 10 ns, on the global latency.

The coherent sum of the baseline subtracted and equalized samples is carried out by 10 layers of parallel digital adders in 10 CLK ticks.

The resulting waveform is finally compared with the energy threshold and, if it is the case, the trigger is fired.

The trigger commercial digitizer saturates a well defined amplitude value, that can be set at 1 V or 2 V, the details of he hardware used are discussed in chapter 6; the saturation affects critically the energy estimator. To compensate for this loss of information, in case of saturation the threshold is automatically lowered by 800 counts ($\approx$ 3 MeV). An example of a typical muon radiative spectrum is shown in Figure 5.2.

Finally, to reject cosmic events a veto threshold is set well above the end point of the LXe gamma-ray spectrum.

Two different thresholds for two different trigger types are available in order to check the goodness of online energy selection with acquired data, see section 5.2 and 11.1.

Gamma time The sampling frequency defines the basic timing of the trigger system. We need to recall here that the trigger system operates synchronously and that the phase jitter between the same sample of different analog channels is less than 0.5 ns. The time is computed when a waveforms exceeds for two consecutive samples a dedicated time threshold, a first T_γ measurement is provided by the index of the last signal sample below threshold. Figure 5.3 shows graphically how the algorithm works. Every signal sample is compared with the time threshold, which is taken as low as possible to minimize the time walk effect. At this point the time estimator has the same 10 ns granularity of the sampling clock.

To obtain a better time resolution the waveform leading edges are interpolated by means of

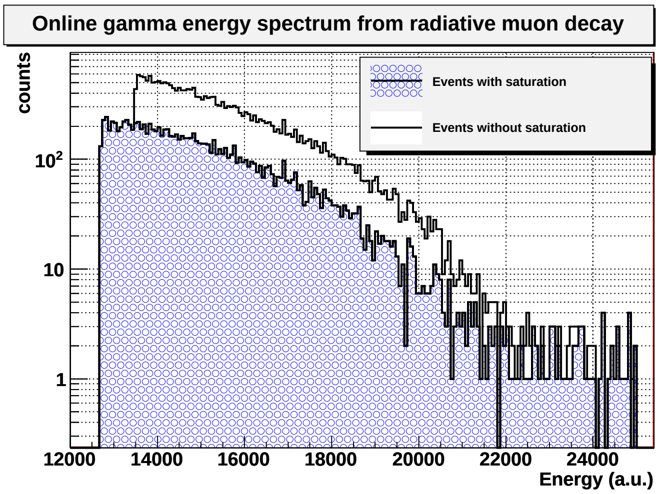

Figure 5.2: Stack histogram of the online γ spectrum in the calorimeter; the E_γ threshold is set at 13400 a.u. for events without any channel saturated and 800 a.u. ($\approx$ 3 MeV) lower in case of saturation; the effect of the cosmic veto threshold (25000 a.u.) is also visible.

a linear function. Once a waveform is over threshold for two consecutive samples the time is computed. The pulse height of the first sample over threshold is subtracted by the threshold value (ΔS1T) and, at the same time, the second sample over threshold is subtracted by the first (ΔS1S2). Depending on the values of these differences a correction is summed to the time with a granularity of 1/4 CLK ticks. The time walk correction factors table is reported in Table 5.1.

Condition	**Time correction**
$\Delta S1S2 \geq 4 \cdot \Delta S1T$	7.5 ns
$\Delta S1S2 \geq 2 \cdot \Delta S1T$	5 ns
$\Delta S1S2 \geq 4/3 \cdot \Delta S1T$	2.5 ns

Table 5.1: Time correction factors as a function of the comparison of the sampled pulse height and the time threshold.

In this scheme the time is measured in 1/4 of clock ticks and a resolution of the order of $3.3/\sqrt{2}$ ns has been measured, the results are reported in section 11.2.

Gamma emission direction The signal photons are emitted from the target with a distribution given by the density profile of muon stops on the target itself.

The γ mean free path into the LXe detector is $\approx$ 3 cm, thus a huge amount of scintillation light is collected by PMTs on the inner face proportionally to the solid angle subtended by the PMT from the first interaction point of photon. A estimator of the interaction point in the calorimeter is therefore the position of the PMT collecting the largest amount of light. Assuming that the

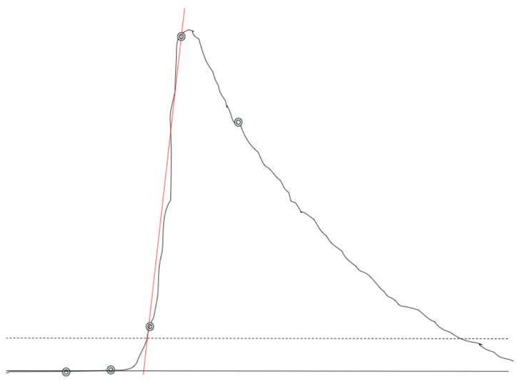

(a)

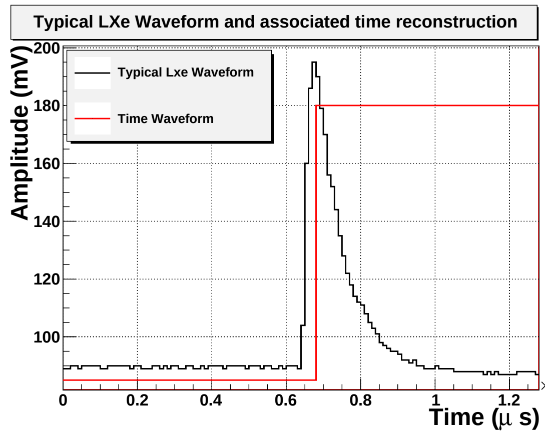

(b)

Figure 5.3: (a) Visual example of online time algorithm, the curved line is an example of waveform, the big dots are the samples, the dashed line is the time threshold and the red line is the tentative online fit; (b) superimposition of typical LXe waveform (black) to the online time waveform (red) which shows the latched time and the relative latency, Y scale refers to the black curve.

photon are emitted at the target centre, this is equivalent to measure the photon flight direction. The difference between online and offline gamma impinging position for z and φ coordinates are shown in Figure 5.4.

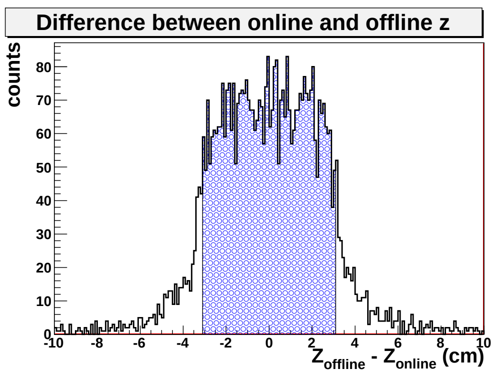

(a)

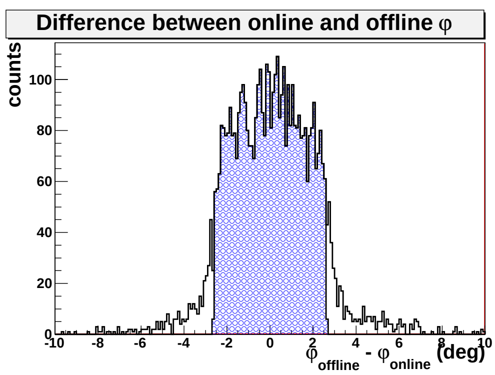

(b)

Figure 5.4: Difference between online and offline z (a) and φ (b) reconstruction; in blue the real dimension of a PMT is reported.

5.1.2 Positron observables

The positron spectrometer is composed by a tracking system of 16 Drift Chambers (DC) and two sections of scintillator bars called Timing Counter (TC), see chapter 3.2.

The long electrons drift time into the chamber volume prevents the trigger system from using DC signals for trigger. The required trigger latency would overcome the time depth of the analog sampling of the DRS chips. The only information about e^+ is coming from the PMT signals of the timing counter.

Hit reconstruction Given a positron hit at z distance far from the PMT in a scintillator bar, the amount of light seen by the PMT is approximately:

$$L_{seen}(x) \approx \alpha E e^{-z/\lambda} \tag{5.3}$$

where E is the energy deposit of the particle in the bar, z is the distance from the hit and λ is the absorption length of the scintillation material ($\lambda \approx 70$ cm) and α the energy to light conversion factor.

The TC bars have got two PMTs at each end of the scintillator, thus the PMT distances from the hit are respectively z and l-z, where l is the bar length $l = 80$ cm, and $\lambda \approx 70$ cm. In Figure 5.5 the relative collected light by each PMT as a function of the distance is reported together with total collected light.

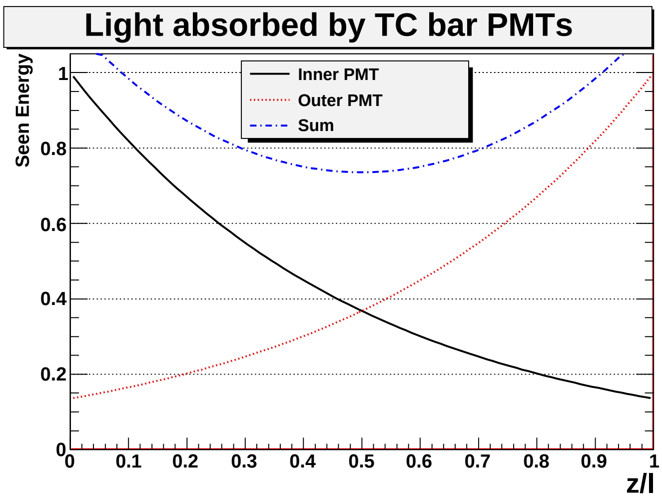

Figure 5.5: Distribution of waveform height pulse as a function of the relative distance from the hit for inner PMTs (black and full line), outer PMTs (red and dotted line) and the sum of the two waveforms (blue and dashed dotted line).

A TC bar is hit when a positron releases in the scintillator a minimum amount of energy, so that both PMT signals must exceed a dedicated single PMT threshold THR_L, while the sum of the two exceeds a higher one, THR_H.This double discrimination ensures an event selection mildly dependent on the positron crossing along the z coordinate, as requested by the experimental needs.

Summarizing a TC hit has:

$$L_{seen}(z) > THR_L \ \& \ L_{seen}(l - z) > THR_L \ \& \ (L_{seen}(z) + L_{seen}(l - z)) > THR_H \tag{5.4}$$

In order to use a common threshold for of the TC bars we equalized the response using cosmic ray events. These events are uniformly distributed along the bars and the energy spectrum is approximately the same for all of them. The Landau peak is used to equalize the energy response of all the bars; the calibration factors are handled as in the case of LXe channels, see paragraph 5.1.1. A set of calibration LUT are loaded at the begin with the TC channel calibration factors to correct the sample pulse heights.

A detailed description of the channel calibration factors is reported in section 8.1.2.

Hit multiplicity Each timing counter section is composed by 15 scintillator bars. The mean value of the number of consecutive bars hit by a e^+ emerging from the target, with a momentum ≥ 40 MeV/c, is ≈ 1.6. The distribution of the number of hit bars is shown in Figure 5.6.

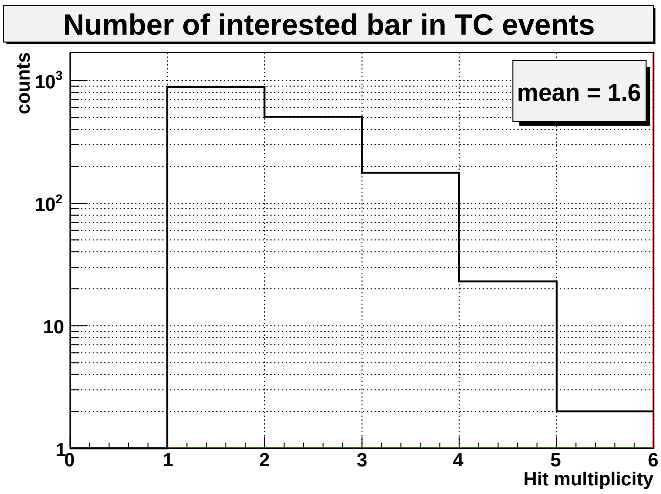

Figure 5.6: Distribution of the number of consecutive hit bar by a positron in the TC.

The positron emission time and direction are estimated from the first hit-bar signals. The online selection exploits a LUT to extract the index of the first hit bar from a hit cluster together with the cluster multiplicity. The LUT logic is reported graphically in Figure 5.7.

The online selection reserves a threshold discriminate on TC multiplicity. Usually the multiplicity threshold is set at 1, different values are used in special calibration runs.

Positron time The positron hit time on a TC bar is estimated by exactly the same algorithm described in the case of the LXe detector (Paragraph 5.1.1). The algorithm acts on the signal sum of the two PMT signals. In case of a hit multiplicity greater than one, the time is computed from the first hit bar signals.

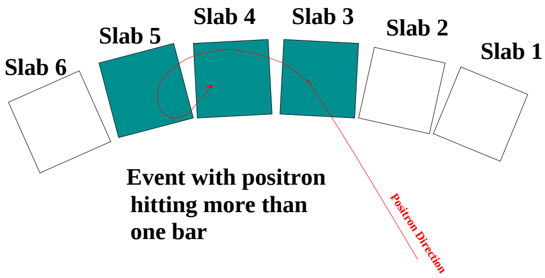

(a)

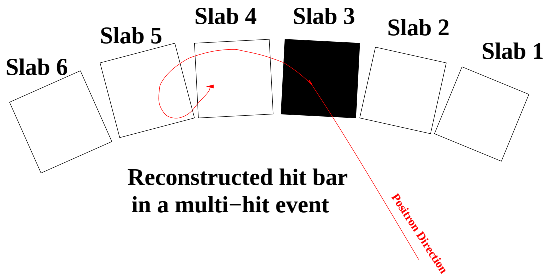

(b)

Figure 5.7: Bar hit in a event (a) and the bar reconstructed by the algorithm (b).

Positron emission direction The positron trajectories in a non-uniform solenoidal magnetic field are not trivial, and the trajectory parameters evaluation requires the information generated by the tracking system. A precise measurement of the positron emission direction is get by the offline tracking algorithm. Furthermore the tracker information is not available at trigger level. However the positron emission direction on TC is so well correlated to the positron emission direction that it can be used as a rough positron direction measurement. The positron impact point is given by the TC bar position along the φ coordinate and by the z coordinate along the bar axis. The positron are assumed to emerge from the target center as in the case of the gamma emission direction.

The z coordinate can be determined in two ways:

1. using the stereo coincidence with the index of the fiber crossed by the positron;
2. using the charge asymmetry of the PMT signals of the hit bar.

The trigger system works in both configurations.

The TC fiber system are read out by both the DRS and the trigger system. The 512 TC fiber signals, before being received into the trigger boards, are analogically summed by a $8 \div 1$ fan-in.

To use the fibers we set up an analogous algorithm to find positron hits on fibers as in the case of the bars. The sum of 4 consecutive fiber trigger channels corresponds to an online z index slice.

On the other hand the z computation obtained by the PMT charge asymmetry utilizes a set of dedicated LUTs.

Given the L_{seen}, the light collected by a PMT as a function of the distance (Equation (5.3)), the z coordinate estimator of the hit is:

$$\log\left(\frac{L_{seen}(z)}{L_{seen}(1-z)}\right) = \log\left(\frac{\alpha E e^{-z/\lambda}}{\alpha E e^{-(1-z)/\lambda}}\right) = (1-2z)/\lambda \tag{5.5}$$

which results linear in z.

Algorithms running online can hardly compute logarithm of a ratio of charges. Approximations are therefore needed to deal with the latency constraints. The goal is to determine the z coordinate with only three clock cycles.

When the sampled PMT signal exceeds the threshold THR_L a simple peak finding algorithm, based on three consecutive samples, latches the maximum of signal amplitude. To reduce sampling fluctuations on the short TC PMT signals the next sample is added to the maximum. This procedure in executed in parallel for all TC PMTs. These are 13 bit signed integer and are named $AMPL_L$ and $AMPL_R$. The words $AMPL_L$ and $AMPL_R$ are truncated selecting the first 6 bits over threshold.

The bi-dimensional function defined in Equation (5.5) is tabulated in a 16 kbit RAM used in LUT mode. The z coordinate is coded in a 4 bits output word, corresponding to a bin width along z of 10 cm, while the two truncated amplitudes are used as two 6 bits LUT inputs.

The LUT has been configured with cosmic ray data obtained through a simulation of the trigger algorithm, the results are shown in Figure 5.8. A brief description of the trigger simulation code is given in section 8.2.

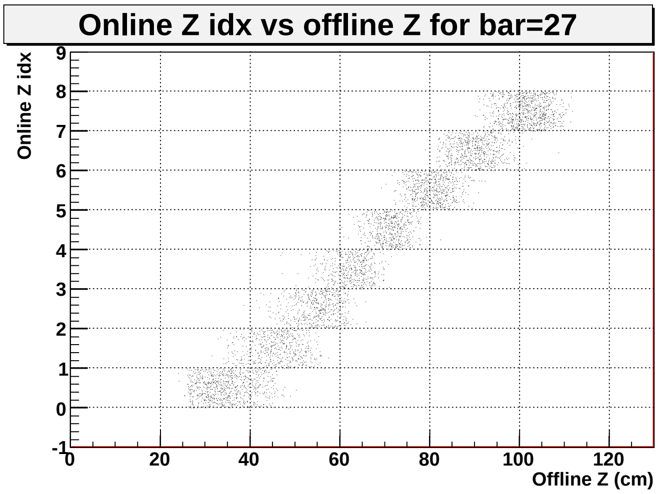

Figure 5.8: Scatter plot of the online z index versus the official measure based on offline analysis of the DRS waveforms.

5.1.3 Combined observables

$\Delta T_{e\gamma}$ The $\Delta T_{e\gamma}$ is simply the difference of the gamma and positron time estimators. Being the predominant experiment background the accidental coincidence of a positron and a photon, the distribution of the time difference is flat. The trigger system picks out all the events contained within a selectable time window.

The time difference has to be centered around the $\mu \to e\gamma$ signal, so the detector and electronics offsets need to be calibrated. The selection algorithm provides two different time windows for $\mu \to e\gamma$ and calibration triggers.

Direction match The direction matching condition is the looser online selection condition of the $\mu \to e\gamma$ trigger. It is based on a comparison of the emission direction estimators of the positron and the gamma which are discussed in the previous section.

Monte Carlo studies on signal events show that the gamma hit points on LXe front face, measured with $[z,\varphi]$ coordinates, are correlated with a region in the TC surface hit by the companion positrons. Figure 5.9 (a) shows the Monte Carlo correlation between the gamma z coordinate in the LXe and the positron in the TC, Figure 5.9 the same for φ. The multiple scattering of positrons, occurring in the material between the tracker and the timing counters, spreads out the direction correlation to the level of Figure 5.9.

A table based on Monte Carlo simulation defines per each LXe PMT index a region on the TC surface collecting the 95% positron hits. This table is applied by means of a dedicated LUT.

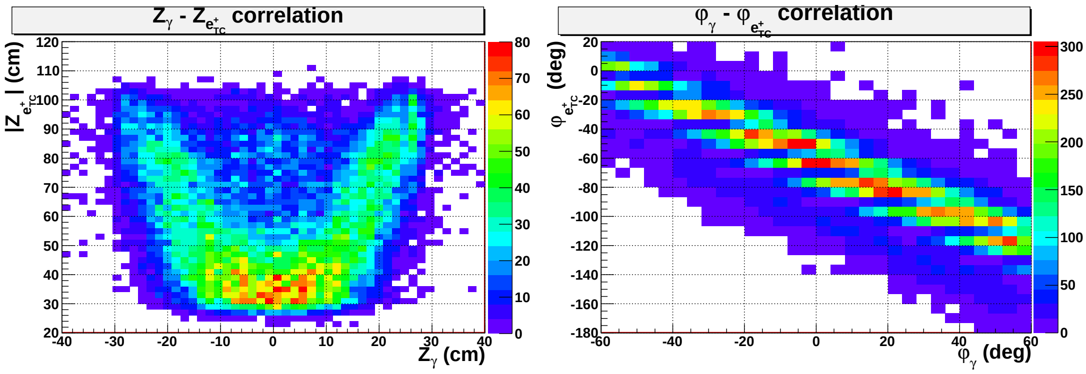

(a) (b)

Figure 5.9: The upper part (a) shows the correlation between z_γ and z_{e^+}, the lower part (b) shows the correlation between φ_γ and φ_{e^+} for simulated signal events; the online selection profits from the clear correlation through the direction match condition.

The method used to define the direction match table is discussed in details in section 8.1.4.

The MEG trigger selects events requiring the direction match correlation here discussed. A looser correlation table is also prepared; it connects a gamma emitted in the positive z space with a positron flying in the negative and vice versa. It is used for efficiency studies.

5.1.4 Pulse shape discrimination: α trigger

The evaluation of the PMT quantum efficiencies measured is one of the key features to achieve the best resolutions on the γ observables. This is obtained by means of 25 ^{241}Am α source (100 Bq of activity each one) deposited on thin wires suspended inside the detector, section 3.3.3 describes this method in details. The α sources are also used to check the attenuation length of the liquid Xenon mean and to measure its purity. It is then crucial to develop an online selection algorithm dedicated to α events acquisition.

Typical α energy deposit in the LXe sensitive region is of the order of 5 MeV. In this energy region, with a muon stopping rate in the target of the order of 3×10^7 μ/s, there is a gamma induced background of $\approx$ 5×10^4 events/s in the [3, 5] MeV region. The global α activity is 2.5$\times$ 10^3 Bq, a factor 20 lower than the beam induced background rate. It is evident that a selection based on the LXe energy deposit is not suitable.

The α mean free path in the liquid Xenon is of the order of 40 μm, the energy deposit is then localized close the source positions. The sources are deposit onto 5 thin wires anchored to the lateral walls of the LXe calorimeter. The sources longitudinal dimension is 1 mm, and their position is known with a precision of 1 mm in all directions. It comes out that a relevant part of the scintillation light is absorbed by the PMTs placed around the wire anchorage points. A chance for selecting α events is to discriminate on the energy deposit, not on the whole detector, but in that small set of PMTs just around the wires. Unfortunately the scintillation light absorbed by the lateral PMTs is not related only to the energy deposit by the γ in the sensitive region. The collected amount of light from α events depends on the distance between the source and the PMTs. For these reasons a simple pulse discrimination on signal pulse height is not adequate.

The valuable way to distinguish α from γ events with the μ-beam switched on is to take advantage of the different scintillation mechanism of the LXe in case of high density ionization particles, like α, and minimum ionizing particles, as in case of γ induced showers.

Here we recall the LXe scintillation mechanism. It involves excited Xe atoms (Xe*) and Xe$^+$ ions produced by charged particles and can be described as follows:

$$\mathrm{Xe}^*\mathrm{+Xe} \rightarrow \mathrm{Xe}_2^* \rightarrow \mathrm{2Xe+}\ h\nu$$

or

$$\mathrm{Xe}^+\mathrm{+Xe} \rightarrow \mathrm{Xe}_2^+,$$

$$\mathrm{Xe}_2^+\mathrm{+e} \rightarrow \mathrm{Xe} + \mathrm{Xe}^{**},$$

$$\mathrm{Xe}^{**} \rightarrow \mathrm{Xe}^* + \mathrm{heat},$$

$$\mathrm{Xe}^* + \mathrm{Xe} \rightarrow \mathrm{Xe}_2^* \rightarrow \mathrm{2Xe+}h\nu$$

where $h\nu$ is an ultraviolet photon emitted by the de-excitement of Xe_2 excimer.

The two different mechanisms have different de-excitement time constant. Highly ionizing particles have a higher probability to excite the Xenon forming Xe* rather than ionize it. On the other hand the electronic part of the γ induced electromagnetic shower, having $\beta \approx 1$, have higher probability on ionizing the Xe rather than excite it. The time constants the two scintillation processes differ for approximately a factor 2, so the waveforms are expected to be rather different and in particular the signal trailing edge is expected to decay down with the scintillation decay constant.

This was investigated inside a prototype of the LXe detector. Figure 5.10 shows a comparison of an α induced waveform (a) with a γ one (b). The time constant for α, τ_α, has been measured to be 19 ns while the on for γ, τ_γ, results 50 ns. These measurements were performed by using 100 MHz FADCs similar to the one used by the MEG trigger system.

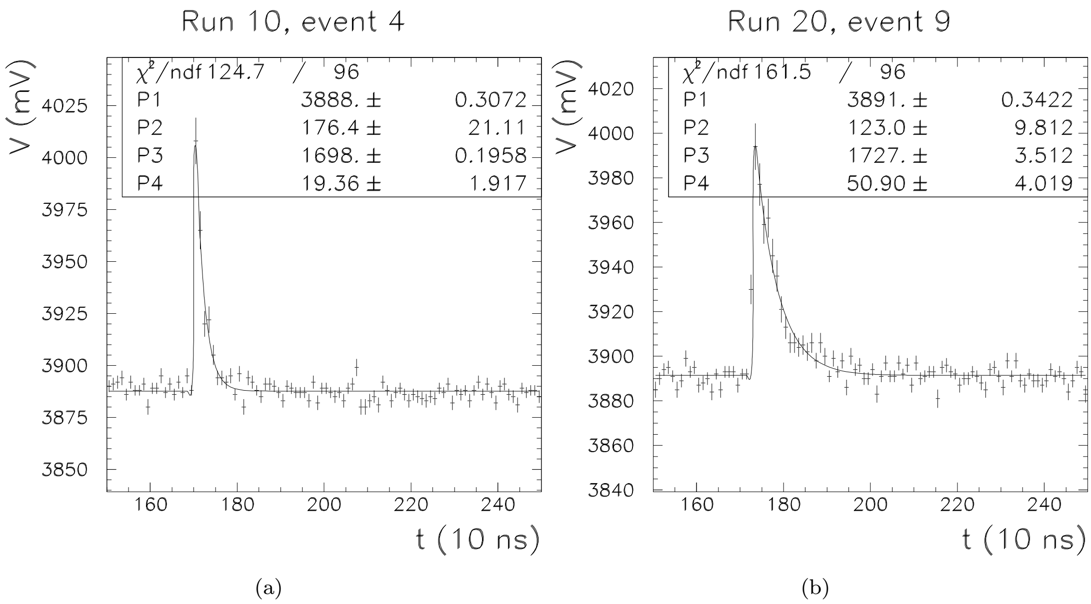

Figure 5.10: LXe waveforms in case of (a) alpha and (b) gamma events.

It is then possible to develop an online algorithm to select α based on the different pulse shapes. At the online stage it is almost impossible to perform a fit and determine the signal τ, it would be time consuming, however with an approximation of $\approx 15\%$ the ratio of the pulse peak amplitude to its charge is proportional to that. We studied the performance of this algorithm with the detector prototype data.

Figure 5.11 (a) shows the distribution of the variable Q/A in a run with mainly α events in the LXe (Run10) and a run with both event types (Run20) acquired with a minimum bias trigger on the energy release. Figure 5.11 (b) is the scatter plot of the waveform charge versus amplitude for all the events of Run20. The two different particles can be distinguished by means of the Q/A ratio.

The mean values for α and γ are:

$$
\begin{aligned}
\langle \mathrm{Q/A} \rangle_\alpha &= 2.82 \quad \sigma_\alpha = 0.40 \\
\langle \mathrm{Q/A} \rangle_\gamma &= 5.43 \quad \sigma_\gamma = 0.54
\end{aligned}
$$

We obtained, applying a cut at $\mathrm{Q/A} \leq 4$, α particle selection efficiency of $\varepsilon_\alpha \geq 96\%$ with a background contamination at 7% level.

This α/γ discrimination had been implemented inside the MEG trigger system. The best compromise between resolution and latency is obtained by integrating the signal charge on 8 consecutive around the peak. Once the charge is computed, the Q/A ratio is performed by a dedicated LUT. The charge integration procedure needs 7 CLK cycles to record 6 samples after

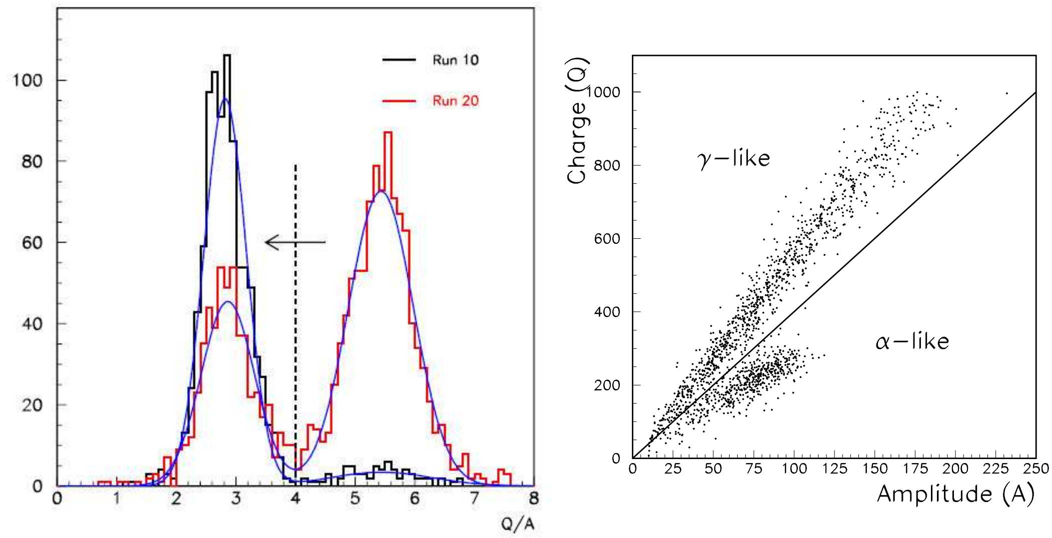

(a) (b)

Figure 5.11: (a) distribution of the variable Q/A in a run with only α (Run10) and in a run with α and γ, (b) scatter plot of waveform charge versus amplitude in Run20.

the waveform peak and then 3 CLK for the charge evaluation. These 10 CLK ticks cannot be added to the LXe energy deposit estimator latency because it would become to much compared to DAQ needs. The best compromise is to take exploit the aforementioned groups of LXe PMT placed around the α sources and apply the selection on this. In this way we gain 3 CLK ticks maintaining the α selection latency at acceptable level, Table 7.1.

A detailed description of the implemented algorithm, together with the firmware implementation, the LUT calibration and the results are presented in chapter 9.

5.1.5 Charge exchange calibration trigger

One of the calibration procedures of the LXe detector employs of the charge exchange reaction, described in Equation (5.6), induced by a negative pion beam onto a liquid hydrogen target.

$$\pi^- + \mathrm{p} \longrightarrow \pi^0 + \mathrm{n} \longrightarrow \gamma\gamma + \mathrm{n} \tag{5.6}$$

The motivations of this calibration is described in section 3.3.3.

The online selection of π^0 decays requires the detection of two γ , one in the LXe and the other in the NaI detector, in a wide time coincidence window with a loose back to back condition.

The NaI calorimeter consists in a 3×3 matrix of NaI crystals, and it is placed on opposite sides of the LXe calorimeter to the target. The online NaI E_γ reconstruction is given by the sum of the 9 crystals signals and the timing is given by its rising edge.

The NaI calorimeter surface is roughly 20 times smaller then LXe one; thus only a section of the LXe detector, placed in the opposite direction to the NaI position, is illuminated by the γ companion of the one seen by the NaI. To increase the purity of the online selected π^0 decays the LXe inner face has been subdivided in several areas, called patches, fulfilling the entire inner face (up to a maximum of 64 different configurations); the online collinearity require that the PMT with the higher pulse height belong to the the patch mirroring NaI position. In Figure 5.12 a subset of possible patches is reported.

The NaI calorimeter can be placed in several position by means of a dedicated mover in order to map the entire LXe inner face.

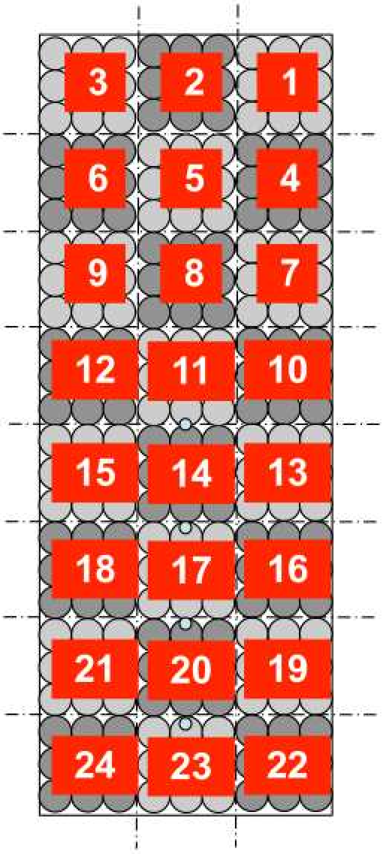

(a)

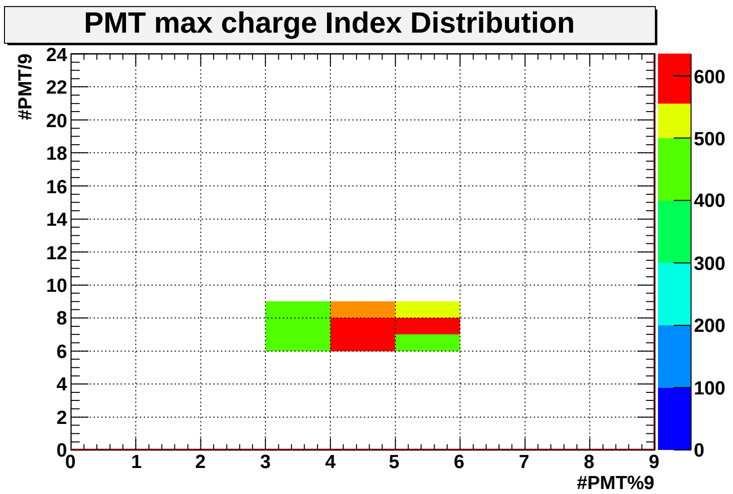

(b)

Figure 5.12: (a) example inner face patches for π^0 trigger online collimation, (b) example of PMT with the higher height pulse when patch#8 was selected; as a reference see Figure 6.7.

The collimation capability of the trigger can be used in all LXe oriented triggers. During LXe position resolution studies two lead collimators have been placed in front of the inner face in the small space between the calorimeter and the COBRA magnet and two dedicated patches were programmed in that positions.

The NaI can be equipped with a small and thin pre-shower counter, read out by fast PMT. This pre-shower can be used as reference to inter-calibrate the LXe detector timing offset of PMT. Two different trigger types are suited for CEX calibration; the first, apart for what presented above, requires also the γ to convert into that pre-shower placed just in front of the NaI calorimeter, the second one does not; the first trigger is used for LXe timing studies, the second for energy resolution. In Figure 5.13 the LXe and NaI energy distributions for π^0 triggered events, without any offline cut, are reported, the 55 and 83 MeV lines are clearly visible.

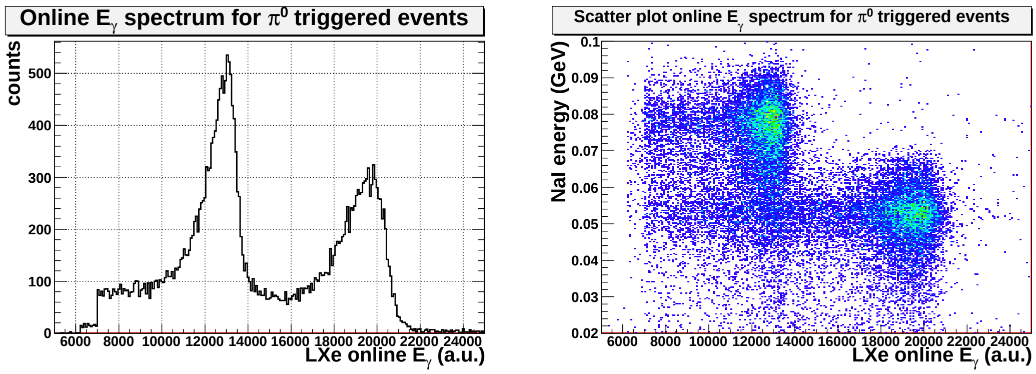

(a) (b)

Figure 5.13: E_γ distribution for π^0 triggered events without any offline cut: (a) online E_γ distribution, (b) scatter plot of energy deposit in LXe and NaI.

5.2 Trigger types and run configuration

The trigger system is designed to provide up to 32 different types of selection algorithms to cover all possible experimental requests, including calibration and monitor of the detectors. Each trigger type can be individually enabled and pre-scaled.

In Table 5.2 trigger types used during physics data taking are reported.

MEG trigger The MEG trigger selects candidate signal events in physics run. It requires an energy release in the LXe over threshold, a hit in the TC in temporal coincidence with the calorimeter and a direction matching accordingly to the algorithm in Paragraph 5.1.3. To check the MEG trigger efficiency, three control triggers are defined by relaxing the trigger requirements on calorimeter energy, time coincidence window and the direction matching LUT.

Radiative decay trigger The radiative decay trigger is identical to the MEG trigger requiring an energy release in the LXe over threshold, a hit in the TC in time coincidence with the gamma one but the direction matching condition is not required. The calorimeter energy threshold is lower than the one used in MEG trigger. The radiative decay time peak is used in analysis to have an

Name	E_γ THR	$\lvert\Delta T_{e\gamma}\rvert$	Direction Match	Id number
MEG	High	narrow	narrow	0
MEG Low E_γ	Low	narrow	narrow	1
MEG Wide DM	High	narrow	wide	2
MEG Wide T	High	wide	narrow	3
Radiative Decay	High	narrow	NO	4

Name	Selection criteria	Id number
LXe alone	Threshold on E_γ	9/10
DC alone	DC hit multiplicity	18
TC alone	TC multiplicity	22
π^0 decay	Threshold on E_γ and coincidence with aux. NaI	6
α	pulse shape discrimination	12
LED	Discrimination of LED driver pulse	14
pedestal	random trigger	31

Table 5.2: List of most the selection algorithms used during physics data taking.

hint of the experimental time resolution and to define the global offset between the LXe and the TC.

This trigger is used in dedicated radiative decay runs and for the CW calibration runs exploiting the boron induced reactions. The boron data are used to evaluate the time offset of each TC bar using the LXe detector as a reference.

Detector calibration The LXe detector energy scale is monitored 3 times per week by checking the position of the 17.6 MeV γ line. The trigger dedicated for this calibration is based only on the LXe energy discrimination. This is also used to study the γ radiative spectrum. This has been used to evaluate the photon detection efficiency of the LXe detector and to model the accidental background E_γ PDF, for details see chapter 12 and 13.

Samples of Michel positrons collected with the specific DC or TC triggers are used to study the DC-TC matching efficiency, and the resolutions in the positron observables measurement. The DC alone trigger requires a positron hits on four out of five consecutive DC chambers, no pattern recognition is performed. The TC alone trigger is based on the TC hit reconstruction with its multiplicity, usually equal to one. Moreover the TC alone trigger was used in computing the experimental normalization, see chapter 12

The system can generate up to 32 different trigger types ordered in a stack. The trigger for MEG signal events is assigned the highest priority, followed by MEG events with looser selection cuts. Trigger types used for single detector calibration and stability monitor are at the bottom of the stack. MEG events can be mixed with any other trigger types with proper pre-scaling settings in order to compute signal efficiency and monitor detector stability during normal data acquisition. It is therefore desirable to program the fraction of each trigger type on a run-by-run basis. This can be tuned by means of pre-scaling factors defined at the beginning of each run. The DAQ trigger list in a normal run contains, besides the main MEG trigger:

- MEG events with released condition on E_γ, $\Delta T_{e\gamma}$ and direction match for efficiency studies;
- single detector events for both detector monitoring and beam normalization;
- pedestal event for electronic noise inspection.

Figure 5.14 shows the number of events collected in a typical physics run and in a π^0 calibration run.

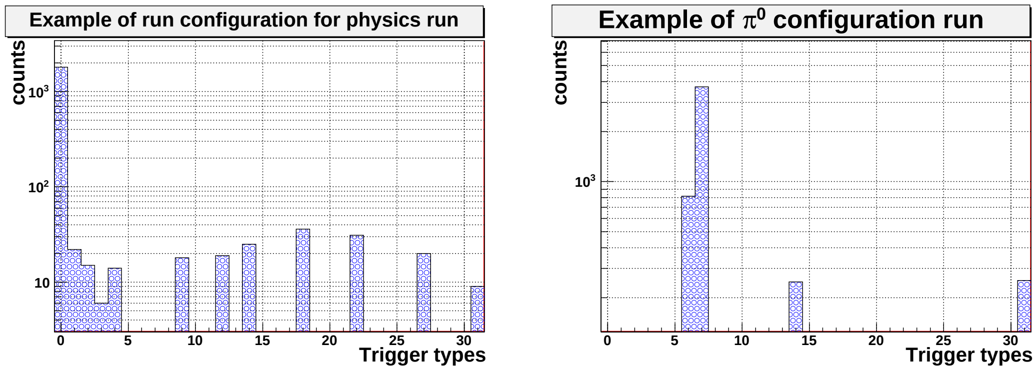

(a) (b)

Figure 5.14: Number of events acquired for different trigger types in a typical physics run (a) or in a π^0 calibration run (b).

5.3 MEG trigger rate and live time

Section 2.3 shows that the dominant background source of the experiment are the accidental coincidence. The MEG trigger rate depends on the online resolutions through the expression in Equation (2.1), the crucial variables are the online E_γ and spatial collinearity. This chapter shows that a refined E_γ is applied in the online selection while a looser cut has to be performed in the online collinearity selection. By Monte Carlo studies we evaluate that a full efficient gamma energy threshold is 45 MeV, the online time resolution is expected to be at the order of 3 ÷ 4 ns. It is then possible to evaluate the expected MEG trigger rate for a muon stop rate of $3{\cdot}10^7$ μ/s.

The requirement of an energy deposit larger than 45 MeV in LXe corresponds to an event rate $R_\gamma = 2$ kHz. On the other hand the overall rate in the timing counter due to Michel positrons is estimated to be $R_{TC} = 2$ MHz. So, if we select events with a full efficient positron-photon coincidence time window of $\Delta T_{e\gamma} = 10$ ns and a spatial alignment, the uncorrelated background trigger rate is estimated in:

$$R_{MEGtrigger} = R_\gamma \cdot \frac{R_{TC}}{f_\theta f_\varphi} \cdot 2\Delta T_{e\gamma} \approx 8 \text{ Hz} \tag{5.7}$$

with a foreseen efficiency $\varepsilon_{TRG} \geq 95\%$. In Table 5.3 all the factors that lead to this expected 8 Hz trigger rate starting form a muon stopping rate is reported.

R_μ	10^7
Geometrical acceptance	10^{-1}
Gamma energy	10^{-3}
Time coincidence	10^{-1}
Spatial coincidence	10^{-1}
Final rate	10 Hz

Table 5.3: Rough estimation of the impact of the online selection algorithms in the final MEG rate.

The dead time t_{dead} of the MEG DAQ system is the time needed to transfer the data corresponding to a triggered event from the electronic boards to the offline disks, see section 3.4.3. During the read out phase the trigger system is not running and the event selection is switched off. The DAQ live time fraction is the ratio between the trigger running time and the total time of the run.

The live time fraction can be computed under the hypothesis that the events occur with a known average rate and independently of the time since the last one. The live time fraction is the probability of having one candidate event during the read out time:

$$\mathrm{LT} \;=\; \mathrm{e}^{-\mathrm{R_{MEGtrigger}} \cdot \mathrm{t_{dead}}} \approx 81\% \tag{5.8}$$

for a t_{dead} equal to 25 ms.

The trigger efficiency and the DAQ live time enter directly in the experiment sensitivity definition, see section 11.5. An efficient choice of the trigger selection conditions it is not only based on the trigger efficiency parameter, however the product of the trigger efficiency and the DAQ live time has to be maximized. This may lead to tighter trigger conditions loosing efficiency or vice versa, increasing the trigger efficiency loosing DAQ live time. This is explained in details in section 11.5.

Double buffer scheme The DAQ dead time is limited by the amount data to transfer from the electronic crates to the online machines and cannot be easily modified. The only chance of improve the experimental live time can be improved a double buffer read out scheme. This is the simplest multi buffer read out scheme, but it is enough for the experimental needs.

The double buffer scheme exploits two parallel memories to simultaneously transfer a triggered event and register a new one. The system is in dead time only if there is the occurrence of two different triggers in a t_{dead} interval:

$$\mathrm{LT} \;=\; \mathrm{e}^{-\mathrm{R_{MEGtrigger}} \cdot \mathrm{t_{dead}}} \cdot \left(1 + \mathrm{R_{MEGtrigger}} \cdot \mathrm{t_{dead}}\right) \;\approx\; 97\% \tag{5.9}$$

This will be implemented for the 2010 run. This scheme will solve the experimental live time issue, it will be also possible to relax the trigger condition to improve the online selection efficiency if needed.

Chapter 6

Electronics

6.1 The trigger tree

The trigger system of the MEG experiment is constituted by three custom electronics circuits in which the online selection algorithms, described in the previous chapter, are executed. Since there are not circuits on the market that meet the experiment needs, they were designed and produce by the collaboration. The trigger system is a direct responsibility of the Pisa group.

The first choice is about the signal handling:

- an analog approach guarantees a reduced trigger latency;
- the digital approach, combined with the use of programmable integrated circuits makes the system flexible and adaptable to the experimental needs.

The choice is to sample the detector signals with analog to digital amplitude converters (FADC) and execute the algorithms on Field Programmable Gate Arrays (FPGA).

The memory depth of the DRS chips, constituting the experiment digitizing system, is ≈ 600 ns, requiring the trigger latency to be lower than 500 ns. Digital electronic technology provides a wide range choice of integrated circuits (FADC, FPGA and transmission devices) operating at 100 MHz, this frequency is high enough to ensure a proper digitization of the waveforms matched with a reasonable computation time. Furthermore, a system that exploits the FPGAs has the advantage of being adaptable to experimental needs and also allow the implementation of new algorithms easily and in every moment.

The trigger system was thought to use two different types of electronic boards, called Type1 and Type2, organized in a tree structure, the scheme is reported Figure 6.1. The first layer is composed by the Type1 boards, the second and the third by Type2 boards. A Type1 board receives the analog signals from the detectors, samples them at 100 MHz and executes a first pre-selection algorithm. The result is sent to the next trigger system layer composed of the Type2 boards. The Type2 boards combine the information from the Type1 and send processed data to a final Type2 board which, having an overall view of the event, generates the trigger signal.

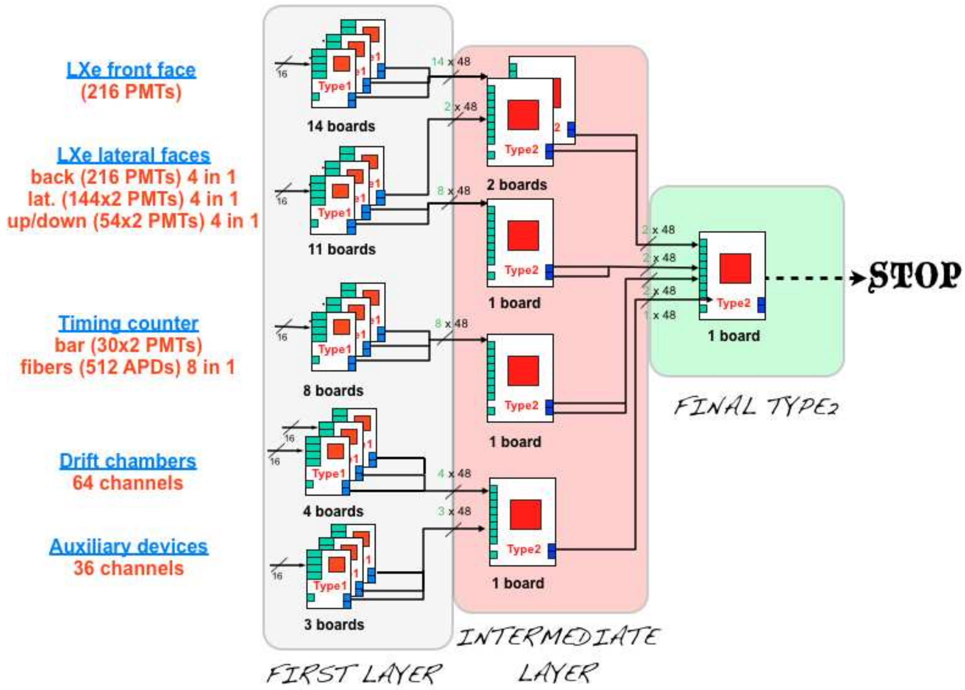

Figure 6.1: Trigger system sketch.

In order to accomplish the requested gamma-positron time selection, all the boards of the system have to be finely synchronized by common and stable clock (CLK) and control signals. For this reason we designed a further electronic board, named Ancillary board, as a CLK and control signal distributor. The Ancillary boards are organized in a master to slaves hierarchy, the master board hosts the main oscillator whose squared signal is fanned out and distributed to the trigger and DRS systems through the slave boards.

The detector signal flow is continuous as the exchange of data between Type1 and Type2. The inter-layer data transmission is accurately synchronized by using dedicated PLL circuits available in each trigger board.

A fourth electronic board has been designed to form, together with some of the Type1 boards, an auxiliary digitizing system for the LXe detector.

The system is composed of 40 Type1 boards, 6 Type2, 5 Ancillary and 20 Type3. A sketch of the trigger system is reported in Figure 6.2. The 9 units crate hosting the Type2 boards is in the center of the picture. The thick white cables provide the LVDS transmission between the boards. The Type2 crate also hosts the Ancillary system, not visible in the picture. The crate above and below the Type2 one host all the Type1 boards.

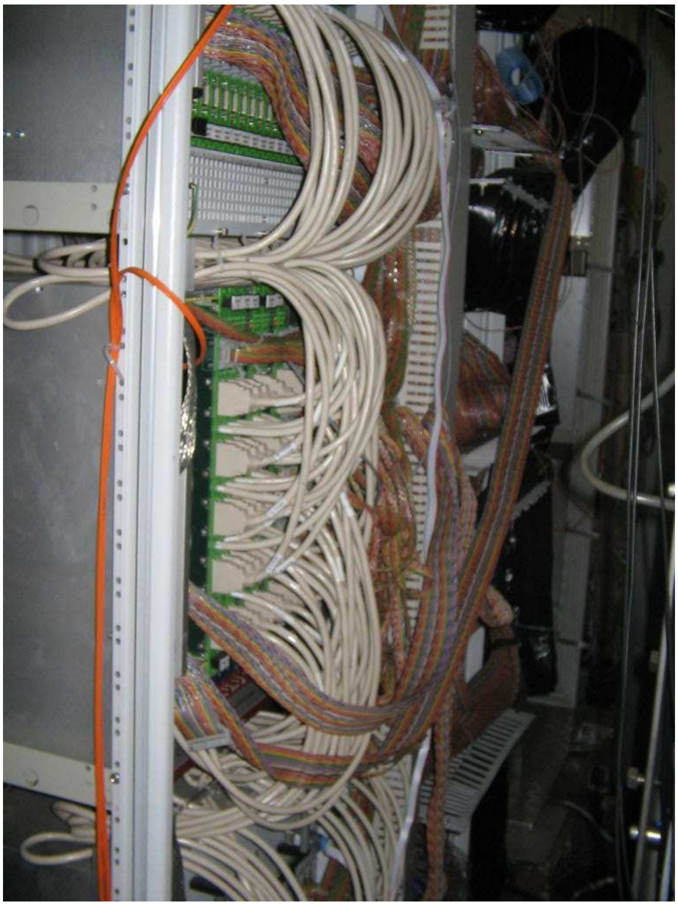

Figure 6.2: Picture of the trigger system crates in the MEG experimental area.

6.2 Type1 board

The Type1 board is implemented in the 6 units VME standard. The board consists of 10 conductive planes, interspersed with insulation planes, on which are etched the connection tracks, see Figure 6.3 where each color denotes a different plane.

A Type1 board receives the analog signals from the detectors, digitizes them and transfers the FPGA computation results to the next layer. Each of the mentioned steps exploits dedicated integrated circuits mounted on the board.

The 16 analog signals are received on the board through custom Front End mini-cards (see section 6.2.1) and digitized by means of 8 AD9218 [80], 10-bit precision on a selectable range of 0-1 V or 0-2 V at a frequency of 100 MHz. Each AD9218 hosts two digitizers.

The digital data are processed by the Xilinx Virtex-II Pro XC2VP20 [81, 82, 83] FPGA. Inside the FPGA the data are simultaneously stored on 8 cyclic 32-bit memory and, at the same time, processed according to the algorithm implemented for each board.

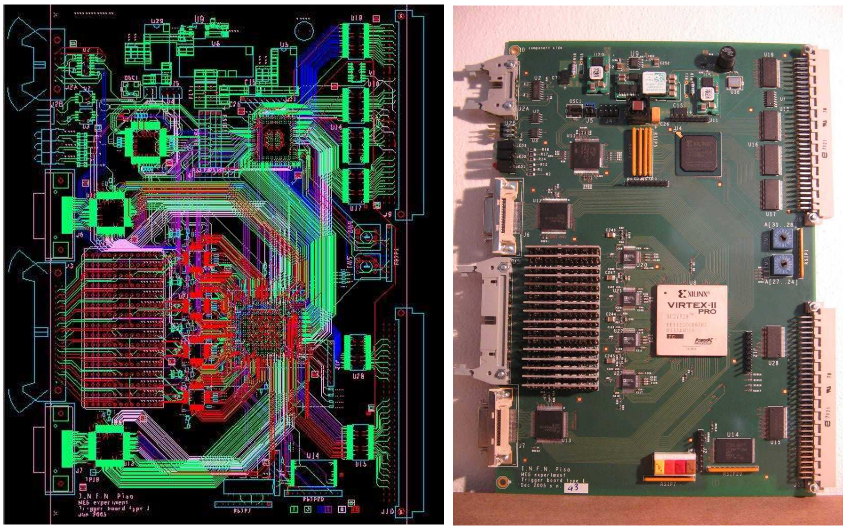

(a) (b)

Figure 6.3: Type1 board (a) PCB and (b) photo.

The computation results are sent to the next board through two LVDS serializers DS90CR481 [84]. The transfer rate of each serializer is 4.8 Gbit/s.

The CLK signal at 20 MHz distributed by the Ancillary system is received into the trigger boards by a Roboclock CY7B994V [85]. The chip can multiply the input frequency up to a factor 12 (in our case a factor 5 is used to get a 100 MHz) and shift the signal on 9 possible phases. The Roboclock produces 16 copies of the input signal, grouped in 4 banks each one having a common output in terms of frequency and phase, distributed to all the other chips of the board.

The VME interface is managed by a Xilinx CPLD XC2C384 [81]. Through the CPLD is possible to perform:

- Roboclock initialization;
- FPGA registers and memories interactions;
- FE electronics adjusting, as described in section 6.2.1;
- FPGA programming.

The Type1 memory area can be accessed by 32-bit VME addressing. The 8 most significant address bits are reserved to the board id, and are simply changeable by two manual hexadecimal switches. The input VME power supply at 5 V is converted by using DC-DC converters which outputs are 3.3 V, 2.5 V, 1.8 V, and 1.5 V. Finally the front panel of the card contains 6 LEDs identifying the board operation mode.

6.2.1 Front-End electronics

Detector raw signals are driven to the DRS and the trigger boards by the active splitter boards already presented in section 3.4.1.

Each trigger board input channel has a dedicated FE mini-card hosting a differential driver AD8138 [74] to the FADCs. The FE cards also host a DAC AD5300 [86] to adjust pedestal level of the signal to the optimum value that exploits all the FADC dynamic range. The electric scheme of the FE boards is shown in Figure 6.4, a picture is reported in Figure 6.5.

The electronic chain linearity has been tested injecting a pulse of known amplitudes (from few mV up to the FADC saturation), in Figure 6.6 is reported an example in case of 0-2V dynamic range FADC configuration. We measured a differential non- linearity less than 1.2% and integral non-linearity less than 2% in agreement with the data sheet values. We also found a global offset less than 1 ADC unit.

FE boards also operate an RC integration on input signals in order to improve online time estimation, the online time computation algorithm and its resolution are described respectively in section 5.1 and 11.2. A low-pass filter with a frequency cut at 30 MHz is mounted on the FE mini-cards dedicated to the LXe signals, while the frequency cut is 15 MHz for the faster TC signals.

6.2.2 Type1 boards cabling

The γ observables reconstruction algorithm requires a proper LXe signals cabling to the trigger system. In order to minimize the E_γ latency an analog sum on groups of 4 PMTs placed in the lateral faces is operated by the splitter boards, while the inner face PMTs have a 1 to 1 correspondence with the Type1 board inputs. The use of this analog fan-in reduces from 848 to 371 the number of LXe channels to be processed by the trigger system algorithm, maintaining the latency of the trigger within 500 ns. The α event selection exploits the the lateral face signals from the PMTs placed around the wires surrounding the α-source wires as described in section 9. This requires a non trivial cabling of the detector lateral faces. The map of the connections between the LXe PMTs and the trigger system is graphically reported in Figure 6.7.

6.3 Type2 board

The Type2 board is implemented in the 9 units VME standard in order to accommodate 9 connectors for the LVDS transmission in the front panel. The board consists of 12 conductive material planes, spaced by insulation planes, on which are etched the connection tracks; Figure 6.8 (a) shows the PCB of the Type2 board and (b) a picture of one of the boards used in the experiment.

The Type2 board is designed to receive data sent by an other trigger board through 48-bit 100 MHz LVDS deserializer DS90CR482 [84] for a total of 4.8 Gbit/s for each receiver. The lines connecting the FPGA to the LVDS receivers have been designed to maintain the impedance of the

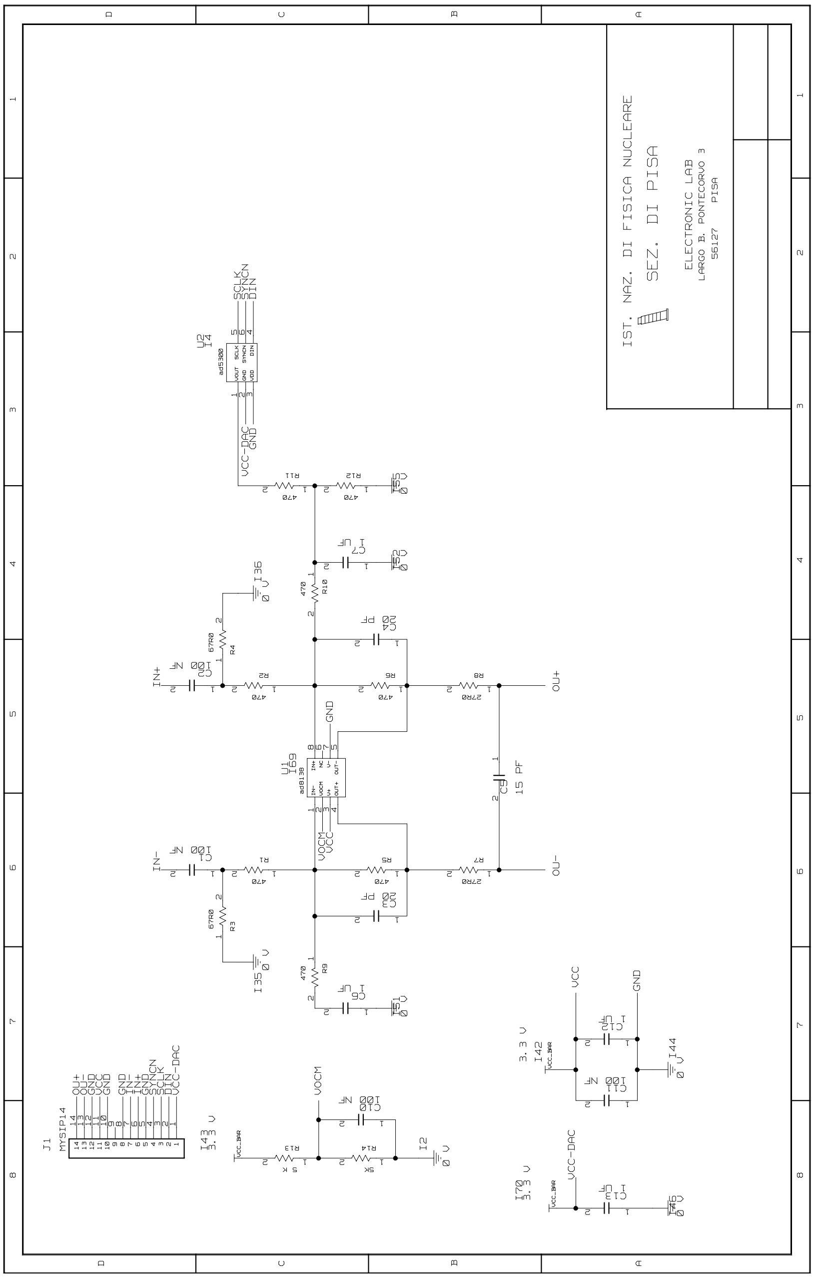

Figure 6.4: Electric scheme of FE boards.

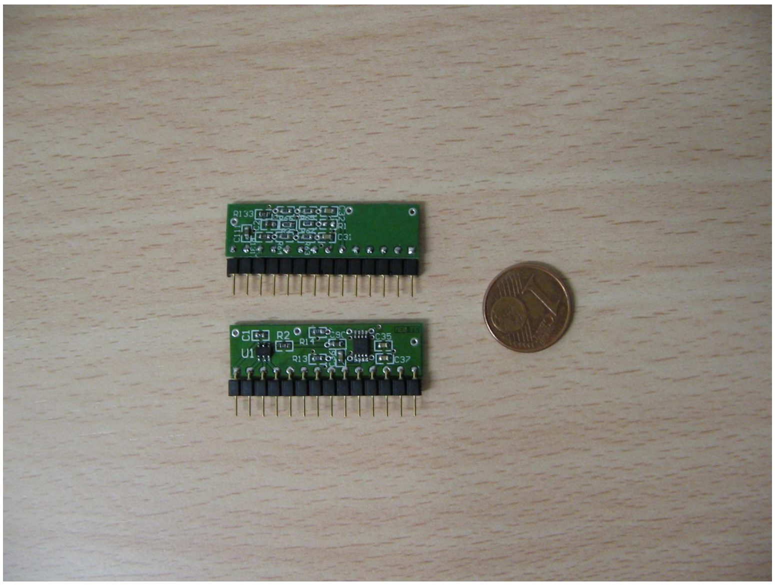

Figure 6.5: Electric scheme of FE boards.

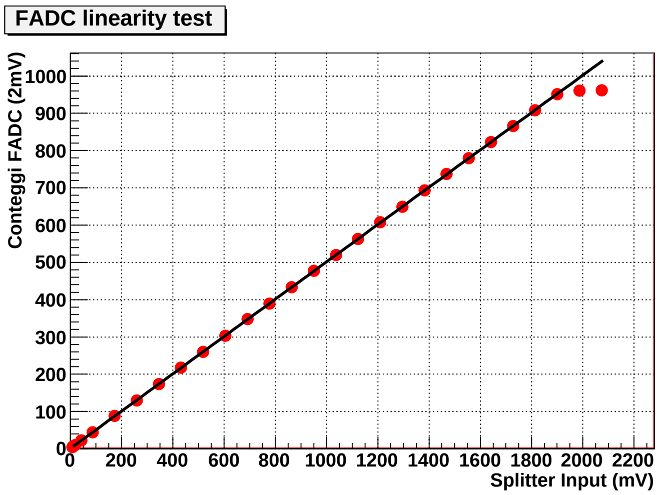

Figure 6.6: AD9218 linearity test in case of dynamic range 0-2V. The baseline value is ≈ 65 ADC counts (≈ 130 mV).

differential tracks equal to 100 Ω and requiring that the relative delay to be lower than ≈ 100 ps.

The data are stored and processed on FPGA Xilinx Virtex-II Pro XC2VP40 [81, 82, 83] and transmitted by means of two LVDS serializers DS90CR481.

In analogy to the Type1 boards, the VME interface is managed by a Xilinx CPLD XC2C384, as well as a Roboclock CY7B994V manages the CLK signal. Two hexadecimal manual switches define the 8 most significant bit of the address.

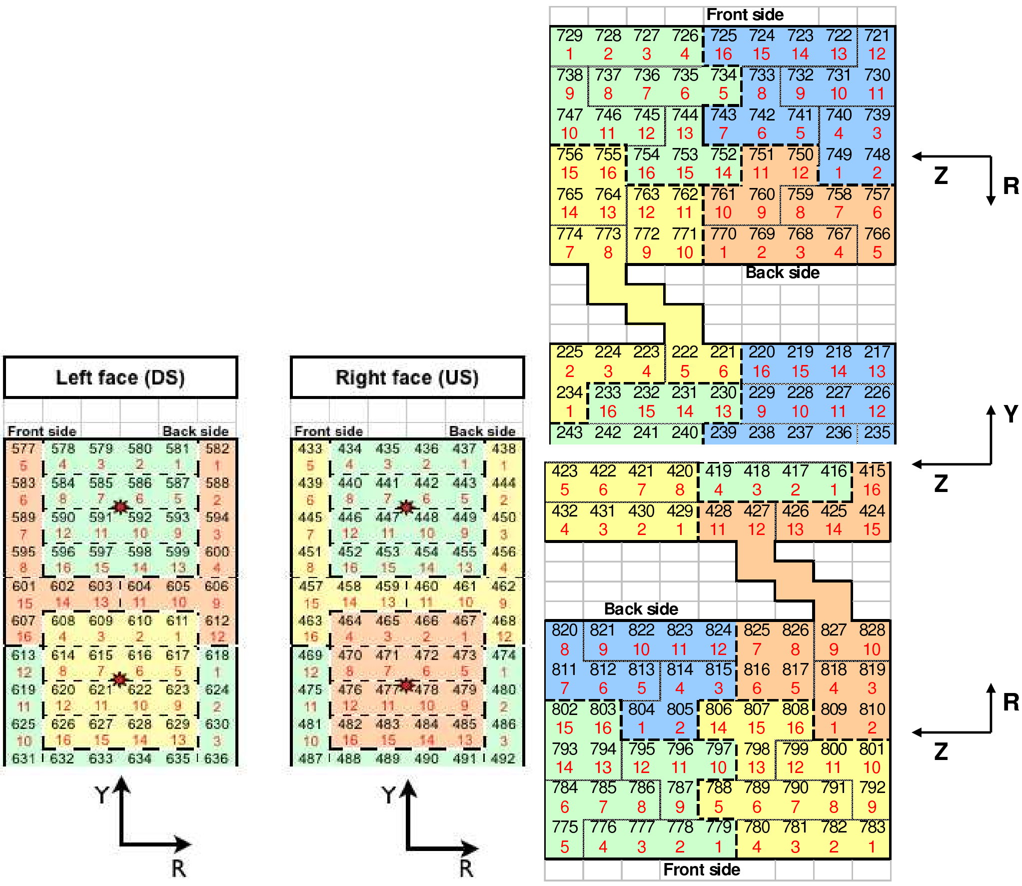

Figure 6.7: Diagrams for the calorimeter lateral faces cabling: each pair of numbers denotes a PMT; numbers in red identify the input channel for the splitter board while the number in black the absolute position of PMT in the calorimeter. The channels surrounded by heavy dashed line and having the same color, are received on the same splitter card. The thin dashed line identifies groups of 4 PMTs whose signals are summed and sent to a single input trigger system. The stars indicate the wire anchor positions with α sources, the 16 PMT surrounding these wires are used to generate the α trigger.

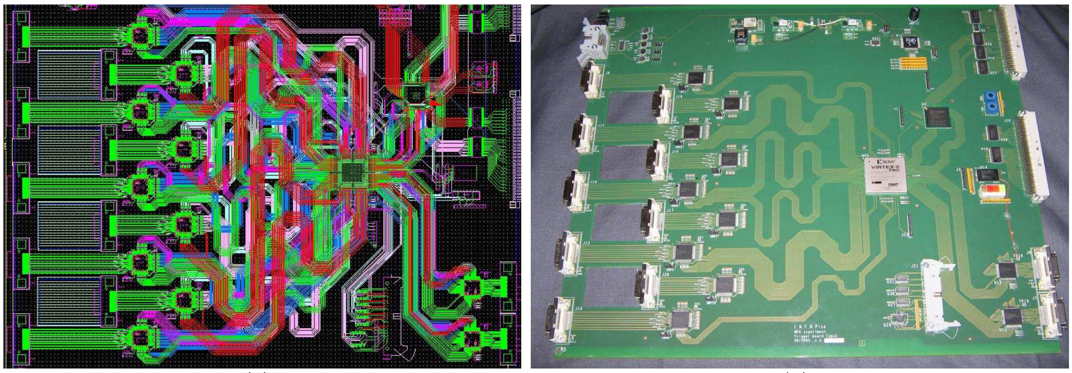

(a) (b)

Figure 6.8: Type2 board (a) PCB and (b) photo.

The Type2 boards mount on the front panel 6 LEDs in the same configuration of the Type1 board and an identical power distribution system.

The connection between the trigger and the DAQ system is obtained by means of a dedicated cable, named trigger bus, hosting the trigger signal, the event type and the event number. This cable is connected to the final Type2 board. The signals are distributed by means of the LVDS standard to limit possible noise pick-up by the 5 meter long trigger bus.

6.4 Ancillary board

Ancillary board is implemented in a 9 unit VME standard and is composed of 6 conductor layers, see Figure 6.9.

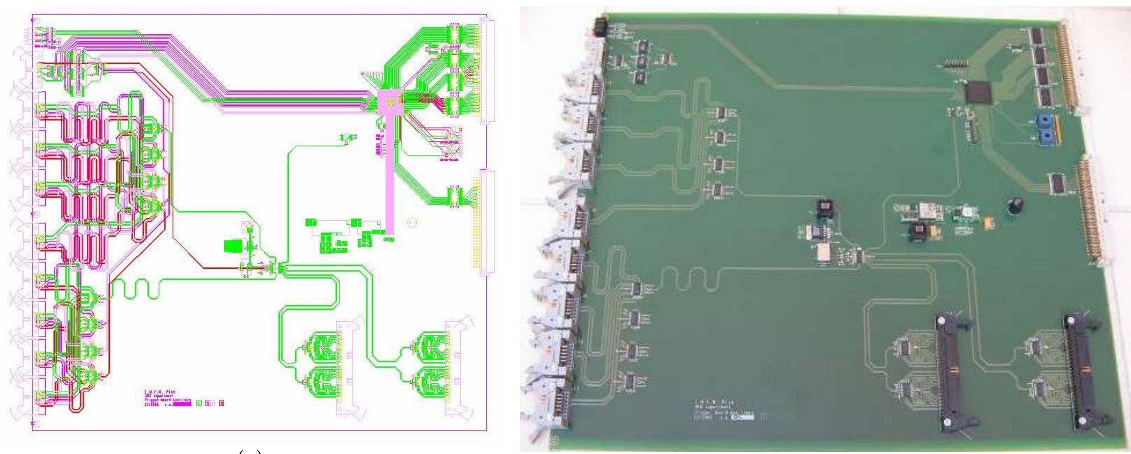

(a) (b)

Figure 6.9: Ancillary board (a) PCB and (b) photo.

The most important component mounted on this board is an oscillator SARONIX SEL3935 at 19.44 MHz [87] which produces the experiment reference CLK signal. This oscillator guarantees a maximum jitter of 30 ps on a range of 100.000 periods and a maximum frequency variation of 100 ppm in all conditions of use. This level of signal stability is not an essential performance of the trigger system but it is crucial for experiment timing. Several copies of the signal CLK are produced by the Maxim MAX9153 LVDS fan-out[88]: it is guaranteed to add a maximum jitter of only 13 ps on the 10 output lines and maintain the relative delay between the outputs less than 60 ps peak to peak. These copies of the CLK signal is sent directly to all of the DRS chips, so that each DRS sample can be temporally associated with common reference. The CLK signal distribution to the DRS crated is obtained by means of shielded twisted pair cables. The global jitter of the CLK signals at the cable shielded outputs have been measured to be less than 20 ps, in agreement with data sheet specifications and the experimental needs.

The Ancillary system distributes the trigger internal control signals received from the final Type2 board to the whole trigger system. The master Ancillary board in a hierarchical scheme provides to the five slave boards the three trigger control signals, namely the stop, the start and the synchronization signals. The slave Ancillary boards can add some delay to the input signals with a step of 0.25 ns by means of three programmable delay generators 3d3418[89]. The delay can to compensate for the different path length of the control signal in Type1 and Type2 boards.

Even for this card is installed a CPLD for interface with the VME. Addressing is managed similarly to other boards. The voltages on the card are: 3.3 V, 1.8 V and V filtered 3.3 V produced by a voltage regulator reg104-33 [90], stable at 2% and used only for SARONIX oscillator.

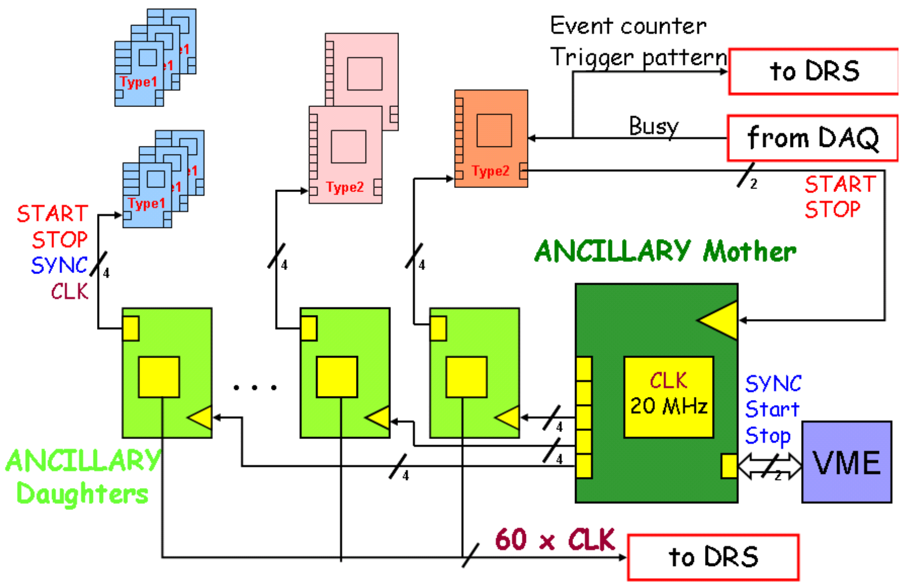

Figure 6.10: Sketch of Ancillary connections to the trigger and DRS systems.

6.5 Type3 board

The Type3 board is implemented in the 6 units VME standard. The board consists of 10 plans conductive material, interspersed with insulation, on which are etched the connection lines, see Figure 6.11 where each color denotes a different plane.

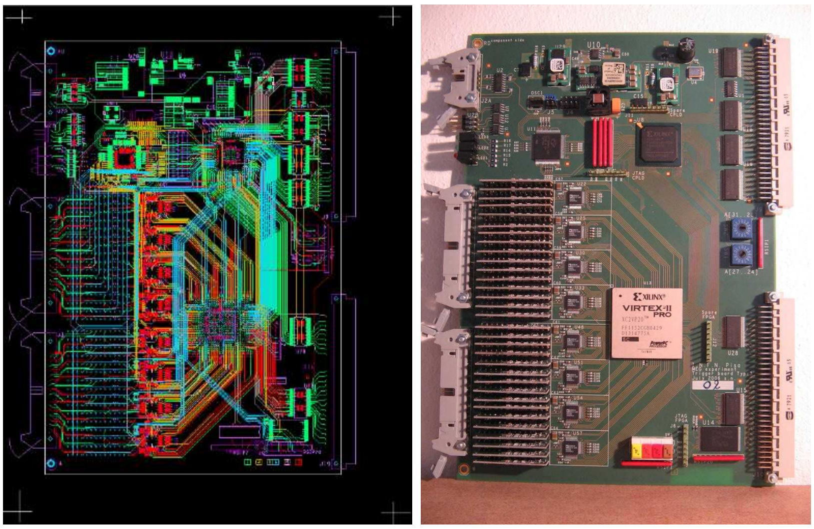

(a) (b)

Figure 6.11: Type3 board (a) PCB and (b) photo.

This board was designed as an auxiliary digitizing system to the one composed by the DRS chip. Therefore the board has in principle the same design of the Type1 one, see section 6.2, apart for the 32 input channels instead of 16, the LVDS transmitter are eliminated. The scheme of the digitizing electronics, as for instance front end electronics and FADCs, is the same as for Type1 boards.

Those boards digitize the signals coming from the lateral faces of the LXe detectors, as described in section 6.2.2, that are analogically summed by the spitter boards before being received by the trigger system. In this way all the LXe channels are digitized by the DRS chips and the commercial trigger FADCs and two quasi-independent analysis are possible.

The 20 Type3 boards are arranged in a dedicated crate shown in Figure 6.12.

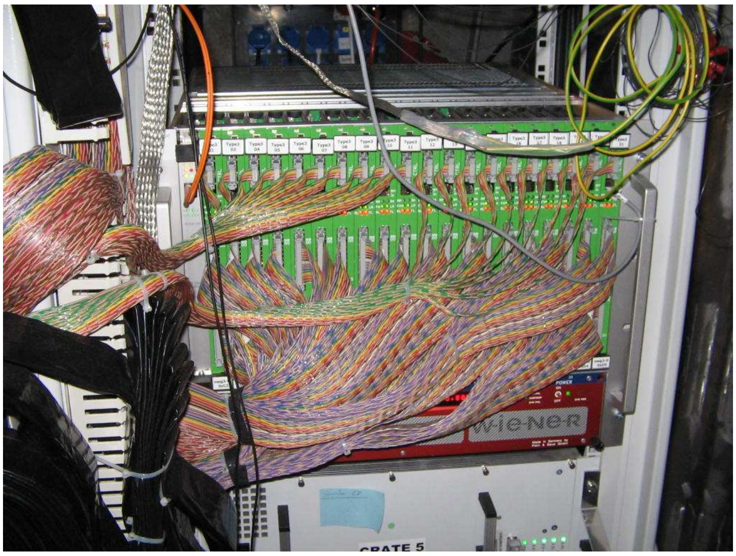

(a)

Figure 6.12: Picture of the Type3 crate.

Chapter 7

Firmware implementation

The event selection algorithms described in chapter 5 must be translated into the appropriate FPGA configuration files, called firmware. The FPGA configuration file is produced by dedicated software hardware oriented distributed by the electronic device supplier, the Xilinx. The version ISE 6.03 is the latest version distributed at that time.

The trigger algorithms have been implemented in the schematic-type language and using, when possible, the FPGA primitive functions. This choice has made the project bound to the Xilinx hardware, but certainly optimized and compact.

The firmware is logically divided into two blocks: a block in which there is the data storing and processing, and a block to handle the VME interface, the control signals and the configuration registers. All projects are designed to run at 100 MHz. The structure of the firmware is represented in Figure 7.1. It has two dedicated storage memories for the input signals and the processed data both recorded continuously in cyclic memories during normal data acquisition. There is, however, the possibility to interrupt the input data flow and to program the memory contents using VME write cycles. In this mode the FADC data are ignored, and the algorithm processes the data previously loaded in the memories with, for example, simulated events. This has been used to debug the algorithm computations and the data transmission.

The trigger boards can operate in two modes, controlled by the RUNMODE signal status. In the acquisition mode, corresponding to RUNMODE high, the data flow through the system, the algorithms search for events and the VME access is inhibited. In the control mode, corresponding to RUNMODE low, the data are stable in the cyclic memories, the algorithms are not executed and is possible the VME access to the boards.

The transition from control mode to acquisition mode occurs synchronously over the entire system when the start signal is issued, the transition from acquisition mode to control mode occurs when the final Type2 board generates the stop signal.

The control block contains all the parameters used in the online data processing, such as the thresholds and the calibration constants. Furthermore the control block controls the VME read and write access to the cyclic memories and registers.

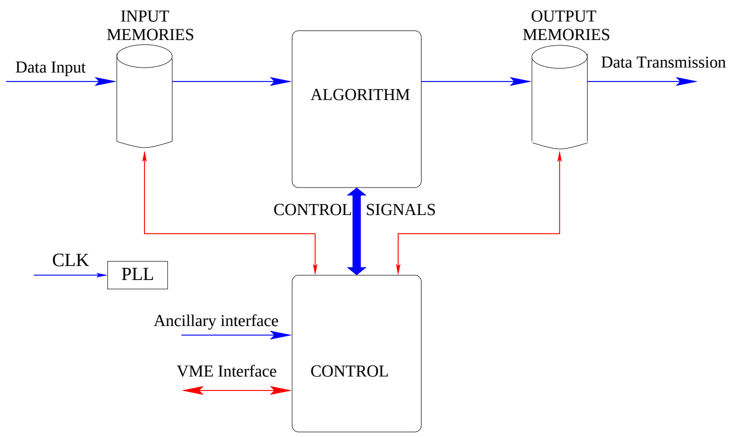

Figure 7.1: Logic structure of the firmware implemented on the FPGA. The program consists of two main blocks: the first for analysis, storage and data transmission handling and the second to control the board operation and the VME access.

The block of data processing differs from board to board depending on the location within the trigger tree and the data to be processed.

7.1 Data storage

Input and output data are stored on 16 Kbit RAM memories available on the FPGA. Each RAM block provides a double data access, one to collect FADC data while the other can be conveniently stored by VME access. Logic storage control is shown in Figure 7.2.

To standardize the firmware we decided to use the same memory configuration for all the boards, based on the Type1 needs. The Type1 board samples every 10 ns the analog signals provided by detectors through 10 bit FADC, the sampled data must be stored inside the FPGA.

The data storage scheme has to ensure a sufficient temporal depth, together with the use of a reasonable number of RAM blocks not to exhaust the resources. The number of memory cells, proportional to the depth of time, is defined by the extension of the data you want to store. Registering 16-bit words in a 16 kbit memory the memory depth is 1024 cells, it is 512 in the case of 32-bit words, corresponding in time to, respectively, 10.24 μs and 5.12 μs.

We choose to pair two channels within the same memory in a 32-bit word. If you use real data, the 26th bit of the word is set to 1 in order to distinguish real from the simulated data. The address of each cyclic memory cell is defined by a 9-bit counter. This counter is driven by CLK and enabled by the RUNMODE signal.

The output from Type1 and Type2 boards are composed of words 48-bit bound by the capacity of the LVDS transmitters installed, see chapter 6. The output data recording is carried on two memories identical to those on the input stage of the Type1, a memory stores the less significant 32 bits, the other the 16 more significant.

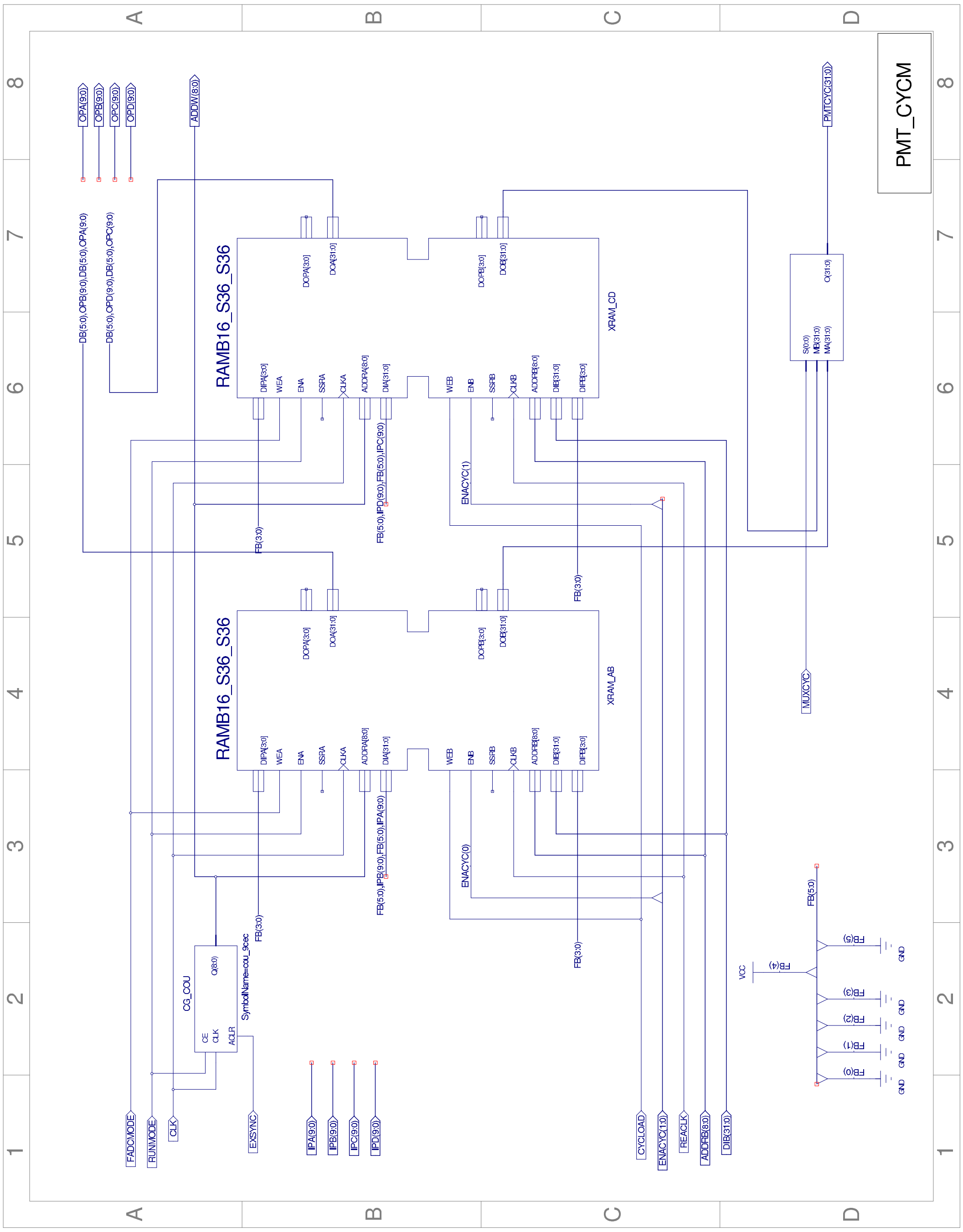

Figure 7.2: FPGA schematic routine for recording data into RAM memories.

In addition to the aforementioned 512 sample memories, a parallel block RAM with $1.28\mu/s$ time depth is used in calibration runs to get a faster data read out and limit the data size. During the physics runs both of them are used. The larger depth memories are important because they provide a measurement of the detector crowding.

7.2 Selection algorithms implementation

In this section the logic implementation of some crucial fragments of the selection algorithms are explained. In particular, the logic of real time pedestal subtraction, the use of the Look Up Tables.

7.2.1 Pedestal subtraction

The first online algorithm step, common to all the firmware versions, is the pedestal subtraction. FADC data, after being stored in the input memories, are driven to the pedestal subtraction block, where the average of four samples registered N CLK periods before the current one is subtracted to that. Figure 7.3 shows the implemented logic. This is accomplished by inserting all the samples into a chain of N registers in cascade, the data is transferred from a register to the next one every 10 ns, at the same time the average of the last 4 register values is updated and finally removed to the current one. Data transition along the chain is interrupted when two consecutive samples differ from the current pedestal more than a dedicated threshold. In this way we do not introduce physical signals in the chain, preserving the removal of incorrect values of the pedestal.

The only parameter of the algorithm is the length N of the register chain. The pedestal estimator is reconstructed using signals temporally far $\approx 10\times$ (N-1) ns from the input, so noise components with frequency close to half of the frequency define by the N value are amplified by the algorithm. In Figure 7.4 shows the result of subtraction of the pedestal on simulated waveform.

The simulation is performed on physical pulses superimposed with the sum of a white noise and a sine wave of 40 mV peak to peak pulse height with frequency 100 KHz, Figure 7.4 (a), and 2 MHz, Figure 7.4 (b). The result shows that the algorithm eliminates completely the noise at frequencies lower than 1 MHz, while for values around 2 MHz it is amplified by a factor of two.

The measured pedestal fluctuations of LXe and TC waveforms are compatible with a white noise, the maximum peak to peak fluctuations are less than 2 mV. N was then set to 20 for all the channels.

7.2.2 Look Up Tables

The implementation of multiplication and division between integers, or even the relatively complex functions of integers, is certainly possible within algorithms operating in FPGA, while maintaining the maximum precision on the operation. For example, the product of an M-bit integer with an entire N-bit integer results in an integer to M + N bits but the result is available with a delay of several clock cycles.

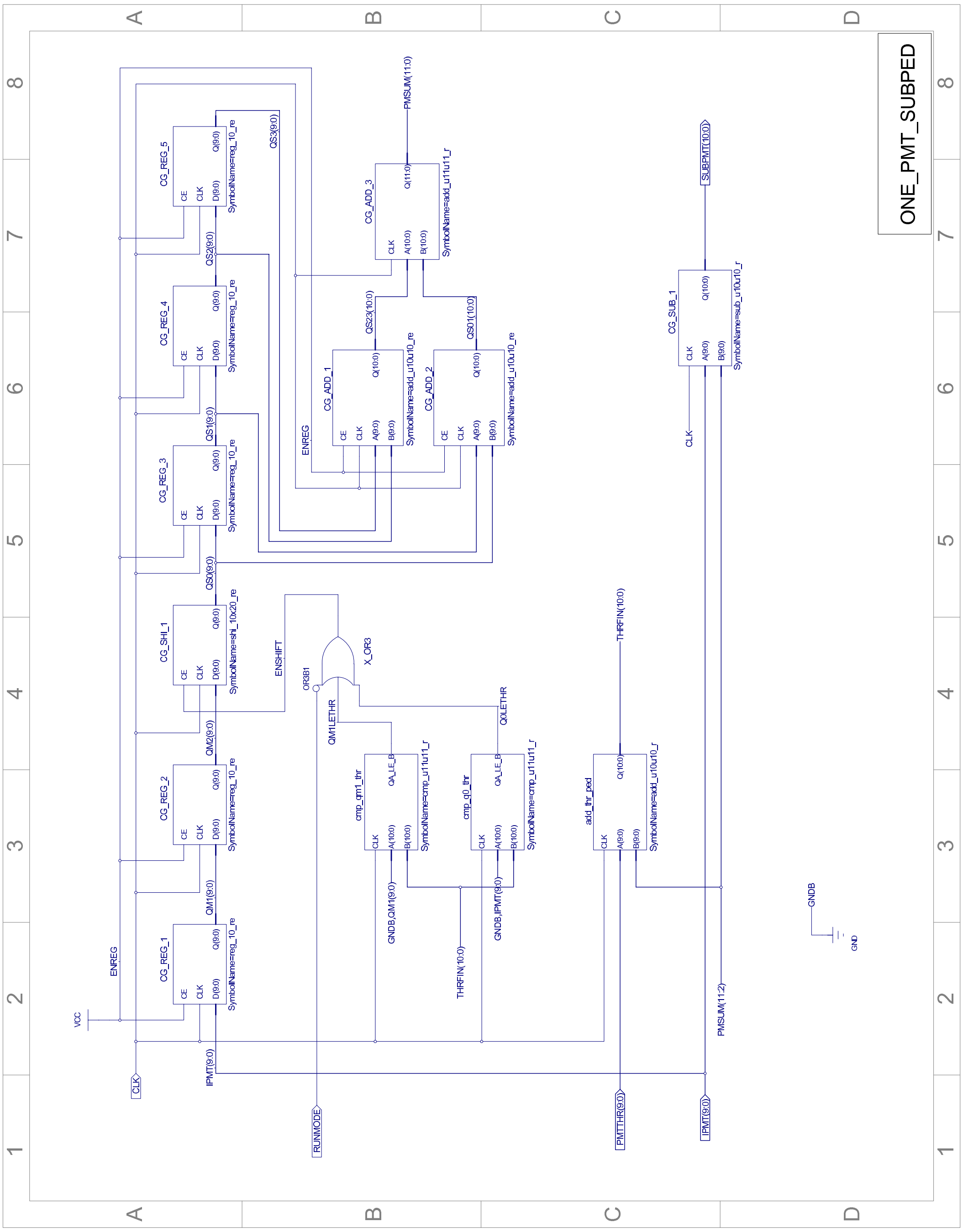

Figure 7.3: FPGA schematic routine for online pedestal subtraction.

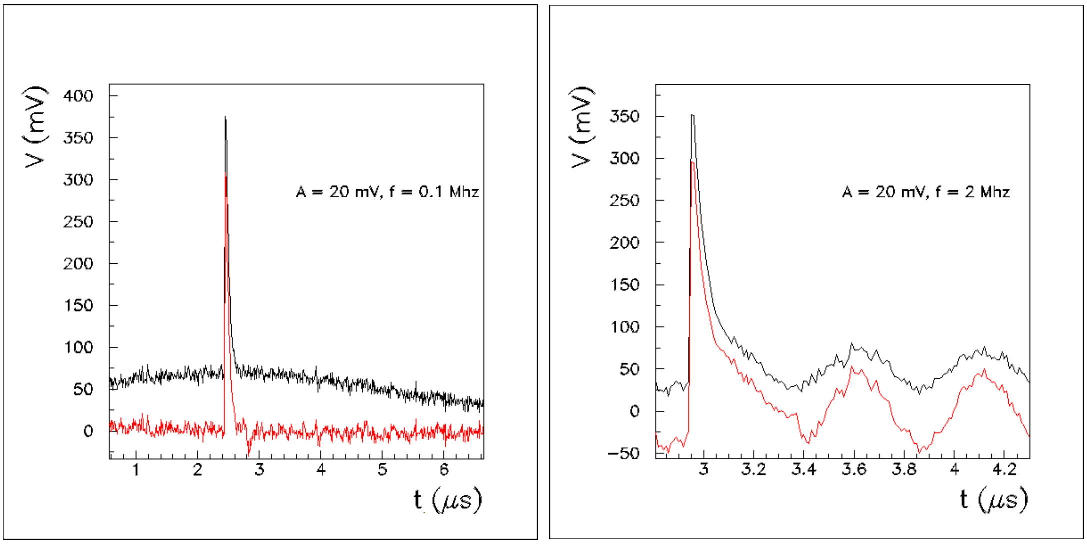

(a) (b)

Figure 7.4: Results from the subtraction of the pedestal where the average is calculated on the last 4 samples of a chain of 26 registers. In black is reported the waveform input, the red waveform pedestal subtracted.

When the application has stringent requirements on the execution time of algorithms, as in the case of MEG, where the trigger signal latency must not exceed 500 ns, or when is necessary to evaluate non-analytical functions, is possible simplify and speed-up the project by using tabulated values of functions. The tables with the tabulated values are stored in memory blocks that are called Look Up Table or LUT.

A LUT is a read-only memory whose address lines are connected to the data to be processed and the content of the pointed cell is the value of the function to be evaluated. The RAM used is identical to the memories on which data is stored, 16 kbit and dual access. The number of bits reserved for input data and to the processed one depends on the capacity of the memory. The maximum capacity of RAM on a single FPGA is 2^{14} bits, the number N of bits reserved for the output data is therefore 2^{14-n} where n is the number of bits of the input. For example with a 14-bit addressing a single bit output is available. If the capacity of a single RAM is not enough and we can not have any precision loss, it is possible to use conveniently in parallel more than one RAM or, if possible, operate data truncation and rounding.

The LUTs are frequently used within the selection algorithms. Each PMT inside the calorimeter is characterized, as well as for placement in the apparatus, by the quantum efficiency and the gain. In order to take into account the PMT characteristics in the gamma energy estimator reconstruction a LUT is conveniently programmed to calibrate the channel amplitudes[1], the same for the TC channels. Other LUTs are used, for example, in the algorithm selection for α events, for calculating the charge amplitude ratio, to calculate the Z coordinate in the TC bars hits and

[1] In this case not to have loss of resolution are used simultaneously two LUTs configured properly

the assessment of collinearity between gamma and positron; for details see chapter 5.

7.3 DAQ set up

The trigger system can select up to 32 different types of events. The selection is made by the final Type2 of the system which provides two control functions to regulate the generation of trigger signals:

1. individual selection enabling;
2. pre-scaling of the trigger frequencies.

Each of the 32 trigger signal can be enabled individually depending on the needs of the acquisition data.

The frequency of each trigger signal can be downscaled for a number between 1 and 2^{32}-1. This operation is required for the acquisition system to select triggers in different proportions depending on the experimental needs on the various events selected. During a physics run the MEG trigger is enabled with pre-scaling factor equal to 1. All the other selection needed are downscaled in order to have an overall calibration trigger rate of $\approx$ 1 Hz to take under control the live time fraction. A typical physics run configuration is reported in Figure 5.14 (a).

7.4 Live and dead time

The DAQ live time is a fundamental parameter to be maximized, together with the online selection efficiency, for the highest possible experimental sensitivity, see section 11.5. The live time, together with the total time, are measured with high precision by means of dedicated counters. A third counter computes the serial event number. Each trigger board is provided with these three counters as a cross check of the system operation, the firmware logic is reported in Figure 7.5.

The biggest counter available in the FPGA primitives has a 32 bits depth, corresponding to a time window of about 43 s if the clock signal has 100 MHz frequency. This resulted inadequate for the needs and also an experimental accuracy of 10 ns is excessive. The signal CLK is then downscaled by a factor of 1000, this brings the counter depth to be about 12 h, enough with respect to the normal length of a run, 5 minutes, with an accuracy of 10 μs, enough for the experimental needs.

The total time counter is a 32-bit counter always enabled, except in case of saturation. The state of the counter is recorded on each falling edge of the RUNMODE signal to make it available for reading in the control phase as described at the beginning of the chapter. The live time counter is implemented in the same way but it is enabled when the system is in acquisition mode, that is when the RUNMODE signal is active.

The counter of the number of events increases by a unit whenever a trigger signal is fired to the DAQ system. This counter is implemented on all the trigger system boards so you can check

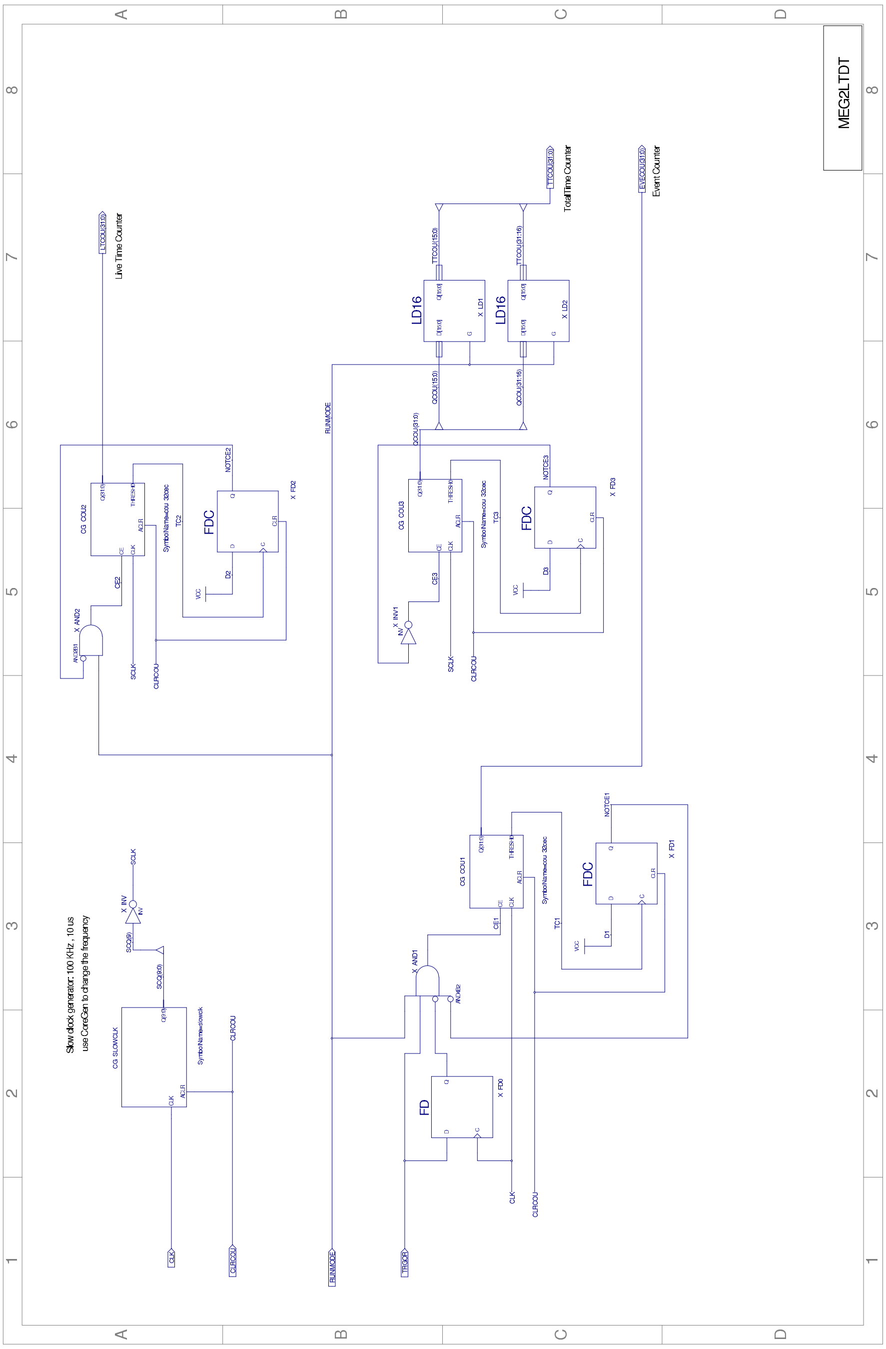

Figure 7.5: FPGA programming the total time counter, live-time counter and event counter.

for any event that every board has the same serial number that identifies each data set and it is used by the *eventbuilder* software, see section 3.4.3.

7.5 DAQ interface

The data acquisition system (DAQ) is interfaced with the trigger system through dedicated cable. named trigger bus, linked through a connector 3M 32-pin on the final Type2 board. On the connector are distributed control signals from the trigger system drives to the DRS boards and the signals used by the DAQ to communicate with the trigger system.

The trigger system provides the DSR three signals:

1. the trigger signal;
2. a code indicative of the selected event type;
3. the serial number of the event.

The event code is used by the DAQ to differentiate the data transfer procedures depending on the event type. For example, in the case of event α event in the calorimeter data about the magnetic spectrometer are not transferred to external memories. This way you operate compression on data and the transfer operation becomes more rapid.

The principal experiment digitizers, the DRS chip (see section 3.4.2), are hosted in VME 5 crates, each one interfaced with a computer and the data transfer phase takes place in parallel on those 5 crates. The number of the event, distributed by the trigger system to the DRS boards, is used to associate data segments at the same event by the *eventbuilder* code. The DRS boards provide to the final Type2 board four signals. During data transfer the DRS system, as the trigger, is not able to sample new data and the DAQ is stopped. Through the signal status EXBUSY the DRS boards tell the trigger system their capability to accept new events. They can also also provide the signal FOSTA which forces the start of the selection of events within the trigger system. The trigger system provides internally the signal INBUSY whose state is high during the read or write VME access. When the signal INBUSY is high it is not possible to restart the data taking.

The final Type2 board is not allowed restart the acquisition system until both the inbusy and the exbusy signals are released.

7.6 Trigger latency

The goal of a trigger system is to perform an efficient selection of events in a limited time window. The time scale is, in this case, the depth of the memories of the DRS system. The DRS samples the waveforms at a frequency of $\approx$ 1.6 GHz on 1024 samples deep cyclical memories, corresponding to a time depth of $\approx$ 600 ns. The task of the trigger system is then to generate the trigger signal no more than 450$\div$500 ns from the front of the signal. It is useful to have at least 100 ns before the event so as to obtain an optimal reconstruction of the pedestal before the signal, in the trigger latency the time needed passing from the trigger generation to the effective stop to the DRS chip is not taken into account, and it is of the order of 20÷30 ns.

We performed several simulations to check the algorithm implementation and synchronize the various signals at the final Type2 stage. The final purpose was to compute the event selection latency. In this calculation there should be taken into account, in addition to the latency induced by the algorithms, the time needed to convert the analog input signal (40 ns) and the LVDS data transmission (60 ns between Type1 and Type2, 80 ns between Type2 and Type2). The measured global latency, reported in number of CLK ticks, for the most important estimators is reported in Table 7.1.

Signal	**Type1**	**Iterm. Type2**	**Final Type2**	**Trasmission**	**FADC**	**Total**
γ energy	8	5	4	14	6	37
γ time	11	5	4	14	6	40
γ angle	8	5	3	14	6	36
e^+ mult	11	3	2	14	6	36
e^+ time	9	5	3	14	6	37
e^+ angle	8	5	3	14	6	36
α	18	3	2	14	6	46

Table 7.1: Relative latency, in periods of CLK, for the reconstruction of the various estimators for the $\mu \to e\gamma$ trigger firmware and the α one.

The $\mu \to e\gamma$ trigger latency is given by the slower estimator, the gamma time estimator. The final latency is then 40 CLK ticks plus 20 ns to form and fire the STOP signal. In total 420 ns. The highest latency trigger is the α one, because of the waveform charge integration, see chapter 9. The α trigger latency is 480 ns, still acceptable for the experiment.

Chapter 8

Trigger system calibration and monitoring

Just before the physical data taking phase a whole week is devoted to set up the online selection. The online event selection operates by reconstructing estimators of the kinematical observables of the muon decay products. The reconstruction needs calibration constants, similar of those needed for the offline event analysis. Each detector is studied and calibrated individually and the corresponding thresholds are located.

During the data taking the trigger and the DAQ system have to be carefully monitored to check the data quality. An automatic procedure, just after the data transfer to the offline disks, processes the file by means of a fast and simple analysis. The functionality of each detector the of MEG experiment is monitored every run by means of a set of distributions produced by the offline process.

In this chapter a set of developed methods for online monitor of the DAQ and the trigger system are presented.

8.1 Calibration

This section presents the calibration methods for the characterization of online selection algorithms of the LXe and the TC detectors. The setup of the direction match table is also discussed.

8.1.1 LXe detector

The online algorithms that evaluate in real time the gamma energy deposit, its emission time and impact point, were already discussed in section 5.1 while the LXe detector was described in section 3.3.

To extract the number of scintillation photons absorbed by each photomultiplier from the charge of the waveform, the PMT gain (g) and its quantum efficiency (QE) are needed. The number of scintillation photon (n_{pho}) are calculated from the PMT anodic charge (Q) as follows:

$$Q = n_{pho} \times QE \times g \tag{8.1}$$

the npho is then used to estimate the energy release in the LXe detector.

A number of approximations are assumed for the reconstruction of the online energy release, which one not assumed by the offline algorithms described in section 4.1.2. The light absorption length is assumed to be infinite, as well as the light losses due to multiple reflections on the calorimeter walls This implies that for an homogeneous PMT coverage the collected light is independent from the photon conversion position. The PMT are not equally spaced on the calorimeter curved faces. This fact restores a residual dependence of the collected light from the photon interaction point. In offline algorithms a coupled energy-position reconstruction is performed so that each PMT light can be weighted for the PMT solid angle subtended with respect to the reconstructed γ interaction point. In case of real time algorithms the charge collected by each PMT is simply weighted for the local photocathode density (phc), which is a pure geometrical factor ,independent from the gamma position.

Summarizing the calibration factors f applied to the LXe trigger channels is:

$$f = \frac{phc}{QE \times g} \tag{8.2}$$

The PMT gains are computed by means of dedicated LED calibration runs as reported in section 3.3.3, while the QE computation takes advantage of the α sources placed inside the LXe detector. The PMT gain values are all scaled to an arbitrary value of $1.6 \cdot 10^6$ and the QE to a value of 16%. The final step is to define the energy scale. This is obtained using the 17.6 MeV peak of the Li line generated by means of the CW accelerator, see section 3.3.3. The online energy is defined by

$$E_\gamma = C \cdot \sum_i f_i \cdot A_i \tag{8.3}$$

where A_i are the TRG waveforms pulse heights. This line is also a powerful tool to follow the detector and electronic chain stability all over the run, as already presented in section 3.3.3. In Figure 8.1 an example of an energy spectrum with the online estimator is reported, the Li 17.6 MeV line is visible. Other calibration γ lines are the 11.7 MeV and 4.4 MeV from the B induced nuclear reactions together with the α line around 5 MeV.

In order to set the gamma energy threshold, and to check the quality of the selection algorithm dedicated calibration runs were acquired: sets of single LXe events runs (trigger#10) (the trigger type definition is reported in Table 5.2) with different energy thresholds were performed.

The reconstructed energy spectrum is given by:

$$\frac{dN}{dE} = k \times \left.\frac{dN}{dE}\right|_{th} \times \Sigma(E_{thr}, \sigma_E) \tag{8.4}$$

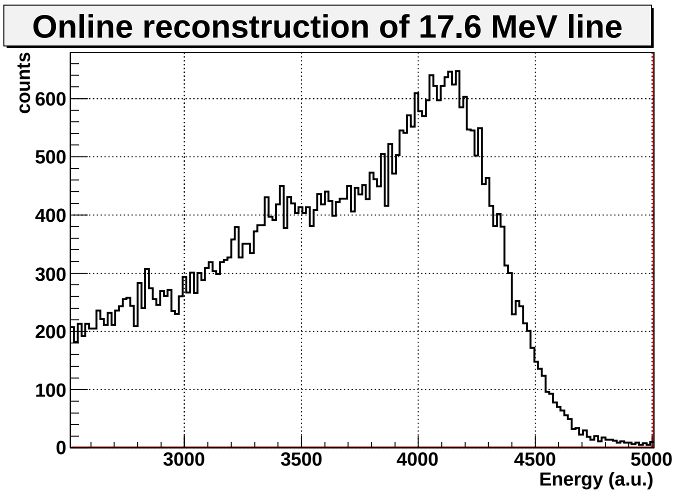

Figure 8.1: CW Li line as online reconstructed by the trigger system.

where k is the normalization factor, $\frac{dN}{dE}\big|_{th}$ is the theoretical gamma energy spectrum for the radiative decay and $\Sigma(E_{thr}, \sigma_E)$ is the sigmoid function applied by the online system where E_{thr} is the energy threshold and σ_E is the width of the cut.

The ratio between two spectra obtained with different thresholds, opportunely normalized, is the trigger sigmoid function. The fit to the ratio of the two spectra by means of a sigmoid function returns the effective selection threshold and its sigma.

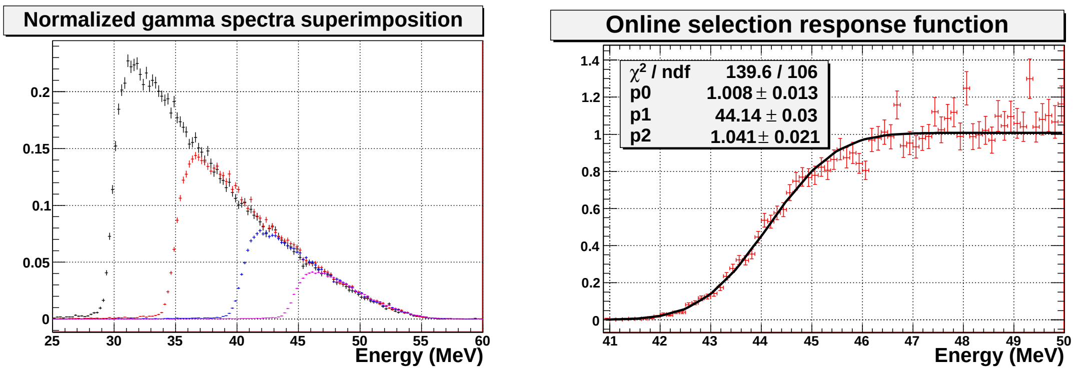

(a) (b)

Figure 8.2: (a) Superimposition of two different E_γ spectra normalized for their native trigger rate; (b) ratio of the spectra fitted with a sigmoid function.

Figure 8.2 (a) shows the superimposition of the normalized energy spectra taken at different energy thresholds. In Figure 8.2 (b) the results of the fit performed on the higher threshold spectrum are reported, ε is the plateau efficiency of the algorithm, ε is a free fit parameter; the threshold value μ and σ its width. The online energy is less that a factor 2 worse than the official one, it would then possible to apply a full efficient threshold at 45 MeV in LXe energy selection with a high gain in trigger rate and DAQ live time. The gas-phase purification of the LXe in the detector was kept active in the last month of the RUN2008 and therefore the light increased, while in the first part of the run it was slightly decreasing due to a leak in a LN_2 cooling pipe inside the detector. This light instability require a gamma energy setting at about 40 MeV for the RUN2008, lower than the aforementioned 45 MeV but safer with respect a LXe light yield small changes during the runs.

The γ time and direction are extracted from the inner face PMT collecting the highest amount of light. The online calibration factors are fundamental in the maximum finding, in particular this is demanded for the gamma flight direction estimator.

8.1.2 TC detector

The TC detector is composed by 30 scintillators bars each one read out by 2 PMTs, one on each bar end. Each single TC bar energy response is calibrated in order to set a common hit discrimination threshold, see section 5.1.2. An intra-bar calibration for the online z evaluation is also applied.

The TC PMTs HV are set to have the same gain with an accuracy of 10%, these relative uncertainties can be compensated by using proper channel calibration factors. The equalization of the intra-bar PMT response and the inter-bar energy scale is based on cosmic ray events.

Cosmic ray events events are uniformly distributed along the z coordinate of the TC bar. One possible estimator for the Z coordinate has been presented in Equation (5.5). Now let's add the gain of the PMTs to the formula, which is modified as follows:

$$\mathrm{L_{seen}(z)} = (\alpha \cdot \mathrm{g} \times \mathrm{QE} \times \mathrm{n_{pho}})\mathrm{e}^{-\lambda \mathrm{z}} \tag{8.5}$$

$$\log\left(\frac{\mathrm{L_{seen}(z)}}{\mathrm{L_{seen}(l-z)}}\right) = \log\left(\frac{\mathrm{G_1}}{\mathrm{G_2}}\right) + \lambda(\mathrm{l} - 2\mathrm{z}) \tag{8.6}$$

where $\mathrm{G_i}$ (i = 1,2) are the product of the gains and the QEs; if these factors are not identical the Z distribution for cosmic events is not centered at 0. This is cured applying a proper calibration factor between the PMTs of the uncompensated bars. In Figure 8.3 an example of the Z distribution given by the charge asymmetry and the mean of those distribution, before and after this calibration, is shown. This calibration is also used to evaluate the z coordinate of a counter hit by means of the charge asymmetry between the PMTs.

The energy deposit of a cosmic muon into the TC counters is distributed accordingly to a Landau energy release distribution convolved with the muon path length in the scintillating material. Given the geometry of the bars with respect to the cosmic ray flux, the peak of the Landau distribution is at the same energy for all the bars. Figure 8.4 shows the influence of the calibration factor.

After the definition of the channel calibration factors the z-computing LUT has been defined. We took benefit from the offline DRS reconstruction, presented in section 4.2.2, which is guaranteed to be of the order of ≈ 1 cm. Figure 8.5 shows the scatter plot of the online z evaluation obtained by

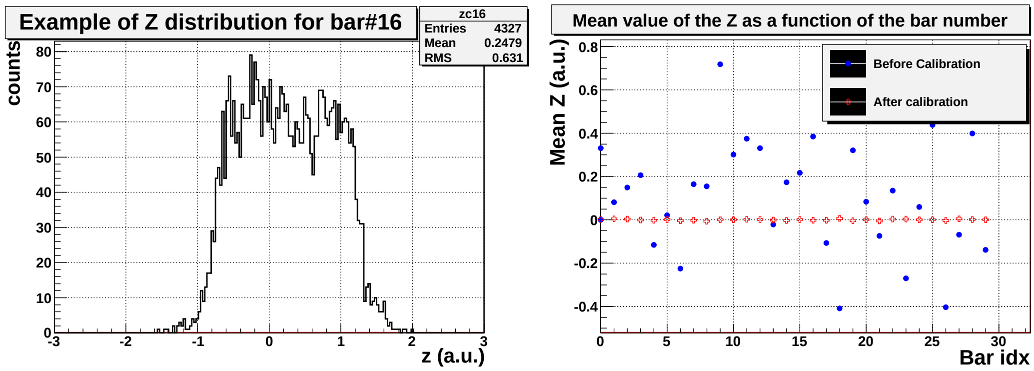

(a) (b)

Figure 8.3: (a) Example of a Z distribution as obtained by the charge asymmetry; (b) distribution of the mean of the distribution before and after the calibration.

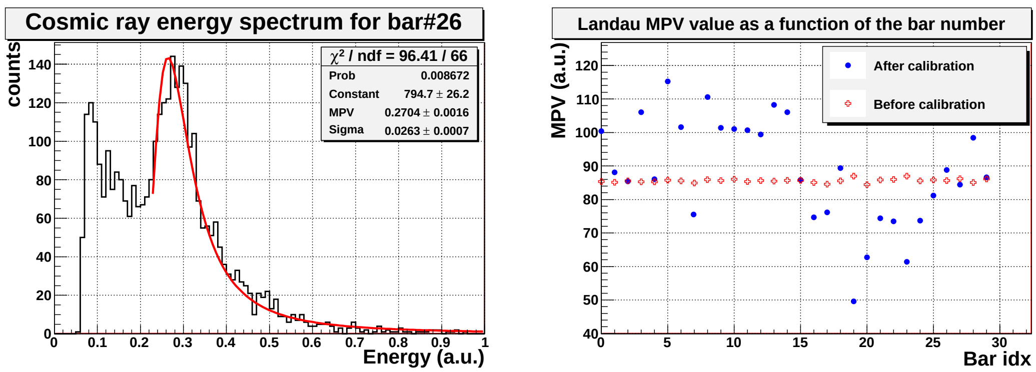

(a) (b)

Figure 8.4: (a) Example of the energy distribution in case of cosmic ray events; (b) distribution of the MPV of the Landau curve before and after the calibration.

the logarithmic ratio of the TRG waveform pulse height as a function of the offline reconstruction. This distribution has been sliced in the 8 online z sectors and the distribution of the waveforms height pulse in the 8 slices is studied. The LUT is filled with the pulse height values in the 8 different slices.

Figure 8.5 shows that this method returns an online resolution equal to 7.2 cm.

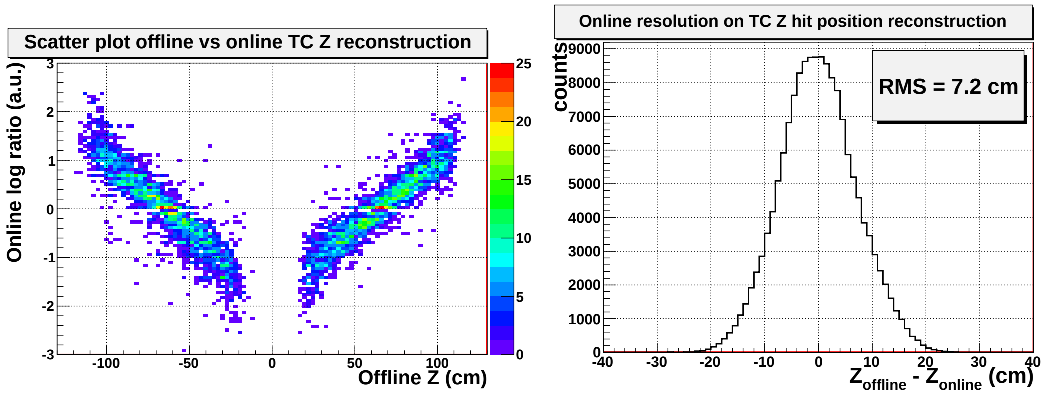

(a) (b)

Figure 8.5: (a) Pool distribution of online Z measurement with respect to the offline one; (b) example of the scatter plot for bar #27 of the online recognized Z index and the offline measurement.

8.1.3 LXe-TC online time offset

The online time reconstruction is based linear interpolation of the rising edge of LXe and TC PMT waveforms. The algorithm selects the LXe waveform belonging to the inner face with the largest pulse height and the TC ones connected to the hit bar, see section 5.1.1. The measured values need to be compensated for the relative offsets, due to both cables and different algorithm latencies. To determine these time offsets, we exploits the simultaneous γs from the Boron nuclear reactions described in section 3.3.3. This provides a fast and simple set of coincident events to study the relative timing of the two detectors. The resulting distribution for the online time difference is shown in Figure 8.6.

This method gives indicates that the online resolution on $\Delta T_{e\gamma}$ to be better than 4 ns, while the offset is $\approx$ 29 ns. The measurement of the relative offset allowed us to center a 20 ns wide time-coincidence window, with a foreseen efficiency $\varepsilon_{\Delta T} \geq 99\%$.

8.1.4 Direction match table construction

The direction match table selects roughly collinear events by connecting the LXe online estimator for the γ direction with the a region of possible positron impact points in the TC surface. In the MEG detector there are no back to back events to be used for a characterization of this table, thus we have to benefit from the Monte Carlo simulation.

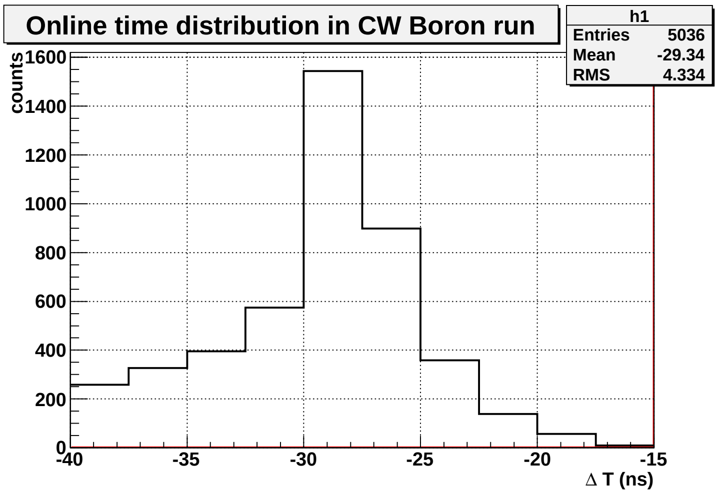

Figure 8.6: Online time spectrum in a $^{12}C^{*} \to {}^{12}C\gamma\gamma$ run.

The official track reconstruction code was not available before the end of the data taking. For this reason the direction matching table was set up only on the generated signal events and not on the reconstructed Monte Carlo events. The validation of the table was therefore delayed to the end of the data taking period when reconstructed Monte Carlo events were available.

We carried a generation of a $\mu \to e\gamma$ signal Monte Carlo. The table is constructed by selecting the LXe PMT collecting the highest amount of light and searching the impact point of the companion positron in the TC surface; only positrons preserving a momentum ≥ 45 MeV/c before impinging of the bar surfaces are selected. Figure 8.7 (a) shows and example for PMT number 54, the most probable impact region is smoothed by the multiple scattering effect . The positron impinging points are accumulated in TC pixels whose dimensions are the physical bar dimension in the φ direction and a slice of 10 cm in the z direction. The TC pixels are ordered by fraction of collected positrons and then added up to form the TC regions of impacts. The region loaded on the LUT is the first with a positron collection efficiency exceeding 95%.

Figure 8.7 shows three entries of the direction match table. Because of the selection on the positron momentum at the TC bars, the regions on can be not simply connected. The materials in the COBRA volume in between the positron tracker and the TC intercepts part of the positrons, inducing shadows on the TC surface. The major contribution to this inefficiency are the DC signal cables passing in the upper part of the COBRA volume. However all the TC inner surface is covered when the entries of all LXe PMTs are superimposed, the reported example on PMT #103 is chosen because it enhances this shadow effect.

Effect of direction match selection on MEG data

The distribution of gamma on the inner face of the LXe calorimeter in a MEG run turned out to be not uniform as shown in Figure 8.9 (a). This behavior is an effect of the direction match

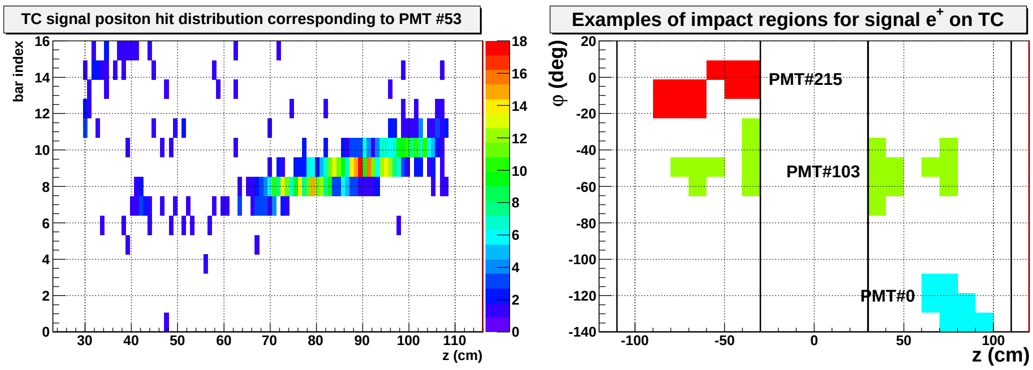

(a) (b)

Figure 8.7: Direction match table set up: (a) an example of signal positron impact region on TC; (b) TC 95% probability region in case of γ direction in coincidence with PMT #0, #103 and #215; the TC hit is defined by a pixel which dimensions are the bar width in the φ direction ($\approx 10°$) and a slice 10 cm wide in the z direction.

selection.

The geometrical acceptance of the TC bars for Michel positrons is not uniform, the first bars have an higher acceptance with respect to the others (Figure 8.8 (a)), while the gamma distribution when acquired using only the γ energy released condition is rather uniform as shown by Figure 8.8 (b). The MEG trigger selects accidental background events, the event distribution is given by the relative probability of firing one of the entries of direction match LUT. It is then biased by the asymmetric positron distribution on TC.

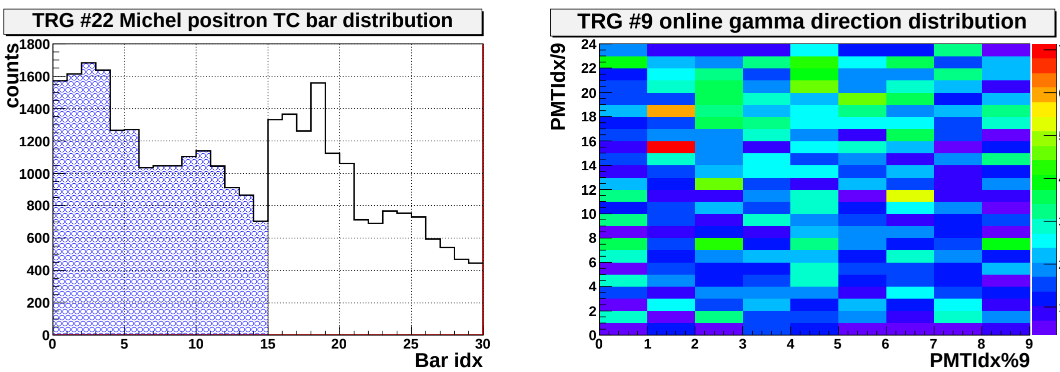

(a) (b)

Figure 8.8: Hit distribution of positrons in TC (b) and gamma in the LXe (a) in the minimum bias trigger sample; the filled part of left plot is the TC downstream sector.

An example of this distribution is reported in Figure 8.18 (b). This TC bar occupancy can be projected back to the LXe inner face by means of the direction match table. Each entry in the TC distribution defines, with its weight, a set of PMT indexes on the LXe surface, the result of this back projection is reported in Figure 8.9. It is in good agreement with the corresponding distribution taken with MEG trigger, this in one side demonstrates the assumption that the gamma distribution is biased by the Michel positron on TC, and on the other confirms that the direction algorithm works properly.

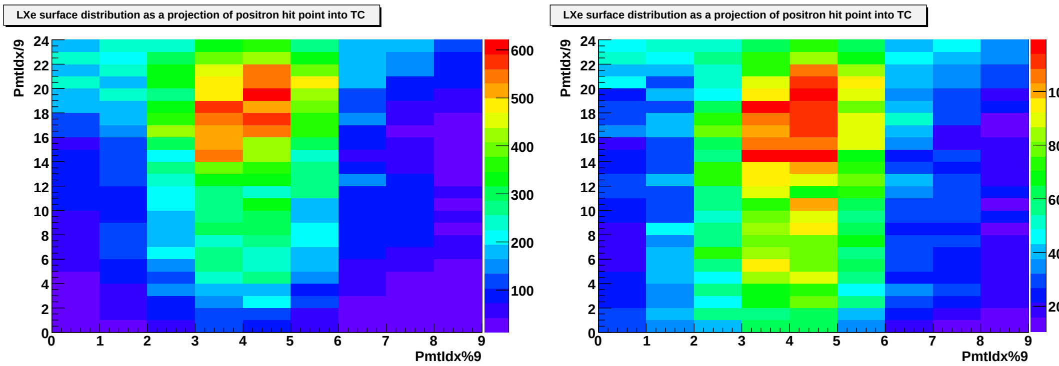

(a) (b)

Figure 8.9: Projection of TC hits on LXe surface using Direction Match table in case of MEG run (a) and TC alone (b).

8.1.5 MEG trigger

The definition of all the trigger parameters and LUTs required almost one month of work. In particular the last week before the beginning of the official data taking was dedicated the refinement and check of the trigger calibration constants.

The trigger MEG threshold applied are summarized in Table 8.1. Figure 8.10 shows a typical MEG triggered event display.

Observables	**Threshold**
E_γ	> 40 MeV
$\|\Delta T_{e\gamma}\|$	≤ 10 ns
$\Delta\theta_{e\gamma}$	Monte Carlo based LUT

Table 8.1: MEG trigger conditions summary.

8.2 Simulation

The firmware simulation is a mandatory debugging method. It can be used to check the logic of the selection algorithms, to measure the signal latencies, to control signal logic and polarities and

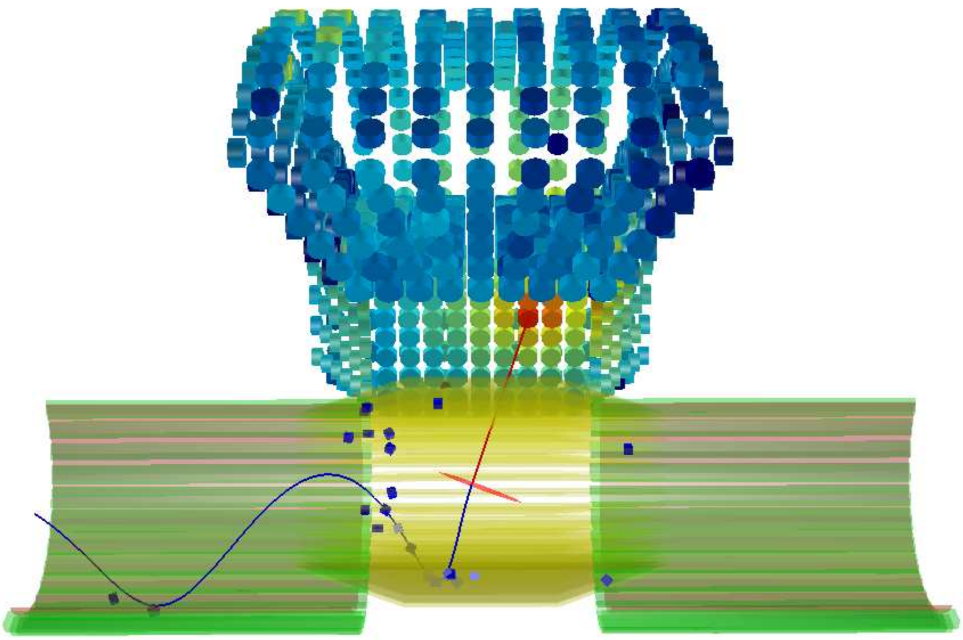

Figure 8.10: Event display of a MEG trigger event.

whatever is needed. The Xilinx ISE 6.03 package provides a logic simulator to check the effective functionality of the code, however it is rather difficult to simulate the whole trigger system firmware with that tool. The Xilinx simulator requires the user to feed in the status to all input signals for each clock tick with an unworthy and slow manner. The idea of this logic simulator is to fix possible logic mistakes and check critical signals synchronization but it is almost impossible to reproduce all the possible input line conditions. It is then useful mostly to control small routines dedicated to the control signal hand-shaking, usually characterized by complex combinatorial logic sequences. We used this tool only to check small, but critical, parts of the code, as for example the BUSY signal hand-shaking logic. The firmware simulation is demanded to a custom C++ dedicated code.

The C++ simulation program receives as input the trigger system waveforms as stored in the trigger buffers and applies on them all the operations implemented into the FPGA firmware. At first the baseline value is subtracted, then the calibration LUT is simulated and then, depending on the input type, all the online observables are reconstructed. The calibration constants and all the threshold referring to all the implemented algorithms can be read out directly from the online data base attached to the data or they can be varied *ad hoc* by the user.

The implementation of the selection algorithms is easier in C++ with respect to the schematic language and more under control. Figure 8.11 shows the comparison of the online E_γ waveform read out from the trigger memories (labeled as firmware waveform) and the output of the C++ simulator; note that they agrees in the baseline value, in the peak position and the pulse height. This means that the implement logic works properly and operates the same algorithms it was demanded for. This is also evident in Figure 8.12; it shows the 17.6 MeV line spectrum as reconstructed by the online by the trigger system and the output of the C++ simulator. The agreement between the simulator output and the firmware one is better than 99.5%.

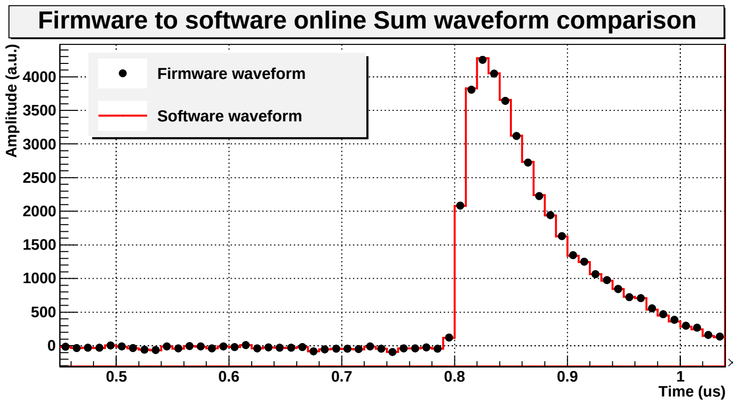

Figure 8.11: Comparison between the online LXe energy estimator waveform (black dots) with the output of the trigger simulation code (red line).

We checked the TC bar hit multiplicity evaluation, see Figure 8.13. It is performed by a LUT whose input is a word coding the positron hit pattern in the TC bars, see section 5.1.2. The agreement is better than the 99%, the small difference is related to the *double* to *integer* rounding in the C++ code that does not reproduce exactly the firmware.

A part from minor incongruences the simulator is capable to reproduce the firmware output, thus it can be used as a powerful probe to investigate the algorithm performance and study possible modification with no DAQ interference. During the physics data taking it is important to use as much as possible the beam time, a modification of the trigger system introduces dead time that can be from few minutes, in case of calibration factor modification, up to one hour if a new version of the firmware is downloaded in the FPGAs. If the modification turns out to be wrong it is necessary to switch back to the previous configuration. By using the “offline” analysis we can perform a detailed test of the modification.

For instance the simulator has been used to define and check the bit truncation range for the TC PMT waveform in the Z evaluation algorithm, see section 5.1.2. We also exploits it in the

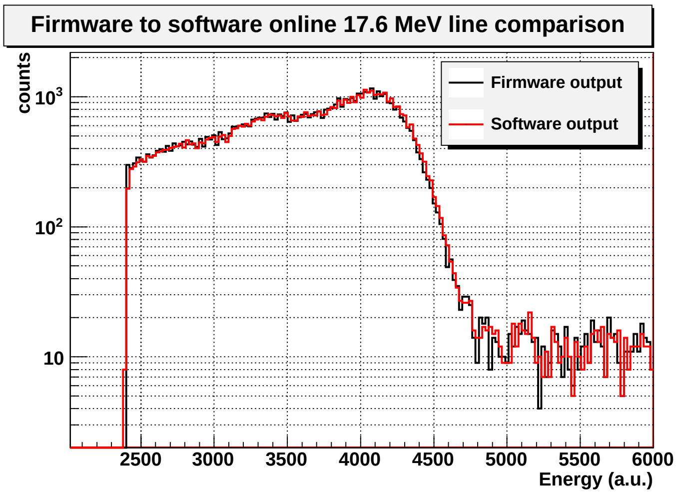

Figure 8.12: Comparison of the online 17.6 MeV energy spectrum with the output of the trigger simulation code.

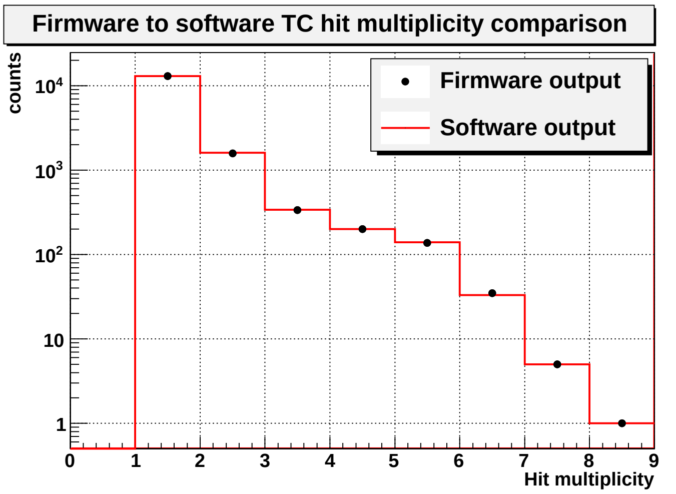

Figure 8.13: Comparison of the online TC hit multiplicity spectrum with the output of the trigger simulation code.

calibration of the TC trigger channels presented in section 8.1.2.

It was also used to check the stability of the E_γ resolution as a function of time. A modification of trigger channel calibration constants needs an energy calibration run, typically a CW run at the Li energy excitation, to check the energy scale and, if needed, modify the thresholds. This delicate operation has to be performed only when necessary. We compared the online resolution at 17.6 MeV as a function of time to the simulator output exploiting the daily gain calibration constants. The online E_γ resolution turned out to be not sensitive to the daily fluctuations of the LXe PMT. We decided to modify the trigger calibration factors if and only if an adjustment of the

PMT HV is required. It never happened during the RUN2008.

The C++ interface will be adapted to process the Monte Carlo waveforms providing a the trigger simulation on simulated events.

8.3 System monitoring

The trigger system generically selects in real time candidate events, but it can also be considered as:

1. a digitizing system;
2. a FPGA based analysis tool;
3. a multilayer system based on LVDS data transfer.

A dedicated set of inspection tools have been prepared to check and improve the functionality of the system.

8.3.1 Front end electronics

The trigger system has got waveform digitization capabilities, the functionality of all the channels has to be carefully checked, a loss of channels would lead directly to a reduced trigger efficiency.

Each Type1 electronic channel is provided by a dedicated scaler implemented on the FPGA to count the signal rate. A graphical panel displays in real time the signal rate of each trigger channel and it is updated every 30 s. The panel is shown in Figure 8.14.

The signals from LXe lateral faces are analogically summed by the splitter boards and digitized by the trigger system through the Type1, while the single channel output is received by the auxiliary digitizing system, the Type3 system as described in section 6.2 and 6.5. The scatter plot of the Type1 recorded charge versus the sum of the correspondent 4 Type3 channels is an easy and fast way to detect problematic channels. An example of this plot is reported in Figure 8.15. It plot is automatically generated $\approx$ 15 minutes after the end of the run to be inspected by the shift crew.

8.3.2 Synchronization and LVDS transmission

Synchronization The trigger system is arranged in a three layer structure, the first one is composed of 40 boards, the second of 6 boards and the last of 1. The whole 47 boards, are synchronized by the control signals distributed by the Ancillary system. The time difference between the detection of the photon and the positron is one of the discriminating variables of the MEG signal search, thus a common time reference for all the boards is mandatory.

All the trigger system boards are provided by a 20 MHz reference clock generated by a stable oscillator and distributed through a low jitter fan outs of the Ancillary system, see section 6.4. The reference clock is received individually into a PLL [85] and multiplied by a factor five in phase with

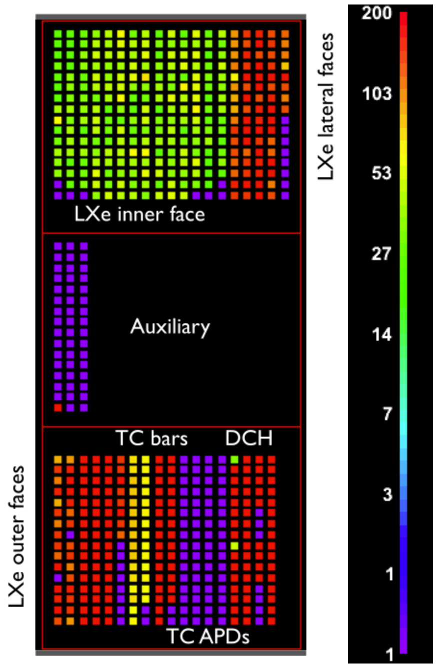

Figure 8.14: The "RateMeterTab", each button is a Type1 channel and its color indicates the rate. The violet buttons are not connected channels for LXe and TC bars detectors, while TC APDs were switched OFF and some DCH channels were not working; on the right is reported the chromatic scale, it is in kHz.

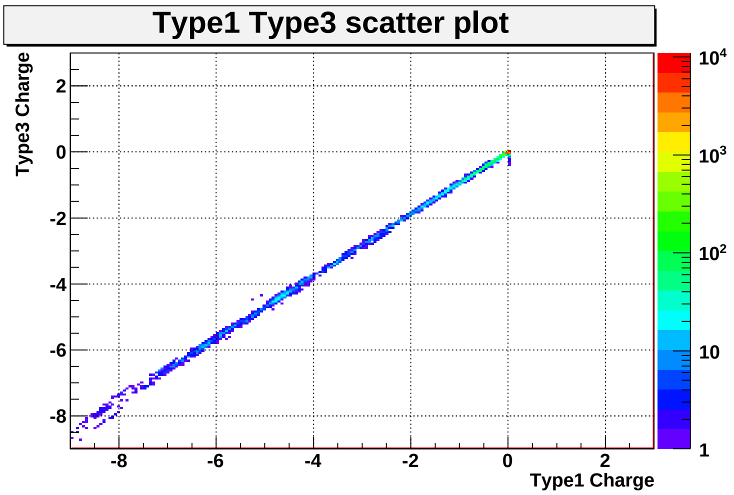

Figure 8.15: Scatter plot of LXe Type1 lateral face channel charge versus the sum of the correspondent Type3 channels.

the carrier signal (section 6.2 and 6.3). Finally the clock signal can also re-phased with respect to the carrier signal to correct for the time propagation of the signal in the Type1 and Type2 boards.

This scheme is also possible for Type3 boards, but in that case the system synchronization is not an issue.

The cycle memories hosted by the FPGAs are addressed by cyclic counters that are all reset by the sync signal, see section 7.1. The cyclic address counters are stopped synchronously by each trigger signal. The stop address value can be read out and compared. Figure 8.16 shows a graphic display of the synchronization status. In case of failure an alert is issued and the run is immediately stopped.

The system synchronization needs to be checked after firmware modifications. The physical track length of the control signals into the FPGA is not bounded in the firmware compilation and so it can differ from one version to the other; the difference can be up to 1 ns large enough to spoil the system synchronization.

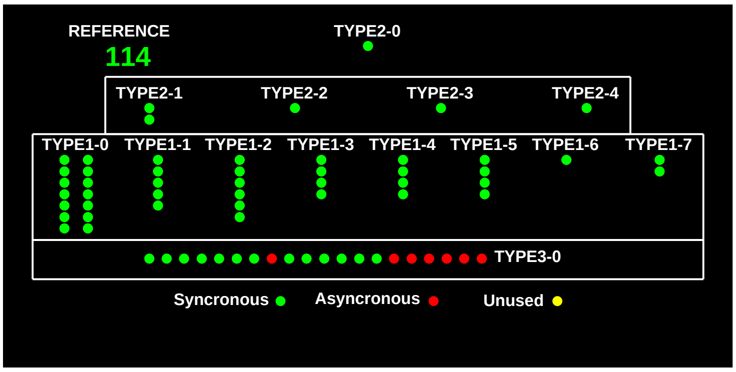

Figure 8.16: Synchronization monitor of the trigger system; a green circle means that the board is synchronous with respect to the reference, read means non-synchronous.

LVDS transmission The correct transmission between consecutive layers of the trigger system is demanded. The 48 bits transmitted data are recorded on cyclic memories just before the LVDS transmission on the source board and right after the reception on the target board, as shown in Figure 8.17.

In case of pedestal events, always acquired at ≤ 1 Hz in physics runs, all memories are downloaded and recorded to disk. The *eventbuilder* task running on the online computers compares the memories belonging to the transmitter and receiver boards: in case of incongruence the run is stopped and the synchronization signal is set again. The malfunctioning can be due to cables unplugged, or a broken transmitter/receiver or a time mismatch in the transmission line. So far this problem occurred only because one of transmitter chip broke and had to be replaced with a new one.

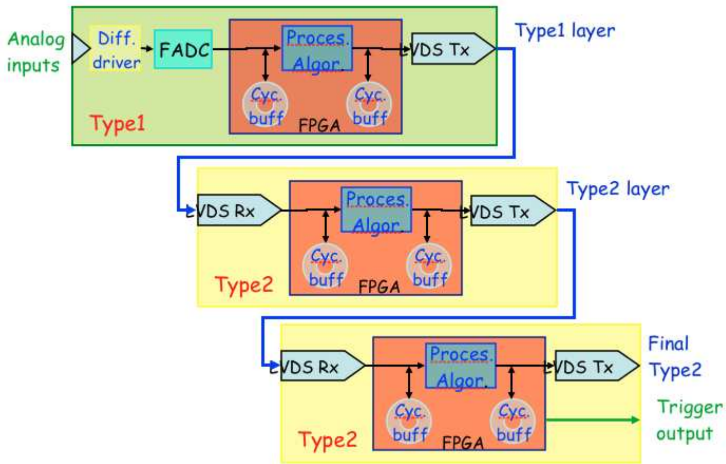

Figure 8.17: Scheme of LVDS data transmission and record on dedicated memories.

8.3.3 Algorithm

To check the correct functioning of the algorithms implemented in the FPGAs, the status of all the relevant variable are stored in the cyclic buffers and read out at each event, the algorithm flow can be traced on each layer of the system. Some examples of the relevant variables are the LXe partial sum waveform, the LXe and TC time and hit coordinates both for the TC and the LXe. In particular the final Type2 buffer register have the information belonging to the online algorithm results.

A few minutes after each run, a set of summarizing plots are ready for operator inspection to check if the algorithms are working properly and if the threshold are correctly set. Figure 8.18 shows some examples. In Figure 8.18 (a) the online energy spectrum is shown, this can be used to check the threshold and the spectral shape, the pre-scaled α events around 1800 a.u. are clearly visible; Figure 8.18 (b) reports the distribution of the events on the TC, the distribution is automatically compared to the reference one.

8.3.4 The TGEN waveform

32 different trigger algorithms run in parallel on the MEG detector data flux. The trigger types are order in a priority stack being the highest priority the MEG trigger (trigger #0) and the lowest one the random trigger (trigger #31). The stop signal is issued when one of the enabled selections satisfies the online requests.

The system provides a 32 bit word, namely the TGEN, reporting every 10 ns the output of the 32 selection algorithms. With the same ordering of the priority stack, the 32 bits status refers about the occurrence of an event in the detector. The algorithms are continuously executed independently from the system RUNMODE status (see chapter 7), and are used for trigger rate measurements.

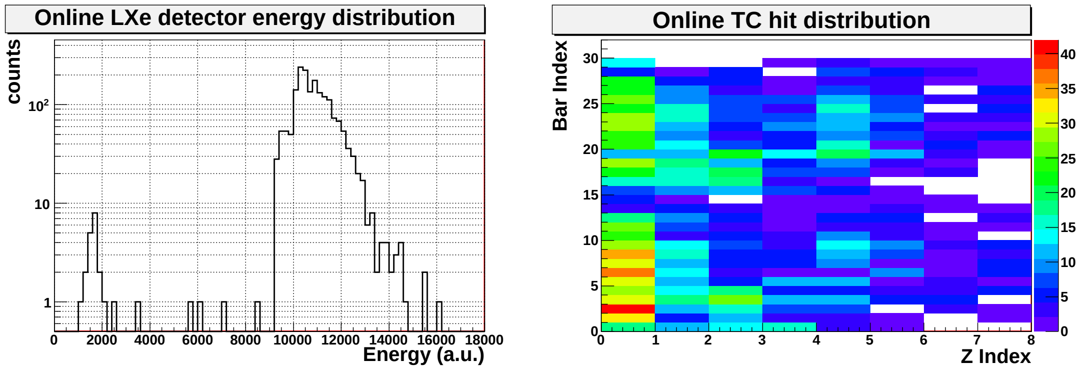

(a) (b)

Figure 8.18: Example of control plots for the data quality check.

We exploit the TGEN information to inter-calibrate the different trigger latencies and to control the implemented algorithm execution. Figure 8.19 shows the control monitor of the TGEN evolution with time, having in the x-axis the time in CLK ticks (10 ns) and in the y-axis the status of the 32 trigger algorithms. Looking at the trigger time position (around 85 CLK ticks) and at the triggers issued (colored in red and green) we recognize that this event is labeled as a the MEG trigger (trigger #0). As expected the relaxed condition MEG triggers (trigger #1, 2, 3) are simultaneously fired, as well as the radiative decay triggers (trigger #4, 5). The MEG selection algorithm requests a energy deposit in LXe calorimeter over threshold and a hit in the TC, thus also the corresponding single detector triggers (trigger #9 and 10 for LXe and trigger #22 for TC), while the DC related triggers (trigger #17, 18 and 20) are delayed by $\approx$ 100 ns.

8.3.5 DAQ

There are several DAQ configurations depending on the recorded data type. They can be grouped in two basic DAQ configurations: the physics data and the calibrations, differing for the enabled triggers and the pre-scaling values.

In case of MEG physics data taking, the DAQ is configured to select for candidate $\mu \rightarrow e\gamma$ events together with pre-scaled calibration data. The live time of the DAQ is requested to be over 80% then the pre-scaling values of calibration triggers is set accordingly.

On the other hand dedicated calibration runs are selected as fast as possible, saturating the capability of the DAQ. The pre-scaling values are chosen to satisfy the required statistical accuracy of the acquired calibration trigger, saturating the bandwidth.

An online graphical panel, reported in Figure 8.20, displays in control room the summary of the relevant DAQ numbers.

In this display the event rate for each individual trigger is shown, together with the dedicated fraction of DAQ and the number of acquired events. Those values facilitates the pre-scaling set

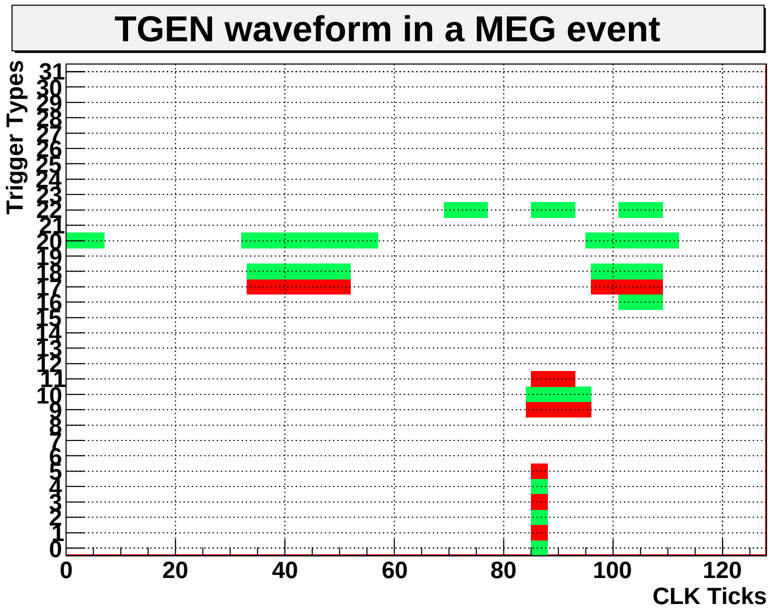

Figure 8.19: Online monitor of the so-called TGEN waveform; each row refers to a trigger type, a colored region indicates the event type recognition.

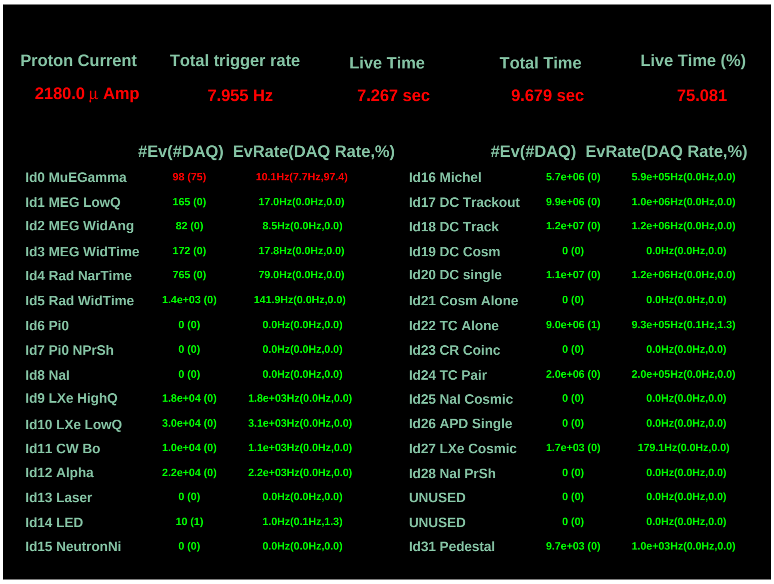

Proton Current	Total trigger rate	Live Time	Total Time	Live Time (%)
2180.0 µ Amp	7.955 Hz	7.267 sec	9.679 sec	75.081

	#Ev(#DAQ)	EvRate(DAQ Rate,%)		#Ev(#DAQ)	EvRate(DAQ Rate,%)
Id0 MuEGamma	98 (75)	10.1Hz(7.7Hz,97.4)	Id16 Michel	5.7e+06 (0)	5.9e+05Hz(0.0Hz,0.0)
Id1 MEG LowQ	165 (0)	17.0Hz(0.0Hz,0.0)	Id17 DC Trackout	9.9e+06 (0)	1.0e+06Hz(0.0Hz,0.0)
Id2 MEG WidAng	82 (0)	8.5Hz(0.0Hz,0.0)	Id18 DC Track	1.2e+07 (0)	1.2e+06Hz(0.0Hz,0.0)
Id3 MEG WidTime	172 (0)	17.8Hz(0.0Hz,0.0)	Id19 DC Cosm	0 (0)	0.0Hz(0.0Hz,0.0)
Id4 Rad NarTime	765 (0)	79.0Hz(0.0Hz,0.0)	Id20 DC single	1.1e+07 (0)	1.2e+06Hz(0.0Hz,0.0)
Id5 Rad WidTime	1.4e+03 (0)	141.9Hz(0.0Hz,0.0)	Id21 Cosm Alone	0 (0)	0.0Hz(0.0Hz,0.0)
Id6 Pi0	0 (0)	0.0Hz(0.0Hz,0.0)	Id22 TC Alone	9.0e+06 (1)	9.3e+05Hz(0.1Hz,1.3)
Id7 Pi0 NPrSh	0 (0)	0.0Hz(0.0Hz,0.0)	Id23 CR Coinc	0 (0)	0.0Hz(0.0Hz,0.0)
Id8 NaI	0 (0)	0.0Hz(0.0Hz,0.0)	Id24 TC Pair	2.0e+06 (0)	2.0e+05Hz(0.0Hz,0.0)
Id9 LXe HighQ	1.8e+04 (0)	1.8e+03Hz(0.0Hz,0.0)	Id25 NaI Cosmic	0 (0)	0.0Hz(0.0Hz,0.0)
Id10 LXe LowQ	3.0e+04 (0)	3.1e+03Hz(0.0Hz,0.0)	Id26 APD Single	0 (0)	0.0Hz(0.0Hz,0.0)
Id11 CW Bo	1.0e+04 (0)	1.1e+03Hz(0.0Hz,0.0)	Id27 LXe Cosmic	1.7e+03 (0)	179.1Hz(0.0Hz,0.0)
Id12 Alpha	2.2e+04 (0)	2.2e+03Hz(0.0Hz,0.0)	Id28 NaI PrSh	0 (0)	0.0Hz(0.0Hz,0.0)
Id13 Laser	0 (0)	0.0Hz(0.0Hz,0.0)	UNUSED	0 (0)	0.0Hz(0.0Hz,0.0)
Id14 LED	10 (1)	1.0Hz(0.1Hz,1.3)	UNUSED	0 (0)	0.0Hz(0.0Hz,0.0)
Id15 NeutronNi	0 (0)	0.0Hz(0.0Hz,0.0)	Id31 Pedestal	9.7e+03 (0)	1.0e+03Hz(0.0Hz,0.0)

Figure 8.20: Online method to check the DAQ set up looking at: single trigger rate, amount of DAQ dedicated to each selection, lifetime and proton current.

up. It also indicated the total time of the data taking together with the live time and the live time fraction. Finally the proton current of the main accelerator is also shown, to have an immediate cross check of the individual trigger rate values.

Chapter 9

The α trigger

α events are collected in dedicated runs without the beam to calibrate the PMT quantum efficiencies and to measure the LXe attenuation length; on the other hand the α events collected during the physics data taking, when muons are stopped on the target, allows the control of the LXe detector stability.

The α online selection is based on pulse shape discrimination of LXe waveforms, as described in section 5.1.4; it is shown that α and γ events can be distinguished efficiently by means of a Q/A discrimination. Thus the online selection algorithm calculates the charge and the pulse amplitude and, by means of a dedicated LUT, operates the Q/A ratio. To minimize the α selection latency the algorithm operates on a limited number of PMTs placed around the source wires. The cabling of the PMT to the trigger system was designed carefully: the 32 PMTs placed around both anchor points of the α source wires are received inside the same trigger board. The cabling scheme is reported in Figure 6.7. The pulse shape discrimination is performed on the sum of 32 LXe PMTs, 16 on the upstream lateral face, and 16 on the downstream.

The algorithm searches for a waveform over a defined threshold and operates a simple peak finding algorithm: it requests a sample over threshold larger than the preceding one and larger or equal to the subsequent one. Once the peak is found the charge is evaluate on 8 consecutive samples starting from the sample before the peak. The peak amplitude and charge values are then truncated to fit the LUT memory capability, see for reference section 7.2.2. The output of the LUT is a single bit indicating if the event is recognized as α or not, this is transmitted to the last Type2 board that generates the stop signal. There is a dedicated trigger board per each wire and so we can discriminate on the wire number.

The following sections present in detail the firmware implementation, its calibration and the results. This represents the only fully described algorithm implementation. The algorithm described here has some relevance for future experiments searching for dark matter candidates with Liquid Xe calorimeters.

9.1 Firmware

The algorithm could be entered in the synthesizer program which prepares the FPGA configuration file (bitstream) in behavioral language or in schematic. This algorithm was entered in schematic similarly to the most part of the trigger code and it is shown in Figure 9.1.

Eight consecutive waveform samples are stored in a pipe line made of 8 register in cascade; the samples are transferred along that pipe line until the peak finding condition is issued. When it happens the register content remains stable for the time needed for the algorithm to be executed. The peak finding algorithm is programmed by means of three 16 bit signed input binary comparators. The output of the comparators is sent to a three inputs logic port AND. When the peak finding condition is issued the registers are disabled for 8 CLK ticks, a time even longer than the charge integration time. The integrated rate in the LXe calorimeter is $\approx\ 3 \cdot 10^4$ Hz, thus the pile up probability in 80 ns is negligible. In parallel the peak value is kept stable waiting for the charge to be computed. The charge integration takes advantage of binary 16 bits adders in a three step cascade.

This logic returns the amplitude and the charge of the waveform and a bit with the peak finding algorithm status. This bit is used to enable the LUT programmed to operate the pulse shape discrimination. As explained in section 7.2.2 the memory capability of the RAM inside the FPGAs is limited, the output of the LUT is a single bit, so we have to arrange in the 14 bits input bus both amplitude and charge information. We decided to reserve 8 bits for the charge values and 6 for the amplitudes. After the adding chain the charge word size is 18 bits long, the amplitude is 16 bits hence, a truncation is needed. The truncation algorithm is reported in Figure 9.2.

The logic of the word truncation is the following: if the sample is lower than 0 then the truncated word is 0. This is obtained by looking at the sign bit and sending it at the Multiplexer input. If it is high the associated outputs are connected to the FB(x:0) word, x = 5, 7, in which all the bits are 0. However if the charge (or amplitude) value is higher that the maximum available within the truncated word bit range, the corresponding maximum value (all bits equal to one) passes; note that the truncated word is unsigned. This is obtained by sending all the most significative bits above the truncation range to the inputs of a logic OR port. If the aforementioned condition is verified, the OR output is high. Finally, if the sample value is covered by the truncation range, a simple bit truncation is performed. The data are finally sent to the LUT which is transferred through the trigger system to the final Type2 board.

The bit range truncation and the pulse shape discrimination operated by the LUT has to be carefully optimized on data.

9.2 Calibration

The real time α selection algorithm requires the definition of several conditions: the charge and amplitude bit truncation ranges, the pulse shape discrimination LUT configuration and the peak finding threshold optimization. As soon as the LXe detector has been operative the algorithm

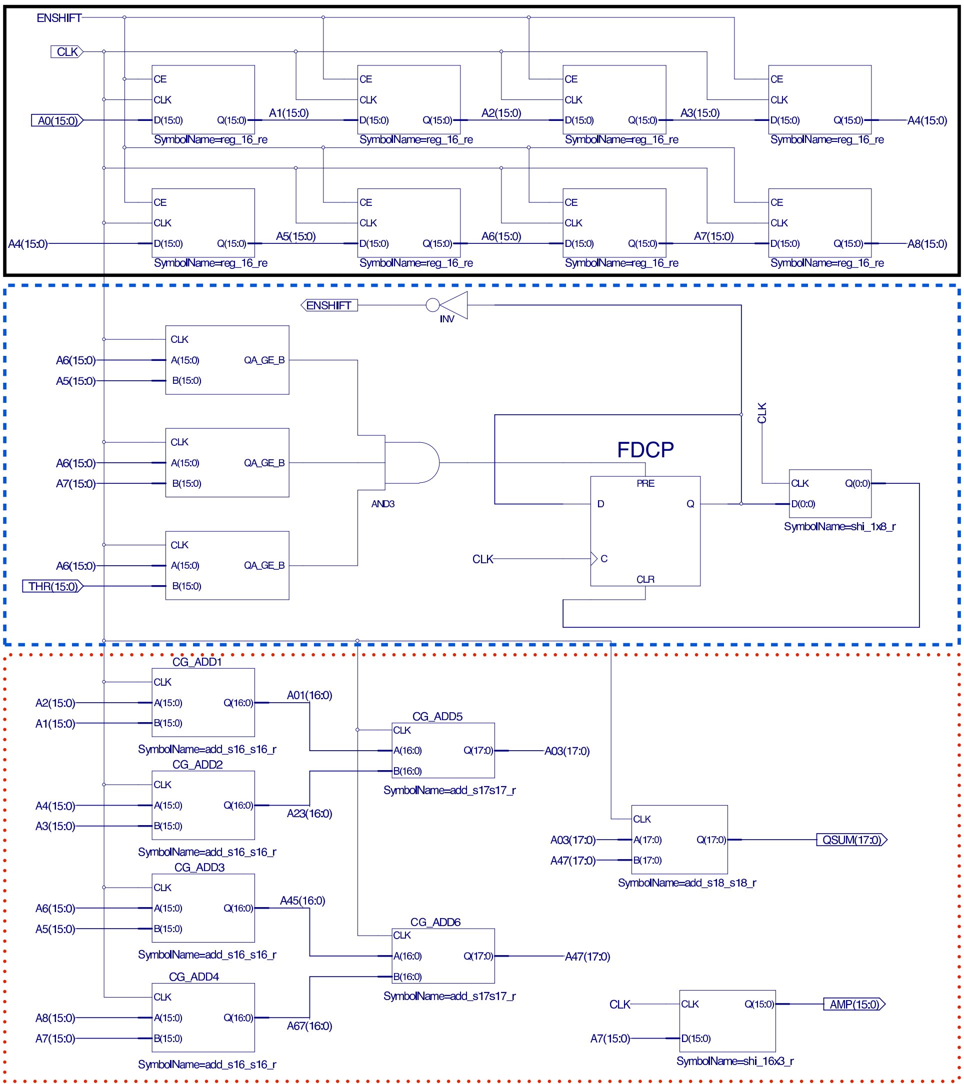

Figure 9.1: Peak finding and charge integration firmware; the uppermost black box (continuos line) is a pipe line of 8 registers used to store the samples used for the charge integration once the peak finding condition is issued, the central blue box (dashed line) contains the logic for the peak finding condition and finally the lowermost red box (dotted line) has the charge integration logic given by 3 steps of binary signed adders.

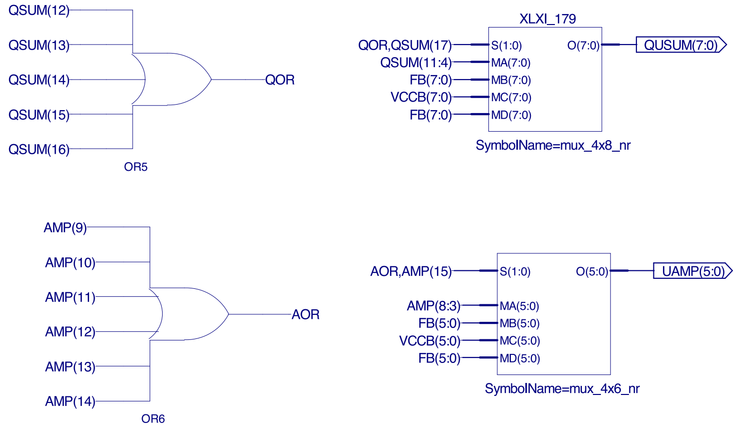

Figure 9.2: Firmware implementation for the word truncation algorithm, it is composed by a OR port in cascade with a multiplexer; the logic in asynchronous.

calibration was performed on real data.

In order to optimize the truncation bit range, the amplitude distribution in α events acquired with LXe alone trigger (trigger #10, see for reference Table 5.2) without the beam was studied. We tried several truncation range algorithm, we found that the most efficient is (8:3) for the amplitude and (11:4) for the charge. Figure 9.3 (a) shows the full resolution amplitude distribution for one of the PMT groups, 9.3 (b) is the same when the truncation is applied.

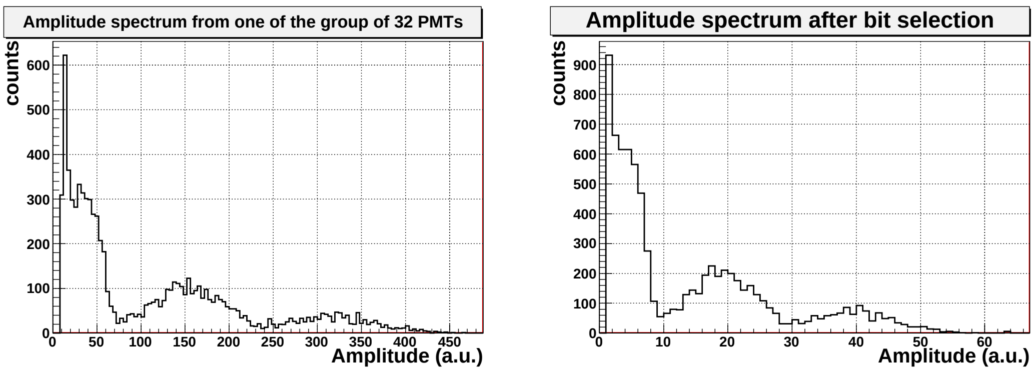

(a) (b)

Figure 9.3: Amplitude spectra from one of the group of 25 PMTs place around of the α wires before and after the truncation.

The α sources are deposited on 5 wires anchored to the lateral walls of the LXe calorimeter equally spaced along the wire. The source close to the detector walls are identified by the higher amplitude bump in the spectrum. The intermediate and the central sources are mixed in the bump centered at 150 in Figure 9.3 (a). The events with amplitude lower that 50 are from the α source deposited on the other wires. The same pattern is visible in the spectrum with the truncated amplitudes. It is evident that the truncation range is well centered around the region of interest. It is also important to notice that, despite the fact that only a part of the scintillation light is used by this algorithm, all the α sources are visible.

The crucial point of this algorithm is the LUT implementation, even in this case the LUT is defined and checked with real α and γ events. The waveform from the sum of the 32 PMTs signals around the wire is recorded into the output memories of the Type1 boards. It is used to compute the online amplitude and charge, by a simple C++ algorithm simulation. Figure 9.4 shows the scatter plot showing the charge as a function of the amplitude in a run with a mixture of α and γ, with the full resolution (a) and as seen by the online algorithm (b). The two populations are well divided both in the offline analysis and online algorithm.

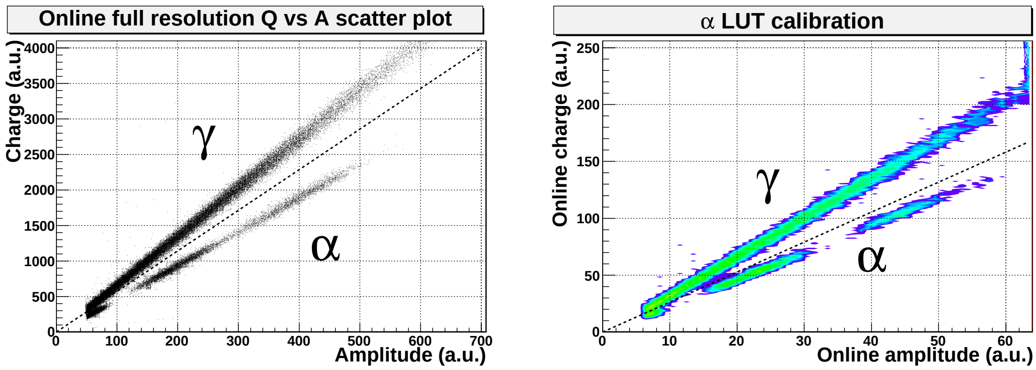

(a) (b)

Figure 9.4: (a) full resolution charge versus amplitude scatter plot; (b) the same using the online LUT variables.

The closer and the middle distance sources are clearly visible, the central one is rather mixed with the γ background.

The dashed line in Figure 9.4 divides the α-like from the γ-like events. The LUT has been programmed to select only the events having the Q/A ratio lower than 2.6 in the online units, the angular coefficient of the aforementioned dashed line.

9.2.1 Configurations

The peak finding threshold has to be to optimize the selection efficiency and the sample purity, taking into account the analysis needs.

The peak finding threshold results in an α energy deposit cut depending on the event position. Given the fact that the scintillation light is emitted isotropically, the amount of light absorbed by a PMT depends on the distance between that PMT and the event. In the algorithm is not applied a correction on the absorbed light with respect to the distance of the event, so the effective energy threshold is higher for α events emerging from the central source with respect to those from the lateral sources. Figure 9.5 shows the effective energy threshold as a function of the distance measured on data, it has the described $1/\mathrm{d}^2$ shape where d is the distance between the event and the PMTs.

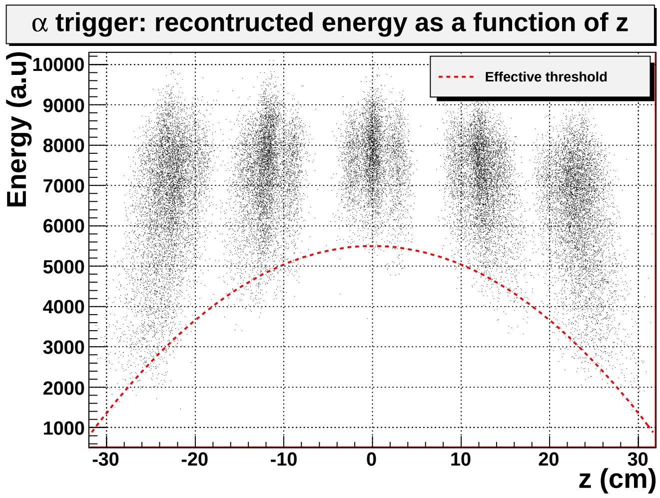

(a)

Figure 9.5: Effective peak finding threshold in energy as a function of the distance between the sources and the PMTs.

The PMT QE efficiency calibration is based on the comparison between Monte Carlo simulation and real data. Any online inefficiency has to be fine tuned in the MC data analysis to have a valuable comparison and it can introduce big systematics. It is then preferable to have the online efficiency as high as possible. For this reason the dedicated run are performed without the muon beam and with the peak finding threshold as low as possible. The value used is 50, to be compared with the Figure 9.4 (a) (x-axis).

On the other hand the energy spectrum of the α events can be used to measure if there is any shift on the energy scale induced by the beam related events. The mean DAQ rate dedicated to a pre-scaled trigger, such as the α trigger in physic runs, is $\approx$ 0.1 Hz, it is important to set the peak finding threshold that guarantees a sample purity higher than 80% without any alteration of the energy spectrum edge used as an energy reference. The threshold value used in this case is 120; this value cuts most of the low energy events emerging from the central source and, partially, from the intermediate one. The selection on the lateral sources in 100% efficient on all the energy spectrum. The high energy edge of the α spectrum is anyhow preserved for all the sources.

9.2.2 Remarks on LXe purity

The presented algorithm could not be efficiently used in 2008 because during the RUN2008 the LXe purity was not yet satisfactory. The Xenon suffered from some external contamination acting as a quencher for the higher τ scintillation process. It resulted in a shortening of the LXe waveforms, making the Q/A online discrimination not suitable. During the shut down in before 2009 run, the LXe purification was completed and Q/A was restored to the prototype measured values: $\tau_{\gamma,2008} \approx 30$ ns, $\tau_{\gamma,2009} \approx 44$ ns. The scintillation decay times and the absolute light yield for α events did not change.

Figure 9.6 (a) shows the difference in the Q/A spectrum for events acquired during the 2008 and during the 2009. The impurities affected only the slow component of the LXe scintillation processes, the α peak did not move at all. In Figure 9.6 (b) the α LUT calibration for 2008 run is shown. The separation between α and γ events is not clear like for 2009 run reported in Figure 9.4 (b). A tentative LUT would have efficiently distinguished only the two sources close to the detector lateral walls, and populating the cluster at online amplitude = 50 and online charge = 120 in Figure 9.6 (b). In 2008 the α and the γ populations can be efficiently distinguished only in the offline analysis.

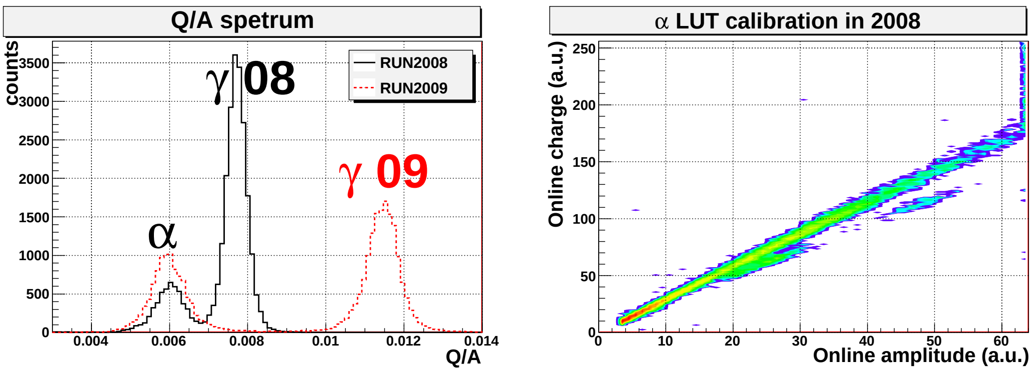

(a) (b)

Figure 9.6: (a) Q/A comparison between 2008 and 2009; (b) α/γ online separation.

The α events were recorded by switching off the beam and exploiting the LXe alone trigger by setting a very low threshold.

9.3 Results

Thanks the improved LXe purity, during the 2009 we succeeded in the online α selection in presence of the 200 times higher beam induced γ background. This was prepared with two different configurations, one with beam on and the second with beam off.

The LXe calibration measurements are performed in dedicated background free runs. In this configuration the peak finding threshold can be set as low as needed to achieve a full efficient selection. We were able to achieve $\varepsilon_\alpha \approx 100\%$.

On the other hand the possibility of acquiring α events in the same conditions as in the physic runs is important to keep under control beam related systematic effects. Section 10.1 shows that the LXe PMT gain is dependent from its mean anodic current. This was continuously monitored by mean of a very stable LED pulses, but, unfortunately, it could not be cross-checked by means of real events of well defined energy. This was done in 2009. The α trigger was added to the list of the pre-scaled calibration selections in the physics runs.

Despite the fact that the the low energy tail of the spectrum is deformed the edge shape can effectively used as an energy reference. Figure 9.8 shows the full efficient α energy spectrum (red dashed line) resulting from the low energy ("beam off" mode) peak finding threshold compared with the online α trigger acquired with the "beam on" threshold but with the beam shutter closed (black continuos line). The blue (dotted line) histogram shows the global gain shift measured with α events acquired with the beam, note that the blue histogram is not normalized to the other two. The gain shift, reflected in a energy spectrum shift, is evident. α events with the beam are a nice tool to check the performance of the gain shift correction directly on data and to measure systematics uncertainties. The γ background events are also present in the long, but tiny, high energy tail. The performance of the detector coupled with the α trigger were remarkable: the purity of the α sample was equal to 80%, corresponding to a background rejection of a factor 10^3, and a mean efficiency of 87%. Figure 9.7 shows the typical α rings acquired in beam on condition with the α trigger.

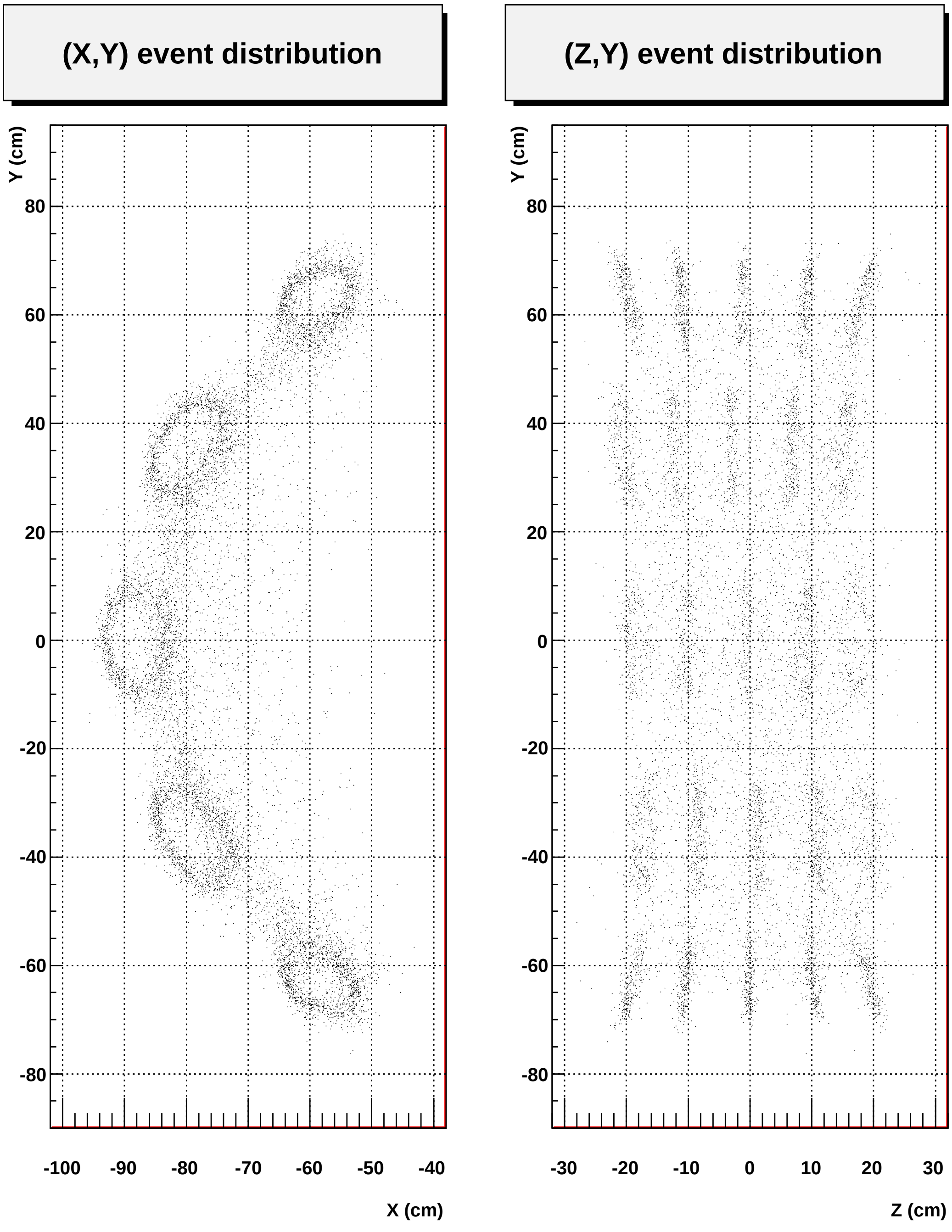

(a) (b)

Figure 9.7: LXe event distribution using the α selection during normal data taking; the typical α-rings are clearly visible.

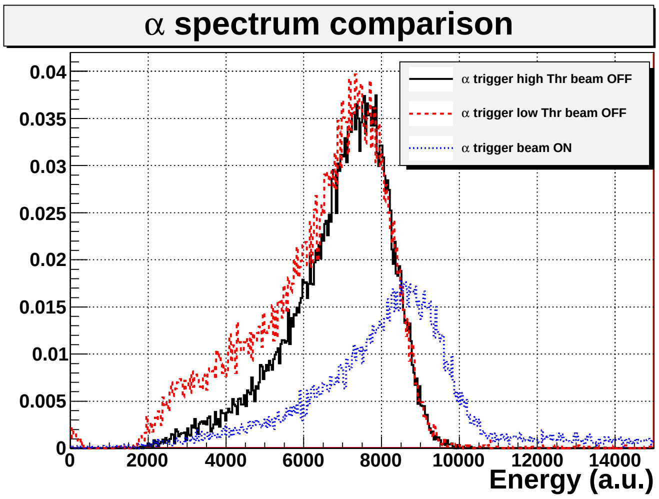

(a)

Figure 9.8: Comparison between α spectra biased by the online selection, note that the black (continuous) and the red (dashed) histogram are normalized, while the blue (dotted) is not.

Part IV

Physics Analysis

Chapter 10

RUN2008

The first physics run of the MEG experiment was performed during the 2008. Starting from the description of the detector performance we report the results of the run. Particular emphasis is given to the online selection efficiency evaluation, the experiment normalization calculation and the physics data analysis [91].

The RUN2008 started in the middle of July with a period of 2 weeks in which a large sample of positrons from normal μ decay (Michel positrons) was collect by the tracking system. Soon afterwards we switched to a full π^0 calibration in which the whole LXe inner face was scanned to study the detector performance at the signal energy. The run lasted $\approx$ 1 month and a half. At the end of the CEX experiment we switched to the MEG beam set up, in particular a week was dedicated to the MEG trigger set up. The signal search period started the 12th of September and ended the 17th of December. In the last week of the run we switched back to the CEX experiment to double check the LXe detector calibration factors.

The effective running time dedicated to MEG trigger was of about 50 days corresponding to $\approx 9.5 \times 10^{13}$ stopped muons in the target at a beam rate of 3.67 $\times 10^7$ μ/s and a muon stopping efficiency of about 82%.

One full day per week was dedicated to radiative decay runs. The goal of these runs was to check the experiment quality of identifying coincident events between LXe and TC, but also to show that the correlated background is at the expected level compared to the uncorrelated background. To limit the accidental background runs the beam intensity was lowered by a factor 10. During the 2008 data analysis we were able to show that the radiative decay peak in the relative timing emerges from the accidental background even in normal beam intensity conditions (Figure 11.4 (a)) and so we decided to skip this calibration run for the next physics runs.

The following sections present the status of the detectors during the run and their performance. The following items are discussed in details: the LXe PMT gain measurement and stability, the light yield monitoring, the DC stability and the hit reconstruction capability and finally the TC intrinsic time resolutions. The experimental observables resolutions are presented in chapter 13.

10.1 LXe detector

From a cryogenic point of view the calorimeter worked properly, there was no problem with the Xe liquefaction and the liquid transfer from the external tank to the detector. The total amount of dead channels was 5 on a total of 846 PMT installed, less than 1%. These dead channels were identified at the begin of the run with no recovering possibility. No electronic channel died during the run. The main issues on the LXe detector were related to the PMT calibrations and the LXe light yield monitoring.

The PMT gains are measured by means of a light emitter diodes system installed on the wall of the active detector volume. The calibration method is reported in section 3.3.3. Figure 10.1 shows the average LXe PMT gain as a function of the date. A twofold comment is mandatory. First of all the PMT showed a gain decrease, with an average value of the order of 1% in one month operation. This is not a issue for the experiment because on one hand there is still place to increase the PMT HV, and on the other the variation rate is not causing detector instability. A second unexpected behavior is a gain dependence on the average anodic current. This turned out while measuring the stability of the LXe detector as a function of the μ-stop rate on the target. The effect is visible in a set of measurements labelled with "Beam ON". They correspond to the gain measurement with LED while the μ beam is stopped on target. In Figure 10.2 (a) the average variation of the PMTs gain is shown while opening and closing the beam shutter. The asymptotic variation is of the order of $\approx$2%.

The gain variation has been individually studied for each PMT in order to apply the correct gain value as a function of the beam rate and the time elapsed since the last modification of the beam shutter (BS) position. The gain variation modeled by a multi-exponential function composed by three components: a fast one of the order of 10 s, a medium one in the interval 10$\div$100 s and a slow one of typically $\geq$ 100 s. In Figure 10.2 (b) an example of the fit is reported.

The PMT QE are estimated and constantly monitored by means of the point-like ^{241}Am α-sources deposited on thin wires stretched inside the active volume. If the PMT gain is known the QE is given by the ratio between the PMT charge obtained in simulation and the measured one for the α-sources seen by the PMT. At the beginning of the run, during the detector filling with liquid Xenon, a dedicated α run in cold gas Xe was performed. The Xe in gaseous phase does not suffer from any light attenuation nor for absorption or Rayleigh scattering so the MC simulation is easier and the QE efficiency determination more reliable. Figure 10.3 shows some examples of QE extrapolation.

The QE are then monitored in LXe by means of daily dedicated α run. The accuracy of the QE estimation is 10% equivalent to 1% uncertainty in the energy estimator resolution.

The LXe is a scintillation mean characterized by having a large light yield but stringent control of contaminants are necessary since the vacuum ultraviolet (VUV) scintillation light is easily absorbed by water or oxygen either at sub-ppm levels. The LXe is circulated in liquid phase through a series of purification cartridges, and in gas phase through a heated getter.

During the first part of the run the LXe light yield was slightly decreasing. During scheduled maintenance of the gaseous phase purification circuit, a damaged diaphragm was replaced. The gas

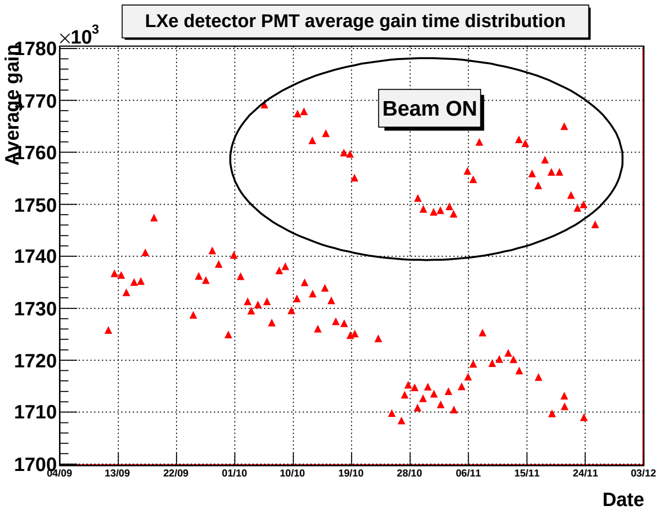

Figure 10.1: Average gain as a function of the date in the RUN2008; the effect of gain increase in with the beam shutter open is evidenced.

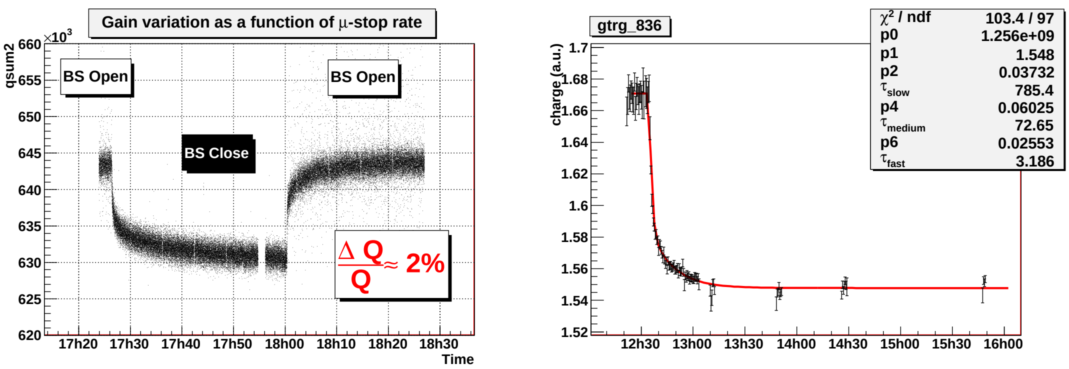

(a) (b)

Figure 10.2: (a) Gain variation after opening or closing the beam shutter (BS); (b) example of a triple exponential fit to extract time constants of gain variation for PMT #836 using the TRG digitizer.

purification was restored after the maintenance work. As reported in section 3.3.3 the light yield was continuously monitored 3 times per week by means of the 17.67 MeV Li peak. Figure 10.4 shows the number of photoelectrons given by the Li line as a function of the time. The light yield stopped decreasing, the maintenance operation corresponds to a big step in the light yield and the gas purification became effective. The calorimeter energy scale is corrected run by run following this light yield variation. The systematic uncertainty of this method is estimated to be $\approx 0.5\%$.

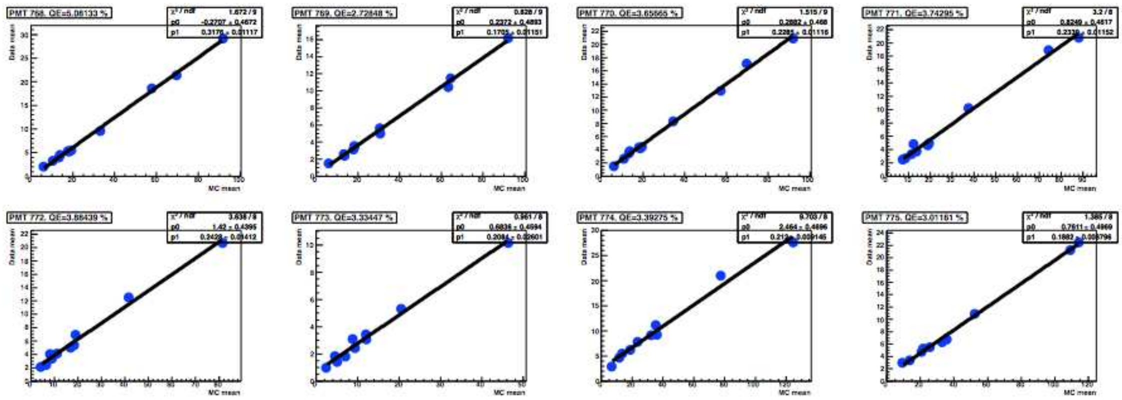

Figure 10.3: Example of quantum efficiency estimation for 8 PMTs in the run by using GXe data, in the x-axis there are the Monte Carlo predictions while in y-axis the measured values.

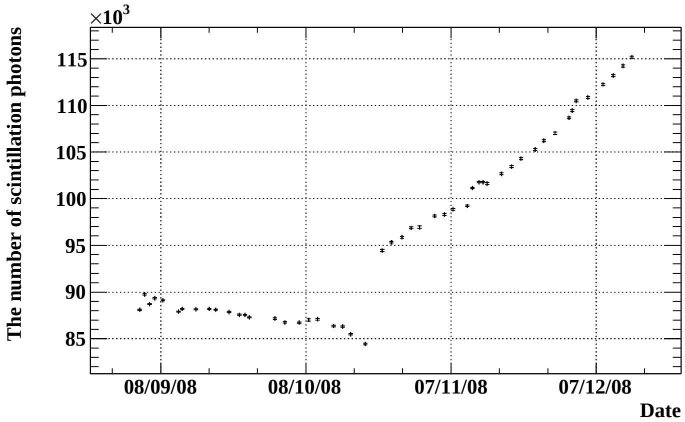

Figure 10.4: 17.6 MeV Li peak in n_{pho} as a function of the date during the whole physics run.

10.2 DC system

The DC system was mounted inside the COBRA magnet in May and switched on in June. After $\approx$ 2 months of immersion in He atmosphere, some modules began to suffer from frequent high voltage trips. The number of DC modules affected by this problem increased with time and caused a reduction of the detection efficiency by a factor two over the period. Figure 10.5 shows the DC system status in 7 different dates inside the run, the red color indicates the malfunctioning chambers.

The problem of the reduced performance of the drift chambers has been solved and the drift chambers functioned successfully during the 2009 run. The problem was caused by an unprotected ground pad surrounding the HV connection in the DC HV distribution circuit.

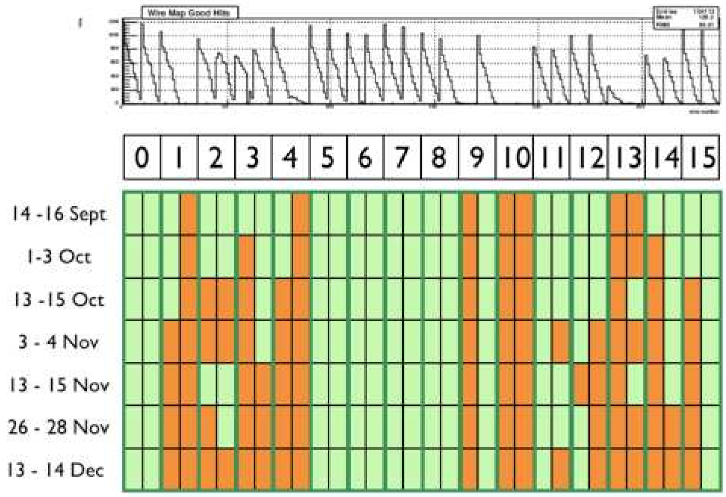

Figure 10.5: Summary of DC performance deterioration during RUN2008.

The hit -coordinate is measured by means hit waveform time measurement. The radial coordinate r is determined by the electron drift time in the cell, corrected for the cell geometry through the calculated correlation between the time and the hit transverse coordinate to the wire, usually referred as TXY table. The time resolution achieved with an offline leading edge discriminator is ≈ 1.5 ns leading to a resolution in the r measurement of $\sigma_{\rm r} = 250\ \mu$m.

The z coordinate is measured by means of the charge induced into the Vernier pads. The charge asymmetries on the pads defines a circle, the phase of the event in this circle is a measurement of the z coordinate. The z resolution is found to be $\sigma_{\rm z} \approx 1$ mm on z. This is a quite worse with respect the experimental needs, $\approx 500 \div 700\ \mu$mm. The reason is a significant noise contribution of the DRS2 chip. This is improved in 2009 by using the DRS4 chip leading to a resolution of $\approx 700\ \mu$m.

10.3 Timing Counter

The Timing Counter was mounted in May. The longitudinal bar detector worked properly, all the PMTs channels were available. The inter-bar time offset was estimated by means of the CW boron calibration and then the intrinsic time resolution was measured exploiting events with positrons crossing at least two consecutive bars. The intrinsic time resolution was found to be in average 70 ps, close to experimental proposal. As a matter of fact this method does not measure the real intrinsic time resolution because the dispersion of the positron propagation time between two bars is not subtracted.

Conversely the transversal fiber detector was not operative, both for offline processing and trigger purposes.

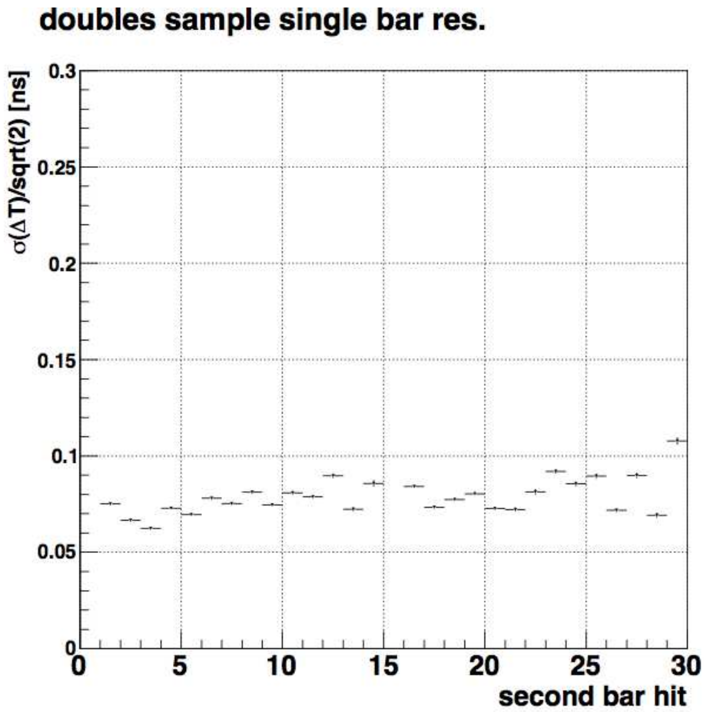

Figure 10.6: TC bar intrinsic time resolution with using Michel positrons crossing at least two consecutive bars; in the x-axis the index of the second of the two consecutive bars hit is reported, the factor $1/\sqrt{2}$ is to extract the single hit resolution.

Chapter 11

Online selection efficiency

11.1 Gamma energy

The online photon energy selection algorithm operates on the sum of all the LXe Type1 waveforms discriminating on the pulse height value, a reference waveform is shown in Figure 5.1. It has been recalled that the online algorithm operates a pedestal subtraction and applies calibration factors taking into account PMT geometrical position, gain and QE.

Taking advantage of back-to-back photons from $\pi^0 \rightarrow \gamma\gamma$ decay it is possible to study LXe energy resolution at 55 MeV, pretty close to signal region, and at 83 MeV, see section 3.3.3 LXe; we measured the γ energy online resolution on the 55 MeV line. The online energy resolution is measured by using directly the trigger variables as stored in the cyclic memories of the final Type2 board. Results are shown in Figure 11.1 for events in the LXe acceptance. The measured resolution is $\Delta E_\gamma/E_\gamma = 9 \div 10\%$ FWHM depending on γ impinging point for events with no online saturation and $\Delta E_\gamma/E_\gamma = 14 \div 15\%$ FWHM in case of online channel saturation with also a lowering of the energy scale by ≈ 2 MeV; this effect is compensated into trigger firmware, see paragraph 5.1.1.

Such a resolution allows us to set the energy threshold around 45 MeV being the selection efficiency for photon energy $\varepsilon_\gamma > 99\%$. To evaluate the trigger efficiency we have then to check the effective threshold applied during all 2008 physic run. This can be achieved using a sample with a known mixture of trigger #0 (MEG trigger) and trigger #1 (MEG trigger with a lower threshold on photon energy selection), see for reference Table 5.2. The offline reconstructed E_γ, normalized to the run live times, are produce for the two trigger types. The ratio of these spectra provides the efficiency curve of E_γ selection and it is fitted by means of a Sigmoid function as reported in section 8.1.1.

The fit of the efficiency curve returns the effective threshold and the resolution. This method was applied to the whole data sample the effective threshold measured both in number of photo-electrons (nphe) and in MeV, is reported in Figure 11.2; in the second part of the run, after a modification of the LXe purification system, the light yield improved by 35%, so the online

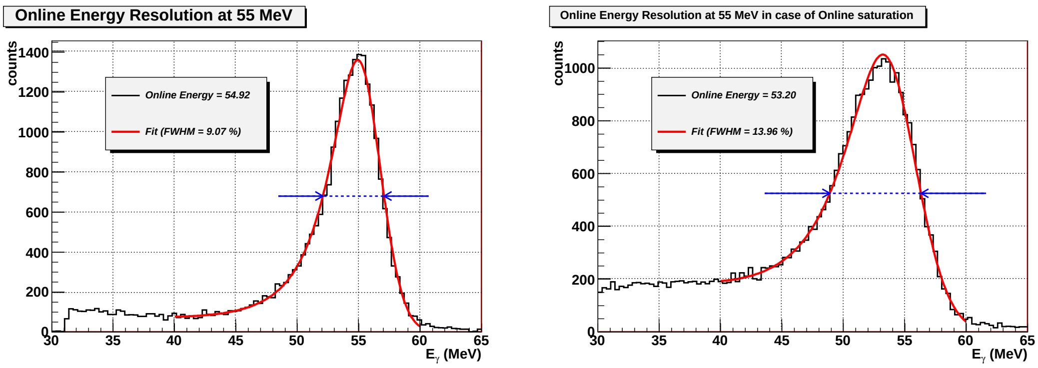

(a) (b)

Figure 11.1: Resolution of the online E_γ algorithm on the 55 MeV line from $\pi^0 \to \gamma\gamma$ decay, (a) in case of no online saturation, (b) in case of online saturation; in the latter case a reduction of ≈ 2 MeV compensates for the channel saturation.

threshold was adjusted three times[1]. The threshold change is a quite delicate operation, so we decided to move it only when the experimental live-time dropped under 80%.

The threshold was checked after every CW run (see section 3.3.3) projecting 17.6 MeV Lithium γ-line to signal region and following LXe light yield improvement in the second part of the run.

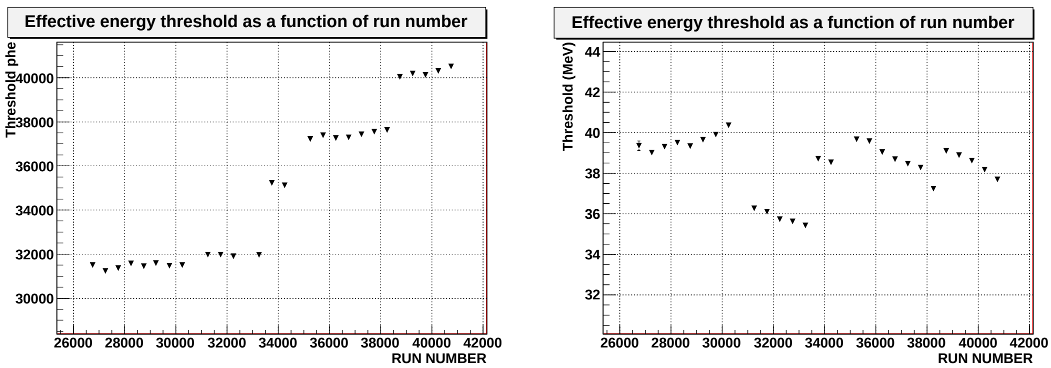

(a) (b)

Figure 11.2: Effective threshold in number of photo-electrons (nphe) (a) and in MeV (b) as a function of Run number.

In conclusion the intrinsic online efficiency on photon energy is $\varepsilon_\gamma > 99\%$. In the next paragraph the trigger efficiency conditioned by the offline analysis reconstruction.

[1] around run #33500, 35000 and 39000

Conditional efficiency In the normalization scheme we have to take into account the conditional probability that given a signal event the trigger is fired. In particular for what concerns E_γ selection, we have to evaluate:

$$\varepsilon(\text{trigger}|E_\gamma = 52.8 \text{ MeV}) \tag{11.1}$$

This value is related to the trigger efficiency itself and the official offline reconstruction.

Given the probability density function (PDF) spectrum used in the physics analysis we can study its distortion due to online selection, the physics analysis is presented in chapter 13. The PDF distribution of the signal is a phenomenological parametrization taking into account low energy tails due to gamma containment reasons with a conservative FWHM = 5.5%, see section 13.2.1; the response function is a Sigmoid defined by the online effective threshold, reported in Figure 11.2 (b), and its sigma.

MEG Likelihood analysis is applied on events having reconstructed energy over 45 MeV, thus the conditional efficiency is given by the integral over 45 MeV of the product of native PDF and the online response function divided by the integral of the native one. This has been checked for all threshold values, see Figure 11.3 and sigma, and it is always > 99%.

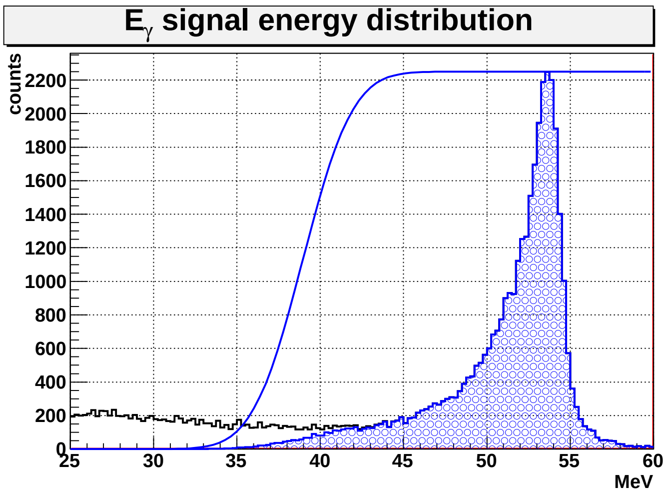

Figure 11.3: Conditional ε_γ efficiency; the blue filled histogram is given by the product of the E_γ PDF with the trigger efficiency sigmoid curve.

11.2 Positron-gamma relative time

The online time reconstruction is based on a linear interpolation of the rising edge of LXe and TC PMT waveforms. acquired by the trigger system at 100 MHz. The algorithm selects the LXe waveform belonging to the inner face with the highest pulse height and the TC ones connected to the hit bar, see section 5.1.1. The LXe-TC online time offset are calibrated by means of boron gammas, see section 8.1.3.

The goodness of the online time selection algorithm is given by the offline $\Delta\mathrm{T}$ spectrum on trigger #0 data which are collected when the online timing is satisfied, Figure 11.4 shows the resulting offline $\mathrm{T}_{\mathrm{e}\gamma}$ distribution. The offline time measurement operates on DRS waveforms acquired at 1.6 GHz with refined algorithms, the resolution is $\sigma \approx 150$ ps, negligible with respect to online one. The distribution of the offline time can be approximated with the sum of two Sigmoid functions ($\mathrm{P}(\mu,\sigma)$) having the same sigma σ and different thresholds μ_{L} and μ_{H}. The fit of the distribution returns both the online resolution and the goodness of the time window centering. The fit function is:

$$\mathrm{F}(\Delta\mathrm{T}) \;=\; \mathrm{A}(\mathrm{P}(\mathrm{Low\ THR},\sigma) \;-\; \mathrm{P}(\mathrm{High\ THR},\sigma)) \;+\; \mathrm{B} \qquad (11.2)$$

where B is a flat background given by random events not correlated with the trigger.

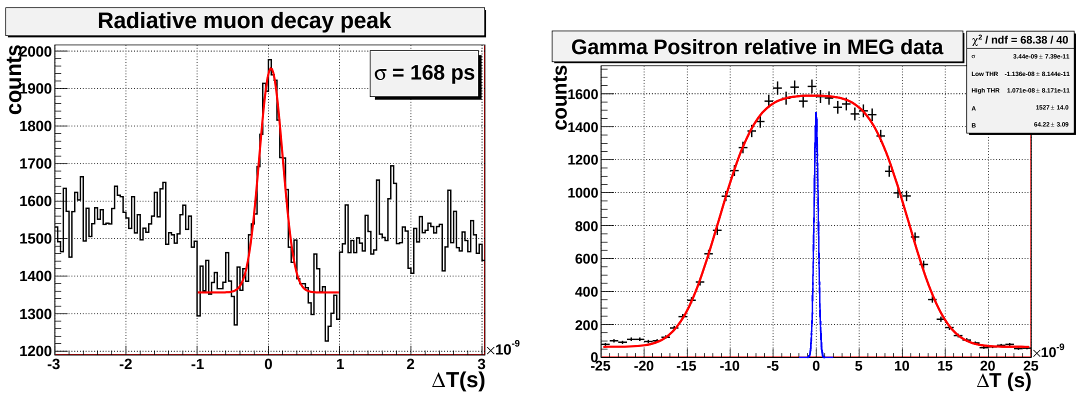

(a) (b)

Figure 11.4: (a) fit of radiative peak into $\mu \to \mathrm{e}\gamma$ data; (b)offline ΔT shape in trigger #0 data given by online selection, in blue a simulation of the signal obtained by radiative decay events.

The results of the fit confirm that the time window is well centered, being Low THR ≈ -11 ns and High THR ≈ 10 ns, and the time resolution is of the order of 3.4 ns (σ) that leads also to estimate $\varepsilon_{\Delta\mathrm{T}} \;\geq\; 99\%$.

11.3 Direction match efficiency

Signal events send γ and e^+ in correlated positions on the calorimeter and the TC. The photon interaction point is assumed to occur at the center of the PMT collecting the largest amount of light, while the hit bar number and the positron crossing coordinate along the bar define the position on the TC.

The correlation between the selected PMT, with index LXePMTId, the selected TC bar, with index TCBar, and the position along the bar, with integer index TCZ, is coded in a LUT, see section 5.1.3 and 8.1.4.

The global efficiency on direction matching, $\varepsilon_{\mathrm{DM}}$, can be factorized as follows:

$$\varepsilon_{\mathrm{DM}} = \varepsilon(\mathrm{LUT} \mid \mathrm{LXePMTId}, \mathrm{TCBar}, \mathrm{TCZ}) \times \varepsilon_{\mathrm{LXePMTId}} \times \varepsilon_{\mathrm{TCBar}} \times \varepsilon_{\mathrm{TCZ}} \qquad (11.3)$$

where $\varepsilon_{\mathrm{LXePMId}}$ is the efficiency of the online reconstruction of the LXe PMT collecting the largest amount of light, $\varepsilon_{\mathrm{TCBar}}$ the efficiency of the online reconstruction of the hit bar, $\varepsilon_{\mathrm{TCZ}}$ is the same for TC Z reconstruction and $\varepsilon(\mathrm{LUT}|\mathrm{LXePMId}, \mathrm{TCBar}, \mathrm{TCZ})$ is the conditional efficiency of the LUT in case of signal given the presented indexes, see as an example Figure 8.7 (b).

The control of the goodness of the online reconstructed indexes is performed by comparison to offline reconstructed quantities on unbiassed data. The LXe PMT collecting the maximum amount of light is well reconstructed by the online algorithm, see Figure 11.5. The agreement is compatible with 100% for the gammas converting in front of the PMTs, while when it converts in between of two PMTs there is a 50% efficiency in the reconstruction. In that case the amount of light collected by the near PMTs is very similar and the online algorithm is sensitive to the jitter of the sampling phase with respect to the peak position. This effect is taken into account while defining the direction match LUT. The TC bar identification is full efficient given the clear signature. The shadow of events in Figure 11.5 (b) are given by the positron crossing more than one bar. The case of the online Z reconstruction is slightly worse. In fact the online evaluation of the Z index was forced to be based on the charge asymmetry between hit bar PMTs being not a precise method with respect to a stereo read out based on the TC fiber detector, see section 5.1.2. We got a resolution corresponding $\sigma_{\mathrm{TCZ}} \approx 7$ cm reflected in the correlation shown in Figure 11.5 (c).

Experimentally we do not have any back to back $\gamma - \mathrm{e}^+$ pairs to check on data the direction match selection efficiency, so we developed an alternative strategy that combines experimental data. The $\mu \to \mathrm{e}\gamma$ decay at rest in the laboratory emits the γ and the e^+ in opposite directions and with the same energy. The e^+ is bent by the COBRA magnetic field, following quasi-helical tracks, while γ preserves the original emission direction flying along a straight path. The measurement of the direction match efficiency is done by Michel positrons tracks at the edge of the spectrum and gammas artificially placed to be back to back with respect to the positron emission direction.

The algorithm selects a sample of well reconstructed tracks recorded without applying the DM selection; we used e^+ acquired with radiative decay triggers with a reconstructed TC match, see section 5.2. Then it retrieves the online measured TC indexes, TCBar and TCZ, associated to the track, it tracks back an hypothetical γ from the muon decay vertex to the LXe detector and finds the inpinging points on the LXe inner face which are finally smeared with the measured resolution of the online algorithm. Finally it controls if the LUT contains the triplet LXePMTId, TCBar and TCZ.

The ratio between the number of triplets found in the LUT and the number of events is the direction match efficiency.

The $\varepsilon_{\mathrm{DM}}$ has been measured to be 66%, which is lower than the expected 95% by construction. The same result comes applying the algorithm to the reconstructed Monte Carlo simulation of both signal and radiative decay. The $\varepsilon_{\mathrm{DM}}$ has been measured only at the end of the data taking period because:

- the statistics needed for the measurement come from the whole data set;

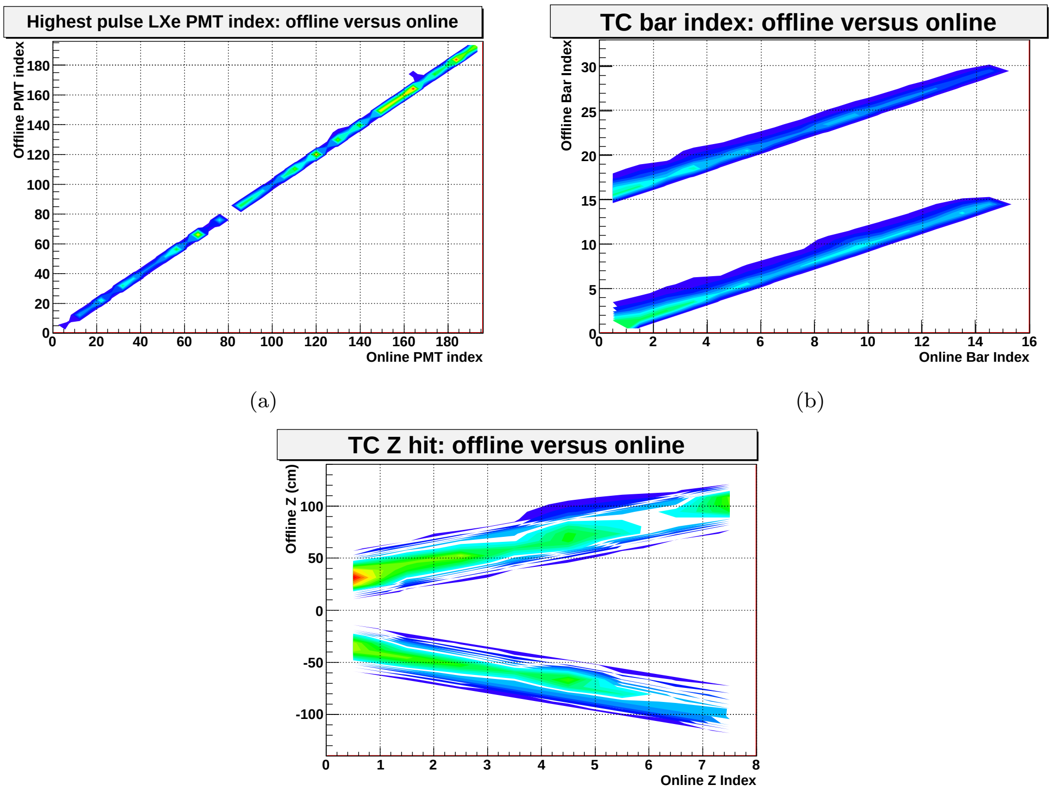

(a) (b) (c)

Figure 11.5: Scatter plot of online inpinging point versus offline reconstruction: (a) index on PMT collecting largest amount of light; (b) TC bar hit by positron; (c) TC Z index of positron hit.

- the tracking code was developed during the data taking period and was released only at the end of the run period.

We searched for all the inefficiency contributions revising the table construction method, in particular looking for the effect of the cuts applied in the DM construction and the impact of the finite resolution on the online hit reconstruction. Figure 11.6 shows, in a pie chart, the inefficiency sources that are discussed in the following paragraphs.

The vertex loss of 5% is due to LXe PMT index reconstruction which has two causes. The relative QEs were not included in the simulation of the calorimeter used to define the LUT because they were measured with high precision only after the begin of the run and a large fraction ($\approx 50\%$) of events has at least one saturated PMT of the calorimeter inner face, larger than the effect foreseen in MC.

The so-called Z reconstruction inefficiency is due to the resolution on online TC Z reconstruction. Remind that each TC bar is divided on eight sections of 10 cm, the online resolution we obtained is of the order of $\sigma \approx 7$ cm, see Figure 8.5. The probability of reconstructing a Z index

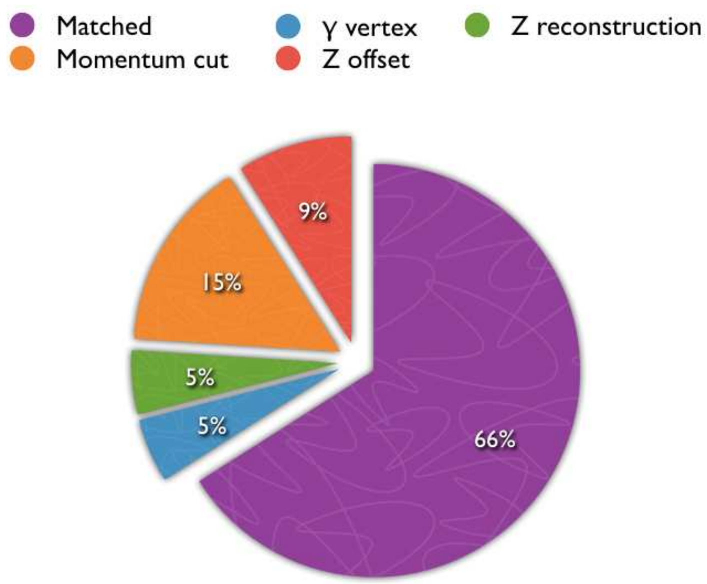

Figure 11.6: Pie chart with the direction match missing efficiency contributions.

out of the LUT, supposing the real value of Z is contained on the table, is not negligible.

The direction match LUT was build-up assuming that the Z coordinate along the TC would have been provided by the TC fibers. Unfortunately the TC fiber signals were not as expected and the Z measurements was changed to the charge asymmetry of the PMT amplitudes. The slant angle of the positron track with respect to the TC normal leads to a mean offset of 3 cm between the Z coordinate at TC fibers with respect to the TC bars, with long tails up to 10 cm as visible in Figure 11.7. This leads at a loss of 9% of efficiency.

Finally we applied a cut at 45 MeV to the signal e^+ momentum before entering the TC. This was set to exclude events in which positrons loosed to much energy into drift chambers and the material into the COBRA magnet modifying its trajectory. This cut turned out to be too tight, leading to a 10% loss.

However the loss on the trigger efficiency it not linearly reflected in a loss of experiment single event sensitivity through the run normalization factor. The impact of this loss of efficiency in the run sensitivity is discussed in section 11.5.

Efficiency of direction match as a function of $\theta_{e\gamma}$ The μ radiative decay (RMD) is a possible source of background, it is measured outside of the physics analysis window and it must be extrapolated into the signal region. Moreover the distortion of the RD $\theta_{e\gamma}$ spectrum has to be taken into account while preparing the RD PDFs, see section 13.2.2. Therefore a simulated sample of RMD event was analyzed as in the case of signal events and the result as a function of the opening angle is reported in Figure 11.8.

The mean direction match efficiency on radiative spectrum came out to be $\varepsilon_{\mathrm{DM}}^{\mathrm{RD}} \cong 50\%$ for

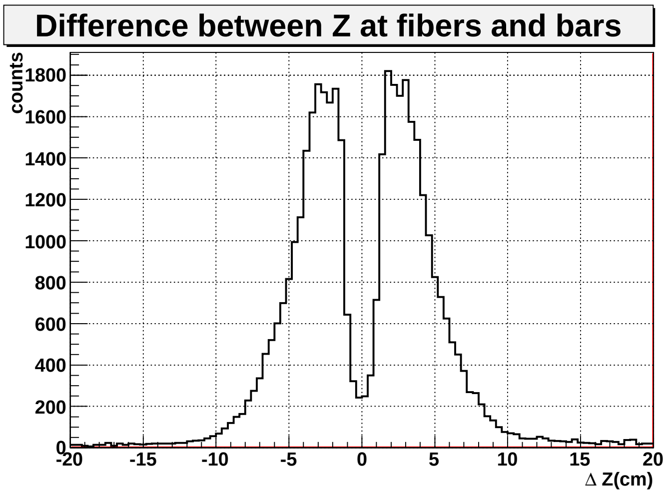

Figure 11.7: Offset between hit Z coordinate at TC fibers and at TC bars due to the slant angle of positron track with respect to the detector.

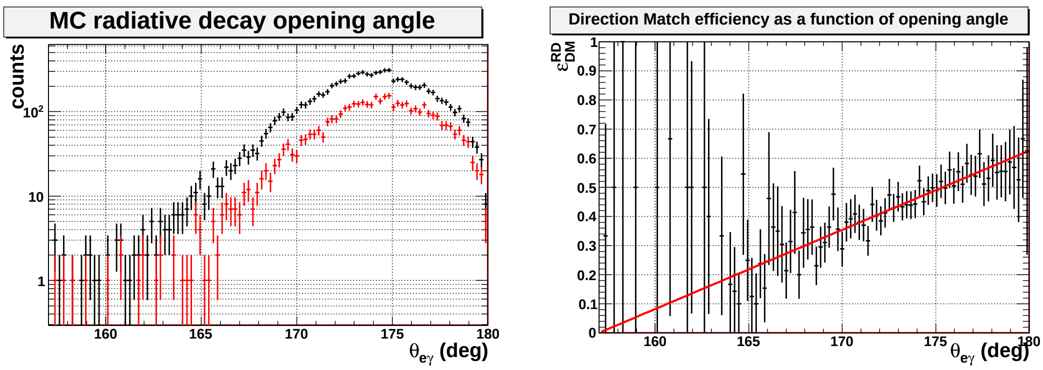

(a) (b)

Figure 11.8: Online direction match efficiency on RD signal: (a) RD $\theta_{e\gamma}$ without direction match request in black and with direction match request in red; (b) ratio between histograms of (a) for direction match efficiency as a function of particles opening angles.

$E_\gamma \in [\,44, 60\,]$ MeV and $E_{e+} \in [\,50, 56\,]$ MeV. The online direction match efficiency decreases linearly with $\theta_{e\gamma}$. The RD angular PDF had been modified accordingly. The edge of the found direction match efficiency curve is $\varepsilon_{\rm DM}^{180^\circ} \approx 65\%$ in agreement with the estimation based on real data. The direction match efficiency decreases by about 2.7% per deg, being equal to 0 for $\theta_{e\gamma} \leq 156^\circ$.

Remarks An online efficiency of 66% in the direction match condition is not suitable with the experimental needs. We found all the contributions to missing efficiency and modified the approach to the table construction.

First of all we prepared two different tables, one exploiting APD fibers for the Z measurement, the other the bar PMT charge asymmetry. Secondly the Monte Carlo hit positions are smeared by means of the measured online resolutions. The positron momentum cut also has been released.

We also improved the Z resolution from the bar PMT charge measurement. We provided a dedicated LUT per each bar to compensate for different offsets achieving an improvement in the resolution from 7 cm to 5 cm.

With these changes, for the 2009 run, we got an efficiency of 83.5%.

11.4 $\mu \to e\gamma$ online efficiency

$\mu \to e\gamma$ trigger is based on gamma energy discrimination, gamma-positron contemporaneity and collinearity. These three observables are uncorrelated thus the global efficiency is given by the product of the single one:

$$\varepsilon_{\mathrm{TRG}} = \varepsilon_{\gamma_{\mathrm{TRG}}} \times \varepsilon_{\Delta\mathrm{T}_{\mathrm{TRG}}} \times \varepsilon_{\mathrm{DM}_{\mathrm{TRG}}} = 66\% \tag{11.4}$$

the uncertainty is 2%, due to systematics related to the track reconstruction.

11.5 Trigger rate and live time

The MEG experiment sensitivity depends on several factors, two of them are the DAQ live time and online efficiency. The experiment normalization k can be defined as follows:

$$\mathrm{k} = \frac{\Omega \mathrm{R}_\mu \mathrm{T}}{4\pi} \times \varepsilon_{\mathrm{e}}\varepsilon_\gamma\varepsilon_{\mathrm{sel}}\varepsilon_{\mathrm{TRG}} \tag{11.5}$$

where R_μ is the beam intensity, T the DAQ live time, Ω the solid angle covered from the apparatus, ε_{e} and ε_γ the probability that positron and a photon reaches the respective detectors, $\varepsilon_{\mathrm{sel}}$ the efficiency of the signal selection and $\varepsilon_{\mathrm{TRG}}$ the online selection efficiency on signal events.

If the number of background event is kept lower than 1, the experimental sensitivity scales linearly with the single event sensitivity, SES = 1/k. An efficient DAQ system coupled with the trigger electronics maximize the product of the data taking live time fraction (LT) and the online selection efficiency $\varepsilon_{\mathrm{TRG}}$.

The $\varepsilon_{\mathrm{TRG}}$ value was discussed in detail in previous sections; it was found to be 66% due to the direction match selection cut.

The read out scheme adopted by the MEG DAQ system is a single buffer read out with no use of pipe lines. Once a trigger system fires the stop signal to the DAQ the DRS chip data are digitized and flushed in dedicated RAMs inside the FPGAs host in the electronics boards. The data transfer to the online machines is based on the VME protocol. The online cluster reads out each electronic crates with a dedicated machine; the event building is finally performed by the master machine linked by Gbit ethernet cables to all the other machines.

The VME data transfer costs $\approx$ 25 ms,it is the bottle neck of the our DAQ system as explained in section 3.4.3. The DAQ live time fraction LT for a acquisition rate R and the read out dead time $\mathrm{t_{dead}}$ is:

$$\mathrm{LT} \;=\; \mathrm{e}^{-\mathrm{R}\cdot \mathrm{t_{dead}}} \tag{11.6}$$

The MEG trigger rate is 6.6 Hz, leading to a DAQ LT = 84%. The value of the DAQ global efficiency (ε_{DAQ}), given by the product of the online selection efficiency and the live time, is:

$$\varepsilon_{\mathrm{DAQ}} \;=\; \mathrm{LT}\cdot\varepsilon_{\mathrm{TRG}} \;=\; 56\% \tag{11.7}$$

At the end of the run we set up 5 more direction match tables to study the direction match selection inefficiency sources. The efficiency values were evaluated on data following the same procedure reported in section 11.3. The efficiency of the direction match together with the dimension is reported in Table 11.1.

Efficiency	**Entries**	**Rate (Hz)**
66%	3903	6.6
75%	4328	8.1
82%	5167	9.1
88%	6063	11.2
92%	7247	12.5
96%	9961	16.2

Table 11.1: Direction matching tables characteristics.

The rate associated to a new table is evaluated by normalizing the table entries for single detector hit position distributions reported in Figure 8.8. Using the trigger rates we evaluated the associated expected live time. All this measurements are put together into the ($\varepsilon_{\mathrm{TRG}}$,LT) plane, see Figure 11.9.

It is clear that unfortunately the run working point is not at the maximum of the found distribution. It is therefore evident that there was margin to relax the direction matching selection, the associated trigger rate increase would not be an issue with our dead time. The $\varepsilon_{\mathrm{DAQ}}$ would be $\approx$ 11% higher, so as the normalization factor. The best working point was found to be around a online efficiency of about 88% and LT equal to 77%.

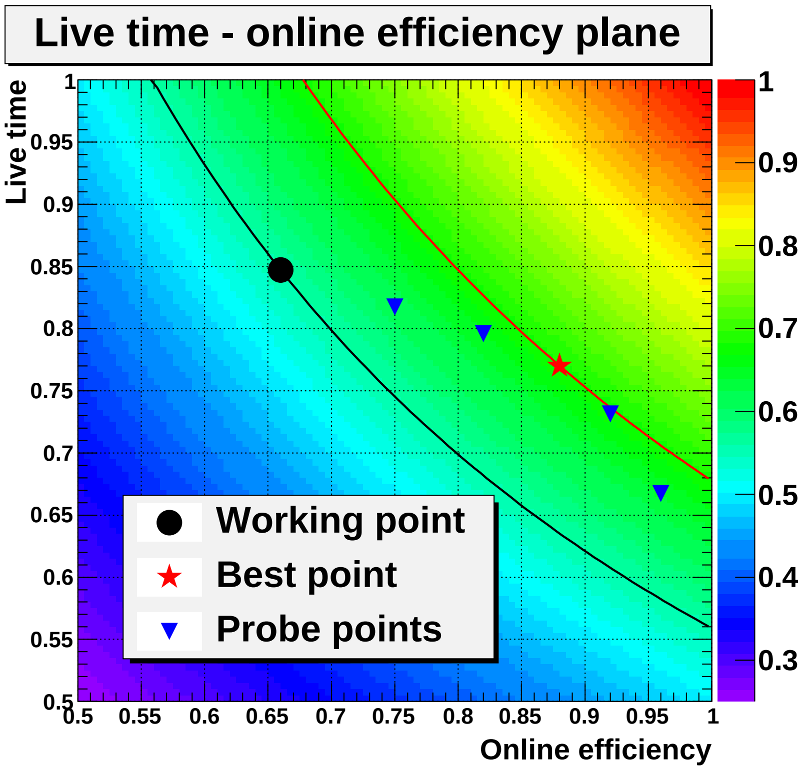

Figure 11.9: Live time - online efficiency plane, in different colors the $\varepsilon_{\mathrm{DAQ}}$ equipotential bands; the black dot is the RUN2008 working point (the corresponding black line the equivalent 56% curve) while the red star is the best DAQ efficiency (the red line at 67%) and the blue triangles are other possible working points used as $\varepsilon_{\mathrm{DAQ}}$ probe points.

Chapter 12

Normalization

In the case of a background-free experiment, the branching ratio is defined as:

$$\mathrm{B}(\mu \to \mathrm{e} + \gamma) \;=\; \frac{4\pi}{\mathrm{R}_\mu \mathrm{T}\Omega} \times \frac{\mathrm{N}_{\mu\to\mathrm{e}\gamma}}{\varepsilon_\mathrm{e}\varepsilon_\gamma\varepsilon_\mathrm{sel}} \;=\; \frac{\mathrm{N}_{\mu\to\mathrm{e}\gamma}}{\mathrm{k}} \tag{12.1}$$

where:

R_μ is the muon stop rate;

T is the live time;

Ω the angular acceptance of the detector;

ε_e and ε_γ are the respective detection efficiencies;

ε_sel is the overall selection efficiency.

The normalization parameter k is defined Equation (12.1), the inverse is the single event sensitivity (SES), parameter discussed in section 2.4.

An accurate determination of the normalization factor k demands for a precise knowledge of all the parameters involved, so as the detector efficiencies as a function of time during the whole data taking period. This might be particularly difficult in the case of positron related variables due to the instabilities of the tracking system during RUN2008, which were described in chapter 10.

We therefore decided to normalize the sample of $\mu \to \mathrm{e}\gamma$ candidate events to a sample of reconstructed positrons from normal muon decay (Michel decay). The Michel positrons exhibits the same dependence on the tracking efficiency as the signal ones. The normalization results in this case almost independent of tracking instabilities. The Michel decays were acquired in parallel with the signal events during the whole data collection period, exploiting a feature of the trigger system.

It may be useful to recall the meaning of some of the trigger masks that will be used in this chapter. With trigger #0 we indicate the $\mu \to \mathrm{e}\gamma$ trigger, it requires an energy deposit in the LXe detector over a threshold of the order of 40 MeV, a hit in the TC within 10 nsec from the γ hit with a correlation between the hit positions in the detectors. The trigger #22 requires only a hit in the TC bars.

12.1 Scheme

During RUN2008, a substantial number of DC HV trips occurred and an increasing number of planes was turned off. The system deterioration forced the collaboration to adopt the mentioned Michel decay sample for normalization.

From Equation (12.1) the expected number of signal events can be expressed in terms of $\mathrm{B}(\mu \to \mathrm{e}\gamma)$ according to:

$$\begin{aligned} \mathrm{N}(\mu \to \mathrm{e}\gamma) &= \mathrm{B}(\mu \to \mathrm{e}\gamma) \times \mathrm{R}_\mu \times \mathrm{T}\times && (12.2)\\ &\times \mathrm{A}(\mathrm{DC} \mid \mathrm{e}^+_\mathrm{s}) \times \varepsilon(\mathrm{track} \mid \mathrm{DC} \cap \mathrm{e}^+_\mathrm{s}) \times \varepsilon(\mathrm{TC} \mid \mathrm{track} \cap \mathrm{e}^+_\mathrm{s})\times && (12.3)\\ &\times \mathrm{A}(\mathrm{LXe} \mid \mathrm{track}) \times \varepsilon(\gamma_\mathrm{s})\times && (12.4)\\ &\times \varepsilon(\mathrm{mask} = 0 \mid \mathrm{e}^+_\mathrm{s}\gamma_\mathrm{s}) && (12.5) \end{aligned}$$

with disentangled contributions from:

- the number of muons stopped decayed during the experiment live time (Equation (12.2));
- the overall probability (comprehensive of acceptance and efficiencies) for a signal positron to enter the signal box, $\varepsilon(\mathrm{e}^+_\mathrm{s})$ (Equation (12.3));
- the same for the γ, $\varepsilon(\gamma)$ (Equation (12.4));
- trigger efficiency for $\mu^+ \to \mathrm{e}^+\gamma$ (mask=0) events discussed in chapter 11 (Equation (12.5)).

Every single quantity is listed and detailed in Table 12.1.

The same factorization can be considered to estimate the number of Michel positrons detected by the TC during physics data taking:

$$\begin{aligned} \mathrm{N}(\mu \to \mathrm{e}\nu\overline{\nu}) &= \mathrm{R}_\mu \times \mathrm{T}\times \\ &\times \mathrm{A}(\mathrm{DC} \mid \mathrm{e}^+_\mathrm{m}) \times \varepsilon(\mathrm{track} \mid \mathrm{DC} \cap \mathrm{e}^+_\mathrm{m}) \times \varepsilon(\mathrm{TC} \mid \mathrm{track} \cap \mathrm{e}^+_\mathrm{m})\times \\ &\times \varepsilon(\mathrm{mask} = 22 \mid \mathrm{track} \cap \mathrm{e}^+_\mathrm{m} \cap \mathrm{TC})/\mathrm{Psc}(\mathrm{mask} = 22) && (12.6) \end{aligned}$$

where mask = 22 is the TC alone trigger, and Psc is its pre-scaling factor[1]. $\mathrm{B}(\mu \to \mathrm{e}\nu\overline{\nu})$ is assumed to be 1.

From the ratio of the two above equations one obtains:

[1]namely the number of triggers of that type to occur before one of those is recorded by the DAQ

Item	Meaning
$A(\mathrm{DC}\vert\, \mathrm{e}^+_{\mathrm{s/m}})$	Acceptance of the DC system folded with the Signal/Michel positron spectra
$\varepsilon(\mathrm{track} \mid \mathrm{DC} \cap \mathrm{e}^+_{\mathrm{s/m}})$	Track reconstruction efficiency as a conditional probability for a positron track within the reconstruction acceptance
$\varepsilon(\mathrm{TC} \mid \mathrm{track} \cap \mathrm{e}^+_{\mathrm{s/m}})$	Matching efficiency for a reconstructed positron of the TC hit with the track extrapolated to TC
$A(\mathrm{LXe} \mid \mathrm{track})$	Conditional probability of a back-to-back photon to enter the calorimeter fiducial volume given a positron tracked by DC system (matter effect excluded)
$\varepsilon(\gamma_{\mathrm{s}})$	Efficiency for a signal γ generated towards the fiducial volume of the LXe detector
$\varepsilon(\mathrm{mask} = 0 \mid \mathrm{e}^+_{\mathrm{s}}\gamma_{\mathrm{s}})$	Trigger selection efficiency for signal events
$\varepsilon(\mathrm{mask} = 22 \mid \mathrm{track} \cap \mathrm{e}^+_{\mathrm{m}} \cap \mathrm{TC})$	Trigger selection efficiency for a TC hit matched with a reconstructed track
$\mathrm{Psc}(\mathrm{mask} = 22)$	Pre scaling factor for trigger #22

Table 12.1: Explanation of the factors contributing to the k-factor definition.

$$\begin{aligned} \mathrm{B}(\mu \to \mathrm{e}\gamma) \quad = \quad & \mathrm{N}_{\mu\to\mathrm{e}\gamma} \times \frac{1}{\mathrm{N}_{\mu\to\mathrm{e}\nu\overline{\nu}}} \times \frac{\varepsilon(\mathrm{e}^+_{\mathrm{m}})}{\varepsilon(\mathrm{e}^+_{\mathrm{s}})} \times \frac{1}{\varepsilon(\gamma)} \times \\ & \times \frac{\varepsilon(\mathrm{mask} = 22 \mid \mathrm{track} \cap \mathrm{e}^+_{\mathrm{m}} \cap \mathrm{TC})}{\varepsilon(\mathrm{mask} = 0 \mid \mathrm{e}^+_{\mathrm{s}}\gamma_{\mathrm{s}})} \times \frac{1}{\mathrm{Psc}(\mathrm{mask} = 22)} \end{aligned} \tag{12.7}$$

In the following sections provides a detailed discussion of each term contributing to the normalization will show how the detector instabilities can be ruled out by this approach.

12.1.1 DC relative efficiency

The tracking system acceptance, the track reconstruction efficiency and the DC-TC matching depend on the bending radius of positron tracks and they can be different for Michel and signal positrons. The DC relative efficiency is the ratio of the two detection efficiencies ($\varepsilon(\mathrm{e}^+_{\mathrm{m}})/\varepsilon(\mathrm{e}^+_{\mathrm{s}})$).

Both quantities vary during the run as a result of the degraded DC performance. Both efficiencies can be evaluated as a function of time by Monte Carlo simulation changing the description of the DC configuration. Unfortunately the number of different DC configuration is huge, more than 100, making the absolute ε determination difficult and somehow unreliable.

The adopted normalization scheme is sensible only to the ratio of the Michel and signal positron detection and reconstruction efficiencies. The Monte Carlo simulation is then used only to prove that the ratio is constant on a wide range of DC configurations.

Seven different configurations were considered as discussed in Section 10.2 and reported in Figure 10.5, in which no hit were associated with inactive DC planes. The global positron detection and reconstruction efficiencies for signal and Michel positrons emitted isotropically is shown in Figure 10.5. The relative efficiencies turned out to be constant; its best value is extracted from the linear interpolation of the points.

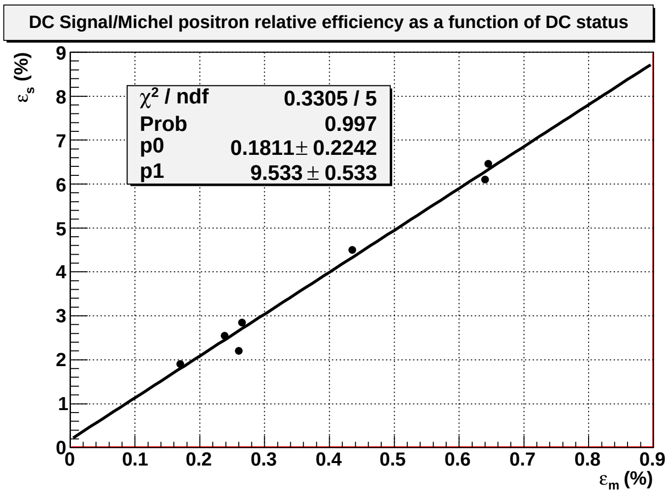

Figure 12.1: Absolute efficiency on detection and tracking of a signal positron and Michel positrons; different points refer to different DC operation conditions as reported in Figure 10.5.

$$\frac{\varepsilon(\mathrm{e}^+_\mathrm{s})}{\varepsilon(\mathrm{e}^+_\mathrm{m})} = 9.53 \pm 0.53 \tag{12.8}$$

This number is substantially different from 1 because the spectrometer is designed to prevent low energy positrons to crowd the TC bars being fully efficient in case of signal events.

12.1.2 Photon acceptance

The photon acceptance is the product of the probability of having a photon inside the LXe acceptance given a reconstructed signal positron track (A(LXe | track)) multiplied by the reconstruction efficiency ($\varepsilon(\gamma_\mathrm{s})$).

Geometrical acceptance Considering a $\mu \to \mathrm{e}\gamma$ decay with a e^+_s emitted along [$\varphi_{\mathrm{e}^+}, \theta_{\mathrm{e}^+}$], the companion γ is emitted in the [$\varphi_{\mathrm{e}^+} + \pi, \pi - \theta_{\mathrm{e}^+}$] direction. The geometrical acceptance of the tracking system is larger than the LXe detector one so the γ could not reach the calorimeter sensitive volume. The conditional geometrical acceptance A(LXe | track) is given by the fraction of signal γ pointing to the calorimeter given a reconstruction signal positron.

The pattern of DC trips during the RUN reflects into a variation of the DC reconstruction efficiency as a function of the positron emission direction. In particular the angular DC acceptance window around [$\varphi = 0, \theta = \pi$] became tighter and tighter with the worsening of the DC performance, as shown in Figure 12.2 (a). The HV problems affected mostly the DC modules at the sides of the DC system and it is reflected on a worsening on the efficiency reconstruction for events in the side band of the geometrical acceptance. However this effect is partially compensated by the conditional gamma acceptance A(LXe | track) being increasing during the RUN as reported in Figure 12.2 (b).

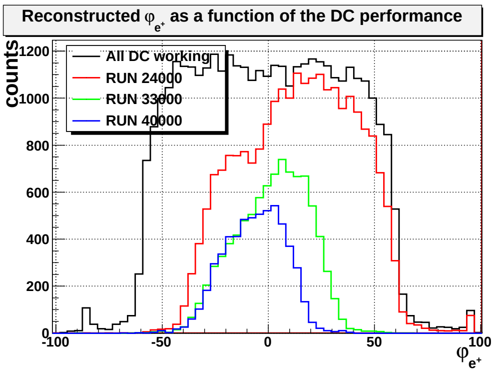

(a)

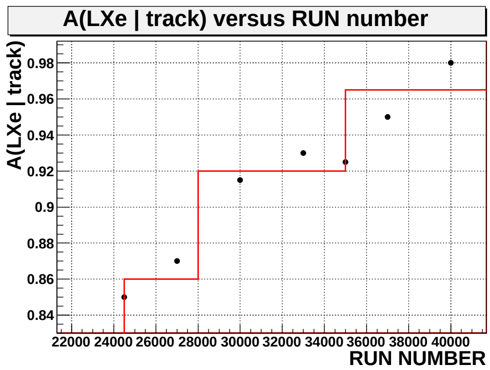

(b)

Figure 12.2: (a) reconstructed φ_{e^+} as a function of DC performance: in black all DC available, in blue RUN2008 worse condition; (b) A(LXe | track) as a function RUN number, in red the mean probability function applied on normalization evaluation.

While counting Michel events a probability function taking into account the variation of the A(LXe | track) during the RUN is applied; the probability function is reported red line in Figure 12.2 as a red line.

Another possibility is to face up this effect from an opposite point of view. Let's define the angular range to be the LXe active area. Thus the parameter become A(track | LXe) and it is equal to 1 by design. In this scheme a cut on the [$\varphi_{e^+}, \theta_{e^+}$] is applied while counting Michel events in order to have a back to back gamma in the LXe detector. In this way the DC inefficiency is not averaged over a set of run, as it is in the previous, but it is automatically applied in a event by event basis.

The second scheme was finally used because is by definition free from systematic uncertainties, but a check with the first scheme was done and the result is fully compatible.

Detection efficiency A photon emitted from the target towards the calorimeter inner face crosses several layers of different materials before reaching the liquid Xenon. In fact along the flight path it may interact with the COBRA coils and support structures; the inner surface of the LXe detector cryostat or with the calorimeter PMTs or their support structures. The amount of material in front of the LXe has been evaluated to be the order of 0.4 X_0. The designed value has been verified by comparing Monte Carlo and real data as described in what follow.

The MEG detector has been modeled into the Monte Carlo code in order to reproduce as faithfully as possible the data. In particular a detailed treatment of the material in between the muon target and the LXe is performed. The effective thickness can be measured counting the number of signal γs that are reconstructed in the analysis region [48, 57.6] MeV and normalizing that number to the total number of generated events. In this method the reconstruction inefficiency is also taken into account. The result is $\varepsilon(\gamma_s) = 63\% \pm 3\%$, showed in Figure 12.3 (a).

This measurement can be performed also during CEX run, see for reference section 3.3.3. The idea is to search for a γ in the LXe detector when its companion photon is detected in the auxiliary calorimeter. For this particular study the NaI detector is placed in the opposite direction with respect to the LXe detector inner face. Once a gamma from π^0 decay is detected in the NaI the other points to the LXe detector sensitive volume. The online selection requires only an energy release over threshold in the NaI scintillator crystals; the number of reconstructed γ events in the LXe divided by the total number of recorded events is the γ detection efficiency (see Figure 12.3 (b)). This measurement gives the same result as the Monte Carlo simulation, it is $\varepsilon(\gamma_s) = 62\% \pm 4\%$.

A third possible estimation of $\varepsilon(\gamma_s)$ comes from the normalization the LXe energy spectrum from the muon decay to the theoretical spectrum. The measured differential RMD γ spectrum is compared to the theoretical distribution computed supposing a μ stopping rate equal to 3×10^7 folded with the LXe energy response function and assuming detection efficiency equal to 1. It is also taken into account that $B(\mu^+ \to e^+ \nu_e \overline{\nu}_\mu \gamma) = 1.4 \times 10^{-2}$ for $E_\gamma \geq 10$ MeV and that the LXe detector covers 10% of the solid angle. $\varepsilon(\gamma_s)$ is the further factor needed to superimpose the two spectra reported in Figure 12.3 (c). In this estimation we found $\varepsilon(\gamma_s) = 65 \pm 9\%$. The uncertainty on the μ stopping rate ($\Delta R_\mu / R_\mu = 10$ %) limits the precision of this method.

The value used in the normalization evaluation is $\varepsilon(\gamma_s) = 62\% \pm 4\%$ being measured directly on data.

12.1.3 Trigger efficiency

The "trigger efficiency factor" is given by the efficiencies ratio of the trigger #22 and trigger #0, see for reference Table 5.2. The efficiency of trigger #0 has been discussed in chapter 11. Here the evaluation of the trigger #22 efficiency is reported.

An unbiassed sample of events were acquired with trigger #18, which requires that at least 4 out of 5 consecutive DC modules are hit. The TC signals are not used at all. The entire TC waveforms are recorded for these events. The collected events are reconstructed and a subsample of positrons tracks matching a TC hit is derived. On this subsample of e^+ hitting the TC the presence of trigger #22 (TC trigger) is searched for. This is obtained by means of the TGEN waveform method presented in section 8.3.4. The number of events in which the trigger #22 is fired divided by the total number of events in the subsample is the online selection efficiency. The $\varepsilon(\mathrm{mask} = 22 \mid \mathrm{track} \cap e^+_m \cap \mathrm{TC})$ is measured to be 97.3% $\pm$0.6%. The major contribution to this small inefficiency is due to the pile-up; the online reconstruction is not capable to separate two positrons inpinging a TC sector once they are closer in time than ≈ 30 ns , if this happens no hit is reconstructed at all. The positron rate into the TC is measured to be ≈ 2 MHz. The probability

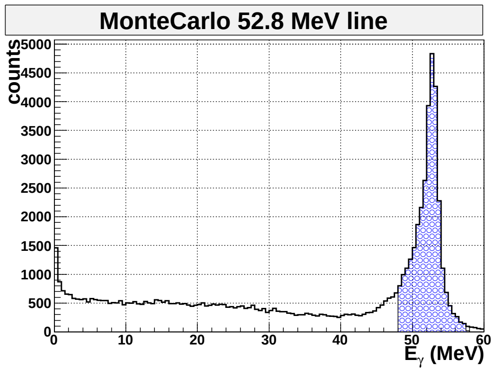

(a)

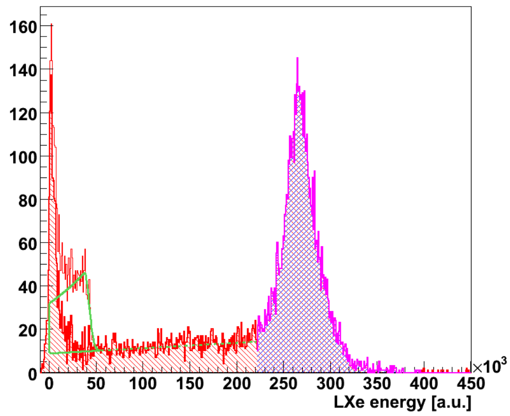

(b)

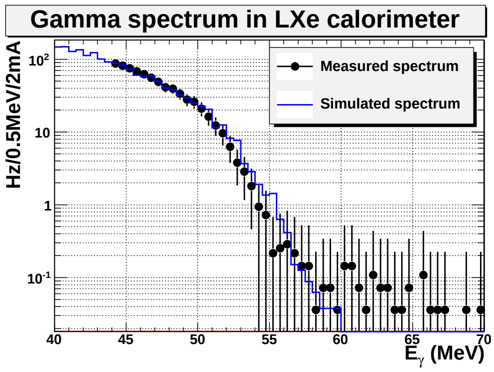

(c)

Figure 12.3: LXe detector detection efficiency; (a) Reconstructed signal Monte Carlo, the blue filled part represents the 63% of the events reconstructed in the analysis region, (b) the LXe distribution in NaI alone trigger run, the magenta filled region in the reconstructed gamma line used in the efficiency estimation, (c) the RD gamma spectrum normalized with the measured rate.

of pileup follows the poisson distribution and is given by:

$$\mathrm{P}(2 \mid \mu) \;=\; \frac{\mu^2}{2!}\mathrm{e}^{-\mu} \;\approx\; 1.5\% \qquad \mu \;=\; 3 \cdot 10^{-2} \tag{12.9}$$

A further contribution comes from the mismatch between online and offline threshold on TC hit reconstruction.

The MEG trigger requires a hit in the TC so this contribution is already taken into account and it is simplified in the ratio.

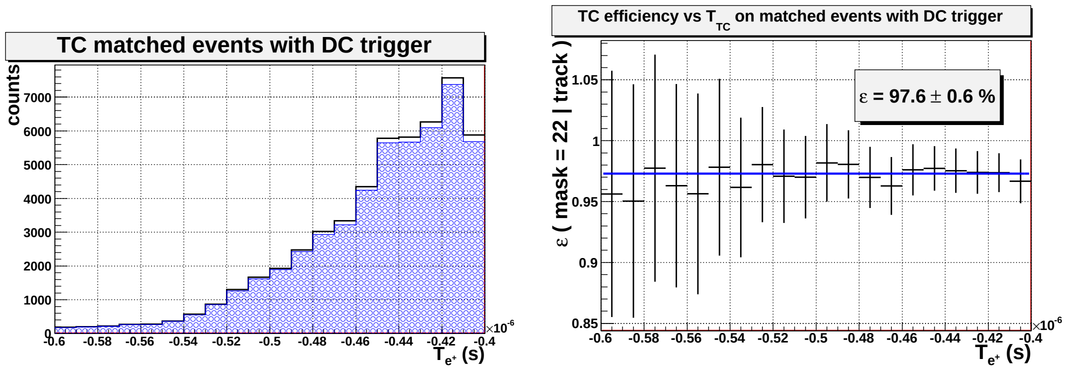

(a) (b)

Figure 12.4: (a) TC time distribution in case of Michel track, the blue-filled histogram shows the number of those events recognized as also trigger #22 by the online system; (b) fraction of Michel tracks recognized as trigger #22.

12.1.4 Michel decay count

The number of Michel decays N($\mu \to e\nu\overline{\nu}$) occurred during the entire signal search period is counted in the event sample collected with the trigger #22. A Michel decay positron is given by a good track track in DC with momentum higher than 50 MeV/c, matching a hit in the TC detector and satisfying all the analysis selection criteria used in the signal search. Figure 12.5 shows the rate of the Michel positrons in the detector as a function of time. As expected the Michel positron rate decreased continuously during the RUN2008, being the effective rate at the end of the run a factor 2 lower than the same at the beginning.

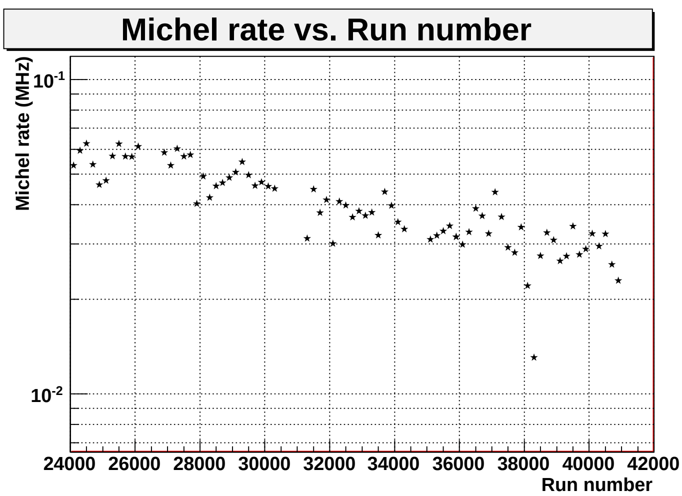

Figure 12.5: Effective Michel rate after that all the analysis cut are applied.

The number of recontructed Michel events is:

$$N(\mu \to e\nu\overline{\nu}) = 12750 \tag{12.10}$$

12.2 RUN2008 normalization

Table 12.2 summarizes all the k factor parameter values.

Parameter	**Value**
$N(\mu \to e\nu\overline{\nu})$	12750
$\varepsilon(e^+_m)/\varepsilon(e^+_s)$	0.105±0.006
$A(LXe \mid track) \times \varepsilon(\gamma_s)$	0.57±0.02
$\varepsilon(TRG)$	1.5±0.03
$Psc(mask = 22)$	10^7

Table 12.2: k-factor parameters value.

The k factor is computed to be:

$$k = (5.2 \pm 0.5) \cdot 10^{11} \tag{12.11}$$

thus the SES for the RUN2008 is

$$SES = (1.9 \pm 0.2) \cdot 10^{-12} \tag{12.12}$$

The differential distribution of the single event sensitivity as a function of the Run number is reported in Figure 12.6. In the final part of the run, due to the DC performance deterioration, the SES distribution is almost flat. In the distribution all runs are taken into account with including calibration runs. The constant of the distribution parts are due to the dedicated radiative decay runs acquired one day every week.

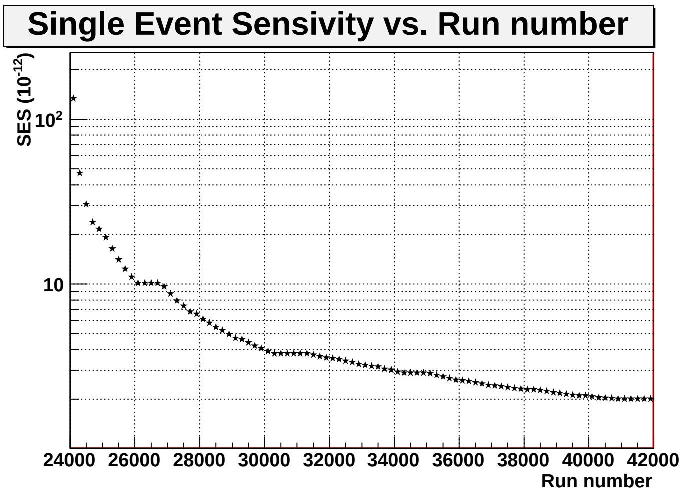

Figure 12.6: Differential distribution of the RUN2008 SES as a function of the Run number.

Chapter 13

Physics data analysis

In this chapter the data analysis scheme is discussed and the analysis results on the data collected in the 2008 run are reported. This scheme can be described as a likelihood analysis applied on a wide blind box. A region in the [$E_\gamma, \Delta T_{e\gamma}$] plane is hidden to the collaboration soon afterward a run is recorded by an automatic process which removes the events inside a pre-defined region in the [$E_\gamma, \Delta T_{e\gamma}$] plane [$|\Delta T_{e\gamma}| \leq 3\sigma_{\Delta T_{e\gamma}}$, $|E_\gamma - 52.8\ \mathrm{MeV}| \leq 3\sigma_{E_\gamma}$] and writes them in a separated and not accessible data stream. This region is usually named the blinding box. The analysis algorithms are calibrated and optimized by means of large event samples contained in the side-bands of this box. The detector response functions are studied by means of calibration events when possible or by using events contained in the side bands. The probability density functions (PDF) are measured on events belonging to side bands for accidental background, are modeled by means of Monte Carlo simulation for radiative decay background and finally derived from the detector response functions for signal events. The number of signal and background events in the blinding box are extracted through a maximum likelihood fit of the events with the described PDFs. The limit on the number of measured events is extracted following the Feldman and Cousins prescriptions [53].

The likelihood function is:

$$\mathcal{L}(N_{Sig}, N_{RD}, N_{BG}) \; = \; \frac{N^{N_{obs}} e^{-N}}{N_{obs}!} \prod_{i=1}^{N_{obs}} \left[\frac{N_{Sig}}{N} S + \frac{N_{RD}}{N} R + \frac{N_{BG}}{N} B \right] \tag{13.1}$$

where Sig, RD and BG are the indexes for Signal, Radiative Decay and accidental background events, $N = N_{Sig} + N_{RD} + N_{BG}$, S is the signal PDF, while R and B are the Radiative Decay and accidental background PDFs; N_{obs} is the measured number of the events in the blinding box.

13.1 Blinding box

Principles of Blinding Box analysis Modern nuclear and particle physics experiments, like MEG, often involve large numbers of data analysts working together to extract quantitative results from complex datasets. More precisely, physicists need to report accurate systematic error estimates for their measurements with no corruption induced by the observer bias. To remove this bias, the experimenters devise blind analysis techniques, where the experimental result is hidden for the analysts until they've agreed on the analysis details and parameters.

The blinding box is a region in the [$\Delta T_{e\gamma}$, E_γ] plane large enough to contain all possible signal candidates, this box is shown in Figure 13.1.

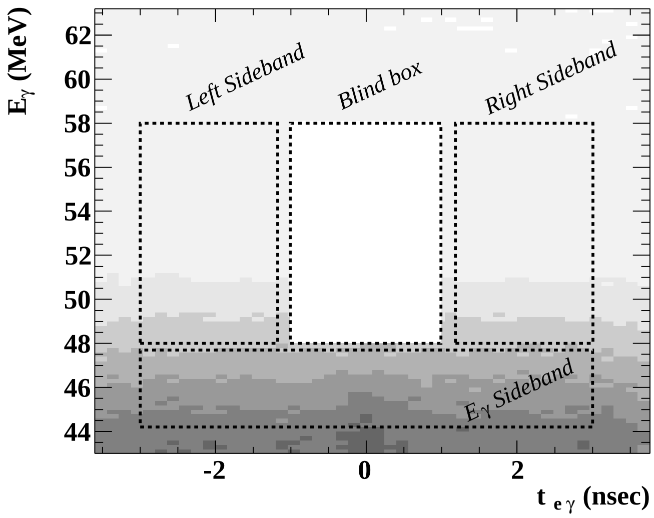

Figure 13.1: The [$\Delta T_{e\gamma}$, E_γ] plane close to the $\mu \to e\gamma$ signal; the MEG blinding box can be clearly identified as the empty region defined by $|\Delta T_{e\gamma}| \leq 1$ ns and 48 MeV $\leq E_\gamma \leq$ 58 MeV.

Once a physics run is recorded on disk, it is automatically processed in order to divide the data stream in different subsamples, namely:

- recxxxxx_unselected: data sample acquired during the physics run not used for physics analysis; it contains detector calibration triggers and MEG trigger discorded by a first offline selection;
- recxxxxx_open: events with full information needed for physics analysis outside the blinding box; those files are available to define analysis criteria and measure the background;
- recxxxxx_blind: events into the blinding box, not accessible before final physics analysis;
- recxxxxx_unbiassed: mixture of all the data in the data stream heavily pre scaled, i.e candidate signal and calibration events.

The blinding box lies in the region defined by 48 MeV $\leq E_\gamma \leq$ 58 MeV and $| \Delta T_{e\gamma} | \leq 1$ ns, the cuts are set to be $\approx 100\%$ efficient on signal.

The side bands are the regions surrounding the blinding box. We identify two different side band categories. The time side-bands are defined by the condition $|\Delta T_{e\gamma}| \geq 1$ ns, they are used to define the accidental energy spectra, in particular for E_γ. The energy side band is defined by the condition 44 MeV $\leq E_\gamma \leq$ 48 MeV. In the energy side band the majority of μ radiative decay events accumulates, they are acquired by means of MEG trigger selection. These events are used to evaluate timing resolution and offsets between the LXe and the TC detectors and to estimate the number of RD events in the analysis region.

13.2 Probability density functions

In order to extract the number of signal events measured in the analysis region a maximization of a likelihood function is performed. The likelihood function is defined by the probability density functions (PDFs) that model the distribution of the physics analysis variables, namely E_γ, $|\vec{p}_{e^+}|$, $\Delta T_{e\gamma}$, $\Delta\varphi_{e^+\gamma}$ and $\Delta\theta_{e^+\gamma}$.

In the below section the extraction of the PDFs for signal, RD and accidental background events are discussed.

13.2.1 Signal

A $\mu \to e\gamma$ signal event is characterized by a γ and a e^+, both of 52.8 MeV energy, emitted at the same time and in opposite directions. The detectors response functions are typically gaussian, multi gaussian or asymmetric gaussian distributions; the widths of those distributions are the experimental resolutions.

Gamma energy The LXe detector response function to 52.8 MeV γ from $\mu \to e\gamma$ decay is extracted by means of the CEX calibration runs (see for reference section 3.3.3). The resolution obtained at 54.9 MeV is scaled to 52.8 MeV using the $1/\sqrt{N_{phe}}$ expected behavior and, taking into account the different background level in case of pion and muon beams; the contribution to the gamma energy resolution caused by baseline fluctuations is evaluated in both cases and then CEX data are rescaled to the muon beam one. The PDFs is reported in Figure 13.2 (a).

The line shape is asymmetric, with a low energy tail due to γ-rays converting in front of the LXe sensitive volume. The resolution has a significant dependence with respect to the gamma interaction point in the LXe volume; this has been corrected by means of a 3D map reported in Figure 13.2 (b). The average resolution for deep events (w$\geq$2 cm) is measured to be $\Delta E_\gamma/E_\gamma = (5.8\pm0.35)$ % FWHM with a right tail of $\sigma_R = (2.0\pm0.15)$ %, where the error quoted includes the variation over the calorimeter acceptance.

The energy scale is constantly monitored by looking at the reconstructed 17.67 MeV energy line from CW protons on Li and confirmed by a fit of the photon energy spectrum from the $\mu^+ \to e^+\nu_e\overline{\nu}_\mu\gamma$ decay, positron annihilation in flight and γ-ray pile-up, folded with the line-shape determined during the CEX run. The systematic uncertainty on the energy scale is estimated, by a comparison of these measurements, to be $\leq 0.4\%$.

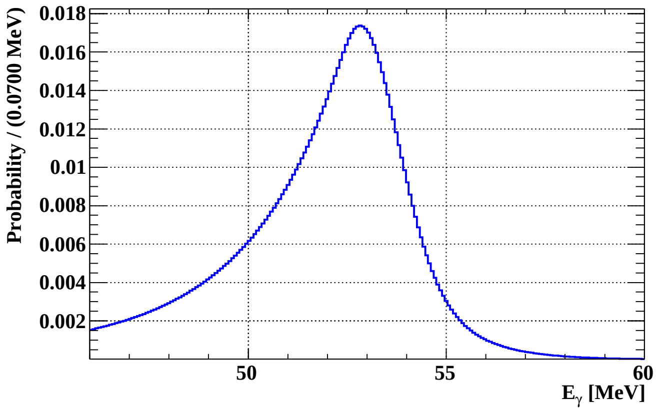

(a)

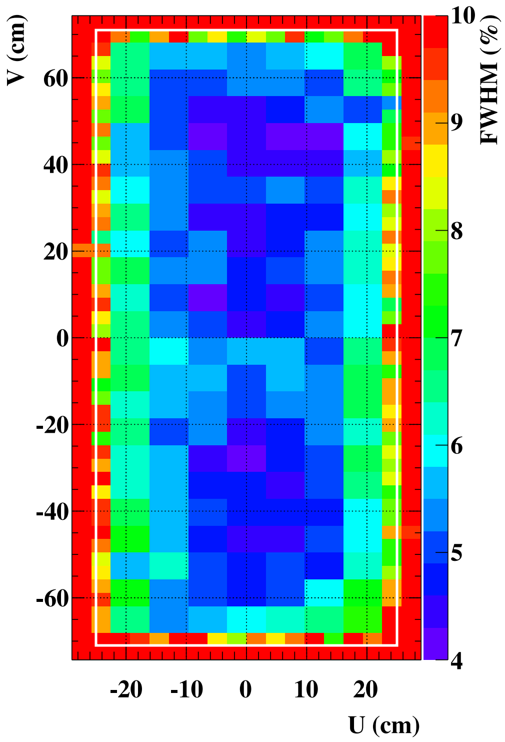

(b)

Figure 13.2: (a) PDF for γ energy in case of $\mu \to e\gamma$ events; (b) distribution of FWHM width of the PDF in the (u,v) plane of the LXe inner face (corresponding to (z,r$\cdot\varphi$) plane).

Positron momentum The positron track is reconstructed with the Kalman filter technique [64], in order to take into account the effect of multiple scattering and energy loss of positrons in the detector materials and the COBRA graded magnetic field. The positron energy scale and resolution are evaluated by fitting the kinematic edge of the measured Michel positron energy distribution at 52.8 MeV/c. The fit function is formed by folding the theoretical Michel spectrum with the energy-dependent detector and the tracker response function to mono-energetic positrons. The latter one is well described in the Monte Carlo simulation of $\mu \rightarrow e\gamma$ decays by a triple Gaussian function (a sum of a core and two tail components). The fit has been performed on the unbiased DC trigger data sample.

The resolutions extracted from the data are 374 keV, 1.06 MeV and 2.00 MeV in sigma for the core component and the two tails, with corresponding fractions of 60%, 33% and 7% respectively. The uncertainty on these numbers is dominated by systematics effects and was determined by performing the fit in data sample obtained in different data taking periods. In Figure 13.3 the PDF for positron momentum reconstruction and the fit to the Michel spectrum is reported.

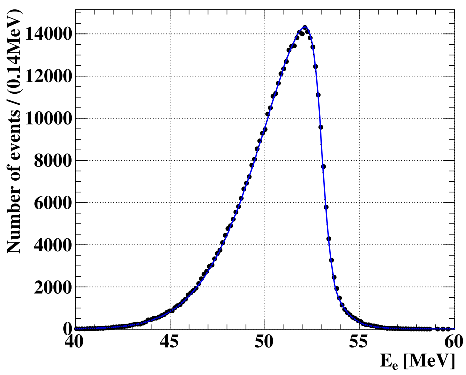

(a)

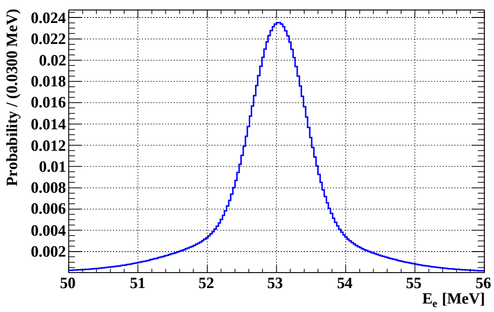

(b)

Figure 13.3: (a) differential distribution of Michel positron energy obtained in a DC trigger data sample used as PDF for accidental background; (b) PDF for e^+ momentum in case of $\mu \rightarrow e\gamma$ events.

Relative time The positron time measured by the scintillation counters is corrected for the time of flight of the positron from the target to the TC, as measured by the track-length in the spectrometer. The photon time is determined by extracting the individual LXe PMT timings from the waveforms and fitting the time distribution over the whole calorimeter taking into account the line of flight from the positron vertex on the target to the reconstructed interaction point in the LXe detector.

In Figure 13.4 the relative time distribution between the positron and the photon in a normal physics run in the energy side band is shown: the RMD peak (in the energy side-band) is clearly visible on top of the accidental background events. The $\Delta T_{e\gamma}$ peak is fitted in the region of 40 MeV $\leq E_\gamma \leq$ 45 MeV and, by taking into account a small E_γ dependence observed in the CEX runs, the timing resolution for the signal is estimated to be $\sigma_{\Delta T_{e\gamma}} = (148 \pm 17)$ ps. The relative time between the LXe detector and the TC was monitored over the whole data taking period with the observed RMD time peak in runs at normal intensity and the CW boron calibration, and found to be stable within 20 ps.

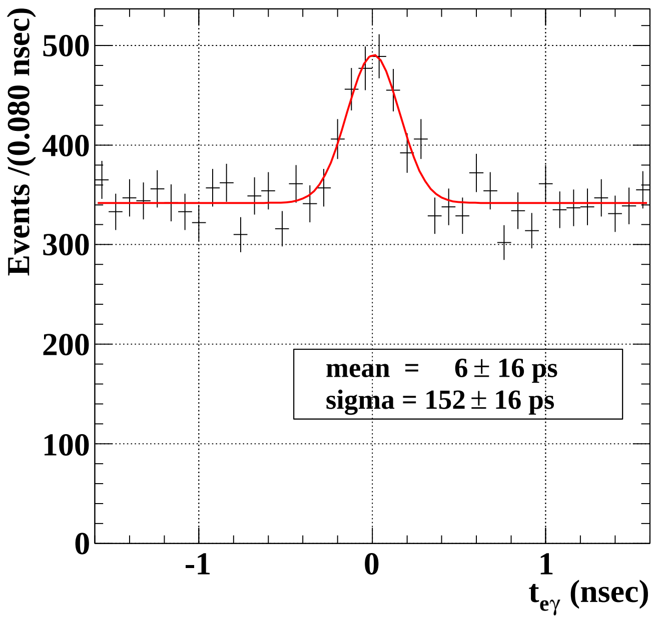

Figure 13.4: Radiative muon decay peak in $\Delta T_{e\gamma}$ in normal physics runs.

Relative angle The positron emission direction and muon decay vertex on the target are determined by projecting the positron track back to the target. The γ-ray flight direction is defined by the line linking the muon decay vertex with the reconstructed photon interaction point in the LXe detector. The resolution of the relative angle between the two particles is evaluated by combining the angular resolution and the vertex position resolution in the positron detector and the position resolution in the photon detector.

$$\sigma_{\theta_{e\gamma}} = (\sigma_{\varphi_{LXe}} \oplus \sigma_{\theta_{LXe}}) \otimes \sigma_{\theta e\gamma_{trk}} \otimes (\sigma_{x,z_{trk}} \oplus \sigma_{y_{trk}}) \tag{13.2}$$

The positron angular resolution is measured by exploiting tracks that cross twice the spectrometer, where each turn is treated as an independent track. The θ- and φ-resolutions are extracted separately from the difference of the two track segments at the point of closest approach to the beam-axis and are $\sigma_\theta = 18$ mrad, $\sigma_\varphi = 10$ mrad. Due to this difference, $\theta_{e\gamma}$ and $\varphi_{e\gamma}$ are treated separately in the analysis.

The vertex position resolutions are measured to be ≈ 3.2 mm and ≈ 4.5 mm in the vertical and horizontal directions on the target plane respectively, by looking at the reconstructed edges of several holes made in the target for this purpose (see Figure 3.7). In Figure 13.5 the fit results are reported.

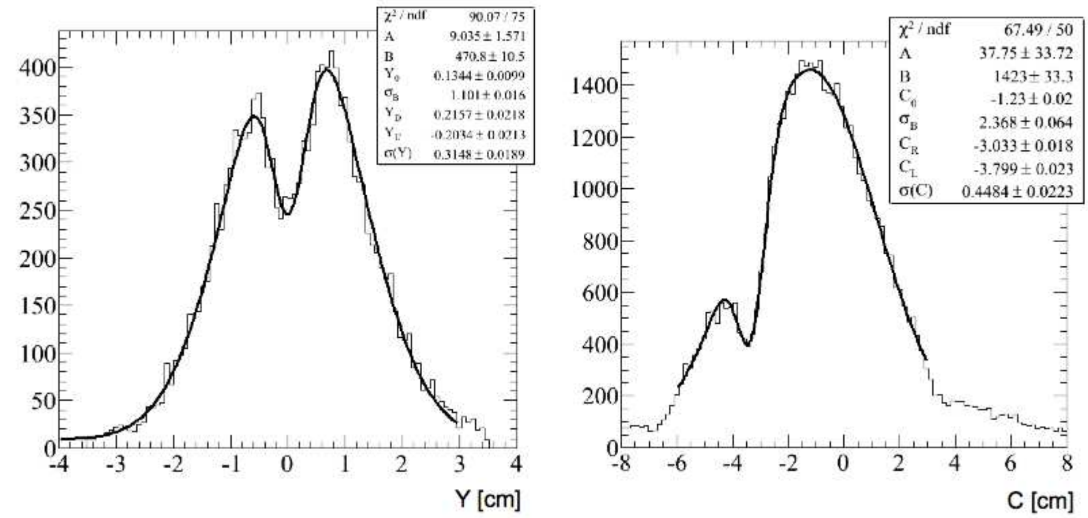

(a) (b)

Figure 13.5: Positron position resolution measured on the holes edges, (a) vertical direction, (b) horizontal direction; The resolution is given by the parameters σ(Y) in (a) and σ(C) in (b).

The photon interaction point is reconstructed by using the distribution of the light seen by the PMTs in the inner face. The performance of the position reconstruction is evaluated by a Monte Carlo simulation and it is validated in a dedicated CEX experiment by placing a lead collimator equipped with horizontal and vertical slits in front of the photon detector. The average position resolutions along the LXe surface and in the radial (w) directions are estimated to be ≈ 5 mm and ≈ 6 mm respectively (see Figure 13.6).

Combining the individual resolutions one gets the following values for the relative positron-gamma angle resolution $\sigma_{\theta_{e\gamma}} = 21$ mrad and $\sigma_{\varphi_{e\gamma}} = 14$ mrad; in Figure 13.7 the PDFs are reported.

13.2.2 Radiative muon decay

The $\mu^+ \to e^+ \nu_e \overline{\nu}_\mu \gamma$ decay kinematical boundaries correlate the E_γ value with $|\vec{p}_{e^+}|$ and the relative angle. The PDF that describe this correlation is obtained by folding the theoretical distribution of the radiative μ decay products [2] with the experimental resolutions reported in section 13.2.1. These are corrected for the direction match efficiency bias in the opening angle as described in section 11.3 and reported in Figure 11.8. The PDF of the time coincidence is the same used for signal events.

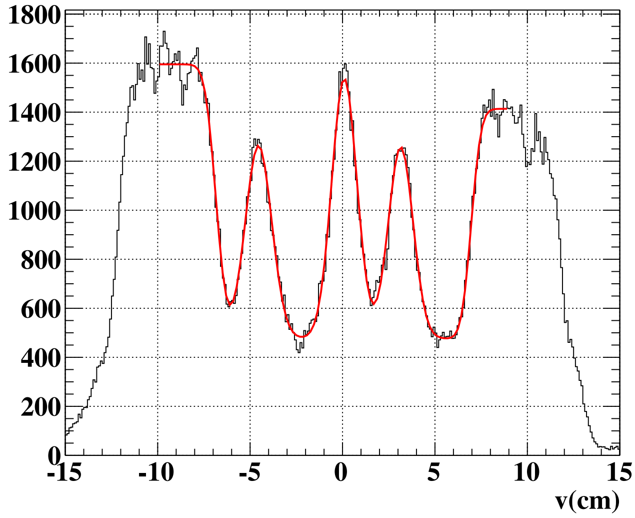

Figure 13.6: Histogram of the number of events recorder in the LXe colorimeter in the region in front of the lead collimator.

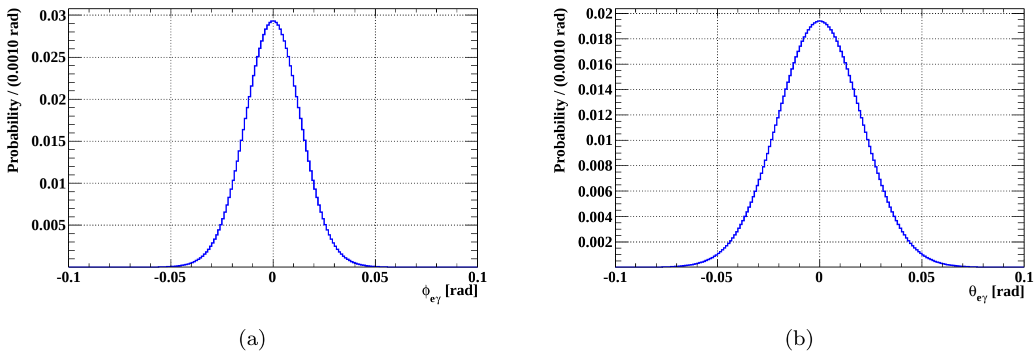

Figure 13.7: PDFs in case of $\mu \to e\gamma$ events for $\varphi_{e\gamma}$ (a) and $\theta_{e\gamma}$ (b).

13.2.3 Accidental background

The accidental background is given by a gamma and a positron in time and spatial coincidence coming from different μ decays. There are no correlations between E_γ, $|\vec{p}_{e^+}|$ and the opening angle and the global PDF is the product of the single distributions.

The gamma energy distribution is given by the radiative muon decay spectrum mixed with the contribution of the annihilation flight; the latter one is prevalent for energies close to the end-point. The resulting spectrum is fitted from the time side-band data using the theoretical spectrum folded with the experimental resolution; accidental γ pile-up in the calorimeter are also included in the fit and this well explain the measured right tail of the distribution. The E_γ PDF is reported in Figure 13.8.

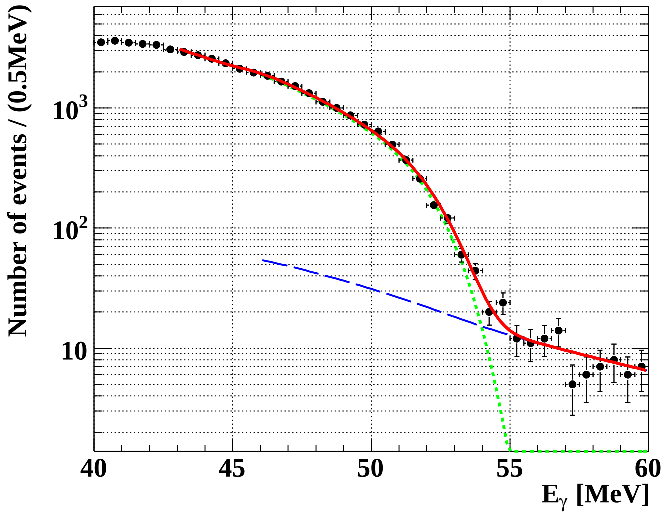

Figure 13.8: PDF for E_γ in case of accidental background; the continuous red line is the PDF, the dotted green line is the RMD and annihilation in flight spectrum and the dashed blue line is the contribution of pile-up.

The PDF for the positron momentum is the normalized Michel spectrum shown in Figure 13.3 (a). This is obtained by the analysis of all the side-band data and an independent data-set acquired with the Timing Counter trigger, namely trigger #22 (see section 5.2).

The relative time PDF is a flat distribution, as expected in case of accidental background.

The PDF for $\varphi_{e\gamma}$ and $\theta_{e\gamma}$ are extracted from all the side-bands data. The distributions are expected to be flat in $\varphi_{e\gamma}$ and $\cos(\theta_{e\gamma})$ but this is not the case. The experimental data are biased by the direction match online selection and also by the detector acceptance effects. For this reason a map of the φ and θ PDFs is performed around 8 possible directions. In Figure 13.9 one example for φ and one for θ are reported.

13.3 Likelihood fit

A likelihood analysis was adopted by the MEG collaboration because it is almost independent of the analysis region size and it is not sensitive to edge effects as in the case of a box analysis. The effects of systematics can also be easily taken into account.

The blinding box is opened after completing the optimization of the analysis algorithms and the background study. The number of $\mu^+ \to e^+\gamma$ events in the analysis region was $N_{obs} = 1189$. The analysis region is defined as $46 \leq E_\gamma \leq 60$ MeV, $50 \leq E_{e^+} \leq 56$ MeV, $|\Delta T_{e\gamma}| \leq 1$ ns,

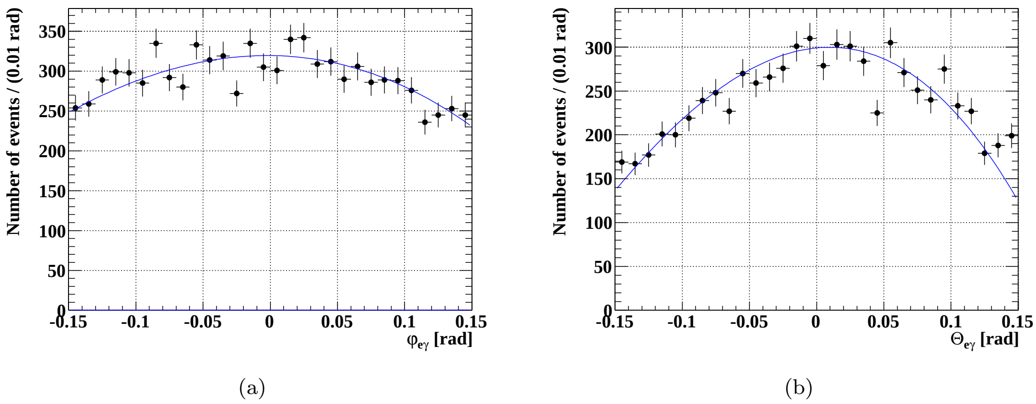

Figure 13.9: PDFs in case of accidental background events for $\varphi_{e\gamma}$ (a) and $\theta_{e\gamma}$ (b).

$\theta_{e\gamma} \leq 100$ mrad and $\varphi_{e\gamma} \leq 100$ mrad.

An extended likelihood function $\mathcal{L}$ is defined as:

$$\mathcal{L}(N_{Sig}, N_{RD}, N_{BG}) = \frac{N^{N_{obs}} e^{-N}}{N_{obs}!} \prod_{i=1}^{N_{obs}} \left[\frac{N_{Sig}}{N} S + \frac{N_{RD}}{N} R + \frac{N_{BG}}{N} B \right] \tag{13.3}$$

where N_{Sig}, N_{RMD} and N_{BG} are the number of $\mu \to e + \gamma$, RMD and accidental background (BG) events, respectively, while S, R and B are their respective probability density functions (PDFs). $N_{obs}(= 1189)$ is the total number of events observed in the analysis window and $N = N_{Sig} + N_{RMD} + R_{BG}$. The signal PDF S is the product of the statistically independent PDFs for the five observables (E_γ, $|\vec{p}_{e^+}|$, $\Delta T_{e\gamma}$, $\theta_{e\gamma}$ and $\varphi_{e\gamma}$), each one defined by its corresponding detector response function with the measured resolutions, as described in the previous section. The dependence of the photon PDFs on gamma ray conversion position is taken into account, together with all their proper normalizations.

The likelihood fit has been initialized with the number of expected RMD events in the analysis region. This number is obtained by scaling the number of events in the peak of $\Delta T_{e\gamma}$ distribution in E_γ side-band for the ratio of the PDFs in the analysis region and the E_γ side band. A further scaling takes into account the different efficiency of the online direction match selection in the side-band region with respect to the analysis one:

$$\begin{array}{lll} 44 \leq E_\gamma \leq 48 \text{ MeV} & \text{Side} - \text{Band} & \varepsilon_{DM}^{RMD} = 45.5\% \\ 48 \leq E_\gamma \leq 57.6 \text{ MeV} & \text{Analysis Region} & \varepsilon_{DM}^{RMD} = 49\% \end{array}$$

The predicted RMD events used in the likelihood fit initialization is 32 ± 10.

The maximum likelihood fit results are:

$$\begin{aligned} N_{Sig} &= 4.3\ (+3.9\ \ -2.9)\ \text{events} \\ N_{RD} &= 25.0\ (+16.9\ \ -16.1)\ \text{events} \\ N_{BG} &= 1159\ (+38\ \ -37)\ \text{events} \end{aligned}$$

The fitted number of RD events agrees with the expected one within the errors. The result of the fit is shown for the 5 variables in Figure 13.10: (a) E_γ distribution, (b) $|\vec{p}_{e^+}|$, (c) $\Delta T_{e\gamma}$, (d) $\varphi_{e\gamma}$ and (e) $\theta_{e\gamma}$.

13.4 CL scan

The 90% confidence level intervals (CL) is determined by the Feldman-Cousins frequentistic approach [53].

The CL scan is performed in the [N_{Sig}, N_{RD}] plane. The starting point of the procedure is the maximum likelihood fit result, $N_{Sig} = 4.3$ and $N_{RD} = 25$. Several sets of pseudo-experiments (1000 toy-experiments per point) are generated at several different "true" (i.e. generated) values in the plane. The generation is based on the measured PDFs distribution; the total number of generated events are the number of events in the blinding box, the number of generated signal and RD events in the toy-experiments are $N^{ToyTrue}_{Sig/RD} = N_{Sig/RD} \pm\ X$ with X = 1,2,3... ; these numbers are free to fluctuate around the nominal value by means of the poissonian distribution.

The maximum likelihood fit is then applied to all the toy-experiments in order to extract $N^{ToyMeas}_{Sig/RD}$. The starting point of the CL definition is the likelihood ration ordering principle. Let's define:

$$r_{likeli}(N^{ToyMeas}_{Sig/RD}) \;=\; \frac{\mathcal{L}(N^{ToyMeas}_{Sig/RD} \mid N^{ToyTrue}_{Sig/RD})}{\mathcal{L}(N^{ToyMeasBest}_{Sig/RD} \mid N^{ToyTrue}_{Sig/RD})} \tag{13.4}$$

r_{likeli} is $\leq\ 1$ by definition; $r_{likeli} = 1$ for the toy-experiment that, after the fit, has the maximum likelihood value $\mathcal{L}(N^{ToyMeasBest}_{Sig/RD} \mid N^{ToyTrue}_{Sig/RD})$.

The toy-experiments are ordered by a decreasing order. If, after the ordering, a fraction ≤ 90 % of these experiments has a r_{likeli} value better than that of the real experiment, the corresponding point belongs to the 90% CL region of the MEG result. A typical contour plot is reported in Figure 13.11 with the CL regions at 68%, 90% and 95% for two hypothetic and uncorrelated quantities A and B. The CL region at 68% is a double-sided interval for both A and B, began single-ended for A at 90% CL and is finally single-ended in both case at 95% CL.

The scan in the N_{Sig} direction is reported in Figure 13.12. The obtained 90% CL region is:

$$N_{Sig} \leq 14.7\ @\ 90\%\ \text{CL} \tag{13.5}$$

therefore an upper limit for the $\mu \rightarrow e\gamma$ process is measured.

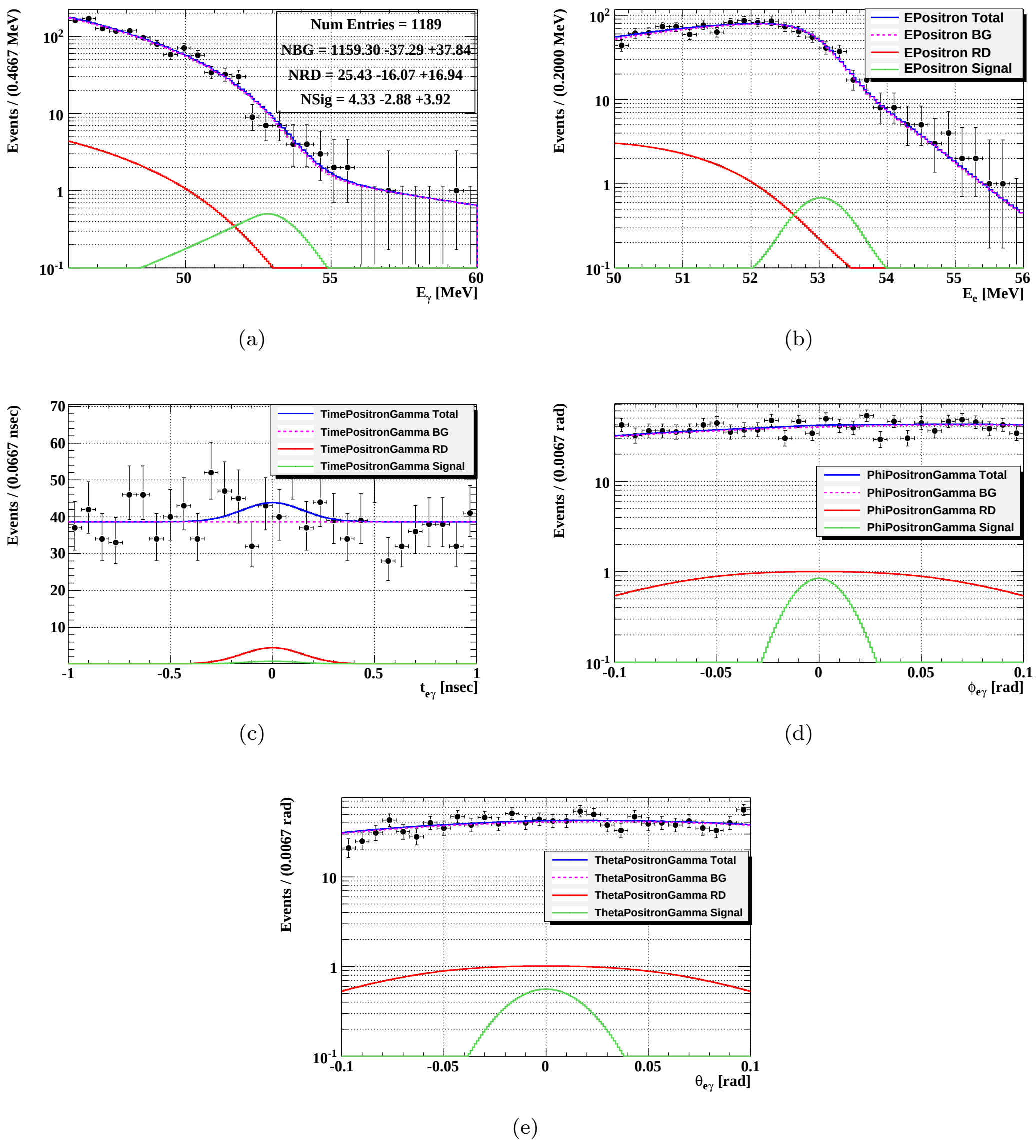

Figure 13.10: Data distribution superimposed with the S, R and B PDFs resulting from the Likelihood fit; (a) E_γ distribution, (b) $|\vec{p}_{e^+}|$, (c) $\Delta T_{e\gamma}$, (d) $\varphi_{e\gamma}$ and (e) $\theta_{e\gamma}$.

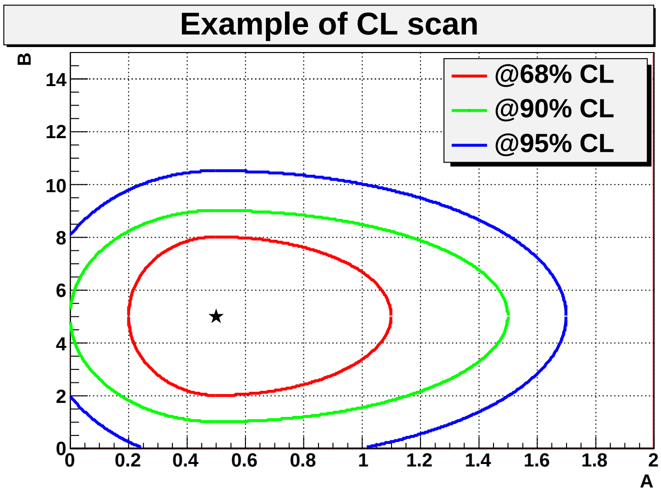

Figure 13.11: Qualitative example of CL scan in a hypothetic (A,B) plane.

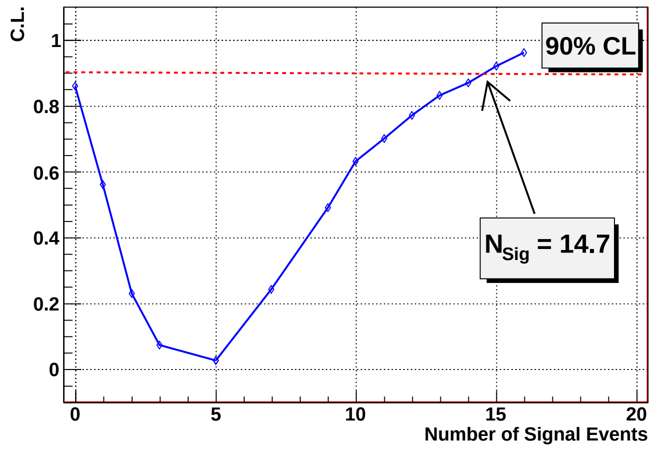

Figure 13.12: N_{Sig} CL scan; the CL band is one sided, 0 is included in the band.

Sensitivity evaluation The sensitivity of the experiment can be verified on the $\Delta T_{e\gamma}$ side bands where the RMD background is not present. The full likelihood analysis performed in the side bands assumes $N_{RD} = 0$ and the upper limit on N_{Sig} is derived. It is $N_{Sig} \leq 4.6$ in the left side-band and $N_{Sig} \leq 10.4$ in the right one. Monte Carlo simulation of the experiments gives a limit on the number of expected equal $N_{Sig} \leq 6.5$ consistent with side-band analysis. In the analysis region we were affected by a over fluctuation of the background.

13.5 Results for 90% CL upper limit

The conversion of an upper limit on the observed number of signal events into an upper limit on the $\mu^+ \to e^+\gamma$ decay branching ratio is given in Equation (12.1).

The procedure for the extraction of the k-factor was described in chapter 12 and that for extracting the number of events in the previous paragraphs.The limit is therefore:

$$\mathrm{B}(\mu^+ \to \mathrm{e}^+\gamma) \; = \; \frac{\mathrm{N}_{\mu\to\mathrm{e}\gamma}}{\mathrm{k}} \; \leq \; 2.8 \cdot 10^{-11} \text{ @ } 90\% \text{ CL} \tag{13.6}$$

The obtained upper limit can be compared with the branching ratio sensitivity of the experiment with this data statistics. The sensitivity is defined as the upper limit of the branching ratio, averaged over an ensemble of experiments, which are simulated by means of a toy Monte Carlo, assuming a null signal and the same numbers of background and RMD events as in the data. The branching ratio sensitivity in this case was estimated to be 1.3×10^{-11}, which is comparable with the current branching ratio limit set by the MEGA experiment [14]. Given this branching ratio sensitivity, the probability to obtain an upper limit 2.8×10^{-11} is $\approx$ 5%, when systematic uncertainties in the analysis are taken into account.

Chapter 14

Conclusions and prospects

The new frontier experiments in particle physics are testing the current model of the fundamental interactions, the Standard Model, searching for evidence of new physics.

The probability of a process is proportional to the energy available in the system compared to the energy scale of the interaction under study.

New physics discovery is then lead on one hand by increasing the energy of the particle interactions and on the other searching for unpredicted processes with high sensitivity measurements, searching for processes at higher $E_{\mathrm{NewPhysics}}$ scale. This document discusses an attempt at the discovery of the Lepton Flavor Violation in the muon sector, which is predicted to be the probe to test possible extensions of the Standard Model. Starting from the theoretical motivations the architecture and the principles of the MEG experiment are discussed, together with the results of the first period of data taking.

Some extensions of the Standard Model, based on Supersymmetric and Grand Unification assumptions, suggest the LFV in the charge sector to be a powerful candidate in the new physics discovery challenge. The highest experimental sensitivity achievable with the current technology in the LFV search is in the $\mu^+ \to \mathrm{e}^+\gamma$ decay. In order to reach the goal sensitivity on the branching ratio of the order of 10^{-13} a new technology based on the LXe calorimetry, which is used to measure the γ observables, has been developed by the MEG collaboration. The LXe guarantees a high light production, as inorganic scintillators, coupled with a fast response, as organic scintillators. The positrons are tracked in a light drift chamber system immersed in a not uniform magnetic field, the time of flight is measured by means of scintillators bars at the end of the positron track.

In this document particular attention is dedicated to the trigger system. A custom electronic system composed by three different electronic boards has been designed to perform the online selection on programmable digital circuits. The trigger system calibration methods are described in details so as the efficiency measurement methods.

A search for the lepton flavor violating decay $\mu^+ \to \mathrm{e}^+\gamma$ was performed with a branching ratio sensitivity of $1.3 \cdot 10^{-11}$, using the data taken during the first three months period of the MEG experiment in 2008. With this sensitivity, which is comparable with the current branching ratio limit set by MEGA experiment, a blind likelihood analysis yields an upper limit on the branching ratio $B(\mu^+ \to e^+\gamma) \leq 2.8\times 10^{-11}$ (90% C.L.).

The RUN2008 started in the middle of September and ended the 17th of December. The effective running time dedicated to the MEG trigger was around 50 days corresponding to $\approx 9.5 \cdot 10^{13}$ muons stopping in the target being the beam rate $3.67 \cdot 10^7$ μ/s and the stopping efficiency measured of about 82%. Both the LXe detector and the tracking system suffered from hardware instabilities: the LXe purity in the calorimeter increased during the run, modifying slightly the response of the detector to the γ radiation, while the DC system suffered from several HV trips leading to a loss in the tracking reconstruction capability.

The trigger selection efficiency has been measured to be equal to 66% associated to an event rate of about 6.6 Hz corresponding to a DAQ live time equal to 84%. Defining a global DAQ efficiency to be the product of the trigger efficiency and the DAQ live time, it is equal to 56%. The single event sensitivity for the run is computed to be $1.9 \cdot 10^{-12}$. It is based on the Michel event count using the pre-scaled trigger in the physics data stream.

The physics analysis scheme is a blind likelihood analysis. A region in the [E_γ, $\Delta T_{e\gamma}$] plane is hidden to the analysis developers, the detector response functions are modeled and calibrated using no candidate signal data. The number of signal events in the MEG analysis box is extracted by means of a maximum likelihood fit to the spectra with the modeled PDFs for signal, radiative decay and accidental background. The 90% CL is extracted following the Feldman and Cousins prescription and it is found to be 2.8×10^{-11}.

RUN2009 preliminary results The problem of the reduced performance of the drift chambers, due to high voltage trips, was solved and the chambers functioned successfully during the 2009 run period. Additional maintenance to the LXe detector has also resulted in a near optimal light yield.

The experience of the run 2008 leads to an improvement of the trigger efficiency up to 85.4%. The goal of the 95% will be accomplished during the 2010 by using the TC fiber signals and an improved data read out scheme. The extreme stability of the LXe light yield allows us to increase the E_γ threshold up to 44 MeV. In this configuration the DAQ rate has been measured to be around 7 Hz reflected in a DAQ live time around 82% being the DAQ efficiency 70%.

The DRS chip was updated for the 2009 run. It has a very good linearity response inside the 0-1V dynamic range needed to reach the goal resolution in E_γ. A unexpected problem in the synchronization between chips in different VME boards deteriorated the experimental time resolution. It has now been solved in the 2010 data taking run.

Despite the run last for only 1 month, half with respect to the RUN2008, the statistics collected is almost a factor 2 larger than in 2008, the detector resolution are also improved. Table 14.1 reports a direct comparison between RUN2008 and RUN2009 in terms detector resolutions and efficiencies.

The improvement in the tracking system performance is reflected in an dramatic increase in the average number of hits usable by the reconstruction algorithm. The resolution on the trajectory parameter reconstruction in the 2009 are a factor 2 better with respect to the 2008, particularly

Parameter	RUN2008	RUN2009 preliminary
$\Delta E_\gamma / E_\gamma$	5.8% FWHM	5% FWHM
$\Delta E_e / E_e$	3.5% FWHM	1.75% FWHM
$\Delta\theta_{e\gamma}$	52 mrad FWHM	26 mrad FWHM
$\Delta T_{e\gamma}$	350 ps FWHM	420 ps FWHM
DAQ efficiency	56%	70%
SES	$1.9 \cdot 10^{-12}$	$1 \cdot 10^{-12}$

Table 14.1: RUN2008 to RUN2009 comparison.

important in case of the relative angle, because the accidental background rejection power depends quadratically from the $\theta_{e\gamma}$ resolution. The improvement is clearly shown in Figure 14.1.

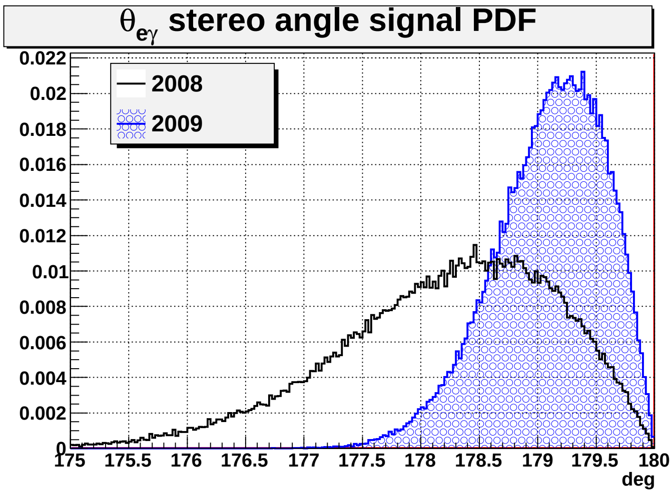

Figure 14.1: Stereo $\theta_{e\gamma}$ signal PDF in 2008 (black plain) and 2009 (blue filled).

The run sensitivity is evaluated by exploiting the same analysis scheme as in 2008. The PDFs for signal and background events were carefully studied to take into account systematic correlations between positron and gamma observables, these correlations are currently under study. The branching fraction sensitivity at 90% C.L. is $6.1 \cdot 10^{-12}$ from the Toy Monte Carlo analysis and $4 \div 6 \cdot 10^{-12}$ from side band data.

The best estimates from the maximum likelihood fit to the $N_{obs} = 370$ events observed in the analysis window is $N_{sig} = 3.0$. The 90% confidence intervals for N_{sig} are calculated by means of a toy Monte Carlo simulation with likelihood ratio ordering principle. The systematic uncertainties for the parameters of the likelihood function and the normalization factor are taken into account in the calculation of the confidence intervals by fluctuating the likelihood functions according to the uncertainties. The largest contributions to the systematic error amounting to 23% of the total error come from the energy scale calibrations, (E_e-φ_e)-correlation and $T_{e\gamma}$-resolution. The 90%

C.L. upper limit for N_{sig} is calculated to be 14.52, with Nsig = 0 inside the 90% confidence interval. This translates into an preliminary upper limit for the branching fraction, using the normalization factor, as

$$B(\mu^+ \to e^+\gamma) \;=\; \frac{N_{\mu\to e\gamma}}{k} \;\leq\; 1.5 \cdot 10^{-11} \text{ @ } 90\% \text{ CL} \tag{14.1}$$

for the 2009 run.

In Figure 14.2 we present the distribution of the events around the signal region projected in the E_e vs E_γ and $\cos(\theta_{e\gamma})$ vs $T_{e\gamma}$ planes, $\theta_{e\gamma}$ being the opening angle between the γ and the positron. In Figure 14.2 (a) a selection that is 90% efficient on the signal is applied on the two variables that are not shown; in Figure 14.2 (b) a selection in E_e which is 90% efficient on the signal and a selection in E_γ which is 42% efficient on the signal are applied on the two variables that are not shown. The contours of the signal PDF are also drawn and the same events in the two plots are numbered correspondingly in a decreasing ranking of relative signal likelihood (S/(R + B)).

Future prospects The $\mu^+ \to e^+\gamma$ branching fraction measurement with a sensitivity around 10^{-13} demands a detection system with the best resolution achievable for the physics variable of the process under study and a careful monitoring by means of dedicated calibration tools.

For the 2010 run a neutron generator is used to induce neutron capture on Ni followed by the emission of 9 MeV photons for the calorimeter calibration. The 9 MeV line is the only possibility for having a physical γ-line in the physics data taking condition, i.e. with the beam blocker open. The neutron emitted by the generator are moderate in a polyethylene brick hosting few layers of Ni. The neutron generator is used as a standard calibration tool in addition to the CW accelerator.

A new calibration method for the tracking system is also operative from the 2010, it takes advantage from the elastic Mott scattering of monochromatic positrons into a dedicated polyethylene target. The positron beam momentum bite has been measured to be $\leq$ 50 keV, so these events can be used to measure the tracker momentum resolution at the signal energy. The Mott events are also used to measure the tracker efficiency and investigate systematic uncertainties in the positron track reconstruction.

In the 2010 run two major hardware upgrades are foreseen. The TC fiber signals will be introduced both in the trigger system and in the offline reconstruction. This will lead to a further improvement in the DAQ efficiency in the online system and in the analysis adding a refined measurement of the positron impact point in the TC detector. The DRS chip synchronization problem has been solved, a substantial improvement in the timing resolution is expected.

Finally a multiple buffer read out scheme will be implemented in the DAQ leading to a dramatic improvement of the DAQ live time.

The MEG experiment will collect statistic until the 2012 when the statistic will be enough to reach the goal sensitivity.

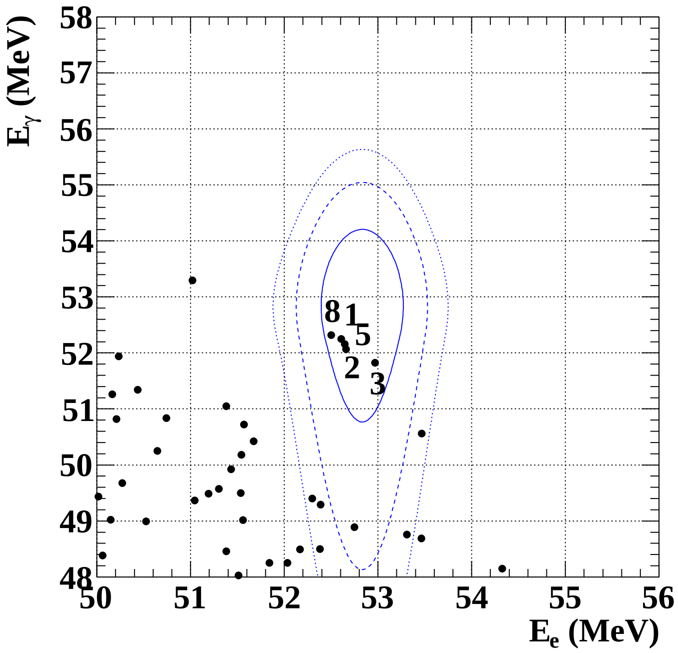

(a)

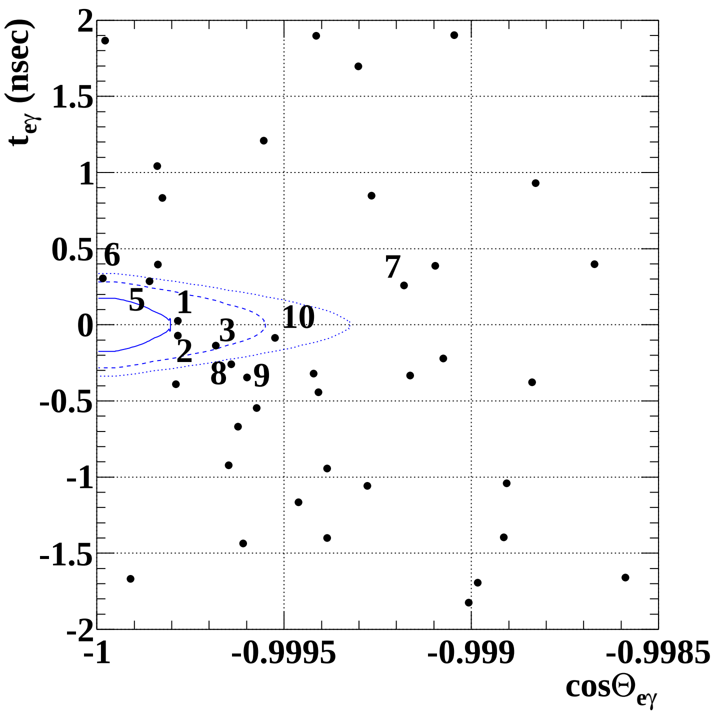

(b)

Figure 14.2: Event distribution in (a) E$_e$-E$_\gamma$ and (b) cos($\theta_{e\gamma}$)-T$_{e\gamma}$ planes around the signal region. The contours of the PDFs (1-, 1.64- and 2-σ) are shown and the same events in the two plots are numbered correspondingly, by decreasing ranking in terms of the relative signal likelihood (S/(R + B)).

Bibliography

[1] F. Halzen, A. D. Martin *et al.*, "Quarks and Leptons: An Introductory Course In Modern Particle Physics", Wiley and Sons (1984).

[2] Y. Kuno and Y. Okada, "Muon Decay and Physics Beyond Standard Model", [arXiv:hep-ph/9909265v] (1999).

[3] Particle Data Group, W.-M. Yao *et al.*, Journal of Physics, HTTP://PDG.LBL.GOV (2006)

[4] D. Chitwood *et al.*, "Improved measurement of the Positive-Muon Lifetime and Determination of the Fermi Constant", Phys. Rew. Lett. **99**, 032001 (2007) .

[5] R. Crittenden *et al.*, Phys, Rev, 121 (1961) 1823.

[6] E. Bertl *et al.*, Nucl. Phys. B **260** (1985) 1.

[7] M. Apollonio *et al.*, the CHOOZ Collaboration, "Search for neutrino oscillations on a long base-line at the CHOOZ nuclear power station", Eur. Phys. J. **C27**, (2003) 331, [arXiv:hep-ex/0301017].

[8] K. Eguchi *et al.*, The KamLAND COllaboration, "First results from KamLAND: Evidence for Reactor anti-neutrino disappearance", [arXiv:hep-ex/0212021].

[9] The K2K Collaboration, E. Aliu *et al*, "Evidence for muon neutrino oscillation in a accelerator-base experiment", [arXiv:hep-ex0411038].

[10] Y. Suzuky, Super-Kamiokande Collaboration, "Neutrino oscillations at Super-Kamiokande", Nucl. Phyw. Proc. Suppl. **81**, 133 (2000).

[11] Q. R. Ahmad *et al.*, SNO Collaboration, "Measuraments of the charged of current interactions produced by 8B solar neutrinos at the Sudbury Neutrino Observatory", [arXiv:nucl-ex/0106015].

[12] G. Giacomelli, A Margiotta and the MACRO Collaboration, "MACRO results on atmosferic neutrinos", Eur. Phys. J. **C36** (2004) 323.

[13] F. Bohem and P. Vogel, "Physics of massive neutrinos", Cambridge University Press (1992).

[14] M. L. Brooks *et al.*, MEGA Collaboration, "New limit for the lepton-family -number non-conserving decay $\mu^+ \to e^+\gamma$ ", Phys. Rev. D **65** (2002) 112002 [arXiv:hep-ex/ 0111030].

[15] A. Masiero, S. K. Vempati and O. Vives, "Flavour Physics and Grand Unification" [arXivhepph/:0711.2903v1]

[16] R. N. Mohapatra, "Unification and Supersymmetry: The Frontiers of Quark- Lepton Physics", 2nd Edition, Springer-Verlag (1992).

[17] H. Georgi and S. L. Glashow, Phys. Rew. Lett. **32**, 438 (1974).

[18] H. Fritzsch and P. Minkowski, Ann. Rew. Lett. **93**, 193 (1975).

[19] H. Georgi, and D. V. Nanopoulos, Nucl. Phys. B **155**, 52 (1979).

[20] R. Barbieri e L. J. Hall, "Signals for supersymmetric unification", Phys. Lett. B **338**, 212, (1994) [arXiv:hep-ph/9408406].

[21] R. Barbieri, L. J. Hall e A. Strumia, Nucl. Phys. B **445**, 219 (1995a).

[22] R. Barbieri, L. J. Hall e A. Strumia, Nucl. Phys. B **449**, 437 (1995b).

[23] J. Äystö *et al.*, "Physics with low energy muons at a neutrino factory", CERN-TH/2001-231.

[24] L. Calibbi *et al.*, "Lepton flavor violation from supersymmetric grand unified theories: where do we stand for MEG, PRISM/PRIME, and a super flavor factory", Phys. Rew. D **74**, 116002 (2006).

[25] D. Bettoni *et al.*, "The high intensity frontier", Physics Reports **434** (2006), 47-111.

[26] Bellgart *et al.*, Nucl. Phys. B **229**, 1 (1998).

[27] Wintz, 1998, "Proceedings of the First International Symposium on Lepton and Baryon Number Violation", edited by H. V. Klapdor-Kleingrothaus and I. V. Krivosheina, p. 534.

[28] Van Der Schaaf *et al.*, NOON03 Conference Proceedings, 2003.

[29] B. Aubert *et al.*, BaBar Collaboration, "Search for Lepton Flavor Violation in the Decay $\tau^\pm \to e^\pm\gamma$ and $\tau^\pm \to \mu^\pm\gamma$" PRL 'textbf104, 021802 (2010).

[30] K. Hayasaka *et al.*, Belle Collaboration, "Search for Lepton Violating Decays into Three Leptons with 719 Million Produces $\tau^+\tau^-$ Pairs" (2010) [arXiv:hep-ex/1001322].

[31] Krolak *et al.*, Phys. Lett. B **(**320), 407 (1994).

[32] Ambrose *et al.* (BNL E871 Collaboration) Phys, Rew. Lett. **81** 5373 (1998).

[33] Lee *et al.*, Phys. Rew. Lett. **64**, 165 (1990).

[34] L. Bellantoni *et al.* [KTev Collaboration], Proc. 36th Rescontres de Moriond (Les Arcs, France) 10-17 Mar 2001 [arXiv:hep-ex/0107045].

[35] Akers *et al.* (OPAL Collaboration) Z. Phys. C **73**, 243 (1997).

[36] Abreu *et al.* (DELPHI Collaboration) Z. Phys. C **43**, 243 (1997).

[37] L. Calibbi *et al.*, "Lepton flavor violation from supersymmetric grad unified theories: Where do we stand for MEG, PRISM/PRIME, and a super flavor factory", Phys. Rew. D **74**, 116002 (2006).

[38] J. Kaulard *et al.*, Phys. Lett. B **422** (1998) 334.

[39] S. Machida *et al.*, Letter of intent to J-PARC, LOI-25, 2003.

[40] S. Machida *et al.*, Letter of intent to J-PARC, LOI-24, 2003.

[41] M. J. Syphers, "Accelerator Preparations for Muon Physics Experiments at Fermilab", [arXiv:0910.3657v1]

[42] Proposal P-973 submitted to Fermilab, 10 Oct. 2008; available as, MU2E-doc-388 (2008), HTTP://MU2E-DOCDB.FNAL.GOV.

[43] S. H. Neddermeyer and C. D. Anderson, Phys. Rev. **52** (1937) 884.

[44] M. Conversi, E. Pancini and O. Piccioni, Phys. Rev. **71** (1947) 209.

[45] E. P. Hincks and B. Pontecorvo, Phys. Rev. **77** (1950) 102.

[46] P. Depommier *et al.*, "A New Limit on the $\mu^+ \to e^+\gamma$ decay", Phys. Rev. Lett. **39**, 1113 (1977).

[47] A. Van der Schaaf *et al.*, "A Search for the decay $\mu^+ \to e^+\gamma$ ", Nucl. Phys. A **340**, 249 (1980).

[48] W. W. Kinnison *et al.*, "A Search for $\mu^+ \to e^+\gamma$ ", Phys. Rev. D **25**, 2846 (1982).

[49] R. D. Bolton *et al.*, "Search for the decay $\mu^+ \to e^+\gamma$, Phys. Rev. Lett. **56**, 2461 (1986).

[50] MEGA Collaboration, "Search for the lepton-family-number non-conserving decay $\mu^+ \to e^+\gamma$ ", Phys. Rev. D **65** (2002) 112002.

[51] Paul Scherrer Intitut Villigen (AG) Swizerland, WWW.PSI.CH .

[52] L. Lyons, "Statistics for nuclear and particle physicists", 1986.

[53] G. J. Feldman and D. Cousins, "Unified approach to the classical statistical analysis of small signals", Phys. Rew. D **57** (1998) 3873.

[54] A. E. Pifer *et al.*, "A high stopping density beam", NIM 135 (1976) 39.

[55] H-W. Reist *et al.*, "Development of a low momentum surface muon' beam for LAMPF", NIM 153 (1978) 61.

[56] TRASPORT - "A Computer Program for Designing Charged Particle Beam Transport Systems", K. L. Brown et al., CERN, Yellow Report 73-16, (1973).

[57] Deay TURTLE - A Computer Program for Designing Charged Particle Beam Transport Systems, including Decay Calculations, K. L. Brown and Ch. Iselin, CERNTellow Report 74-2 (1974).

[58] T. Mori *et al.*, "Search for the $\mu \to e\gamma$ down to 10^{14} branching ratio", proposal to PSI (1999).

[59] GEANT - "Detector Description and Simulation Tool', Application Software Group CERN, CERN Program Library Writeup W5013 (1993).

[60] W. Ootani et al., "Development of a Thin-wall Superconducting Magnet for the Positron Spectrometer in the MEGExperiment", IEEE Trans. Appl. Superconductivity 14 (2005).

[61] H. Nishiguchi, "The MEG positron spectrometer", NIM-A **581** (2007) pp. 538-541

[62] H. Nishiguchi, "An Innovative Positron Spectrometer to Search for the Lepton Flavour Violating Muon Decay with a Sensitivity of 10^{-13}", doctoral thesis, March 2008, University of Tokyo

[63] J. Allison, et al., Nucl. Instr. and Meth. A 310 (1991) 527.

[64] R. Frühwirth, *et al.*, Data Analysis Techniques for High-Energy Physics, Cambridge University Press, Cambridge, 2000.

[65] A. Baldini *et al.*, "Liquid Xe scintillation calorimetry and Xe optical properties" [arXiv:physics/0401072].

[66] G. Signorelli, "A sensitive search for lepton-flavour violation: the MEG experiment and the new LXe calorimetry", PhD thesis, Pisa Scuola Normale Superiore (2002).

[67] A. Papa, "Search for the Lepton Flavour Violation in $\mu \to e\gamma$. The calibration methods for the MEG experiment.", Doctoral thesis at Pisa University (2004).

[68] G. Gallucci," Studio della prestazione del calorimetro elettromagnetico dell'esperimento MEG", master thesis at Pisa University (2006, in Italian).

[69] HAMAMATSU Photonics, http://www.hamamatsu.com.

[70] MEG Pisa, Technical notes 014; http://meg.pi.infn.it.

[71] A. Baldini, C. Bemporad, F. Cei, M. Grassi, D. Nicol'o, A. Papa, R. Pazzi, G. Signorelli, "Considerations on the Calibration and Monitoring of the MEG experiment", 2005.

[72] Analog Devices, AD8009, 1 GHz 5500 V/μs Low Distortion Differential, documentation available at WWW.ANALOG.COM.

[73] Texas Instruments, THS4500, wideband, low-distortion, fully differential amplifiers, documentation available at WWW.FOCUS.TI.COM.

[74] Analog Devices, AD8138, Low Distortion Differential ADC Driver, documentation available at WWW.ANALOG.COM.

[75] S. Ritt, "The DRS2 Chip: a 4.5 GHz Waveform Digitizing Chip for the MEG Experiment", proceedigs for IEEE 2004.

[76] S. Ritt, "Design and Performance of the 6 GHz Waveform Digitizing Chip DRS4", proceedings for IEEE 2006.

[77] MIDAS home page, WWW.XILINX.COM.

[78] L. Galli, 2008 IEEE Nuclear Science Symposium Conference Record "An FPGA-based for the search of $\mu^+ \to e^+\gamma$ decay in the MEG experiment";

[79] L. Galli, 2009 IEEE Nuclear Science Symposium Conference Record "An FPGA-based for the search of $\mu^+ \to e^+\gamma$ decay in the MEG experiment";

[80] Analog Devices, AD9218, 10-bit 3V Dual A/D Converter, documentazione disponibile sul sito internet WWW.ANALOG.COM.

[81] VirtexII-pro, documentation available at WWW.XILINX.COM.

[82] Xilinx, Virtex II Pro and Virtex II Pro X FPGA users guide, UG12(v3.0) (2004) WWW.XILINX.COM.

[83] Xilinx, Virtex II Pro Platform FPGAs: Complete Data Sheet, DS083 (2004) WWW.XILINX.COM.

[84] DS90CR481/DS90CR483 48-bit LVDS Channel Link SER/DES-65-112 MHz, documentation at WWW.NATIONAL.COM.

[85] Cypress, High-speed Multi-phase PLL clock Buffer, documentation at WWW.DATASHEETCATALOG.COM.

[86] Analog Devices, AD5300, Rail to Rail Output 8-bit DAC, documentation available at WWW.ANALOG.COM.

[87] SaRonix, Crystal Clock Oscillator, documentation available at WWW.PERICOM.COM/SARONIX.

[88] Maxim, Low-Jitter 800 Mbps 10-Port LVDS Repeaters, documentation available at WWW.MAXIM-IC.COM.

[89] Monolithic 8-bit programmable delay line, documentation available at WWW.DATADELAY.COM.

[90] DMOS, 1A Low-Dropout Regulator, documentation available at FOCUS.TI.COM

[91] J. Adam *et al.*, MEG Collaboration, "A limit for the $\mu \to e\gamma$ decay from the MEG experiment", Nucl. Phys. B, doi:10.1016/j.nuclphysb.2010.03.030, [arXiv:0908.2594v2];